Experimental Characterization of Cryogenic Helium Pulsating Heat Pipes

By

Luis Diego Fonseca Flores

A dissertation submitted in partial fulfillment of

the requirements for the degree of

Doctor of Philosophy
(Mechanical Engineering)

at the

UNIVERSITY OF WISCONSIN-MADISON
2016

Date of final oral examination: 12/15/2017

The dissertation is approved by the following members of the Final Oral Committee:

Franklin Miller, Professor, Mechanical Engineering
John Pfotenhauer, Professor, Mechanical Engineering
Gregory Nellis, Professor, Mechanical Engineering
Douglas Reindl, Professor, Engineering Professional Development
Frank Pfefferkorn, Professor, Mechanical Engineering

Experimental Characterization of Cryogenic Helium Pulsating Heat Pipes

Under the supervision of Professors Franklin Miller and John Pfotenhauer at the University of Wisconsin-Madison

Abstract

This study was inspired to investigate an alternative cooling system using a helium-based pulsating heat pipes (PHP), for low temperature superconducting magnets in MRI systems. In addition, the same approach can be used for exploring other low temperature applications such as cooling space instrumentation. The advantages of PHP for transferring heat and smoothing temperature profiles in various room temperature applications have been explored for the past 20 years. An experimental apparatus has been designed, fabricated and operated and is primarily composed of an evaporator and a condenser; in which both are thermally connected by a closed loop capillary tubing. The main goal is to measure the heat transfer properties of this device using helium as the working fluid. The evaporator end of the PHP is comprised of a copper winding in which heat loads up to 10 watts are generated, while the condenser is isothermal and can reach 4.2 K at 1 W via a two stage Sumitomo RDK408A2 GM cryocooler. Various experimental design features are highlighted. Additionally, the thermal performance for the presented design remained unchanged when increasing the adiabatic length from 300 mm to 1000 mm. Finally a spring mass damper model has been developed and proven to predict well the experimental data, such models should be used as tool to design and manufacturer PHP prototypes.

Graduate Student: Luis Diego Fonseca Flores

Campus ID: 906-637-3128

Title: Experimental Characterization of Cryogenic Helium Pulsating Heat Pipes

Approved by

Professor Franklin Miller
Department of Mechanical Engineering

Professor John M. Pfotenhauer
Department of Mechanical Engineering

Acknowledgements

There is so many individuals that I will like to extend my gratitude throughout my research at the University of Wisconsin-Madison. First of all to my wife Karla, the love of my life, who was always there for me in the good and bad times. Karla gave me great strength to move forward to complete my graduate studies, but mostly importantly balanced my life style when I was too dedicated and focused in work. Undoubtedly, this thesis is dedicated to you, I am grateful for your caring and specially patience, you have made me a better person throughout the years and I am eternally grateful. I do not know what I would have done without you, but I know great things await us together. To my wife's family as well, who have shown admiration in the work I do.

To my parents, Milton Fonseca and Elsa Flores, for giving me an example of the importance and benefits of achieving a PhD degree. Since a young child, I used to pay close attention to the engineering problems my father solved, it made me love science and engineering and encouraged me to pursue all my goals, "Thanks Papa". My mother, one of the most determined persons I have ever known, she has taught me never to surrender, continue always and pass through all obstacles encountered … "Te quiero mucho". My sister Patricia, I am grateful and could not have asked for a wiser person to grow up with. I have always admired her focus on life and strong character that has gotten her so far professionally, socially and spiritually. To my niece Celeste and Clemence, the most beautiful children I have ever seen, you have illuminated the souls of our family. To my aunts, Olga and Elizabeth Fonseca, who helped me through my application to UW, they are definitely the two pillars of the family Fonseca.

To my advisor Dr. Frankin Miller, I have never seen anyone do so many quick calculations in an iPhone and mind, thanks for teaching me all those computational tricks to verify my enormous simulations. Most of all, you have become a close friend and I know you will enlighten future students. I would like to thank deeply my co-advisor Dr. John Pfotenhauer. You have made me become a better engineer and have showed great trust in my abilities for designing, thank you for choosing me as a graduate student. To Dr. Greg Nellis, the best heat transfer professor I have ever had, thank you for listening to me when I had no

idea what was going on during the first time my experiment operated successfully, you gave me a great suggestion and it worked.

To my former undergraduate students Christian Herrera, Jacob Nellis and Benjamin Kufahl I cannot thank you guys enough for the great effort you put into your projects. Christian, you learned so quickly doing lab work, I have no doubt that your abilities will expand, I was very pleased you stayed and achieved your master's degree and we shared an office. I am very proud of you and miss our conversations about how Costa Rica is better than Mexico in soccer. Jacob, you are so dedicated in your work and classes, you listen carefully and finish your tasks on time. Your skills in precision machining are outstanding, any employer will be lucky to have you. Benjamin, I am happy you were able to work with me fixing the cryocooler's heat exchanger, you showed me how a great professional you are and hope that in the near future you come back to get a master's degree. To my three best friends Andres Soto, Jason Coley and Rogelio Rosas, I miss drinking beer with you guys. Also to my dearest soccer buddy Mason Mok, you are a great engineer and I know you will participate in amazing projects at JPL. To my office mates Max Brennan, Courtney Leeds and Jake Boxleitner, I deeply enjoyed our conversations of politics and life, you guys always laughed at my terrible jokes and sorry for talking too much and distracting you.

Finally, I would like to thank the Ministry of Science, Technology and Telecommunications (MICITT) and the National Council for Scientific and Technological Research (CONICIT) of Costa Rica for funding my first year of graduate studies.

Table of Contents

List of Figures

List of Figures

1 Pulsating Heat Pipes

1.1 Introduction

A Pulsating Heat Pipe (PHP) or Oscillating Heat Pipe (OHP), shown in Figure 1-1, is similar to a conventional heat pipe except that it has no wick, and includes multiple lengths of capillary tubing traversing back and forth between the condenser and evaporator. PHPs rely on the oscillation of vapor plugs and liquid slugs [1] within the pipe in order to transfer heat from the evaporator to the condenser. Vapor plugs grow in the evaporator region pushing other vapor plugs and liquid slugs towards the condenser section where the vapor plugs contract due to condensation. This volumetric expansion and contraction provides the oscillatory flow of the fluid throughout the tube necessary to transfer heat.

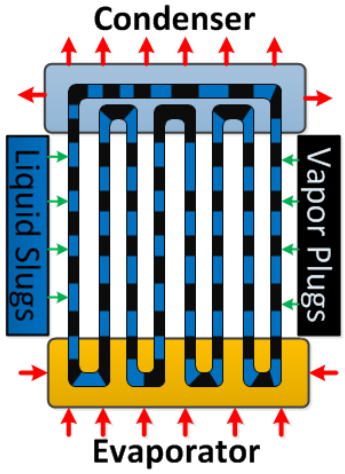

Figure 1-1: Schematic of a closed loop PHP/OHP.

1.2 Design Parameters

When designing a heat pipe the following parameters affect the performance of a PHP [2]:

- Working fluid: it is important to know the quantity, in moles or mass, required to fill the capillary tubing for an optimal performance.
- Inner diameter: in order to maintain the separate liquid and vapor regions, the capillary forces must be larger than gravitational forces. This condition, along with the fluid properties of density and surface tension defines a maximum allowable inner diameter, as described below.

- Condenser, evaporator and adiabatic lengths: the rate of condensation and the volumetric fraction of liquid are factors that contribute to an adequate mass flow. The evaporator length depends on the geometric dimensions of the object being cooled, and on the desired heat flux. The adiabatic section is an additional length parameter that depends on the distance between the condenser and evaporator, larger lengths may contribute to friction forces.
- Number of turns or loops: the heat transfer from the evaporator and condenser depends greatly in the number of turns. For example, Khandekar [4] showed that his one loop PHP could not operate continuously until the number of turns were increased. However until this day, there is no rule of thumb that suggest a minimum number of turns N_{crit} that should be used. Previous studies have also shown that a large number of turns can reduce the influence gravity on the PHP performance.

1.3 Calculating the critical Diameter under gravitational conditions

Figure 1-2 illustrates a vapor bubble moving through a liquid inside a vertical tube. The terminal velocity V_∞ depends between the interactions of the buoyancy force (F_b), the liquid's viscous force (F_μ), inertial force (F_i) and surface tension force (F_s). Therefore the following equation shows the resulting force on a vapor bubble

$$F_b + F_i + F_\mu + F_s = 0 \tag{1-1}$$

Where the buoyancy force can be expressed as

$$F_b = c_1\left(\rho_L - \rho_g\right) g D^3 \tag{1-2}$$

The inertial force is:

$$F_i = c_2 \rho_L V_\infty^2 D^2 \tag{1-3}$$

The viscous force is:

$$F_\mu = c_3 \mu_L V_\infty D \tag{1-4}$$

And finally the surface tension force is:

$$F_s = c_4 \sigma D \tag{1-5}$$

Here c_1 to c_4 are constants, D is the inner diameter of the tube, ρ_L and ρ_g are the liquid and gas densities, σ is the surface tension, and μ_L is the liquid's dynamic viscosity.

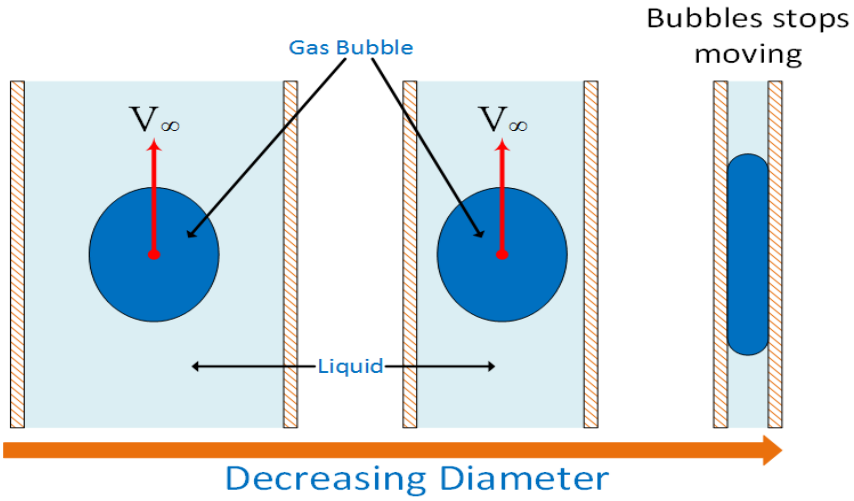

Figure 1-2: Result for a gas bubble in a liquid flow when decreasing the tube's inner diameter

Using the four forces above, the following dimensionless numbers can be deduced as

- The Reynolds number (Re):

$$Re = \frac{F_i}{F_\mu} = \frac{\rho_L V_\infty D}{u_L} \tag{1-6}$$

- The Weber number (We):

$$We = \frac{F_i}{F_s} = \frac{\rho_L V_\infty^2 D}{\sigma} \tag{1-7}$$

- The Froude Number (Fr) :

$$Fr = \frac{F_i}{F_b} = \frac{\rho_L V_\infty^2}{(\rho_L - \rho_g) g D} \tag{1-8}$$

- The Poiseuille number (Ps):

$$Ps = \frac{F_\mu}{F_b} = \frac{\mu_L V_\infty}{(\rho_L - \rho_g) g D^2} \tag{1-9}$$

- The Eötvös number (Eo):

$$Eo = \frac{F_b}{F_s} = \frac{(\rho_L - \rho_g) g D^2}{\sigma} \quad \text{1-10}$$

The Eötvös number is also mentioned as the Bond number (*Bo*) and is expressed as:

$$Bo = \sqrt{Eo} \quad \text{1-11}$$

The dimensionless numbers can be used to correlate the velocity for specific cases as discussed by Khandekar [4]. For example if viscous and surface tension forces are insignificant, then equation 1-8 can be used to correlate the terminal velocity V_∞. Also, if the viscous and buoyancy forces are dominant then the Poiseulle number (*Ps*) can be use the correlate V_∞. Note that the Eötvös number (*Eo*) is different since it does not include any velocity term, but allows one to determine the inner diameter for a PHP. The importance of the Eötvös number regarding PHP design can be explained in Figure 1-3 as developed by White and Beardmore (1962) [3]. The figure shows the Froude number versus the Eötvös for various liquid fluids were air bubbles are introduced.

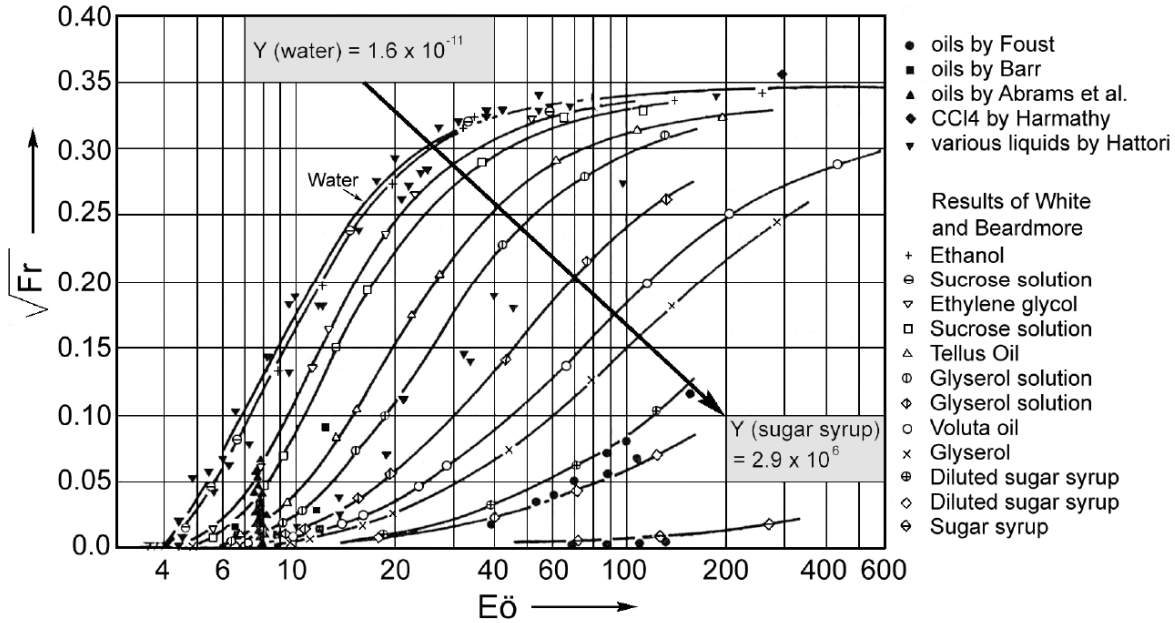

Figure 1-3: Froude number versus Eötvös, White and Beardmore (1962) [3].

It can be observed that for water, ethanol and other low viscosity fluids, the terminal velocity converges to an associated value of $\sqrt{Fr}$ = 0.345 when *Eo* > 70. As the *Eo* number decreases so does the

Fr number; hence it can be observed that at *Eo* = 4 the Froude number decreases to zero. Such a condition is depicted in Figure 1-2 and occurs when the surface tension force dominates, causing the gas bubble to stop. Using equation 1-11 and assuming $Eo \leq 4$ the following equation can be derived to calculate the critical diameter (D_{crit}) to design a PHP

$$Eo = Bo^2 = \frac{(\rho_L - \rho_g) g D_{crit}^2}{\sigma} \leq 4 \qquad 1\text{-}12$$

Hence

$$D_{crit} \leq 2\sqrt{\frac{\sigma}{(\rho_L - \rho_g) g}} \qquad 1\text{-}13$$

Where g is the acceleration due to gravity and σ, ρ_l and ρ_v are the surface tension, liquid density and vapor density properties of the fluid respectively. Figure 1-4 shows a representation of the motion of a fluid inside a vertical closed-loop pulsating heat pipe (CLPHP) when a heating system is turned on at one end. In cases A and B the surface tension forces are not dominant and the liquid sections are not evenly distributed throughout the capillary tubing. Neither vapor plugs nor liquid slugs are formed until cases C and D where surfaces tension forces dominate and the liquid is well distributed. In these last cases, the vapor plugs expand and collapse in the evaporator and condenser sections, causing the desired oscillations for heat transfer.

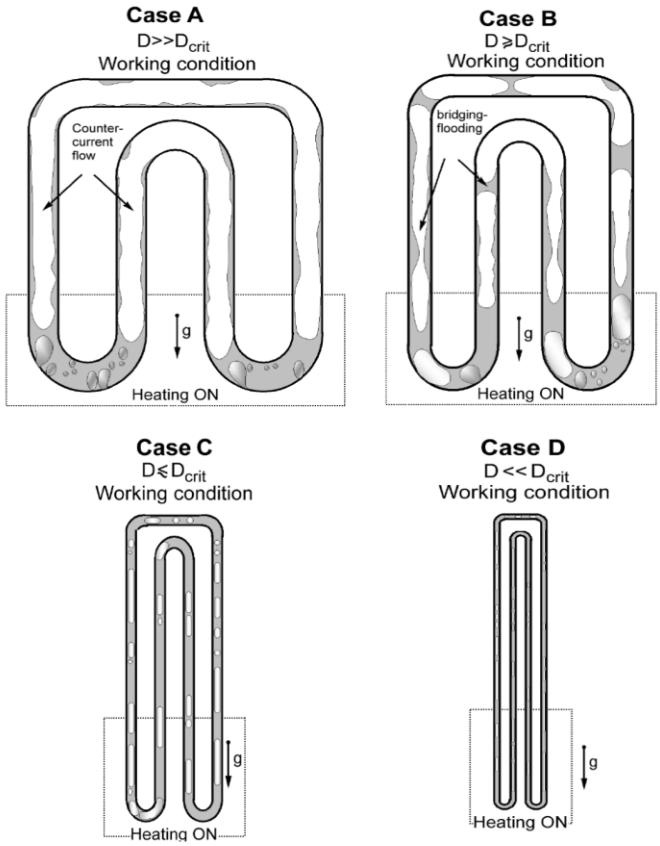

Figure 1-4: Critical Diameter cases, Khandekar [4]

Figure 1-5 shows the critical diameter D_{crit} as a function of saturation pressure P_{sat} for helium, hydrogen, nitrogen, neon and argon. This research uses helium as the working fluid; therefore, the critical diameter D_{crit} = 0.5 mm for the capillary tubing was chosen. Note that the same diameter could be used for the other cryogens as well. It should be mentioned that helium has a critical pressure P_{crit} = 227 kPa; however, as described and discussed further in the Results section, it has been proven that the helium PHP was able to operate above the critical point due to high density differences between the evaporator and condenser section.

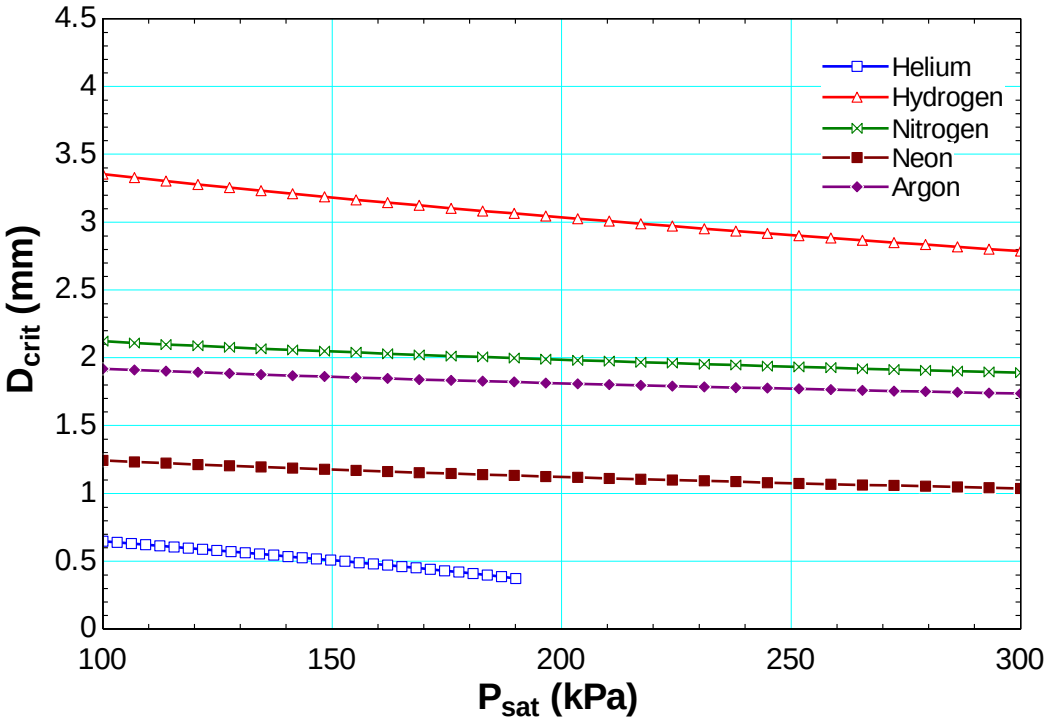

Figure 1-5: Critical diameters (D_{crit}) vs saturation pressure (P_{sat}).

1.4 Microgravity conditions

For microgravity conditions Gu et al. [5] states that to prevent the liquid slugs and the flow pattern from changing to churn or annular flow the forces of inertia and surface tension should be considered (Webber number). Gau followed the following equations to derive the critical diameter for microgravity conditions:

- Step 1: The kinetic energy per volume of the liquid slug can be determined as

$$E_k = \frac{1}{2}\rho_l \bar{V}^2 \qquad 1\text{-}14$$

Where $\bar{V}$ is the average velocity of the fluid and ρ_l is the liquid density.

- Step 2: The surface energy per volume of the vapour bubble can be determined as the ratio of the surface tension over the radius of the meniscus.

$$E_s = \frac{\sigma}{r} \qquad 1\text{-}15$$

- Step 3: to prevent any change in the slug flow regime, it was assumed that the surface energy Es is greater than the kinetic energy Ek. Where C is a constant of order one in magnitude.

$$E_s \geq C E_k \tag{1-16}$$

- Step 4: Combined equations 1-14 to 1-16 the critical diameter can be expressed as

$$We = \frac{\rho_l D_{crit} V^2}{\sigma} \leq \frac{4}{C}$$

Remembering that $D_{crit} = 2r$

$$D_{crit} \leq \frac{4\sigma}{C\rho_l \bar{V}^2} \tag{1-17}$$

Zhao et al. [6] have assumed values for *C* equal to 0.8 and 1. It should be noted that the average velocity $\bar{V}$ of the PHP can change at different operating conditions, such as the heat load applied. Therefore when designing a PHP, an estimated maximum velocity PHP should be assumed as a safety factor.

1.5 References

[1] Okazaki, S., Fuke, H., Miyazaki, Y., & Ogawa, H. (2014). "Development of Meter-Scale U-Shaped and O-Shaped Oscillating Heat Pipes for GAPS". *Journal of Astronomical Instrumentation*, 3(02), 1440004.

[2] Reay, D. A. and P.A. Kew, *Heat Pipes, 5th Edition*, Butterworth-Heinemann, MA, 2006.

[3] White, E. T., & Beardmore, R. H. (1962). The velocity of rise of single cylindrical air bubbles through liquids contained in vertical tubes. *Chemical Engineering Science*, 17(5), 351-361.

[4] Khandekar, S. (2004). Thermo-hydrodynamics of closed loop pulsating heat pipes.

[5] Gu, J., Kawaji, M., & Futamata, R. (2004). Effects of gravity on the performance of pulsating heat pipes. *Journal of Thermophysics and Heat Transfer*, 18(3), 370-378.

[6] Zhao, J. F., & Hu, W. R. (2000). Slug to annular flow transition of microgravity two-phase flow. *International journal of multiphase flow*, 26(8), 1295-1304.

2 Literature Review

2.1 Room Temperature Pulsating Heat Pipes

Since PHPs exhibit high heat transfer rates they can be useful for many applications involving room temperature cooling systems. For example, PHPs could be used to cool down photon detectors since they can provide a bridge from the detectors to the cold sink instead of using a copper thermal buss. The main

advantage in replacing the thermal copper busses with PHPs would be to minimize mass constraints and lower temperature differences between the evaporator and condenser section. Recently, The Japanese Aerospace Exploration Agency (JAXA) has tested two room temperature PHP prototypes [1] in order to cool down their photon detectors. These detectors will be used in the balloon-borne General Anti-Particle Spectrometer (GAPS). These two prototypes have a U-shaped and O-shaped configuration and have a total length of 6 and 8 meters, respectively. They are longest room temperature PHPs reported yet. For the U-shaped configuration, the condenser, evaporator and adiabatic section were 2 m long each and with a total of 16 loop turns, while the O-shaped configuration has two parallel adiabatic section. Another characteristic is that these PHPs have check valves installed at every other turn in order to guarantee fluid circulation throughout the capillary tubing. This PHP used R410A as the working fluid and was built with copper capillary tubing with an inner and outer diameter of 1 mm and 1.6 mm, respectively. The O-shaped PHP performed best and retrieved a total of 250 W. GAPS requires 800 W of cooling capacity therefore four O-shaped PHPs will be necessary.

One of the most important application for room temperature PHPs are to cool down electronics components such as CPU Chips. For this reason, Rittedech et al. [2] tested a Closed-end Oscillating Heat Pipe (CEOHP) which was designed to cool a Pentium 4 CPU, model SL 6 PB 2.26 GHz, with an electric power of 58 W. The CEOHP used R134a as the working fluid and operated at a fill ratio of 50 %. The condenser section was air cooled using a fan set 2000 rpm and 4000 rpm. Results show that when the fan operated at 2000 rpm the CEOHP was able to dissipate a maximum heat load 34.4 W which maintained the chip at a working temperature of 54 ^{o}C. While at 4000 rpm, the maximum heat load dissipated was 44.5 W and maintained a chip temperature of 53 ^{o}C. This successful testing stated that this CEOHP module had a better performance than conventional heat sink

In addition, investigation using other fluids at different fill ratios have been a priority for researchers to characterize and pin point the maximum heat that can be transferred. For example, Verma et al. [3] tested

a PHP using methanol and de-ionized water as the working fluids. They reported that for the DI water case, the minimum thermal resistance achieved was 0.492 K/W (2.03 W/K) at a filling ratio of 50 % and at a heat load of 100 W. While using methanol as the working fluid, the PHP reached a minimum thermal resistance of 0.51 K/W at a fill ratios of 40 % and heat load of 100 W. V. Patel et al. [4] tested more working fluids such as dionized water, ethanol, methanol, acetone and including water based mixtures with ethanol, methanol and acetone. A heat load between 10 W to 110 W was applied at a 50 % fill ratio. Results showed a thermal resistance down to 0.95 k/W for water and 0.64 k/W for acetone at an average heat load of 57.3 W. Faghri et al. [5] and Cui et al. [6] summarized work done on room temperature PHPs/OHPs experiments.

2.2 Cryogenic Pulsating Heat Pipes

Results from the testing of a few other cryogenic pulsating heat pipes using nitrogen as the working fluid have been reported in the literature. A.J. Jiao et al. [8] constructed a N_2 PHP using copper capillary tubing with an inner diameter of 1.65 mm. This experiment had a configuration of 16 parallel tubes and consisted of a 4 x 18.5 cm evaporator section, a 6 x 18.5 cm condenser section and a 10 cm length adiabatic section. A fill ratio of 50 % was used and a heat load from 20.5 W to 380.1 W was applied resulting in a thermal resistance of 0.256 K/W to 0.112 K/W, hence giving an effective thermal conductivity between 18,268 W/(m-K) to 41,757 W/(m-K) respectively.

Yi Li et al. [9] constructed a nitrogen pulsating heat pipes with a configuration of 10 parallel tubes, inner diameter of 2.1 mm and an adiabatic length of 10 cm. A heat load was applied and gradually increased from 0 to 22 W resulting in effective thermal conductivities between 12,000 W/(m-K) and 15,800 W/(m-K) in a vertical orientation where the evaporator is at the bottom and condenser is located at the top. This experiment was conducted using a fill ratio of 50 %.

T. Mito et al. [10] used a pulsating heat pipe to investigate an alternative way to cool down high temperature superconducting magnets using hydrogen, neon and nitrogen as the working fluids. Their

experiment consisted of 10 parallel stainless steel tubes with an inner diameter of 0.78 mm and adiabatic length of 10 cm. Maximum heat loads applied for hydrogen, neon and nitrogen cases were 1.2 W, 1.5 W and 7 W. This resulted in effective thermal conductivities ranging from 500 to 3000 W/(m-K) for hydrogen at fill ratio between 31-80%, 1000 to 8000 W/m/K for neon at fill ratios from 16-95 %, and 5,000 to 18,000 W/(m-K) for nitrogen at fill ratio from 17-70%.

My work done here at the University of Wisconsin in the cryogenics group, Luis Fonseca et al. [11],[12], included the construction of a nitrogen based pulsating heat pipe with a condenser, adiabatic and evaporator lengths of 70 mm, 80 mm and 70 mm respectively. The capillary tubing was composed of stainless steel 304 with an inner and outer diameter of 0.5 mm and 0.8 mm respectively and with a total of 40 turns. The PHP operated at a temperature range of 79 K to 82 K. A fill ratio of 20 % showed a maximum effective thermal conductivity of 70,000 W/(m-K) at 2.8 W.

The Institut Nanosciences et Cryogenie INAC [13], reported on the successful operation of a helium PHP apparatus, where the effects of inclination were measured, using tilt angles from 0^o to 40^o. The PHP was composed stainless steel capillary tubing with an inner diameter of 0.5 mm and condenser, adiabatic and evaporator section lengths of 40 mm, 92 mm and 45 mm with a total of 5 turns. This configuration was able to transfer a maximum of 145 mW of heat using a cold source at 4.2 K at the 40^o tilt angle. A constant thermal resistance of 2.5 K/W was measured between the evaporator and condenser with a capability of transferring 75mW at a tilt $\theta^o = 10^o$ and at a tilt of $\theta^o = 0^o$ the PHP was able to transfer a total of 10 mW.

In addition I was able to [14] successfully operate a helium based pulsating heat pipe, which operated at temperature between around 5 K and achieved thermal conductivities up to 2393 W/(m-K) at fill ratios around 50 %. The PHP was built with 60 turns with stainless steel 304 tubing of inner diameter 0.5 mm and outer diameter 0.8 mm and with a condenser, an adiabatic and an evaporator length of 125.2 mm, 90 mm and 116.85 respectively.

In 2015, Dong Xu et al [15] constructed and tested a helium based pulsating heat pipe with an inner diameter of 0.5 mm and with 8 parallel channels, and the lengths of the evaporator, condenser, and adiabatic section were 50 mm, 50 mm, and 100 mm. An optimal thermal performance was achieved at a fill ratio of 70 %, resulting in thermal conductivities between 4800–13,000 W/(m-K) at an inclination angle of 30 ^{o}.

H. Deng et al. [16] conducted an experiment of a hydrogen pulsating heat pipe at Zhejiang University, China. The PHP was constructed with an inner diameter of 2.3 mm and a condenser, adiabatic and evaporator sections of length of 50 mm, 100 mm and 50 mm respectively. The thermal performance of the PHP was tested at fill ratios of 35 %, 51 % and 70 % and at evaporator heat loads up to 9 W. The highest effective thermal conductivity achieved was 18,700 W/(m-K) at a fill ratio of 35 % and a heat load of 5 W, in which the temperature difference between the evaporator and condenser section was 1 K.

2.3 Microgravity Pulsating Heat Pipes

The Japanese Exploration Agency (formerly NASDA) [17] financed a reduced gravity PHP project while the parabolic flight opportunity was provided by the Canadian Space Agency aboard a Falcon 20 aircraft, gravity levels were changed between hyper-gravity up to 2.5 g and reduced gravity of 0.02 g. The PHP was charged with refrigerant R-114 inside a 0.52 mm inner diameter capillary tubing and it was observed that steady pulsations where achieved under reduced-gravity with effective thermal conductivities up to 3000 W/m/K at a heater power of 4.4 W while under normal gravity a value of 2000 W/m/K at 4.4 W was achieved.

Other room temperature pulsating heat pipes have been tested during the ESA's (European Space Agency) 58th and 59th parabolic flight campaigns [18]. During both these campaigns the same PHP was tested using FC-72 aircraft at fill ratios of 50 % and 70 % using R-114. The PHP's was built with 32 parallel copper tubing with an inner and outer diameter of 1.1 mm and 2 mm respectively. The evaporator, condenser and adiabatic sections had lengths of 6 mm, 180 mm and 17.5 mm respectively. Throughout the parabolic flight and when the PHP was maintained in a vertical orientation, it was observed that hyper-

gravity assists the flow motion, the heat transfer is slightly enhanced thus a small decrease of the evaporator temperatures is appreciable [18]. But in a microgravity and in the vertical orientation the gravity force is negligible and results in a temperature increase in the evaporator section [18]. When the second hyper-gravity period is reached the gravity forces are able to bring the PHP back to the previous thermal regime [18]. In a horizontal orientation at normal gravity conditions of 1 g, it had the same thermal resistance values around 0.8 K/W or an effective thermal conductivity of 719.32 W/m-K in microgravity conditions. Figure 2-1 shows a summary of the literature review of the effective thermal conductivities achieved with the fluids used.

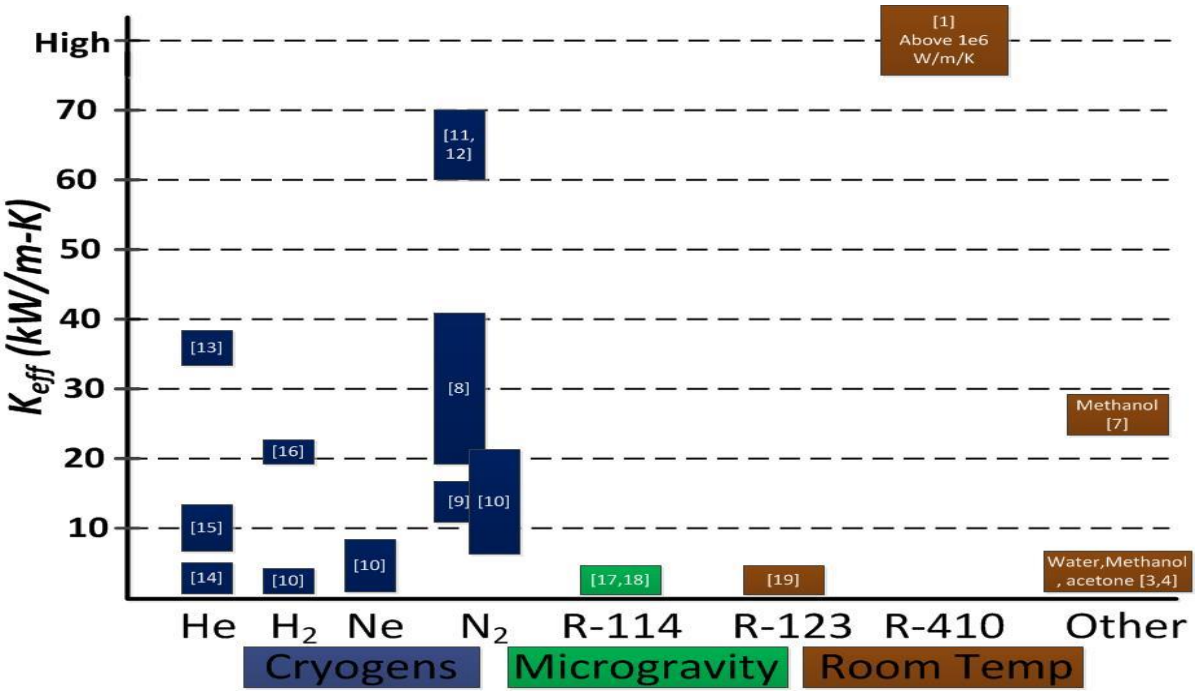

Figure 2-1: Literature review summary

2.4 References

[1] Okazaki, S., Fuke, H., Ogawa, H., Miyazaki, Y. "Development of Meter-scale O-shaped and U-shaped Oscillating Heat Pipes for GAPS", Aerospace Conference, 2014 IEEE, pp. 1 – 9.

[2] Rittidech, S., Boonyaem, A., & Tipnet, P. (2005). CPU cooling of desktop PC by closed-end oscillating heat-pipe (CEOHP). American journal of applied sciences, 2(12), 1574-1577.

[3] Verma, B., Vijay, L., Srivastava, K. "Experimental Studies on Thermal Performance of a Pulsating Heat Pipe with Methanol/DI Water", Journal of Electronics Cooling and Thermal Control, Vol. 3, pp. 37-34, March 1, 2013.

[4] Patel, V., Gaurav, Mehta, B. "Influence of working fluids on startup mechanism and thermal

performance of a closed loop pulsating heat pipe", Applied Thermal Engineering, Vol. 110, pp. 1568-1577, January 2017.

[5] Faghri, A., & Zhang, Y. (2001). Thermal modeling of unlooped and looped pulsating heat pipes. *J. Heat Transfer*, *123*(6), 1159.

[6] Cui, X., Qiu, Z., Weng, J., & Li, Z. (2016). Heat transfer performance of closed loop pulsating heat pipes with methanol-based binary mixtures. *Experimental Thermal and Fluid Science*, *76*, 253-263.

[7] Tseng, C., Yang, K., Chien, K., Wu, S., Wang, C. "A novel double pipe pulsating heat pipe design to tackle inverted heat source arrangment", Applied Thermal Engineering, Vol. 106, pp. 697-701, August 2013.

[8] Jiao, A., Ma, H., Critser, J. "Experimental investigation of cryogenic oscillating heat pipes", International Journal of Heat and Mass Transfer, Vol. 52, pp. 3504-3509, July. 2009.

[9] Li, Yi., Wang, Qiuliang., Chen, Shunzhong., Zhao, Baozhi., Dai, Yinming. "Experimental investigation of the characteristics of cryogenic oscillating heat pipe", International Journal of Heat and Mass Transfer, Vol. 79, pp. 713-719, Dec. 2014.

[10] T. Mito, K. Natsume, N. Yanagi, H. Tamura, T. Tamada, K. Shikimachi, N. Hirano, and S. Nagaya, "Achievement of high heat removal characteristics of superconducting magnets with imbedded oscillating heat pipes," IEEE Trans. Appl. Supercond., vol. 21, no. 3, pp. 2470–2473, Jun. 2011.

[11] Fonseca, L. D., Miller, F., & Pfotenhauer, J. (2017). "Design and Operation of a Cryogenic Nitrogen Pulsating Heat Pipe", in Advances in Cryogenic Engineering: Part 1, edited by J. G. Weisend II et al. Volume 101, pp. 012064, 2015.

[12] Fonseca, L. D., Miller, F., & Pfotenhauer, J. (2017). Experimental Heat Transfer Analysis of a Cryogenic Nitrogen Pulsating Heat Pipe at Various Liquid Fill Ratios. Applied Thermal Engineering. https://doi.org/10.1016/j.applthermaleng.2017.11.029

[13] Bonnet, F., Gully, P., Nikolayev V., Development and Test of a Cryogenic Pulsating Heat Pipe and a Pre-Cooling System, Proceedings of the AIP Conference Heat Transfer-I, Vol. 1434, June 2011, pp. 607-614.

[14] L. Fonseca, F. Miller, J. Pfotenhauer "A Helium Based Pulsating Heat Pipe for Superconducting Magnets", in Advances in Cryogenic Engineering 59A, edited by J. G. Weisend II et al, Melville, New York, 2014, pp. 28-35.

[15] Dong Xu, Laifeng Li, Huiming Liu, "Experimental investigation on the thermal performance of helium based cryogenic pulsating heat pipe," Journal of Experimental Thermal and Fluid Science, Vol. 70, pp. 61–68, Jun. 2016.

[16] H. Deng, Y. Liu, R. Ma, D. Han, Z. Gan, J. Pfotenhauer, "Experimental investigation on a pulsating heat pipe with hydrogren," Advances in Crogenic Engineering , Vol. 101, pp. 012064, Jun. 2015.

[17] Gu, J., Kawaji, M., Futamata, R., "Microgravity Performance of Micro Pulsating Heat Pipes", in Microgravity-Science and Technology, Vol. 16, Issue. 1, pp. 181-185, March 2005.

[18] Mameli, M., Araneo, L., Filippeschi, S., Marengo, M., Testa, R., Marelli, L., "Thermal Response of a Closed Loop Pulsating Heat Pipe under varying Gravity Force", in International Journal of Thermal Sciences, Vol. 80, pp. 11-22, June 2014.

[19] H. Yang, S. Khandekar, M. Groll, "Operational limit of closed loop pulsating heat pipes", *AppliedThermal Engineering*, Vol. 28, pp. 49-59, 2008.

3 Experimental Apparatus and Design

3.1 Dewar

Table 3-1 and Figure 3-1, shows the main components used in the test apparatus for the present research. The experiment is mounted and operated inside a vacuum dewar with an inner diameter 510 mm and height of 1650 mm. The convective heat transfer to the PHP was minimized by conducting the experiments in a high vacuum (1e-6 torr) environment.

Table 3-1: Main Experimental Apparatus Components

1) Sumitomo Cryocooler Model RDK-408-A2 GM (2 stages).
2) Aluminum 6061 Dewar Endplate.
3) Vacuum pump feedthroughs.
4) Electric Feedthroughs.
5) Vacuum Dewar.
6) G10 supports for thermal jacket.
7) Thermal Jacket.
8) PHP Core (3 sections).

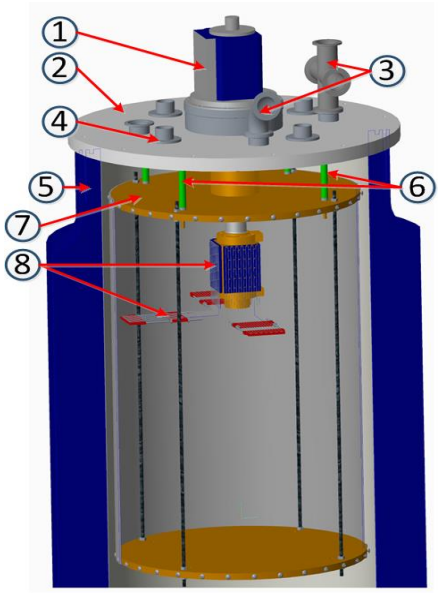

Figure 3-1: Experimental Apparatus

3.2 Dewar endplate

The dewar endplate was made from a 1 inch thick aluminum 6061 plate machined to a final diameter of 605 mm. Figure 3-2 shows the final construction of the endplate which included a total of four electrical feedthroughs which were used to connect to the temperature sensors, pressure sensors and heaters. Also, four vacuum feedthroughs were integrated to the endplate to connect the vacuum pumping system as well as the gas lines to the PHP. A 133 mm diameter through hole and an o-ring groove were machined in order to mount and seal the cryocooler to the endplate and avoid any air leak to the dewar.

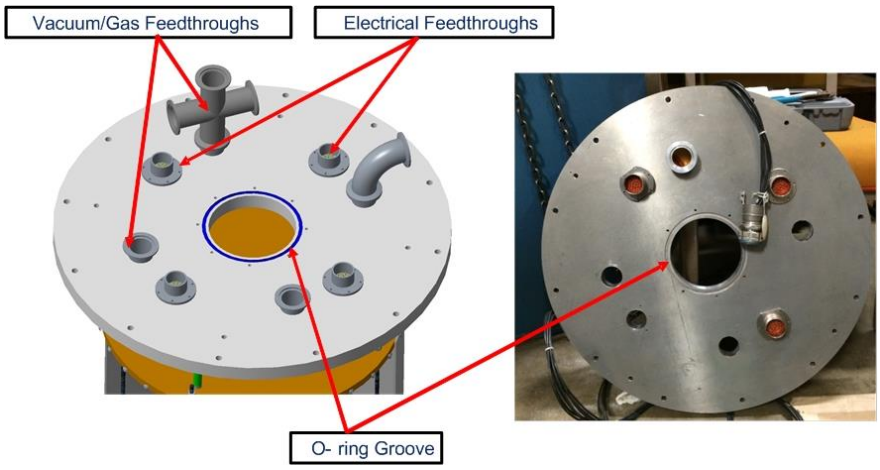

Figure 3-2: Dewar Endplate

3.3 Cryocooler

A Sumitomo cryocooler model RDK-408-A2 GM was used for the experimental apparatus. It consists of two cold stages, as shown in Figure 3-3. The first stage has a cooling power of 44 W at 41.6 K and 0 W at 25 K. The second stage has a cooling power of 1 W at 4.2 K. Since the 2nd stage of the cryocooler lacked of any threaded attachment holes, a copper support sleeve was constructed and anchored to the 2nd stage via a pair of copper clamps to attach the PHP sections.

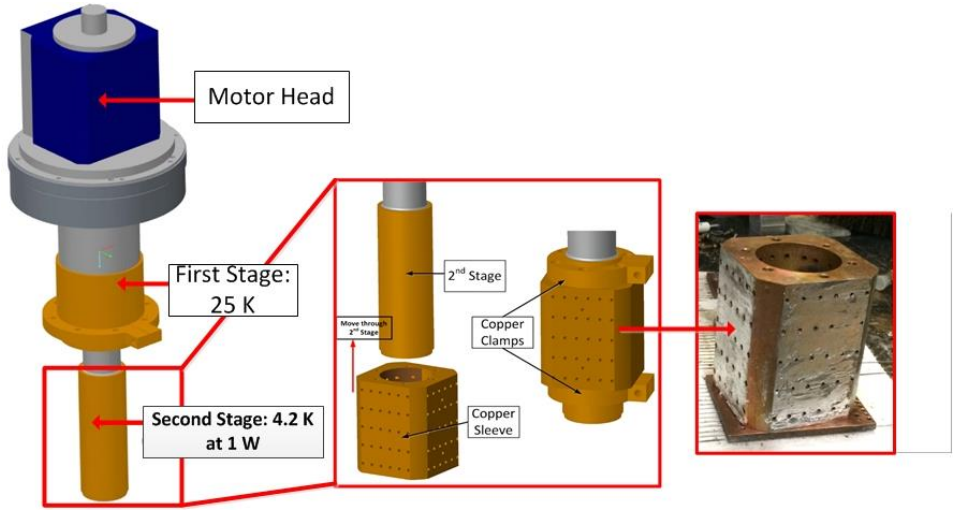

Figure 3-3: Cryocooler and clamping mechanism

As shown in Figure 3-4, six 9 mm holes were drilled on each copper clamp, where six M5x0.8 threaded holes were machined on the top and bottom face of the copper sleeve. One out of the two copper clamps was first anchored to the 2nd stage and indium foil was placed between the contact surfaces in order to assure high thermal contact. The copper sleeve was then bolted into the clamp using M5x0.8 screws where the 9 mm holes permitted enough spacing to center the copper sleeve in place. Finally the second copper clamp was attached and bolted to the bottom face of the sleeve as shown in Figure 3-5. A total of thirty M5X0.5 threaded holes were machined at each side face of the copper sleeve in order to anchor the three condenser sections of the PHP as shown in Figure 3-5.

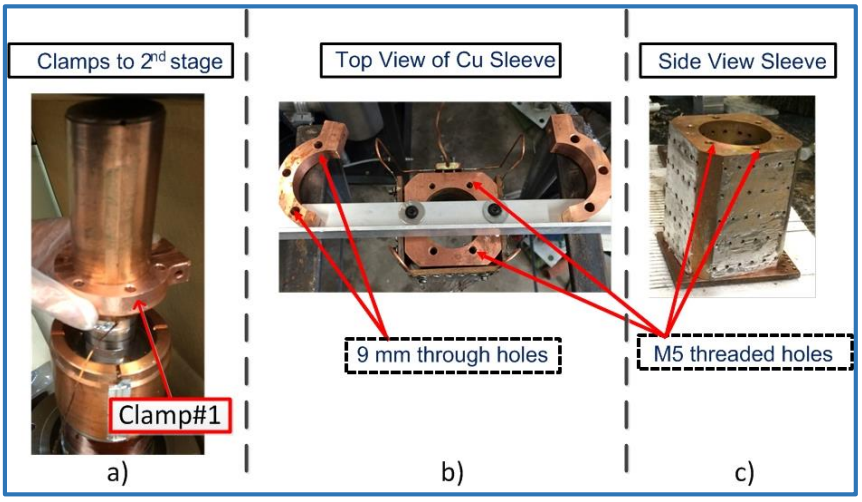

Figure 3-4: Copper clamp and sleeve

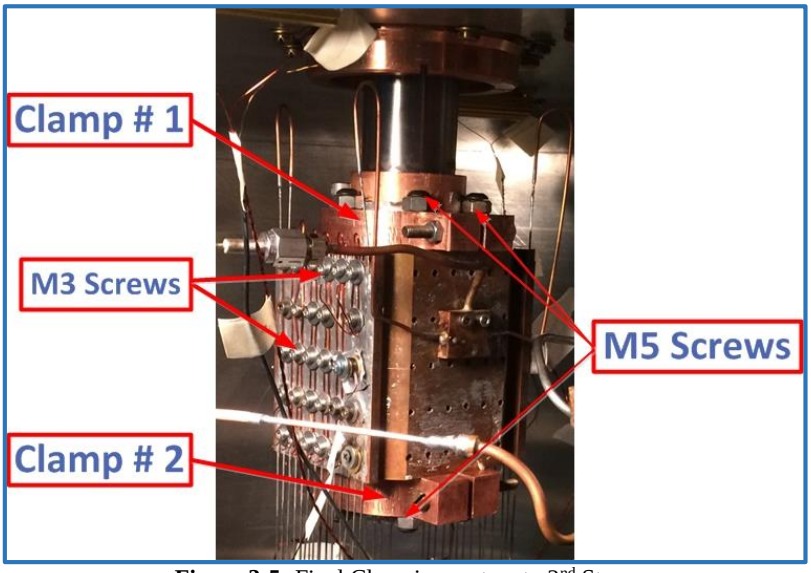

Figure 3-5: Final Clamping system to 2nd Stage

3.4 Thermal Jacket

As shown in Figure 3-6, the thermal jacket is composed of 5 major components: G10 supporting rods, top plate, bottom plate, 1st stage clamp and finally the aluminum covers. The thermal jacket intercepts any parasitic thermal radiation from the Dewar's warm wall so that it does not reach the PHP core.

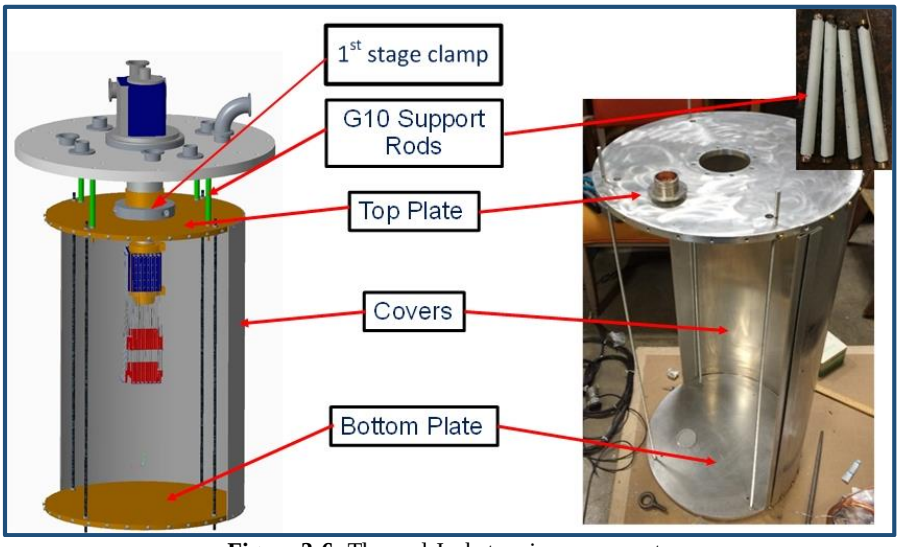

Figure 3-6: Thermal Jacket main components

The thermal jacket is supported by the dewar endplate using four G10 rods. G10 is used since it has a high tensile strength and a low thermal conductivity of 1.4 W/m/K. These rods have an outer diameter, inner

diameter and length of 9.525 mm, 9.017 mm and 97 mm respectively. Since the dewar endplate is at room temperature, T_o = 300 K, it is can be assumed that one end of the G10 rods are also at room temperate, while the other end of the rod, in contact with the thermal jacket, is at 25 K. Hence, the parasitic heat transfer due to conduction of the G10 rod can be calculated using the integrated thermal conductivity, eqn (3-1), which results in an estimated 48.53 mW heat load.

$$Q_{cond} = \int_{T\,=\,25K}^{T=\,300K} \frac{Nk(T)A_c dT}{L} \tag{3-1}$$

Which simplifies to

$$Q_{cond} = \frac{NA_c}{L} \int_{T\,=\,25K}^{T=\,300K} k(T)dT \tag{3-2}$$

Where N = 4 is the number of G10 rods, *k(T)* is the thermal conductivity as a function of temperature *T*, A_c is the cross-sectional area of the rod, L is the length of each rod and finally *dT* is the differential in temperature.

The top plate of the thermal jacket is thermally anchored to the cryocooler's 1st stage using an aluminum clamp as shown in Figure 3-1. Also, 0.2 mm thick indium foil with was placed between the contact surfaces to assure good thermal contact even in a vacuum environment. This clamp was divided in a C-shaped geometry with an outer diameter, inner diameter and height of 140 mm, 90 mm and 25.4 mm respectively.

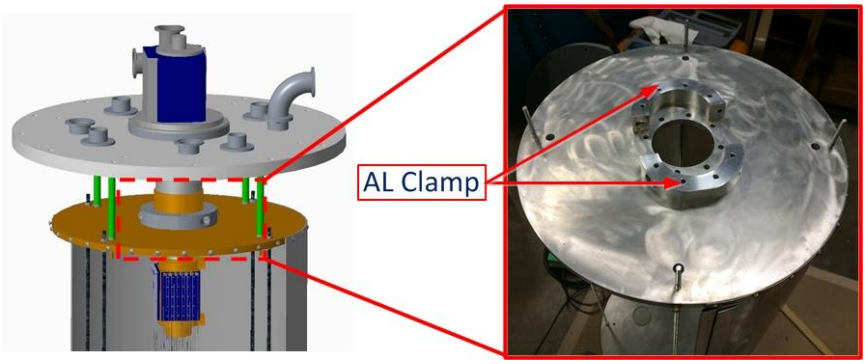

Figure 3-7: Aluminum clamp to first stage

As shown in Figure 3-8, the top and bottom plates are 914 mm apart and are thermally attached using two 1 mm thick aluminum 6061 sheets. Both plates have an outer diameter and a thickness of 460 mm and 12.7 mm respectively. A total of 30 8-32 threaded holes were machined on the outer diameter of each plate in order to attach the aluminum covers.

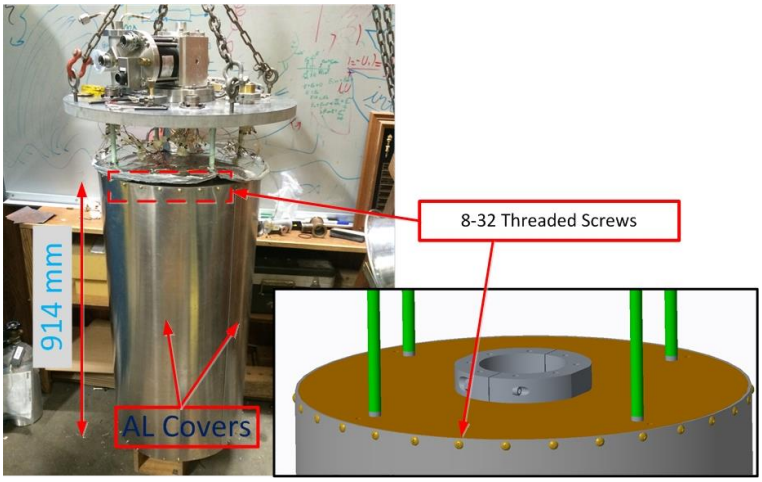

Figure 3-8: Thermal Jacket's Aluminum Covers

3.5 Pulsating Heat Pipe Core

As shown in Figure 3-9, the PHP core is comprised of 3 PHP sections connected in series to each other using copper unions. The capillary tubing chosen was 304 stainless steel with an outer and inner diameter of 0.8 mm and 0.5 mm respectively. Each PHP has an adiabatic section of 300 mm with a total of 14 loops, 7 loops on the evaporator section and 7 loops on the condenser section. The total capillary tube length was 21.32 m.

The condenser section was made of copper grade 110 with a rectangular geometry of width 69.2 mm, height 90 mm and thickness 4.25 mm. The evaporator section was composed of two subsections with a width of 76.2 mm, height 30 mm, thickness 4.25 mm and separated by 50 mm. In order to bend the capillary tubing easily, a total of 14 evenly spaced rectangular grooves of width 0.85 mm and depth 0.6 mm were machined throughout the height of the evaporator and condenser sections and latter bent using 4 mm diameter shoulder screws located at both ends of sections, as shown in Figure 3-9 and Figure 3-10. This bending process

prevented crimping at the curved locations. In addition the condenser section has a total of thirty 4 mm diameter holes that are needed later to anchor the PHP core to the cryocooler's 2nd stage. Finally the capillary tubing was soldered to the condenser and evaporator sections in order to achieve a high thermal contact.

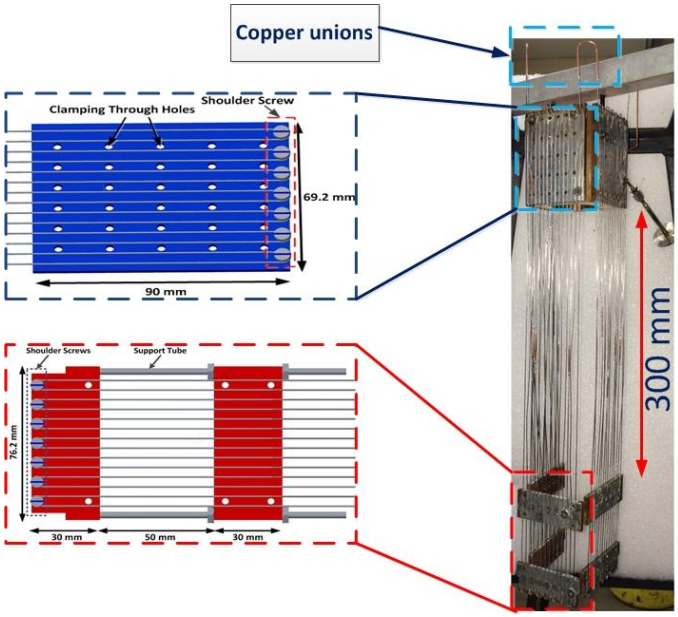

Figure 3-9: PHP Geometry

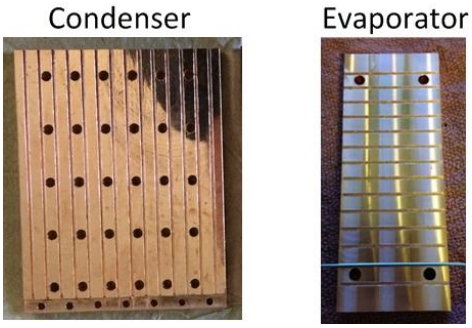

Figure 3-10: Machined Condenser/Evaporator sections

3.6 Experimental Setup

Figure 3-11 shows the actual experimental setup. A 3.8 L gas supply tank supplies the necessary charge to the PHP. On the atmospheric side, this helium gas supply is connected to a 6.35 mm copper tube that extends through a KF 25 gas feed-through located on the dewar's endplate. Inside the vacuum chamber, the

gas feed-through line is reduced to the PHP capillary tubing size and connected to the condenser section via a 1/8" T fitting. The vacuum chamber is connected to the pumping system using a KF-25 metal bellows hose. This pumping system is composed of a mechanical pump in series with a turbo-molecular pump. A second evacuation line and valve was installed in order to provide the option to evacuate and purge the gas supply tank directly, see Figure 3-12. In addition, a high purity helium supply-line was used to refill the gas supply tank when needed.

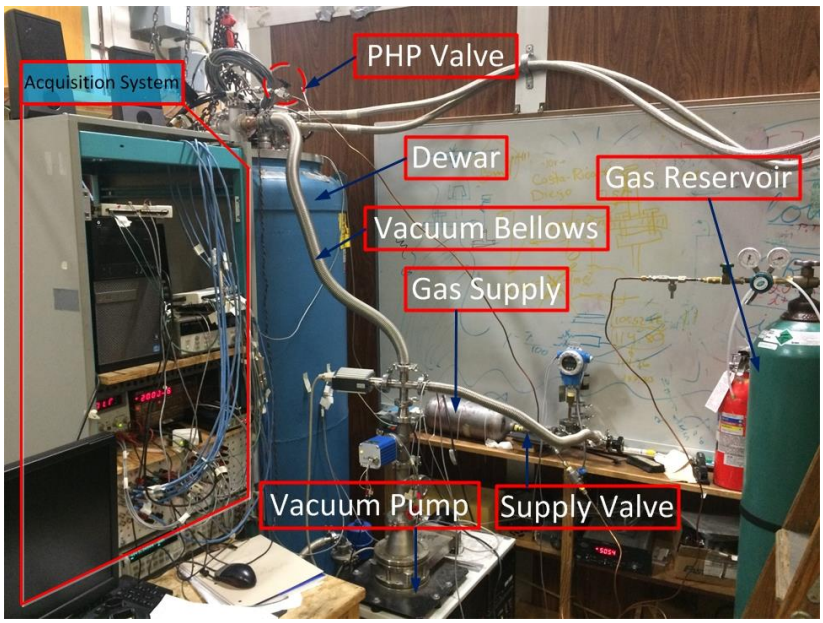

Figure 3-11: Evacuation and gas lines

Figure 3-12 shows a simplified schematic of the evacuation and gas lines. A pressure transducer installed on the gas supply tank was used to measure the initial charged of helium required for the PHP. A second pressure sensor is connected via a shorter capillary gas-line directly to the condenser section of the PHP. It should be noted that this pressure sensor is located outside the vacuum at room temperature because the sensor cannot function at cryogenic temperatures. The PHP fill valve is also located at room temperature and outside the vacuum space. It should also be noted that the gas line configuration connecting the PHP is much more complicated as shown Figure 3-12; therefore section 3.7 will be dedicated to describe its design in much more detail.

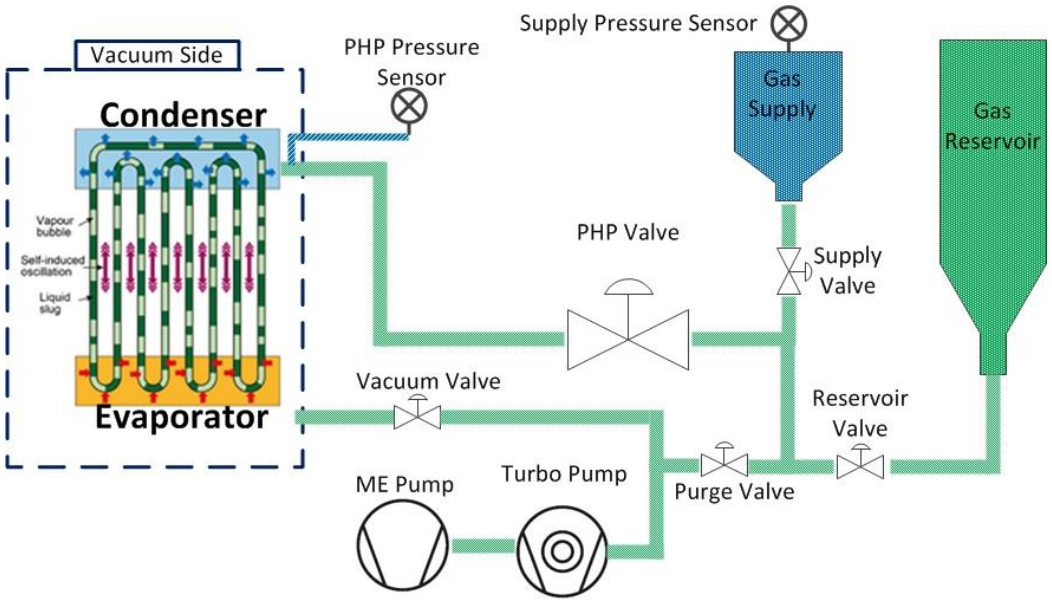

Figure 3-12: Simplified Experimental Apparatus

3.7 Gas Line Dimensions

This section is dedicated thoroughly to describe the gas line design connecting the helium gas supply to the PHP core. It is important to note that the numerical values for the volumes of all the gas-lines supplying the gas to the PHP core will be necessary to calculate the fill ratio.

3.7.1 Gas supply to feedthrough

A more detailed schematic for the gas lines connecting the gas supply to the gas feedthrough located at the dewar's endplate is shown in Figure 3-13. In addition, Figure 3-14 shows the actual gas feedthrough used which was composed of two 1/4 stainless steel tubes with 1/4 VCR connections at both ends and welded to a KF-40 flange. This feedthrough was latter clamped onto a KF-40 cross that serves as the vacuum port for the dewar which is connected directly to the vacuum pump system. Only one of the two gas feedthroughs was used; therefore the unused one was hermetically sealed. This feedthrough has an inner diameter of 3.175 mm and of length 355.6 mm which results in a total volume of 2815 mm^3. The PHP valve was directly connected to the atmospheric end of the gas feedthrough and then connected to the gas supply tank

via a 1/4” (6.35 mm diameter) copper tubing, KF-20 feedthrough and extra tubing which resulted in a total volume VG1 = 227143 mm^3, this gas line will be called ***G1*** for further reference.

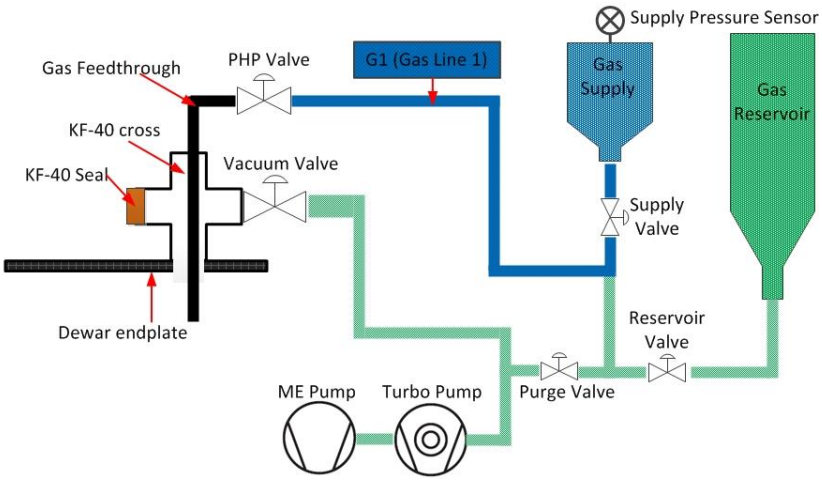

Figure 3-13: Gas Line 1 schematic

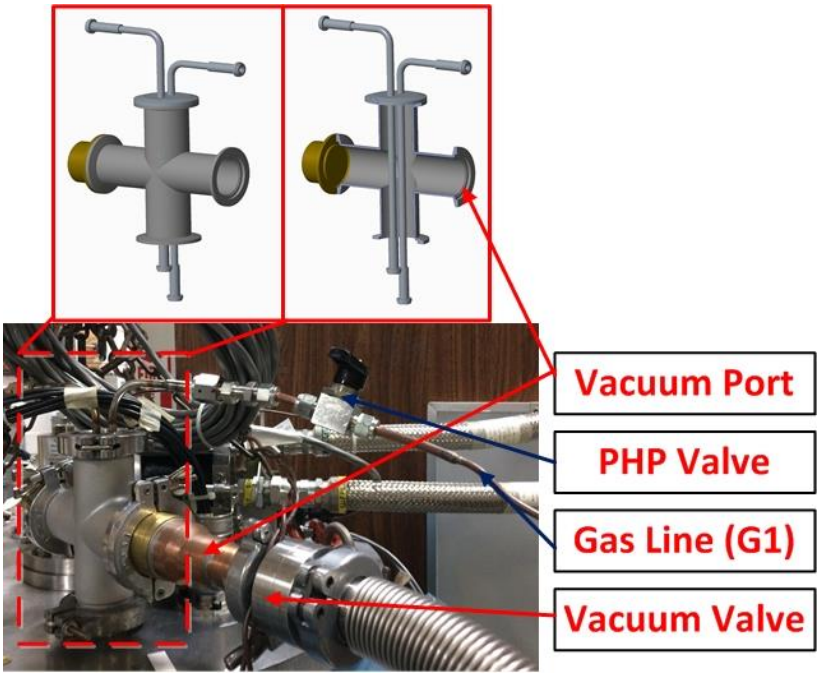

Figure 3-14: Gas feedthrough and vacuum port

3.7.2 Gas Feedthrough to Heat Exchanger

Figure 3-15 shows a schematic of the gas-line named G2 that connects the vacuum side of the feedthrough to a copper heat exchanger. The gas-line G2 is composed of stainless steel tubing grade 304 with an outer diameter, inner diameter and length 1.574 mm, 0.5 mm and 410 mm respectively, see Figure 3-16. Adding

the total volume of the VCR connection and copper unions, the total volume in gas-line G2 was estimated to be 913.3 mm^3. Stainless steel 304 was chosen to reduce the heat transfer from the gas feedthrough (room temperature conditions) to the cold end of the heat exchange (T = 25 K). This heat transfer was estimated to be Q_{G2} = 0.133 mW. The heat exchanger is thermally anchored to the thermal jacket's top plate that is maintained at 25 K by the cryocooler's first stage. The heat exchange is clamped using nine 8-32 bolts and has Apiezon® grease between the contact surfaces to ensure adequate thermal contact and heat transfer. The purpose of the heat exchanger is to allow the first stage of the cryocooler to precool the helium to make the filling process faster by reducing the load on the lower powered second stage and to adsorb any impurities that are in the gas. As shown in Figure 3-17, the heat exchanger is composed of ¼ copper tubing of length 1.382 m that was looped back and forth and brazed onto copper plate. The copper plate has a length, width and thickness of 168 mm, 120 mm and 6.35 mm respectively. The total volume of the heat exchange was resulted in V_{HX} = 2118 mm^3.

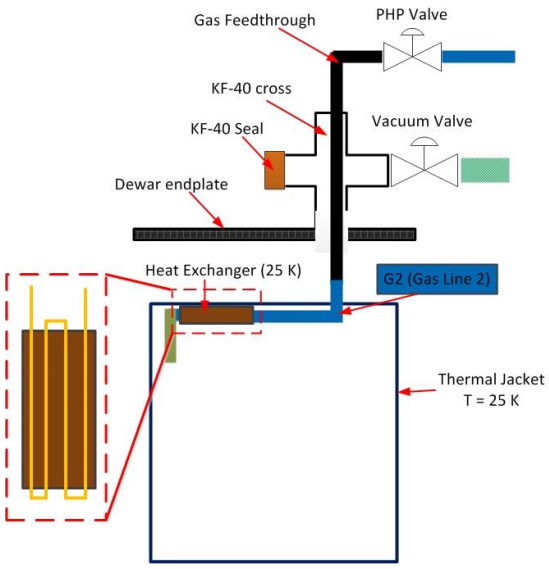

Figure 3-15: Gas line 2 Schematic and Heat Exchanger

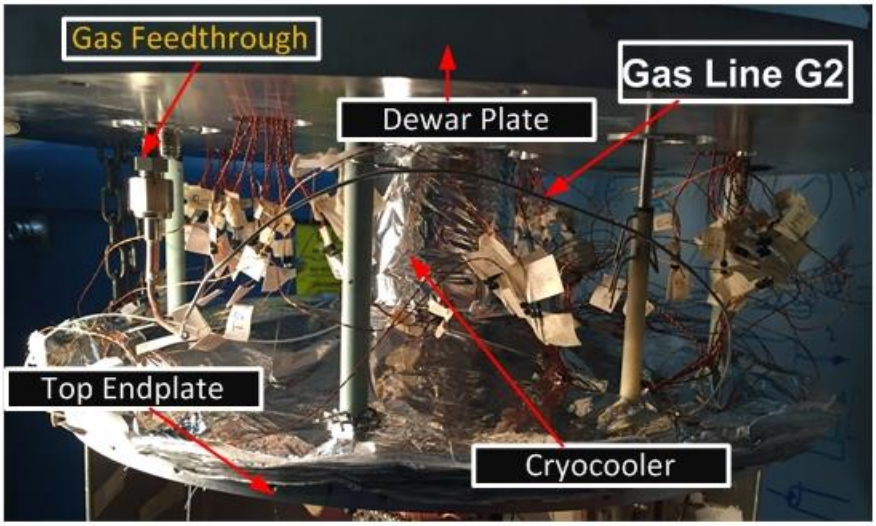

Figure 3-16: Gas Line in experimental apparatus

Figure 3-17: Copper Heat Exchanger

3.7.3 Heat Exchange to secondary PHP valve

As shown in Figure 3-18, a second secondary valve was connected to the other end of the heat exchanger and connected via a SSL tube referred as gas-line G3. This gas-line has an outer diameter, inner diameter, length and volume of 3.175 mm, 1.397 mm, 246.9 mm and V_{G3} = 378.4 mm^3 respectively. This valve was also anchored to the thermal jacket's top plate and was intended to serve as the primary PHP valve as discussed before, but a hermetic seal could not be achieved when closed, therefore the valve connected to the gas feedthrough mentioned before was used as the primary PHP valve instead. The valve has a total volume of V_{valve2} = 291.2 mm^3.

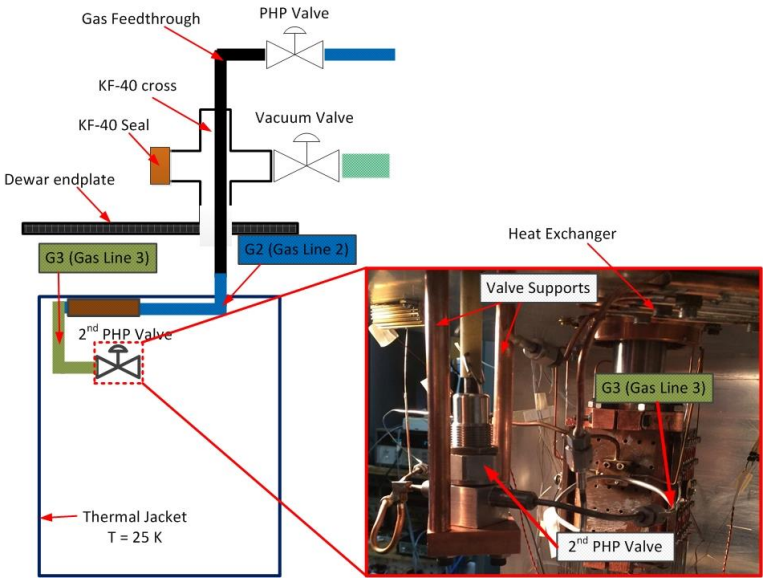

Figure 3-18: Heat Exchange and Gas-line 3

3.7.4 Gas-Line 4

As shown in Figure 3-19, gas-line 4 referred as G4, is a copper T shaped union composed of one section of 1/8 tubing and two sections 1/16" tubing. Copper tubing was used due to the fact that this configuration is easy to construct and solder. As shown, gas-line 4 is divided in three subsections named T-line 1, T-line 2 and T-line-3. A small hole was machined to T-Line 2 and then T-Line 3 was carefully soldered to avoid any clogging inside the tubing. Helium leak checking and pressure testing were performed prior to testing the experiment. The importance of gas-line 4 serves as a path to measure the pressure of the PHP through T-Line 3. A schematic of this line is shown in Figure 3-20, it is important to note that T-Line 3 was connected to one of the gas feedthroughs on the dewar's endplate via a stainless steel capillary tubing. The total volume of only the copper section of G4 was measured to be V_{G4} = 263.21 mm^3.

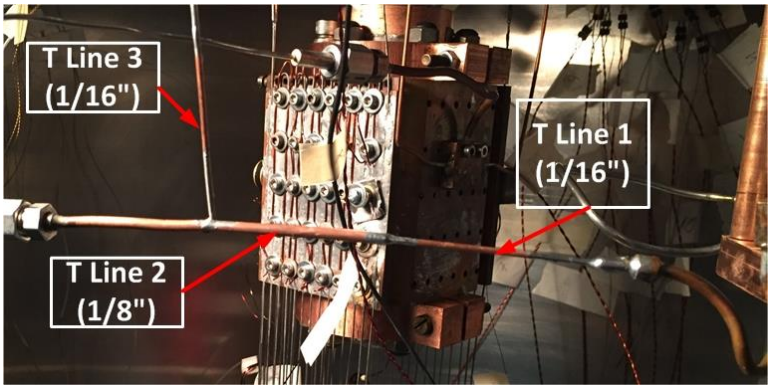

Figure 3-19: Gas Line 4

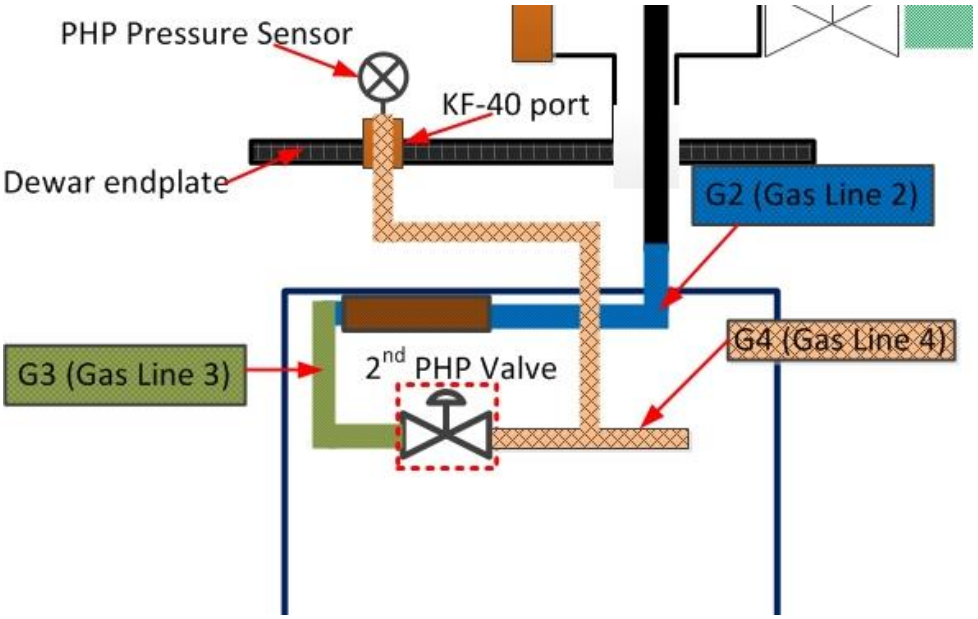

Figure 3-20: Gas Line 4 schematic

As mentioned before stainless steel 304 capillary tubing was chosen to connect the PHP pressure transducer to T-line 3 in order to reduce the heat transfer by means of conduction. Therefore the ends of these sections can be assumed to be at 300 K and 25 K. In addition, the inner, outer diameter and length of the tubing was 0.8 mm, 0.5 mm and 470 mm respectively. Figure 3-20 shows the pressure transducer location on the endplate. Using the integrated thermal conductivity shown in equation (3-1) the heat transfer was estimated to be 1.92 mW; hence it can be assumed to be negligible. The total volume of this stainless steel section including union and soldering connections was estimated to be $V_{trans} = 262.88\ mm^3$. Figure 3-23 shows the

location of the PHP pressure sensor on the dewar endplate which is connected to a KF-40 to KF-20 adapter. A small gas feedthrough was made by soldering a 1/16” tube onto a brass KF-25 blank which served to install and adapt the pressure sensor to the corresponding gas line.

3.7.5 Gas-line 4 to PHP

As shown in Figure 3-21, a stainless steel 304 extension gas-line referred as G5 was used to connect the PHP and gas-line G4 with an outer diameter, inner diameter and length of 1.5875 mm, 0.8382 mm and 245 mm respectively. It is important to note again that the gas line G4 was not connected directly to the PHP since copper has a low thermal resistance, and by using stainless steel line G5 the heat transfer by conduction from 25 K to 4 K is reduced to 0.18 mW. The cryocooler’s heat load capacity is about 1 W at 4.2 K therefore any parasitic heat must be minimized so that the PHP can operate at low temperature. Again in Figure 3-1, the PHP inlet connection is composed of 1/8” copper tubing and sealed against the gas-line G5 using VCR fittings. This PHP connection will be referred as PHP Line and has an inner diameter and length of 1.397 mm and 130 mm respectively, resulting in a total volume of $V_{PHPLine}$ = 378.4 mm^3. Figure 3-22 shows a schematic with gas-line G5, PHP Line and the PHP.

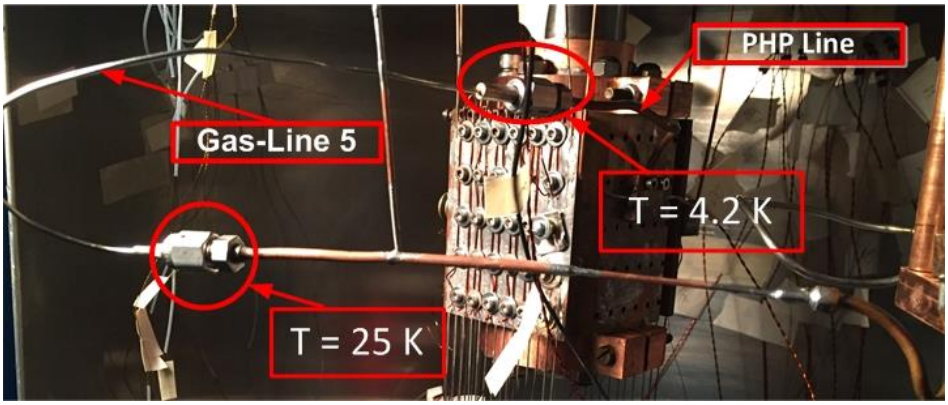

Figure 3-21: Gas-Line 5 to PHP Line

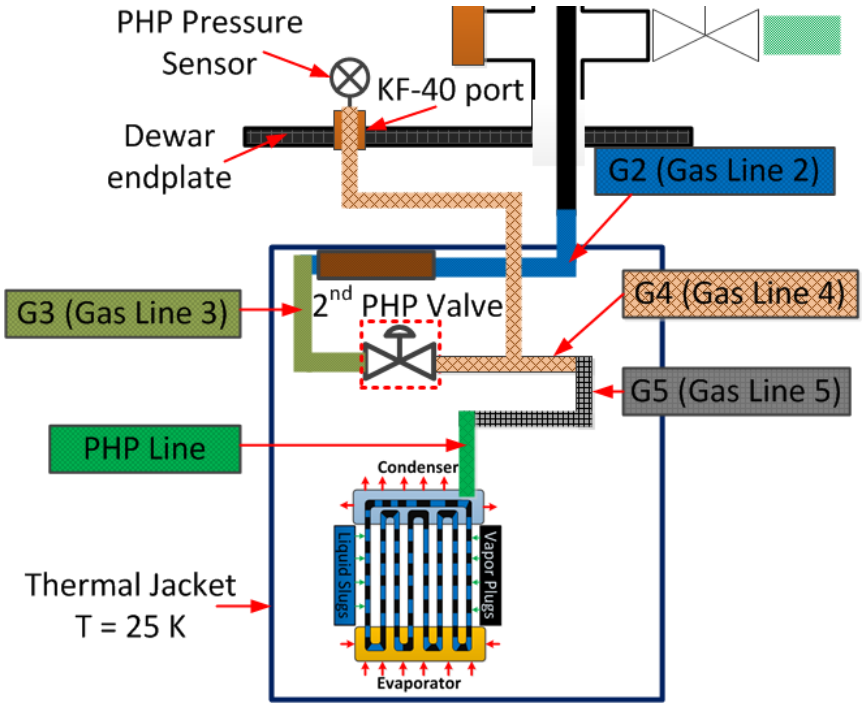

Figure 3-22: Gas Line 5 and PHP Line Schematic

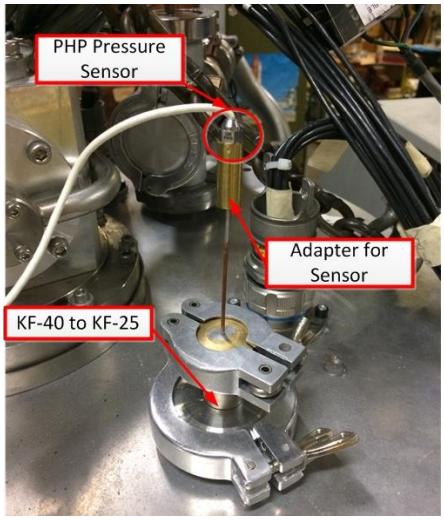

Figure 3-23: PHP Pressure Sensor Location

3.7.6 Capillary Tubing and Unions

As shown in Figure 3-24, the PHP Line was connected to a rectangular manifold composed of two more 1/16" copper unions that are connected the adjacent PHP sections. While additional 1/16" copper unions are soldered to the middle PHP section. The total volume composing these 1/16" unions was estimated to be V_{union} = 142.8 mm^3. Finally, the PHP sections are composed of stainless steel 304 with an inner diameter,

outer diameter and total length of 0.5 mm, 0.8 mm and 21.32 m respectively, resulting in a total capillary tubing volume of V_{cap} = 4186 mm^3. The total PHP volume is the sum of $V_{PHPLine}$, V_{union} and V_{cap} resulting in a total volume of V_{PHP} = 4707.2 mm^3.

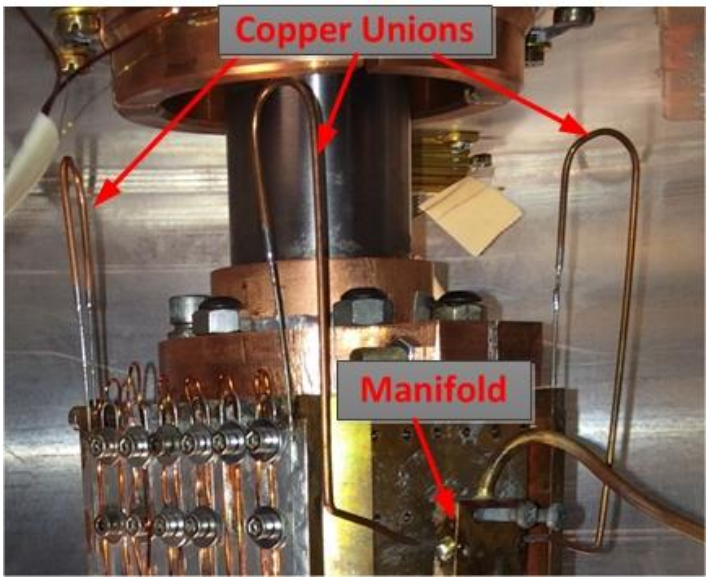

Figure 3-24: PHP copper unions

3.8 Measurement Devices and Instrumentation

3.8.1 Thermometer Specifications and Instrumentation

A total of 10 temperature sensors were installed throughout the experiment one of which was a Cernox ® type CX-1050-CU-HT-1.4L and the other 9 were germanium type GR-200A sensors. The Cernox sensor was calibrated by Lakeshore from 300 K down to 1.4 K. All temperature sensors have a 4 wire configuration as shown in Figure 3-25, where two leads were used as the excitation source at a fixed current *I* and the other two were used to read the voltage *V*, hence ohms law can be utilized to solve the electrical resistance *R=V/I* and temperature can be determined by using temperature versus resistance calibration curves.

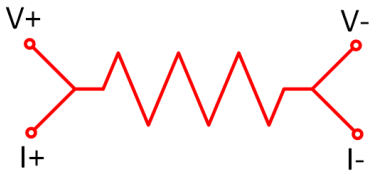

Figure 3-25: 4-wire configuration

As shown in the following schematic, the current leads for the Germanium were electrically connected in series so that a constant current of 20 μA could be supplied to all of the sensors using a single Keithly Model 224 current supply. Similarly, a constant current of 3 μA was supplied to the Cernox sensor using a Lakeshore Model 120 current supply. All of the output voltages were read using a National Instruments Model USB-6218 DAQ.

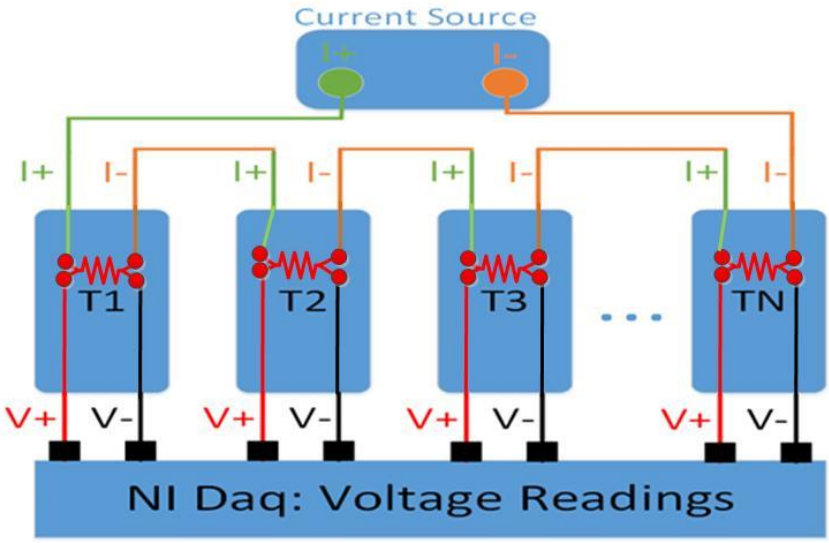

Figure 3-26: Thermometer connection schematic

As shown in Figure 3-27, a total of 9 temperature sensors are connected throughout the 3 PHP sections, located at each evaporator and condenser sections. Also, temperature sensor T8 was placed on the thermal jacket. In this figure T indicates a temperature sensor and H indicates a heater. The Cernox® sensor, referred as T1, was attached to the condenser section of PHP 1. Table 3-2 shows which temperature sensors and heaters are used for each PHP section.

Table 3-2: Temperature and heater numbering for each PHP section

PHP Section	Temperature Used	Heaters Used
PHP1	T10, T5 and T1	H1 and H2
PHP2	T6, T7 and T9	H3 and H4
PHP3	T2, T3 and T4	H5 and H6

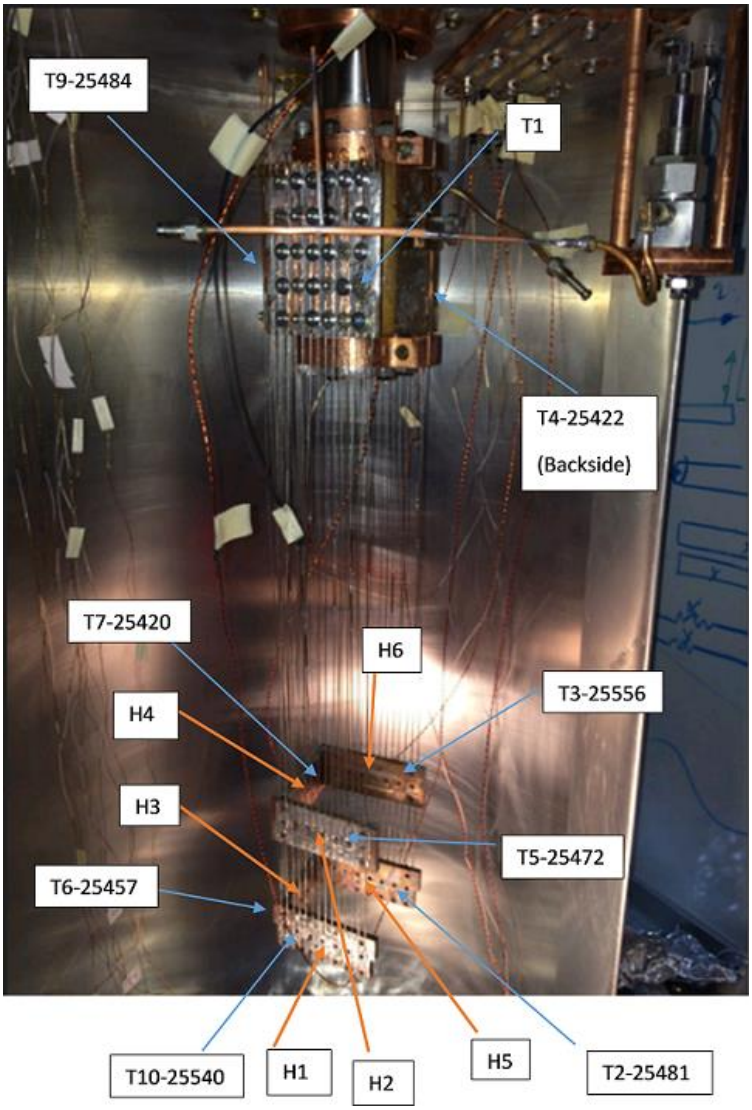

Figure 3-27: temperature and heater locations

3.8.2 Heater Specifications and Instrumentation

As shown in Figure 3-29 and Figure 3-29, 10 W heaters model Kal-10, with resistance of 50 Ohms and tolerance of 1 %, were installed onto the evaporator sections. These resistors have a nichrome wire that is epoxied inside an aluminum casing of width, length and height of 10.5 mm, 19.05 and 9.9 mm respectively. Two through holes on the casing allow the heater to be bolted onto the evaporator sections. Two wires were soldered at each lead in order to have a 4-wire configuration; therefore Ohms Law can be applied to calculate the electrical power of the heater. It is important to note that a seventh heater was

installed at the copper sleeve in order to temperature control the cryocooler if needed. A second National Instruments DAQ model USB-6211 was used to read all output voltages for the heaters.

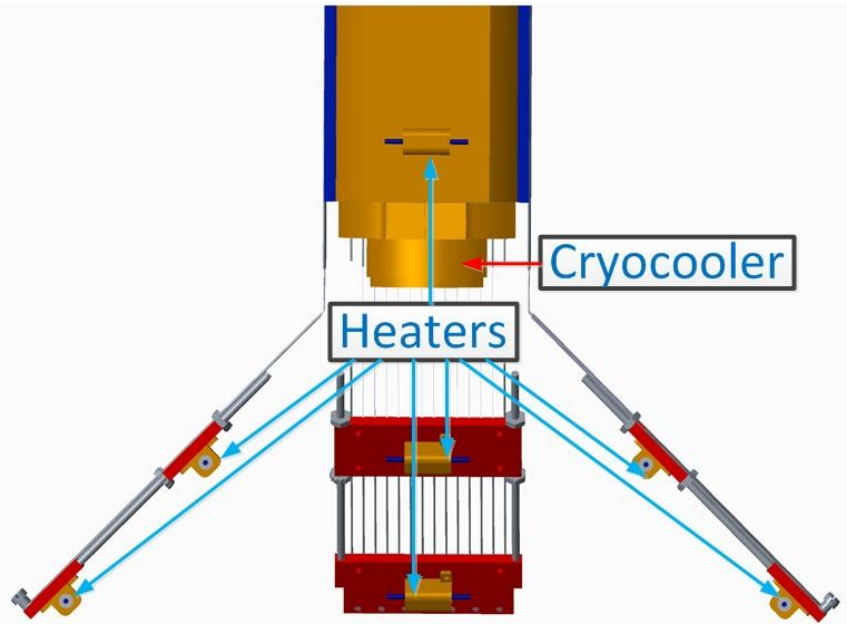

Figure 3-28: Heater Locations

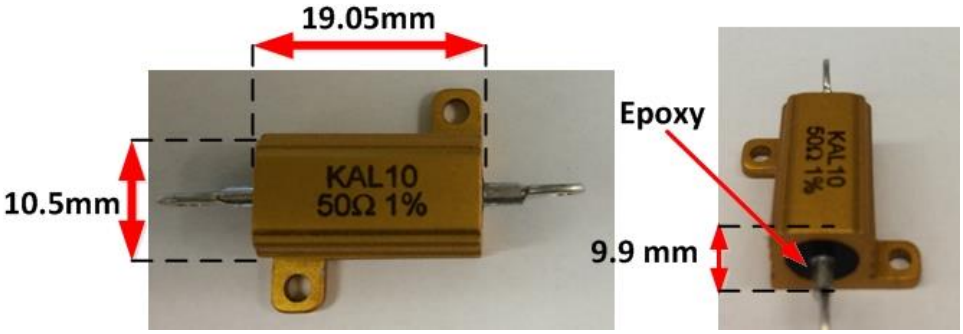

Figure 3-29: 10 W Heater

It is important to mention that the power lines of the heaters were designed to minimize any parasite heat transfer caused by electrical heat generation as well as the heat conduction through the wires. Heat transfer by convection is negligible since experimental apparatus is under vacuum conditions. Two separate types of power lines were made in order to minimize the any parasite heat transfer to the evaporator sections and will be referred as extension 1 and extension 2. As shown in Figure 3-30, extension 1 was connected from the electrical feedthrough to an electrical bridge. As shown in Figure 3-31 the electrical bridge was

composed of multiple pairs of copper wires, 0.7 mm in diameter, and epoxied to an aluminum plate that was latter clamped to the thermal jacket in order to achieve a constant temperature of 25 K. Extension 2 power lines were then connected from the electrical bridge to the corresponding heaters. A 0.4 mm and 0.7 diameter wires were chosen for extension 1 and extension 2 respectively and are coated with insulation material. Each heater requires one pair of wires, six heaters were clamped at the evaporator sections and one heater at the copper sleeve; therefore a total of 14 wires per extension type were constructed. As shown in Figure 3-31, each pair of power lines was twisted in order to reduce any electrical emf noise.

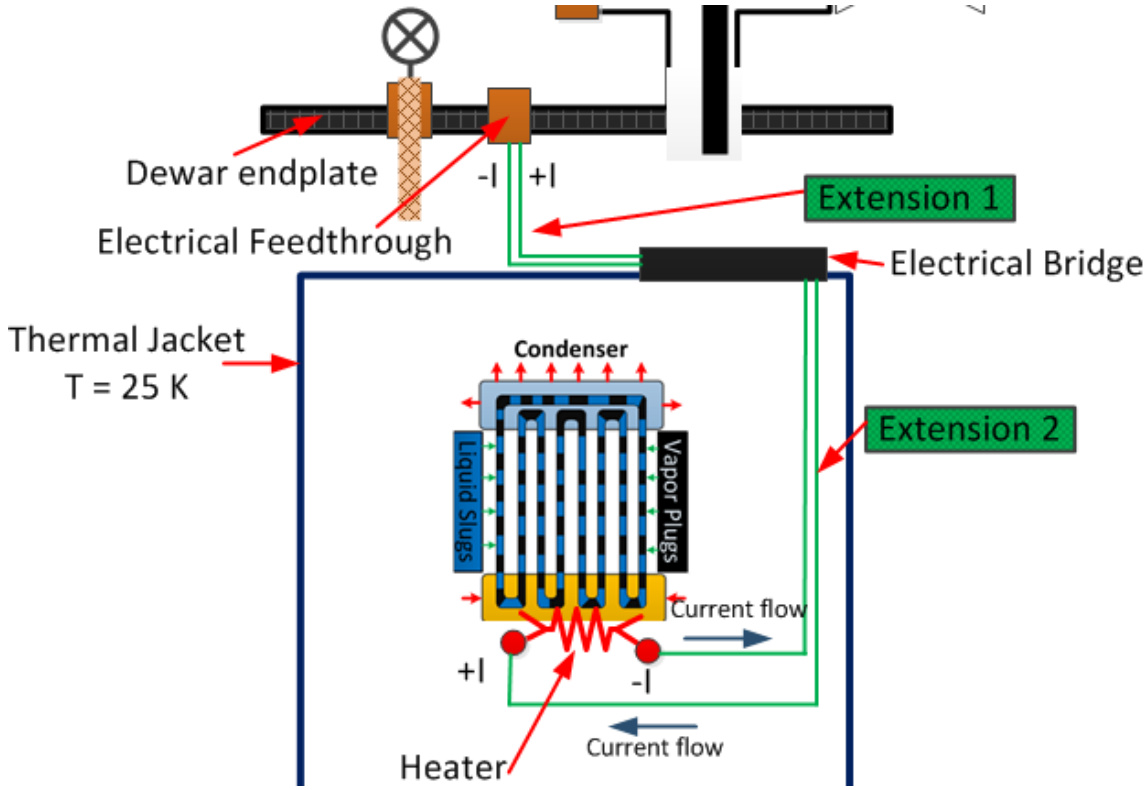

Figure 3-30: Simple schematic for heater power lines

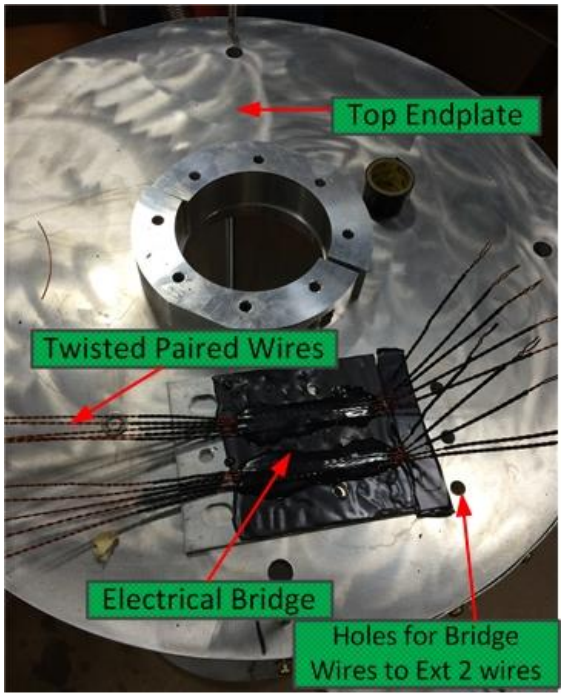

Figure 3-31: Electrical Bridge

As shown in Figure 3-2, a 1-D finite control volume analysis in steady state conditions was performed on a copper wire with thermal and electrical dependent properties in order to choose the correct dimensions for the power lines as mentioned before.

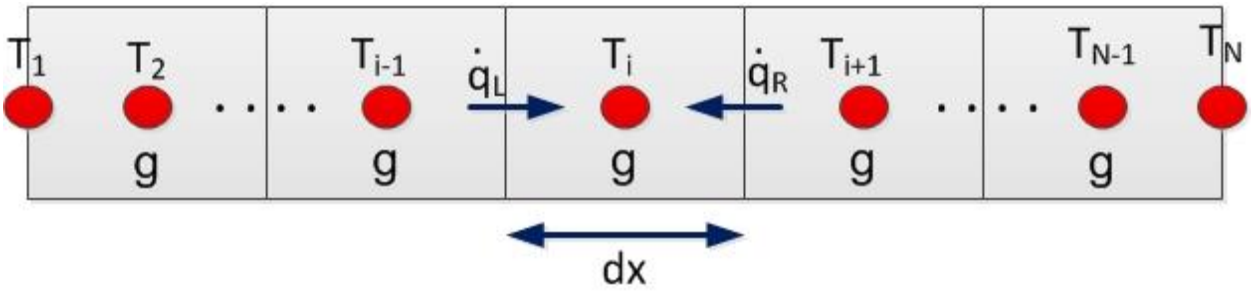

Figure 3-32: 1-D finite control volume

Where T_1 and T_N represent the temperature boundary nodes, dx is the distance between the nodes and the control volume width, $\dot{q}_L$ and $\dot{q}_R$ represent the heat transfer from the left and right respectively and g represents the electrical heat generation. Since heat generation has to be considered, the integrated thermal conductivity equation cannot be used. The boundary conditions at each end represent the fixed temperature that the extension lines were connected too. For extension 1, the hot end temperature T_1 was assumed to be

the temperature of the dewar's endplate T_1 = 300 K, while the cold end temperature T_1 was assume to be the temperature of the thermal jacket T_N = 25 K. Similarly, the boundary temperatures for extension 2 were assumed to be 25 K and 2.7 K. Therefore the heat equation for each control volume can be represented by the following equation.

$$\dot{q}_L + \dot{q}_R + g = 0 \tag{3-3}$$

The heat transfer rates and heat generation for nodes between i = 3 and N-2 can be represented by the following equations:

$$\dot{q}_L = \frac{k_L A_c (T_{i-1} - T_i)}{dx} \tag{3-4}$$

$$\dot{q}_R = \frac{k_R A_c (T_{i+1} - T_i)}{dx} \tag{3-5}$$

$$g = \frac{\rho I_c^2 dx}{A_c} \tag{3-6}$$

Where k_l is the thermal conductivity using an average temperature with the left adjacent node $T_{avg} = (T_{i-1} + T_i)/2$ and k_r is the thermal conductivity at an average temperature with the right adjacent node $T_{avg} = (T_{i+1} + T_i)/2$. A_c is the circular cross-sectional area of the wire, I_c and ρ are the electrical current and resistivity of the wire. The electrical resistivity is a function of the temperature of T_i. Using these equations the energy balance yields

$$k_L T_{i-1} - (k_L + k_r) T_i + k_r T_{i+1} = -\frac{\rho(T_i) I_c^2 dx^2}{A_c^2} \tag{3-7}$$

Similarly, the energy balance at nodes T_2 and T_{N-1} were simplified to the following equations

$$2k_L T_1 - (2k_L + k_r) T_2 + k_r T_3 = -\frac{\rho(T_2) I_c^2 dx^2}{A_c^2} \tag{3-8}$$

$$k_L T_{N-2} - (k_L + 2k_r) T_{N-1} + 2k_r T_N + = -\frac{\rho(T_{N-2}) I_c^2 dx^2}{A_c^2} \tag{3-9}$$

Using left hand side of the energy balances a stiff matrix A was constructed with the k_L and k_R parameters while the right hand side is just an array *b*. Using Matlab, the temperature array was solved by getting the inverse of matrix A and multiplying it by *b*.

$$AT_m = b$$

or 3-10

$$T_m = A^{-1}b$$

It is easily seen that heat transfer by conduction is directly proportional to the cross-sectional are A_c and inversely proportional to the length L; therefore small diameters and long lengths are required to reduce the heat conduction but additionally reducing the diameter at a fixed electrical current I_c would increase the electrical resistance at a specific location and could cause the wire to burn. An example of an undesirable case is shown in Figure 3-33, were a diameter D = 0.5 mm, length L = 50 m, I_c = 1 A and a total number of 50 nodes were used. It can be observed that a domed shaped temperature distribution along the length was caused by high heat generation, therefore the maximum electrical current is an important constraint to be considered while running the experiment

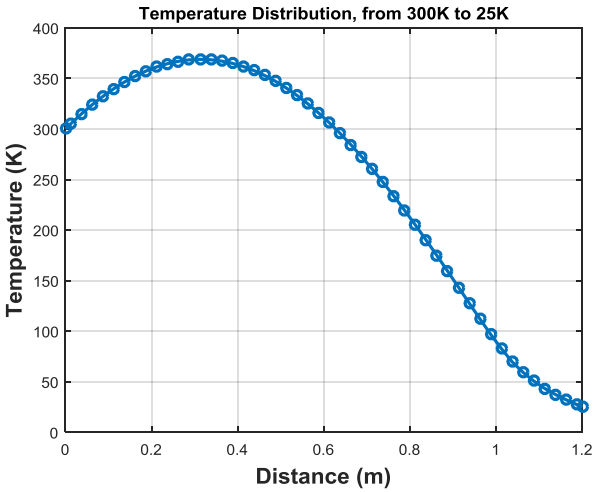

Figure 3-33: Undesirable extension line

Six 50 Ohms heaters will be set to dissipate a maximum overall heat load of 1.5 W or 0.25 W per heater, resulting in a total current of I_c = 0.0707 A per heater. Since it is easier to fix or replace any damaged lines

outside the thermal jacket (extension 1 lines) the diameter for the extension 2 lines was chosen to be 0.7 mm in case the current was mistakenly increased to an undesirable level. Figure 3-34 shows the temperature distribution for both extension 1 and extension 2 lines with 0.4 mm and 0.7 mm respectively. In addition, the total heat transferred of all 14 paired wires for extension 1 to the thermal jacket was calculated to be 0.2068 W while for extension 2 was calculated to be 0.0866 W.

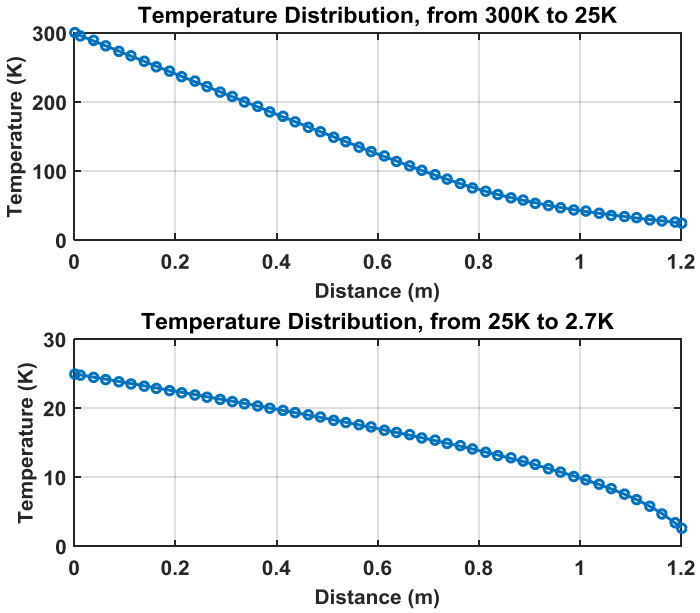

Figure 3-34: Extension 1 and Extension 2 distribution lines

4 Effective Thermal Conductivity and Fill Ratio Calculations

4.1 Effective Thermal Conductivity K_{eff}

The effective thermal conductivity k_{eff} of the PHP is defined according to equation 4-1. Here, the heat flow Q_{load} is the heat load applied to one of the three PHP sections. A_c is the cross-sectional area through which the helium flows in a single capillary tube, multiplied by the number of tubes, N = 14 per PHP section. $\bar{T}_{evap}$ and $\bar{T}_{cond}$ are the average evaporator and condenser temperatures, and L_{eff} is the adiabatic length.

$$Q_{load} = \frac{Nk_{eff}A_c(\bar{T}_{evap} - \bar{T}_{cond})}{L_{eff}}$$

or 4-1

$$k_{eff} = \frac{Q_{load}L_{eff}}{NA_c(\bar{T}_{evap} - \bar{T}_{cond})}$$

and

$$A_c = \frac{(\pi CAP_{ID}^2)}{4} = 0.963\ mm^2 \quad 4\text{-}2$$

where the capillary's inner diameter is CAP_{ID} = 0.5 mm and L_{eff} = 300 mm or 380 mm depending on which heaters are used.

4.2 Liquid Fill Ratio f_{liq}

The liquid fill ratio of the entire PHP core is calculated based on the known volumes of the supply tank, gas lines, capillary tubing and connecting tubing. Table 4-1 shows a summary of all these volumes discussed in section 4. In addition the table describes which pressure sensors and temperature values are used to calculate their respective densities.

Table 4-1: Volume Summary and mass calculation

Volumes names	Volume (m^3)	Temperature (K)	Pressure Sensor to use when PHP valve closed	Phase	Density Calculation $\boldsymbol{\rho(P,T)}$	Mass id
V_{tank}	3.6000E-03	T_o = 300	P_{supply} (Supply sensor)	gas phase	ideal gas law	**m1**
V_{G1}	2.2714E-04	T_o = 300	P_{supply} (Supply sensor)	gas phase	ideal gas law	**m2**
V_{feed}	2.8150E-06	T_o = 300	P_{PHP} (PHP sensor)	gas phase	ideal gas law	**m3**
V_{G2}	9.1330E-07	T_o = 300	P_{PHP} (PHP sensor)	gas phase	ideal gas law	**m4**
V_{HX}	2.1180E-06	T_1 = 25	P_{PHP} (PHP sensor)	gas phase	ideal gas law	**m5**
V_{G3}	3.7840E-07	T_1 = 25	P_{PHP} (PHP sensor)	gas phase	ideal gas law	**m6**
V_{valve2}	2.9120E-07	T_1 = 25	P_{PHP} (PHP sensor)	gas phase	ideal gas law	**m7**
V_{G4}	2.6321E-07	T_1 = 25	P_{PHP} (PHP sensor)	gas phase	ideal gas law	**m8**
V_{trans}	2.6288E-07	T_1 = 25	P_{PHP} (PHP sensor)	gas phase	ideal gas law	**m9**

V_{G5}	1.3520E-07	T_2 = (25+2.9)/2	P_{PHP} (PHP sensor)	gas phase	ideal gas law	**m10**
V_{PHP}	4.3288E-06	T_3 = 2.9	P_{PHP} (PHP sensor)	two phase	equation of state [x]	**m11**

First, it is very important to indicate that before supplying helium to the PHP, all the gas lines and the PHP capillary are evacuated using a turbo-molecular vacuum pump. As shown in equation 4-3, the known volume of the helium tank (V_{tank}), its initial charge pressure (P_o), and the ambient temperature T_o, combined with the ideal gas law are used to calculate the total mass m_o before opening the supply valve and filling the rest of the volumes.

$$m_o = \frac{P_o V_{tank}}{R T_o} \tag{4-3}$$

Once the supply valve is opened the total mass m_o in the system is still conserved and can now be expressed as the sum of all the masses shown in Table 4-1, the only difference is that the initial charge pressure P_o decreases to a final pressure called P_{supply}

$$m_o = m_1(T_o, P_{supply}) + m_2(T_o, P_{supply}) + \cdots m_{11}(T_{12}, P_{PHP}) \tag{4-4}$$

The php mass m_{11} can be rewritten as

$$m_{11} = \bar{\rho}_{l,sat} V_l + \bar{\rho}_{v,sat}(V_{PHP} - V_l) \tag{4-5}$$

Where $\bar{\rho}_{l.sat}$ and $\bar{\rho}_{v.sat}$ are the densities of the saturated liquid and saturated vapor respectively, and V_l is the volume occupied by the liquid in the PHP.

$$\bar{\rho}_{l,sat} V_l + \bar{\rho}_{v,sat}(V_{PHP} - V_l) = m_o - \sum_{i=1}^{10} m_i \tag{4-6}$$

Therefore V_l can be simplified to

$$V_l = \frac{m_o - \sum_{i=1}^{10} m_i - \bar{\rho}_{v,sat} V_{PHP}}{\bar{\rho}_{l,sat} - \bar{\rho}_{v,sat}} \tag{4-7}$$

Finally, the fill percentage is calculated from the liquid and total volumes in the PHP:

$$f_{liq} = \frac{V_l}{V_{php}} \quad 4\text{-}8$$

5 Experimental Results and Configurations

The PHP core has been tested by applying electrical power through the heaters attached to the evaporators over a range of heater power values in order to understand the power limitations and thermal performance of the PHP. The heater's power supply was controlled through Labview® by outputting an analog DC signal in the range from 0 V to 10 V from the NI DAQ 6218 to the power supply. Labview® software was used to control power supply and all data acquisition systems. The power supply and data collection automation simplified the data collection process so that a large range of heater power values could be tested. In addition to varying applied heat loads the fill ratio of the PHP was varied between 20 % and 90 %. The data were used to map the PHP performance as a function of fill ratio and to determine the optimal fill ratio for each configuration. All of the results were obtained using helium as the PHP working fluid. Additionally, two configurations of the experiment were tested. The two configurations were identical except that one had an adiabatic length of 300 mm and the other 1000 mm.

5.1 Case 1: Constant heat load applied for adiabatic of 300 mm

Figure 5-1 shows a Labview® snapshot of temperature versus time. Temperatures are increased by ramping the power supply to a higher voltage every 2000 seconds to achieve high precision. Each ramp is called a run following by a specific identification number, which are then saved to a separate text file for later analysis. It is important to note that the power supply was ramped up and then ramped down with the same voltage values in order to observe any hysteresis in the PHP. A total of 2500 runs have been performed therefore only the most important data will be discussed.

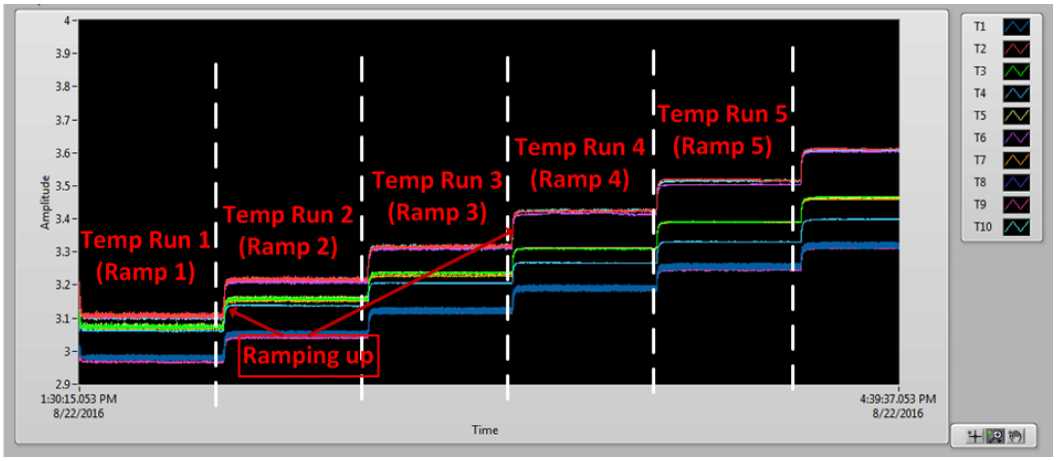

Figure 5-1: Ramping process, Labview snapshot

5.1.1 Fill ratio at 43.65 %

The first time the PHP operated was at a fill ratio of 43.65 %. During this case only the bottom heaters, H1, H3 and H5, were active. Each of these heaters was connected to a different PHP section as mentioned in section 4.8. Heat loads from 0 W to 0.24 W with 35 gradual increments were applied to each heater in a ramp up process and another 35 runs for the ramp down process, as shown in Figure 5-2. It can be observed that the temperature distribution over time is very symmetric indicating that there is no hysteresis.

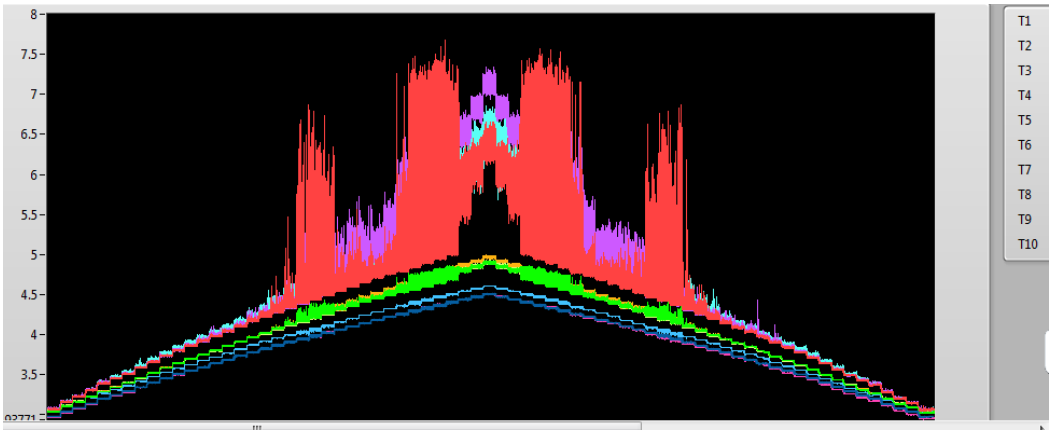

Figure 5-2: Labveiw® Snapshot of bottom heaters on at 43.65 % fill

Furthermore, all temperatures in each run were averaged in order to calculate the effective thermal conductivity for each PHP section given by equation 4-1. These results were plotted versus the applied heat

load as shown in Figure 5-3., No hysteresis was observed during the ramp up and ramp down for this case. The effective thermal conductivities plots show a dome shaped behavior were the maximum k_{eff} for PHP1 was 36,550 W/m/K at 0.154 W, for PHP2 was 40,100 W/m/K at 0.1266 W and for PHP 3 was 41,470 W/m/K at 0.1677 W/m/K. The decrease in k_{eff} occurred when the evaporator section dried out, causing a high change in temperature ΔT between the evaporator and condenser section as shown in Figure 5-4.

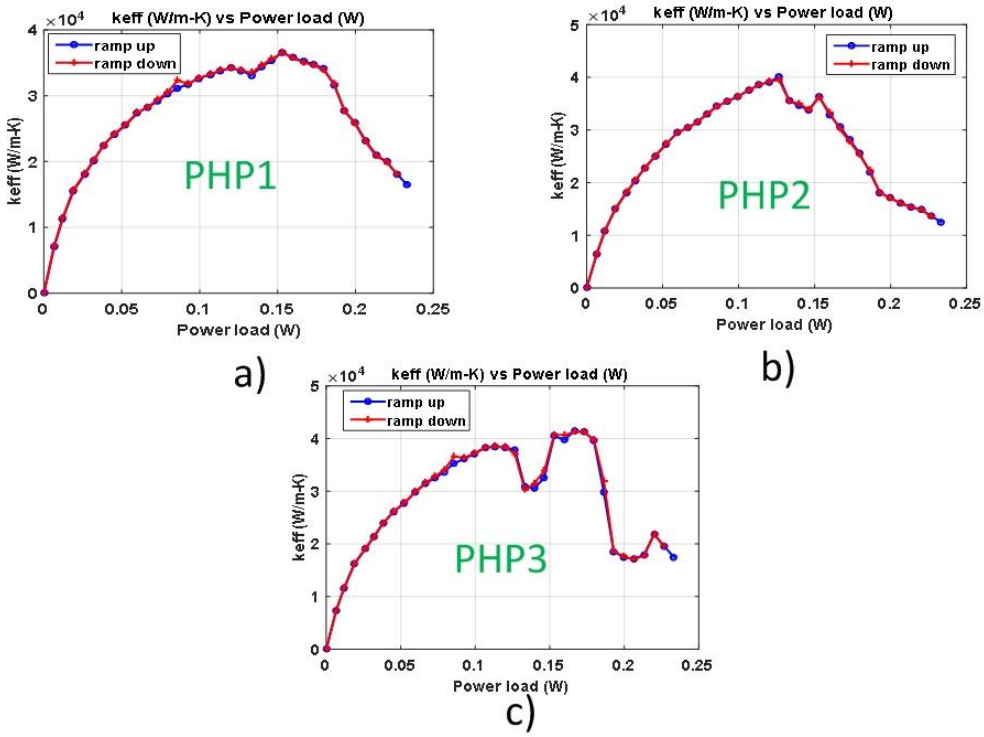

Figure 5-3: Effective Thermal conductivity for Bottom Heaters at 43.65 %

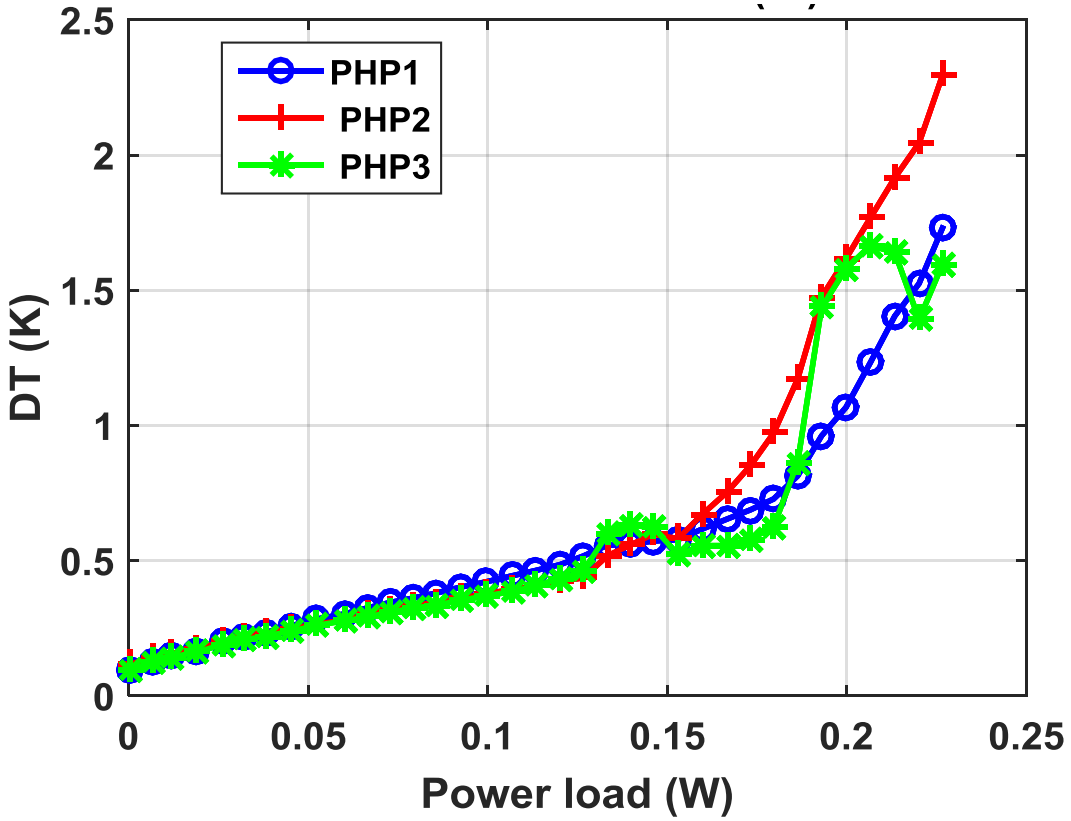

Figure 5-4: Temperature change ΔT versus Power

5.1.2 Fill ratio at 70 %

5.1.2.1 Constant Heat Loads

The maximum effective thermal conductivities versus fill ratios for cases with bottom heaters "on" are shown in Figure 5-5. The fill ratio was varied from around 20 % to 90 % in a series of experiments. The maximum effective thermal conductivity was achieved with a 70 % fill ratio. Cases with only bottom heaters "on", only top heaters "on" and both top and bottom heaters "on" were performed for all these fill ratios. For the rest of this section only cases at fill ratios of 70 % will be discussed. The results from experimental runs with other fill are shown in Appendix 8.1.

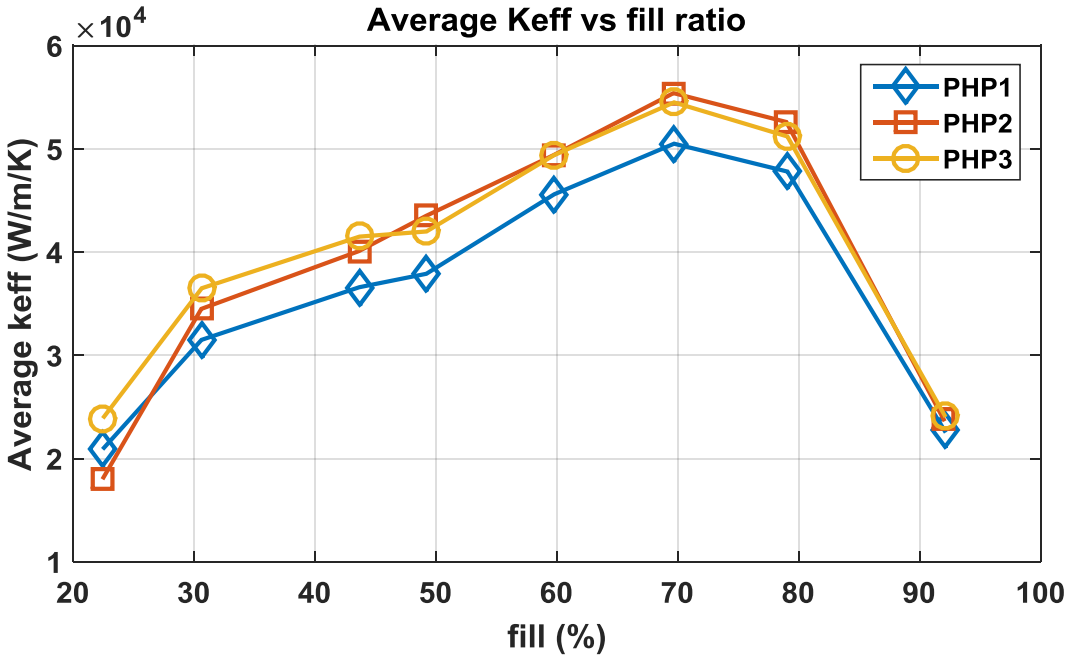

Figure 5-5: Maximum k_{eff} versus fill ratio

Figure 5-6 shows a plot of the temperature distribution in time of 43.65 % and 70 % fill ratios. High amplitude temperature oscillations at high heater powers are significantly reduced for the PHP operating with a 70 % fill ratio compared to the PHP operating with a 43.65% fill ratio.

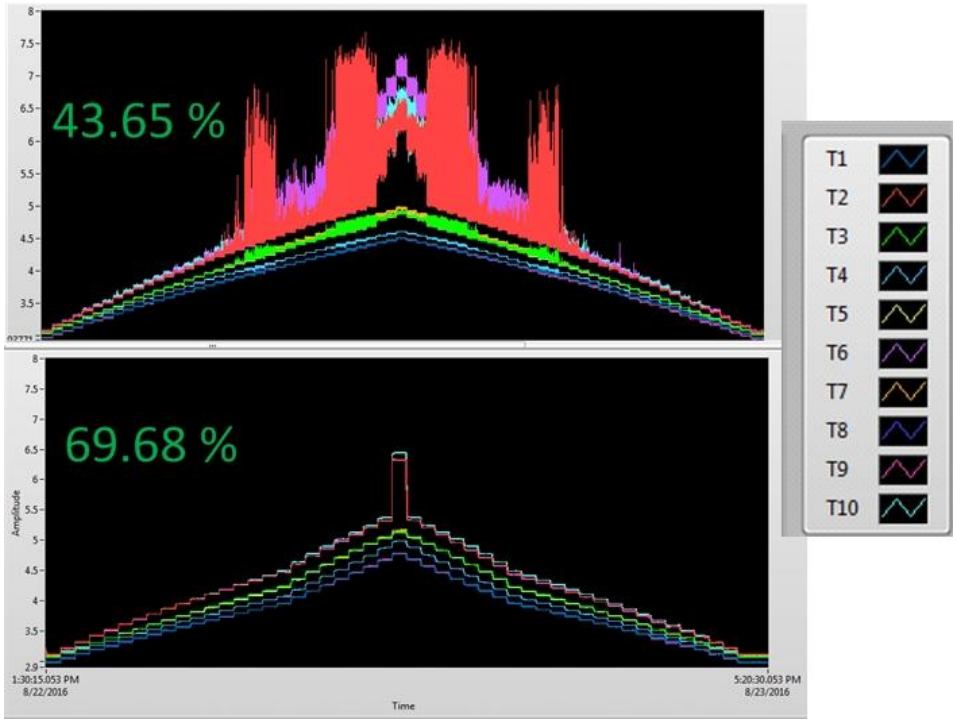

Figure 5-6: Fill ratio comparison

One possible explanation is that at low fill ratios and high heat loads the two-phase flow at the evaporator section becomes single phase vapor as the liquid boils away before reaching the condenser section. While at fill ratios above 80 %, as shown Figure 5-7, high temperature oscillations were also observed but at lower heat loads. For this case, a possible explanation could be that the two-phase flow inside the condenser section completely transitions to a single liquid phase plugging and preventing any vapor from moving into the condenser section. The flow conditions in both of these cases stops the desired pulsating motion of the PHP, These results show that the thermal performance of a PHP is very sensitive to the fill ratio due to the effects of fill ration on the flow regime.

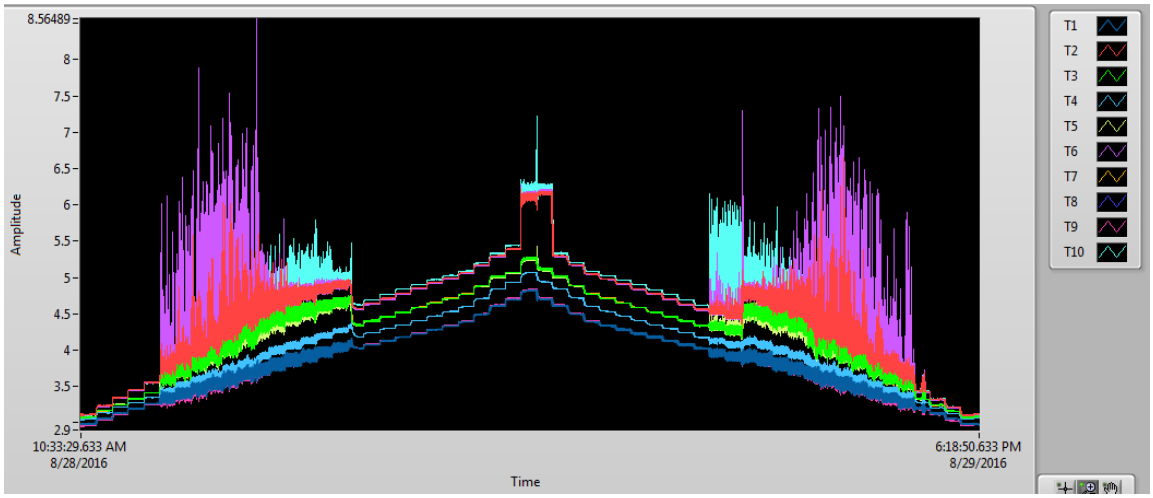

Figure 5-7: Bottom Heaters On at 80 % fill ratio, Y values are in Kelvin

Figure 5-8 shows the effective thermal conductivity versus heat load applied to the bottom heaters at 70 % fill ratio. As observed some hysteresis is present, were the down ramp values are slightly higher than the ramp up conductivities. Effective thermal conductivities around 50,000 W/m/K were achieved.

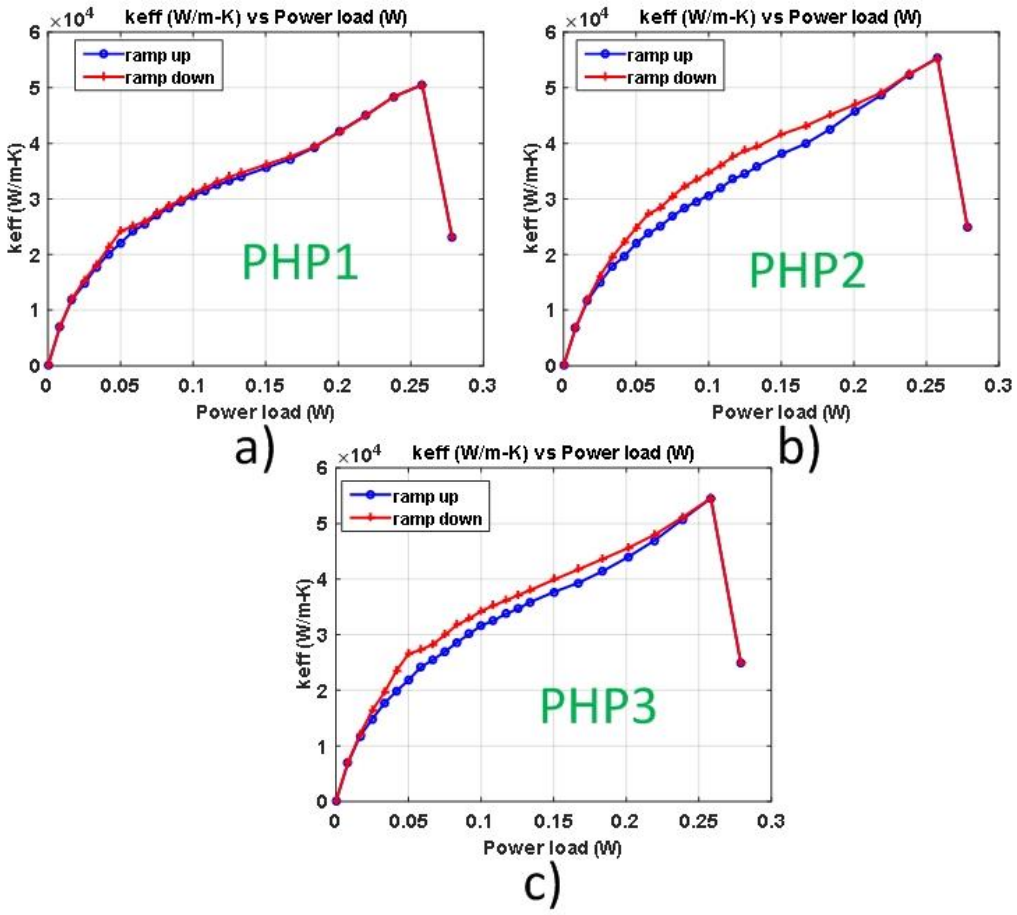

Figure 5-8: Effective thermal conductivities PHP1, PHP2 and PHP3

A power spectral analysis was performed on the temperature and pressure data as shown in Figure 5-9. The power spectrum of the temperature was performed on temperature T1, which is located at the condenser section of PHP1. Even though these spectra were obtained at the maximum k_{eff} achieved for 70 % fill ratio and with bottom heaters "on", it was observed the same frequency of 1.3 Hz were obtained at any heat load applied as shown in Figure 5-10. This frequency was always observed as the dominant frequency at the other fill ratios and heat loads. After reviewing the cryocooler's specifications, it was determined that the physical frequency of the cryocooler oscillates around 1.2 Hz. The difference in 0.1 Hz was due to the fact that the data acquisition daqs were not synchronized to the same sampling clock and therefore there was a timing acquisition lag. Once the NI-Daqs were synchronized to the same clock, the power spectra matched exactly 1.2 Hz. It is important to note that this frequency is dominant and could provide the necessary

disturbance to start the PHP to operate in an oscillatory manner. It is possible to change the crycooler's frequency using a special power adapter recommended by Sumitomo, therefore future tests could verify how the thermal performance changes as a function of the cryocooler's frequency.

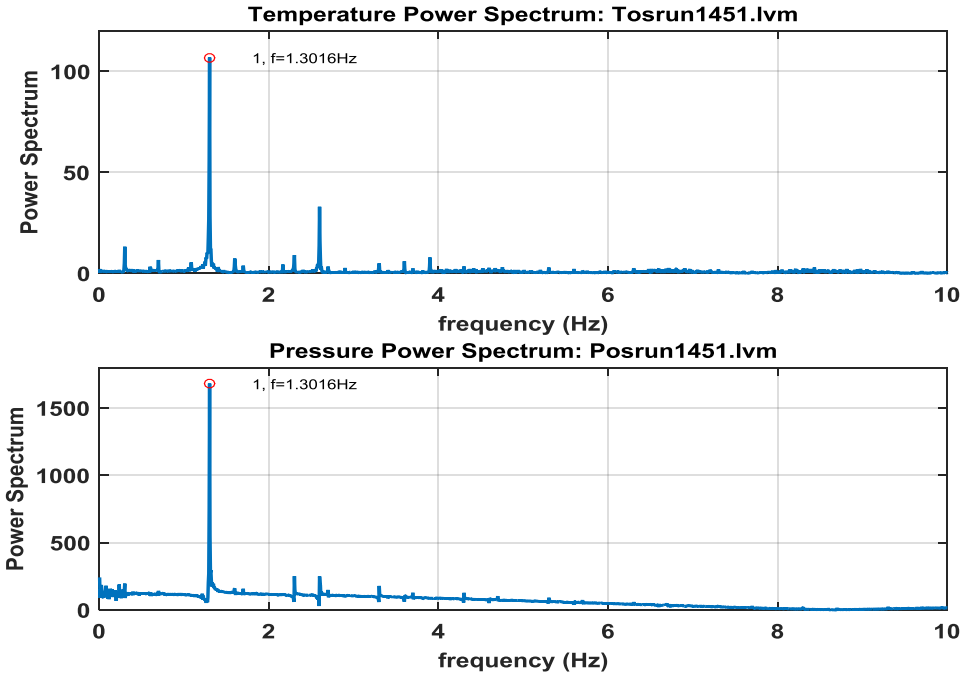

Figure 5-9: Power Spectrum for 70 % and bottom heater on at max k_{eff}

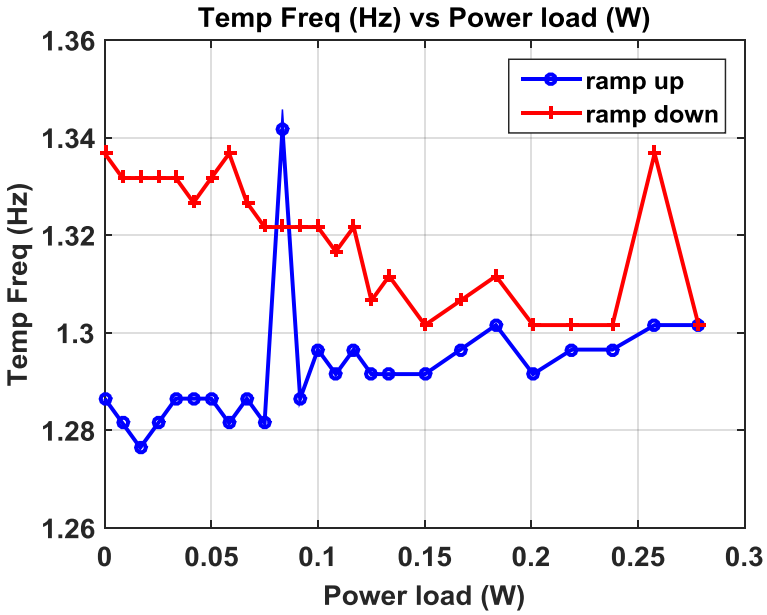

Figure 5-10: Frequency vs heat load for 70 % and bottom heaters on

Figure 5-11 shows how the initial fill ratio changes as more liquid was boiled off due to an increase in heat load at the evaporator sections where this figure is for the ramped up cases only. It can observed that a decrease in fill ratio is found between heat loads of 0.2385 W and 0.2583 W with pronounceable peaks close to 55 % for PHP2 and PHP3 while for PHP1 was found to be 69.64 %. In addition, the fill ratio was plotted versus the evaporator temperatures as shown in Figure 5-12 and it was determined that these peaks are found between 5.087 K and 5.188 K that are close to the critical temperature of helium T_{crit} = 5.195 K.

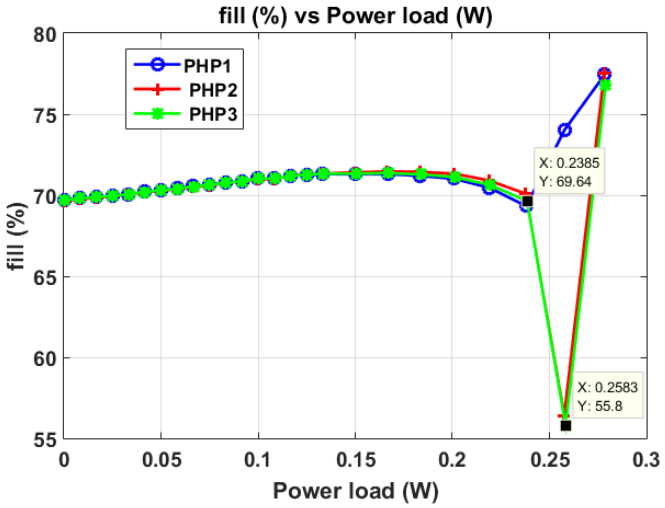

Figure 5-11: fill ratio vs heat load, bottom heaters on and ramp up cases

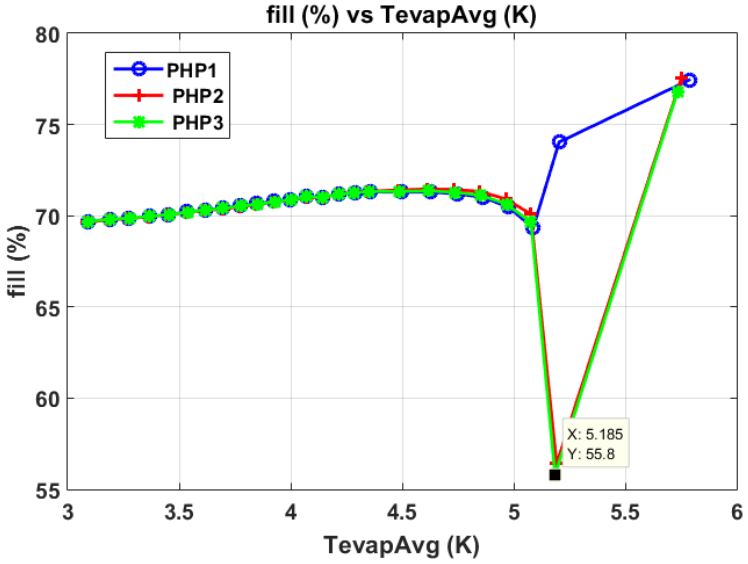

Figure 5-12: Fill ratio vs T_{evap}, bottom heaters on and ramp up cases

5.1.3 The PHP contour plot

As mentioned throughout this section, the fill ratio and heater power are primary parameters that influence the effective thermal conductivity k_{eff}. Figure 5-13 shows a contour plot of all three variables, where the power ($\dot{Q}$) is on the *y*-axis, and the fill ratio (f_{liq}) is on the *x*-axis and finally the contours and colors represent the k_{eff}. Where fill ratios correspond to the heat load changes as shown in Figure 5-12, starting at initial fill ratios from 20 % to 90%. It can be concluded that this PHP configuration achieves highest values of k_{eff} at high heater powers and fill ratios close to 70 %, where the maximum conductivity achieved was 50,000 W/m-K at 0.25 W.

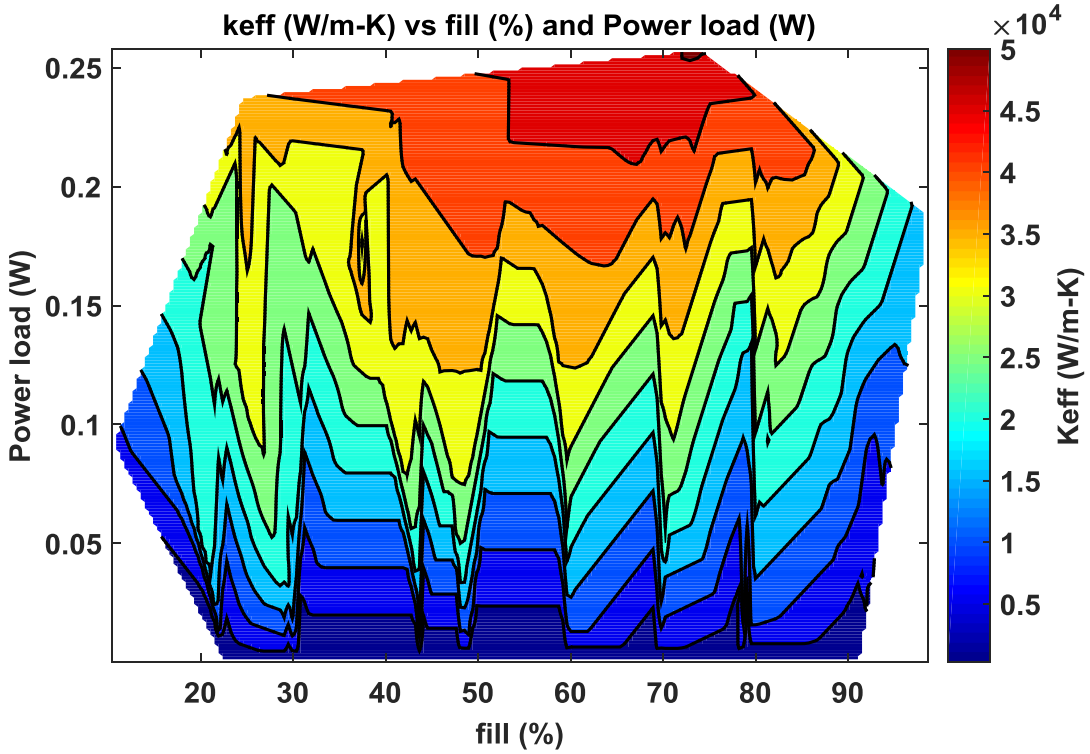

Figure 5-13: PHP1 contour plot

5.2 Variable Heat Loads

Variable heat loads with a sine wave configuration were conducted in order to verify that PHPs can operate as these conditions. All papers regarding cryogenic PHPs have been conducted at constant heat loads and no references using variable heat loads have been found.

For each case, the power supply was controlled to create a frequency sweep from 0.1 Hz to 4 Hz, but at a fixed DC offset and amplitude. After each frequency sweep was performed, the DC offset was increased and the same frequency sweep was restarted again. The sweep consisted of a total of 19 frequencies in the range mentioned above and each frequency was operated for 1000 seconds. During these experiments a 70 % fill ratio was used throughout the whole experiment since it exhibited the best thermal performance. Power spectra for temperature and pressure data were performed in order to investigate which frequencies were the most dominant ones and to verify if the sinusoidal heat loads degrade the PHP's thermal performance. For this section the bottom heaters "on" cases will be discussed but data regarding top heater "on" and all heaters "on" will be shown in the appendix.

5.2.1 Frequency Sweep for Bottom Heaters "on" with small voltage amplitude

A sine wave with the following form was applied to each bottom heater:

$$\mathrm{G(t)} = A\sin(2\pi f t) + C \qquad 5\text{-}1$$

Where A is the voltage amplitude, C is the DC voltage offset, f is the frequency in Hz and t is the elapsed time in seconds. Table 5-1 shows a summary of the cases performed at this amplitude. For all these cases the amplitude was kept constant at about A = 0.592 V. After each case the offset was increased with increments of 0.591 V. The heat load applied to each heater ranged from 0.010 W to 0.448 W.

Table 5-1: sine wave applied to each 50 Ohm heater

Cases	Offset (V)	Amplitude (V)	V_{rms} (V)	P Heat Load (W)	Frequency range (Hz)
Case 1	0.581	0.591	0.716	0.010	0.1 Hz to 4 Hz
Case 2	1.172	0.591	1.244	0.031	0.1 Hz to 4 Hz
Case 3	1.762	0.591	1.810	0.066	0.1 Hz to 4 Hz
Case 4	2.352	0.592	2.389	0.114	0.1 Hz to 4 Hz
Case 5	2.943	0.591	2.972	0.177	0.1 Hz to 4 Hz
Case 6	3.533	0.592	3.558	0.253	0.1 Hz to 4 Hz
Case 7	4.125	0.592	4.147	0.344	0.1 Hz to 4 Hz
Case 8	4.717	0.592	4.735	0.448	0.1 Hz to 4 Hz

The root-mean squared voltage V_{rms} was calculated using

$$V_{rms}^2 = \left(\frac{A}{\sqrt{2}}\right) + C^2 \quad 5\text{-}2$$

Therefore by using ohms law the power *P* was calculated using

$$Power = P = \frac{V_{rms}^2}{R} \quad 5\text{-}3$$

Where the resistance R per heater is equal to 50 Ohms.

Figure 5-14 shows the effective thermal conductivity vs. frequency of PHP 1 using a sine wave on the bottom heaters (H1, H3 and H5) with the heat loads shown in Table 5-1. A contour plot was used to show the effect of the frequency, heat load and effective thermal conductivity. It was observed that an optimal thermal performance was achieved at k_{eff} = 50,000 W/m-K around heat loads of 0.25 W, which are similar results shown for cases at constant heat loads as shown previously in Figure 5-8. It can be concluded that the thermal performance is not a strong function of the heat load frequency.

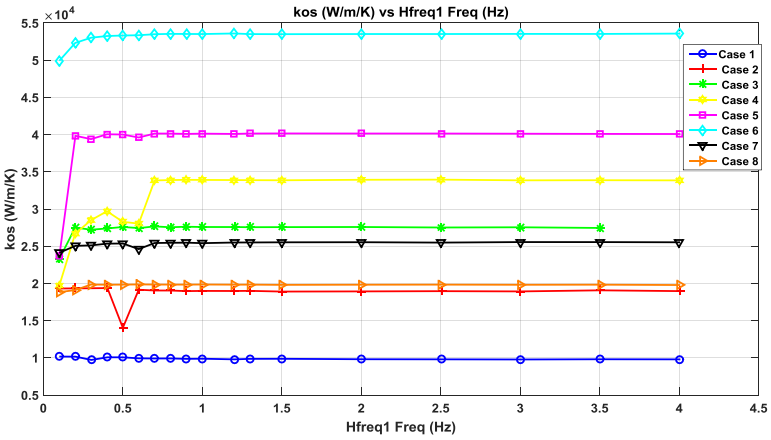

Figure 5-14: PHP 1 effective thermal conductivities vs heat load frequency

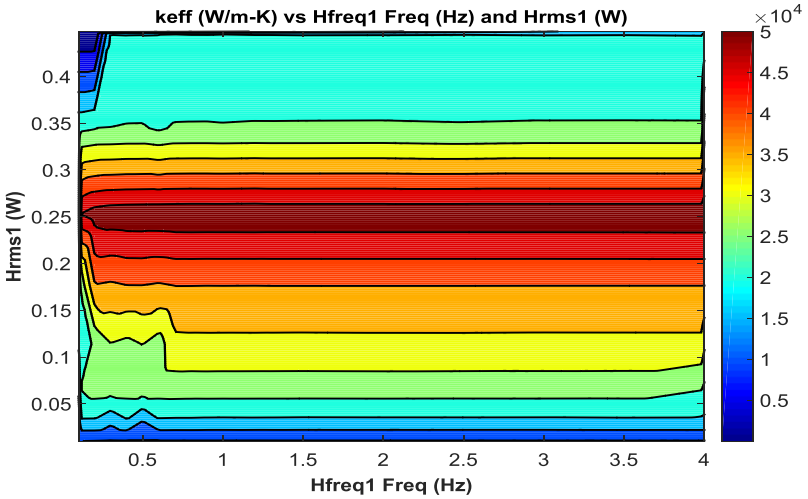

Figure 5-15: Contour plot of heat load frequency, Heat load and k_{eff}

5.3 Constant Heat loads for adiabatic length of 1000 mm

The adiabatic length of the PHP was extended to one meter in order to determine changes in its thermal performance. This configuration was tested at different fill ratios ranging from 20 % to 80 % with increments of 5 %, and applied heat loads up to 0.3 W per heater. Figure 8-25 shows the raw temperature data vs time at fill ratios of 20 %, 30 %, 40 %, 50 %, 55 %, 58 %, 71 % and 80 % when equal heat loads were applied to the bottom heaters, more fill ratio cases are shown in Appendix 8.2.1. Similar to the 300 mm adiabatic length case, fill ratios below 40 % cause the evaporator section to dry out at lower heat loads.

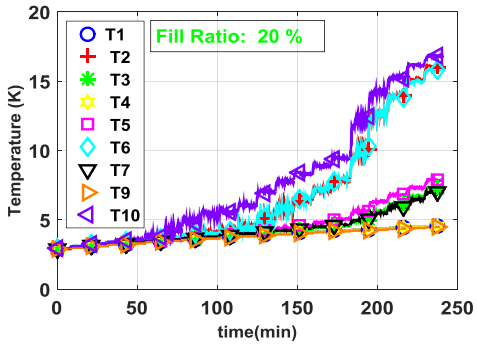

a)

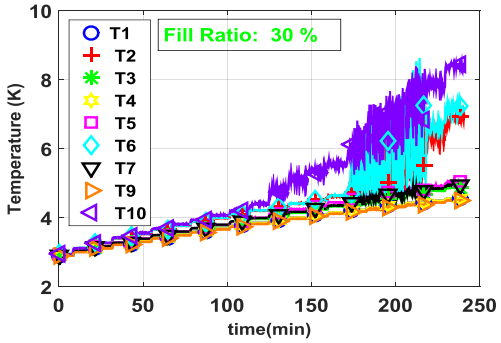

b)

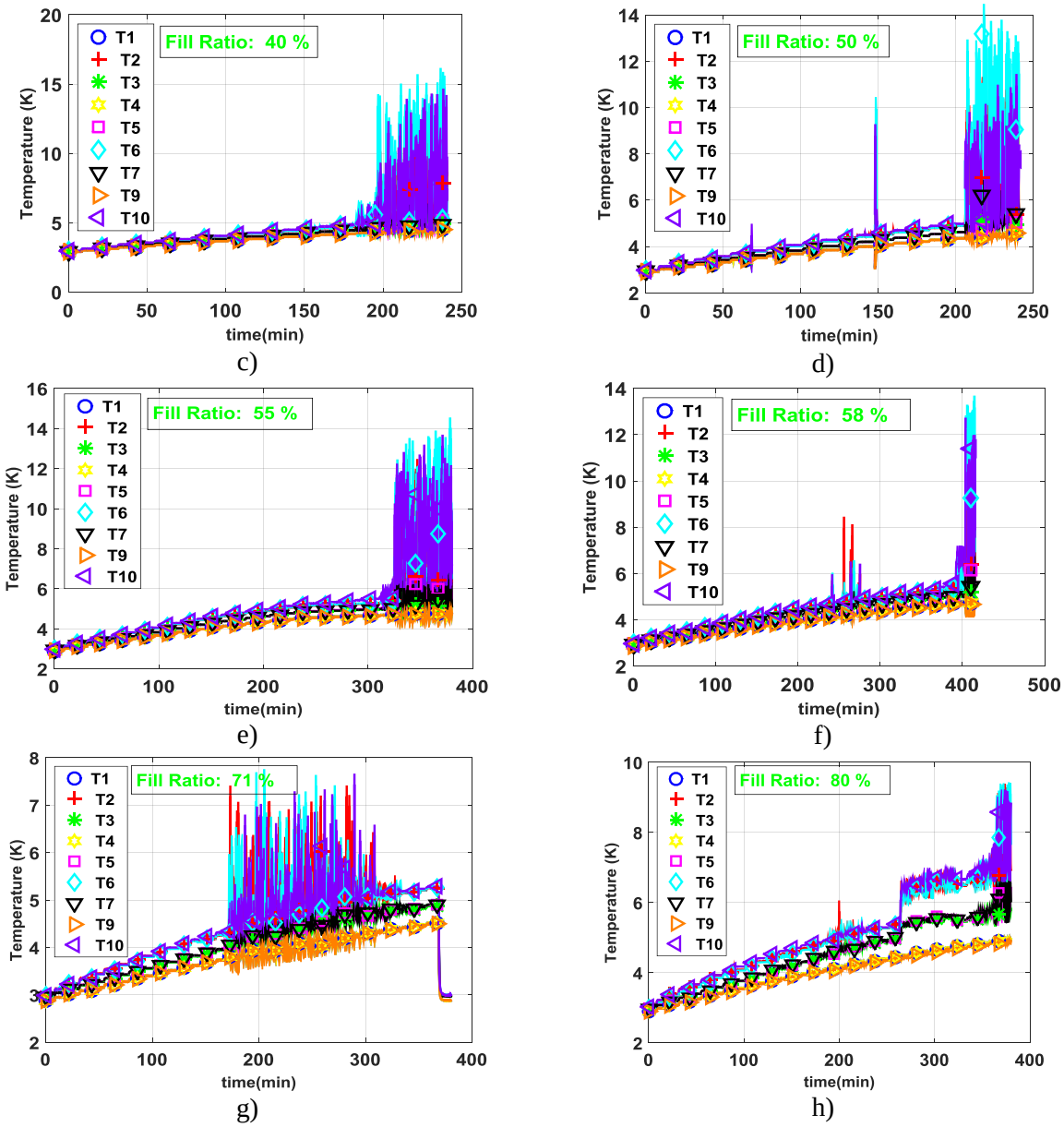

Figure 5-16: Fill ratios for one meter PHP at with uniform heat loads for bottom heaters

As shown in Figure 5-17, the effective thermal conductivities of PHP1 were plotted vs heat load at fill ratios between 20 % and 60 %, While Figure 5-18, shows the effective thermal conductivities from 58 % to 80 %. It is important to mention that for the 300 mm adiabatic section the PHP achieved an optimal fill ratio of 70 %, but for the 1 meter PHP the optimal initial fill ratio was determined to be 58 % at a heat load of 0.24 W. It can also be observed that lower fill ratios tend to dry out at lower heat loads. However, the

thermal performance of fill ratios above 58 % start to decrease drastically due to the fact that high amplitude temperature oscillations are encountered as shown previously in Figure 5-16. Finally Figure 5-19 shows the maximum effective thermal conductivity vs fill ratio for each PHP section, where an optimal fill ratio range between 55 % and 58 %.

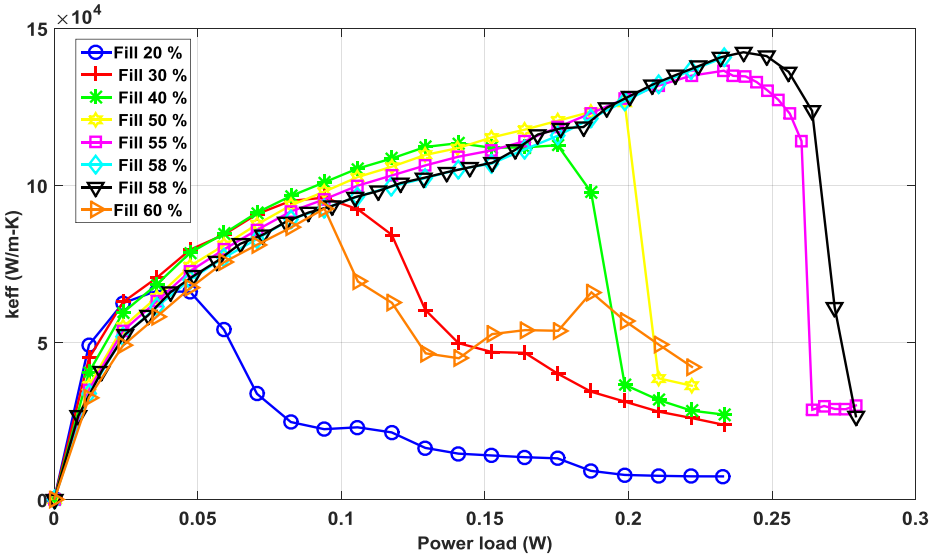

Figure 5-17: PHP1 effective thermal conductivities vs Heat Load for fill ratios between 20 % and 60 %

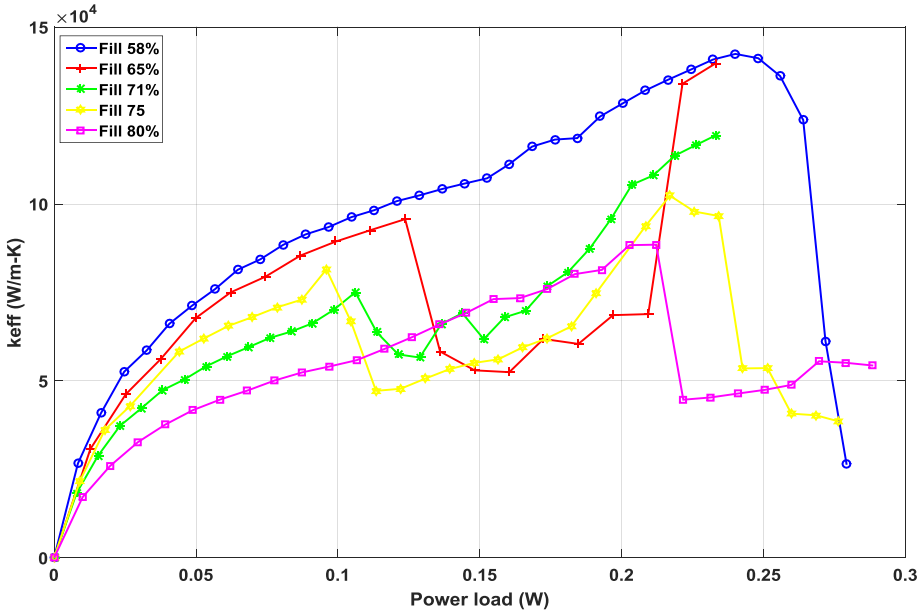

Figure 5-18: PHP1 effective thermal conductivities vs heat Load for fill ratios between 58 % and 80 %

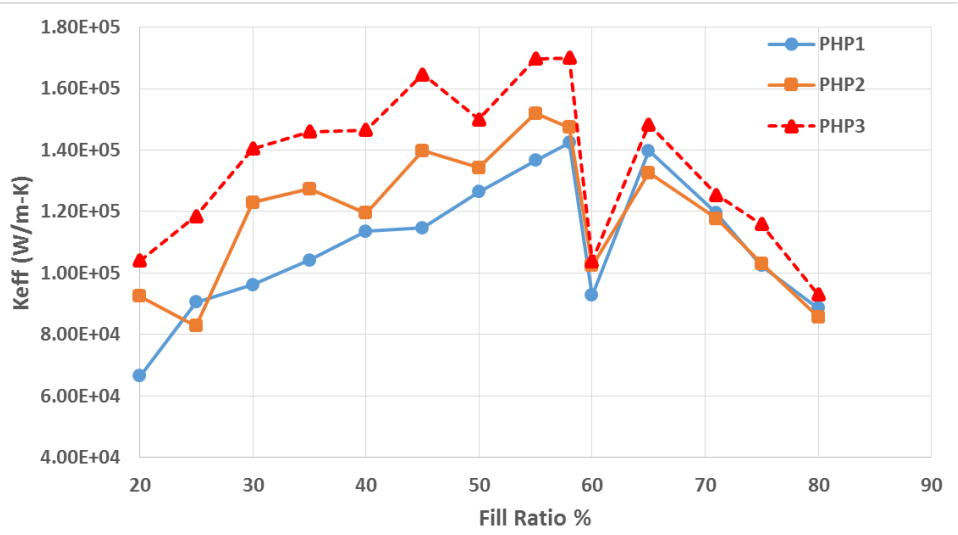

Figure 5-19: maximum effective thermal conductivities vs fill ratio for bottom heaters on at equal heat loads

5.3.1 Other methods of measuring thermal performance

As shown in Figure 5-20, it is important to note that the thermal conductivity for the 1 meter PHP is one order of magnitude higher than the results achieved for the 300 mm PHP. This is due to the fact that the effective thermal conductivity shown in equation 4-1 is proportional to the adiabatic length. For example, if both PHPs transported the same amount of heat and resulted in a similar temperature difference between the evaporator and condenser sections, the adiabatic length would be the parameter that would differentiate the large change in effective thermal conductivity results. Therefore as shown in Figure 5-21, the thermal performance can also be plotted as the effective conductance C_{eff} which is the ratio of the heat load to the temperature difference, $(Q/\Delta T)$ resulting in a thermal performance that can be compared for both configurations. It is important to observe that the effective conductance for both configurations are very similar, concluding that the temperature differences for both configurations are very similar since the same heat loads where applied to the bottom evaporator sections. The heat loads matching the maximum thermal performance (k_{eff} or C_{eff}) for the 300 mm and 1000 mm adiabatic lengths were determined to be 0.2578 W and 0.24 W, respectively. These heat loads also match with evaporator temperatures close to the critical temperature of helium (5.19 K), therefore the evaporator section will be operating in a single phase region

resulting in a decrease in thermal performance. Finally the most important conclusion is that no drastic changes in thermal performance were observed as the adiabatic length was increased from 300 mm to 1000 mm.

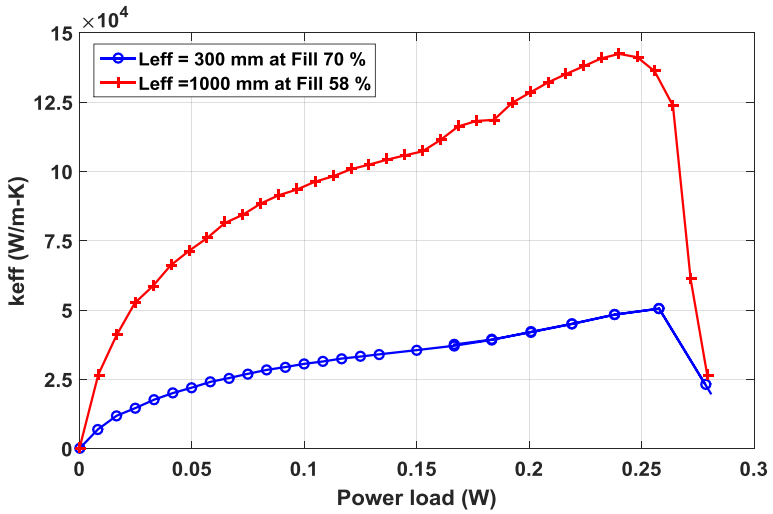

Figure 5-20: Effective thermal conductivity for PHP1 at 300 mm and 1000 mm adiabatic length at equal heat loads

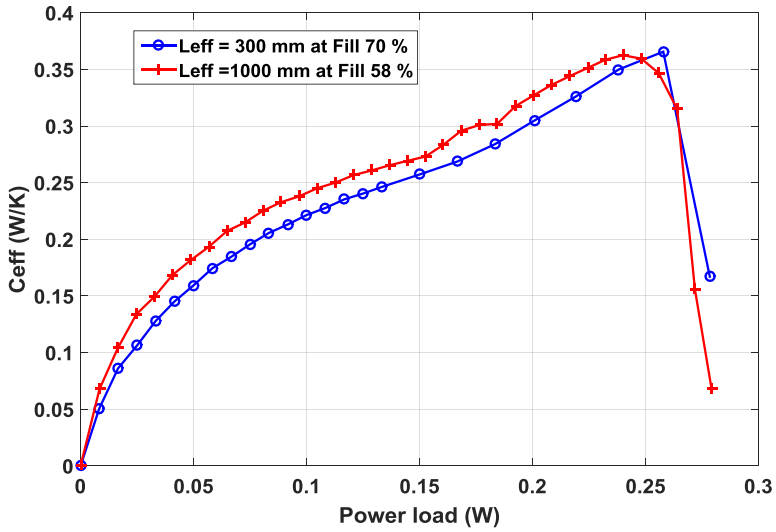

Figure 5-21: Effective Conductance vs Heat Load for PHP1 at 300 mm and 1000 mm adiabatic length at equal heat loads

Figure 5-22, shows another method for comparing the thermal performance by plotting the temperature difference between the evaporator and condenser vs the heat load applied. In addition, Figure 5-23 shows the temperatures of the condenser and evaporator sections in order to illustrate the same temperature reading for a 300 mm PHP and a 1000 mm helium PHP.

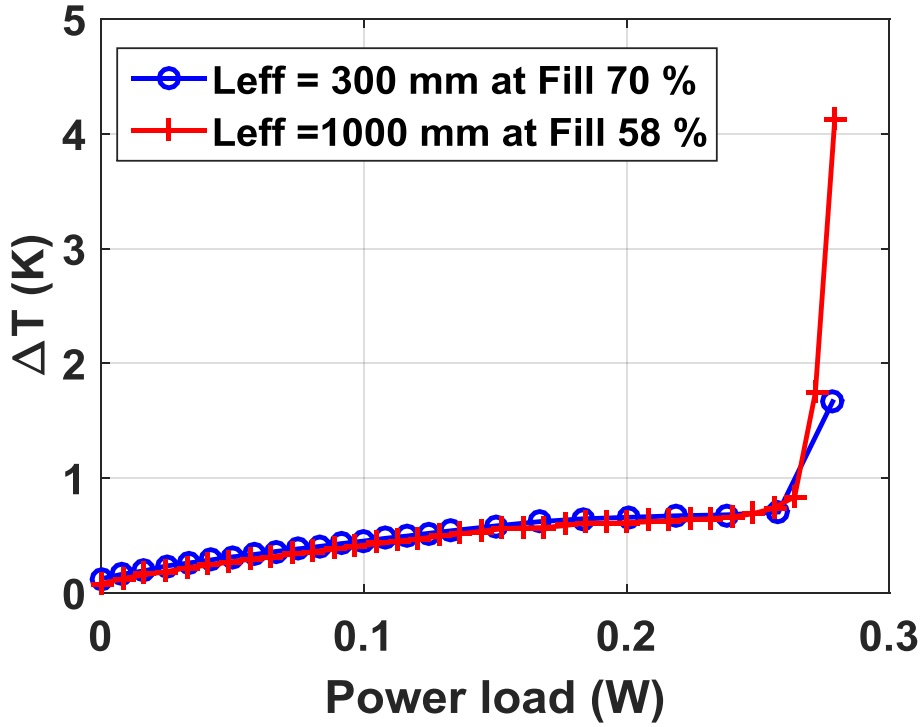

Figure 5-22: Evaporator/Condenser Temperature difference for PHP1 at 300 mm and 1000 mm adiabatic length at equal heat loads.

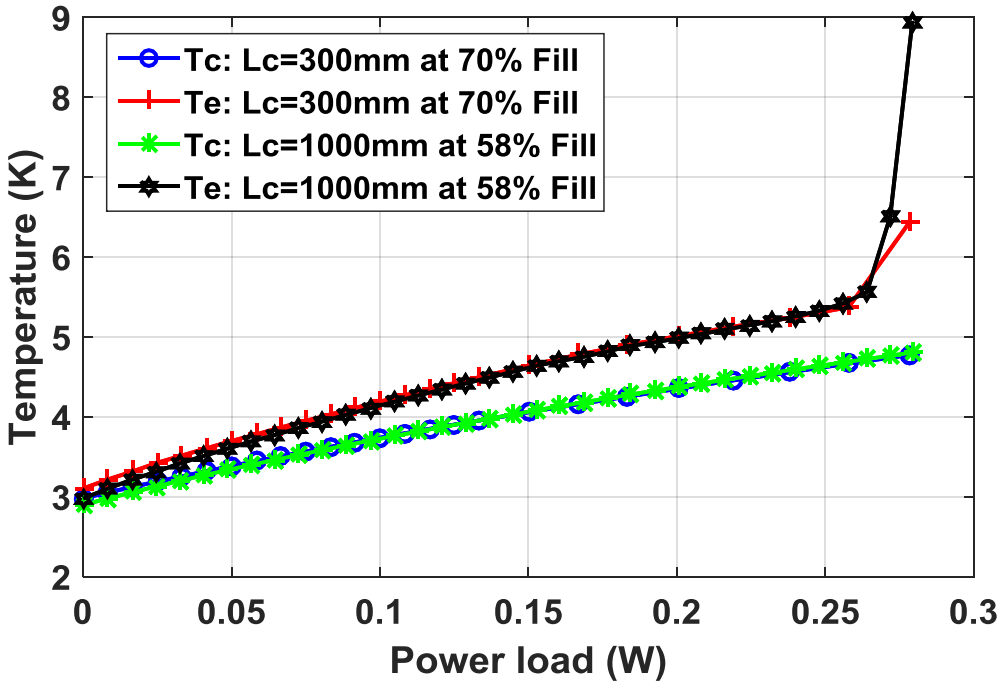

Figure 5-23: Averaged Condenser and Evaporator data for PHP1 for a 300 mm and 1000 mm adiabatic length.

5.3.2 Fill ratio and specific volume calculation for the one meter PHP

An additional pressure sensor has been installed at the bottom evaporator section of PHP1, which will help improve and upgrade the equations to solve for the specific volume and fill ratio. It is very important to calculate and estimate the specific volumes of the condenser, evaporator and overall specific volume of the PHP and observe its behavior in a *T-v* diagram, which will be shown in the next section.

Previously, for the 300 mm adiabatic length PHP, the fill ratio was calculated using the equations in section 4.2. The reader is encouraged to review these equations before continuing. In section 4.2 the mass of the PHP m_{php} was calculated using the following equation

$$m_{php} = m_c + m_e = \bar{\rho}_{l,sat} V_l + \bar{\rho}_{v,sat}(V_{PHP} - V_l) \quad 5\text{-}4$$

Where the mass of the condenser (m_c) and evaporator (m_e) section are expressed as

$$m_c = \bar{\rho}_{l,sat} V_l \quad 5\text{-}5$$

$$m_e = \bar{\rho}_{v,sat}(V_{PHP} - V_l) \quad 5\text{-}6$$

For the one meter PHP, equations (5-5) and (5-6) can be improved and rewritten as

$$m_c = \bar{\rho}_{c,l,sat} V_{c,l} + \bar{\rho}_{c,v,sat} V_{c,v} \quad 5\text{-}7$$

$$m_e = \bar{\rho}_{e,l,sat} V_{e,l} + \bar{\rho}_{e,v,sat} V_{e,v} \quad 5\text{-}8$$

Where *c and e* stand for the condenser and evaporator sections, following l and v which stand for liquid and vapor saturation properties. Hence, $\bar{\rho}_{c,l,sat}$ and $\bar{\rho}_{c,v,sat}$ are the condenser's liquid and vapor saturation densities (kg/m^3), respectively. Variables $\bar{\rho}_{e,l,sat}$ and $\bar{\rho}_{e,v,sat}$ are the evaporator's liquid and vapor densities (kg/m^3), respectively. Volumes $V_{c,l}$ and $V_{c,v}$ are the condenser's liquid and vapor volumes (m^3), respectively. Volumes $V_{e,l}$ and $V_{e,v}$ are the evaporator's liquid and vapor volumes (m^3), respectively. Notice that an equation for the adiabatic section was not added due to the lack of temperature and pressure sensors attached to this section. Therefore, it is assumed that the adiabatic section is part of the evaporator section. The mass of the php (m_{php}) can be rewritten as the following

$$m_{php} = \bar{\rho}_{c,l,sat} V_{c,l} + \bar{\rho}_{c,v,sat} V_{c,v} + \bar{\rho}_{e,l,sat} V_{e,l} + \bar{\rho}_{e,v,sat} V_{e,v} \quad 5\text{-}9$$

In addition the total volume of the PHP (V_{php}) is equal to 9.7377E^{-6} m^3, for the entire one meter PHP, and can be expressed as.

$$V_{php}^{*} = V_c^{*} + V_e^{*} = 1.0480\text{E}^{-5}\, m^3 \qquad 5\text{-}10$$

From now on, a variable with an asterisk * represents a known variable, symbols without the asterisk are unknown variables. Volumes V_c^{*} and V_e^{*} are the known condenser and evaporator volumes, respectively, and where calculated using the geometry of the PHP. Recall that V_e^{*} includes that adiabatic length volume. These volumes can be written as

$$V_c^{*} = V_{c,l} + V_{c,v} = \ 7.4220\text{E}^{-7} m^3 \qquad 5\text{-}11$$

$$V_e^{*} = V_{e,l} + V_{e,v} = \ 9.7377\text{E}^{-6}\, m^3 \qquad 5\text{-}12$$

Notice that volumes $V_{c,l}, V_{c,v}, V_{e,l}$ and $V_{e,v}$ do not have an asterisk because they are unknowns and more equations are required to solve them. Equations (5-11) and (5-12) and be substituted into (5-9) to form the following equation

$$m_{php}^{*} = (\bar{\rho}_{c,l,sat}{}^{*})V_{c,l} + (\bar{\rho}_{c,v,sat}{}^{*})(V_c^{*} - V_{c,l}) + (\bar{\rho}_{e,l,sat}{}^{*})V_{e,l} + (\bar{\rho}_{e,v,sat}{}^{*})(V_e^{*} - V_{e,l}) \qquad 5\text{-}13$$

All densities are known variables due to the fact that temperature and pressure sensors were placed at the condenser and evaporator sections. In addition, the mass of the php (m_{php}^{*}) is a known variable by using equation (4-6) in section 4.2

$$m_{php}^{*} = m_o - \sum_{i=1}^{10} m_i \qquad 5\text{-}14$$

The reader could have deduced by now that there is a dilemma in equation (5-13), there are two unknowns which are the condenser's liquid volume $V_{c,l}$ and the evaporator liquid volume $V_{e,l}$. Until this point, equation (5-13) cannot be solved and two more assumption must be made. Reviewing equation (5-7) we can assume the following:

- The vapor density of the condenser section is much smaller compared to its liquid density.

$$\bar{\rho}_{c,l,sat}{}^{*} \gg \bar{\rho}_{c,v,sat}{}^{*} \quad (5\text{-}15)$$

- Vapor bubbles collapse/contract inside the condenser section resulting in a higher liquid volume than the vapor volume; therefore the condenser's vapor volume can be considered negligible.

$$V_{c,l} \gg V_{c,v} \quad (5\text{-}16)$$

Using equation 5-15 and 5-16, equation (5-13) can be arranged as follows

$$m_{php}^{*} = (\bar{\rho}_{c,l,sat}{}^{*})V_{c,l} + \underbrace{(\bar{\rho}_{c,v,sat}{}^{*})(V_c^{*} - V_{c,l})}_{negligible} + (\bar{\rho}_{e,l,sat}{}^{*})V_{e,l} + \bar{\rho}_{e,v,sat}{}^{*}(V_e^{*} - V_{e,l}) \quad (5\text{-}17)$$

$$m_{php}^{*} = (\bar{\rho}_{c,l,sat}{}^{*})V_{c,l} + (\bar{\rho}_{e,l,sat}{}^{*})V_{e,l} + \bar{\rho}_{e,v,sat}{}^{*}(V_e^{*} - V_{e,l}) \quad (5\text{-}18)$$

And since $V_{c,l} \gg V_{c,v}$ then $V_{c,l} = V_c^{*}$ and therefore equation (5-18) is simplified to

$$m_{php}^{*} = (\bar{\rho}_{c,l,sat}{}^{*})V_c^{*} + (\bar{\rho}_{e,l,sat}{}^{*})V_{e,l} + \bar{\rho}_{e,v,sat}{}^{*}(V_e^{*} - V_{e,l}) \quad (5\text{-}19)$$

As observed, $V_{e,l}$ is the only unknown and can be now be solved. Therefore the evaporator's fill ratio $f_{e,l}$ and specific volume $v_{e,l}$ for the evaporator can be expressed as

$$f_{e,l} = \frac{V_{e,l}}{V_e^{*}} \quad (5\text{-}20)$$

$$v_{e,l} = \frac{V_e^{*}}{m_e} = \frac{V_e^{*}}{(\bar{\rho}_{e,l,sat}{}^{*})V_{e,l} + \bar{\rho}_{e,v,sat}{}^{*}(V_e^{*} - V_{e,l})} \quad (5\text{-}21)$$

The condenser fill ratio $f_{c,l}$ and specific volume $v_{c,l}$ is expressed as

$$f_{c,l} = \frac{V_{c,l}}{V_c^{*}} = 1 \quad (5\text{-}22)$$

$$v_{c,l} = \frac{V_c^{*}}{m_c} = \frac{V_c^{*}}{(\bar{\rho}_{c,l,sat}{}^{*})V_c^{*}} = \frac{1}{\bar{\rho}_{c,l,sat}{}^{*}} \quad (5\text{-}23)$$

The overall/combined PHP's fill ratio and specific volume can be written as

$$f_{php} = \frac{V_{c,l} + V_{e,l}}{V_c^{*} + V_e^{*}} = \frac{V_c^{*} + V_{e,l}}{V_{php}^{*}} \quad (5\text{-}24)$$

$$v_{c,l} = \frac{V_{php}^{*}}{m_{php}^{*}} \quad (5\text{-}25)$$

It should be mentioned this is an approximate fill ratio and specific volume calculations, and that it is extremely difficult to solve for an exact value. For precise calculations, instrumentation such as high quality cameras would have to be implemented, requiring more resources and budget costs. In addition, the sum of masses that fill the connecting volumes from the PHP valve to the PHP is accounted for, as shown in equation 5-14 and mentioned entirely in section 4.2. Once the valve is closed, the total amount of mass from the PHP valve and down through the gas-lines and PHP is always constant; however, this does not mean that the mass of the PHP (m_{php}) remains constant nor the gas-lines, as the PHP is operated the pressure will rise causing the gas-lines up to the PHP valve to fill up with more mass. For this reason, the overall calculated specific heat cannot be constant as discussed in the next section.

5.3.3 Tracking the one meter PHP in a T-v diagram

Imagine a box with a volume of 1 m^3 and equal sides. Initially the box is filled with 50 % by volume of liquid helium and 50 % of vapor helium at a saturation temperature of 2.9 K. The saturated specific volumes of liquid and vapor at 2.9 K are 7.0373E-3 m^3/kg and 0.2562 m^3/kg, respectively. This would result in a total mass of 73.03 kg and a specific volume of 0.01369 m^3/kg. Note that the critical specific volume for helium is 0.01437 m^3/kg; therefore, the systems specific volume is on the left side of the critical specific volume in the T-v diagram shown in Figure 5-24. An initial fill ratio of 47.53 % would be achieved if the system had the same specific volume as the critical specific volume. It is important to note that fill ratio will change even though the specific volume is constant. Furthermore, the system will finally reach a liquid or vapor phase, depending on the initial fill ratio or specific volume of the system, as the saturation temperature is gradually increased.

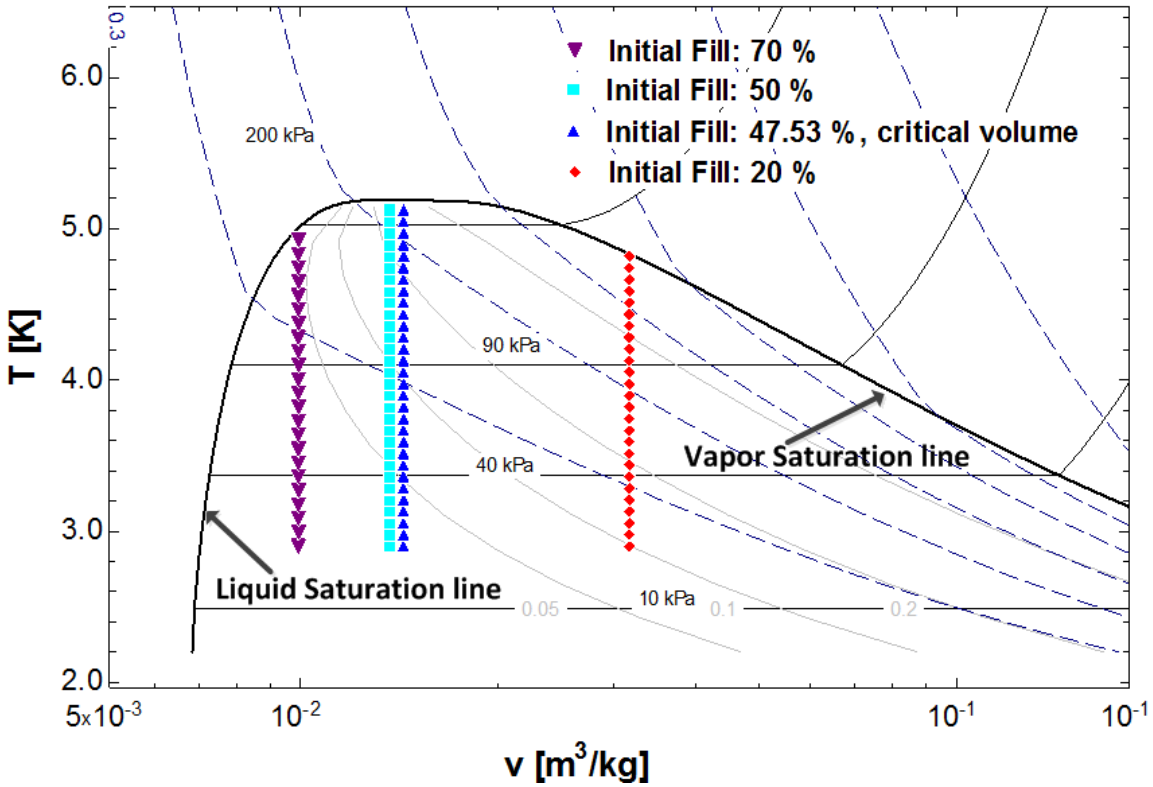

Figure 5-24: Behavior of a two-phase helium container in a T-v diagram.

Figure 5-25 shows the change of fill ratio as a function of saturation temperature at different initial conditions. It can be observed that the fill ratio increases if the initial fill ratio is higher than 47.53 % (left side of the critical specific volume); however, the fill ratio will decrease as a function of temperature if the initial fill ratio lower than 47.53 %. The importance of analyzing this type of behavior is to approximate an adequate initial fill ratio for the PHP in order to avoid single phase limitations such as dry-out or liquid overfilling. In addition, since helium has a low critical temperature and pressure in comparison to other cryogens, it is very easy to transition to a single phase and impact the PHP's performance.

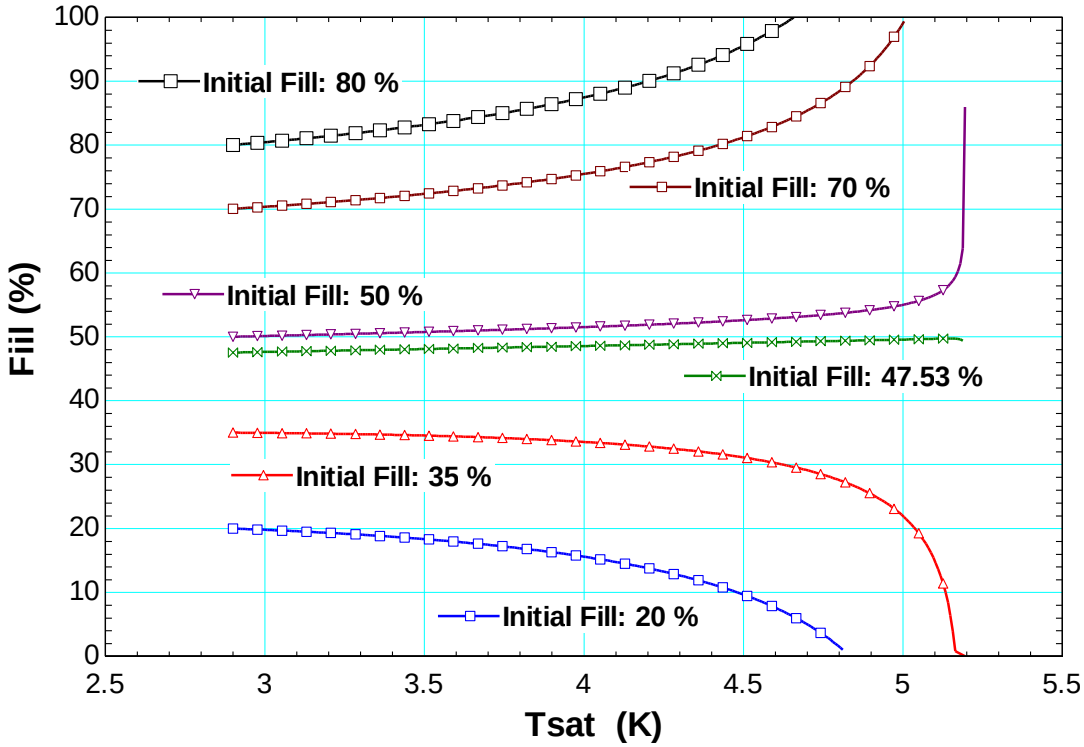

Figure 5-25: Fill ratio versus Saturation Temperature for helium container.

Figure 5-26 shows the PHP's behavior inside the two phase T-*v* diagram with an initial fill ratio of 20 %, in which the specific volumes of the condenser, evaporator and total/combined PHP were calculated. As mentioned in the previous sections, a pressure transducer was installed at the evaporator section of PHP1 for just the one meter configuration, which helped in calculating its properties in a T-*v* diagram. This graph is of the utmost importance in give a starting idea of the behavior of the helium PHP. As observed, the evaporator's specific volume is on the right hand side of the critical volume, causing this section to reach the vapor saturation vapor line at 4.552 K and dry out. It is important to observe that the condenser section does not surpass the critical pressure and temperature; therefore the condenser section remains near to the liquid saturation line. However, the evaporator section is located in the superheated region since it's below the critical pressure of helium (227 kPa). It can be deduced that there will be a two-phase flow along the adiabatic length. It can be observed that the specific volume of the evaporator section and combined are not perfectly vertical, this is due to the fact that the PHP is not a perfect closed system, where the fill ratio

calculations account for the pressure/mass change of the gas lines that connect the PHP valve to the PHP's capillary tubing. This factor causes vaporized liquid to fill these gas-lines and slightly changes the total/combined specific volume of the PHP itself. Figure 5-27 shows the effective thermal conductance vs the evaporator temperature, the red dashed line represents the vapor saturation temperature that the evaporator section reaches before leaving the dome, note the thermal performance values are the lowest in the superheated region.

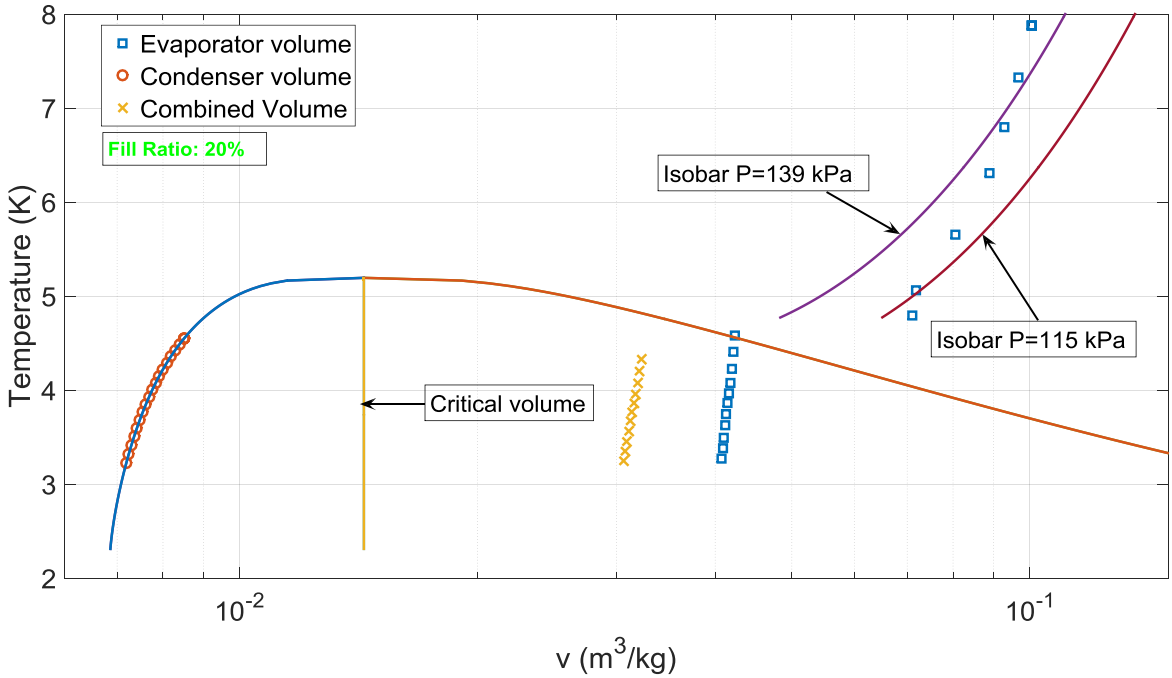

Figure 5-26: T-*v* diagram of PHP1 with an initial fill ratio of 20 %, one meter PHP configuration and equal heat loads

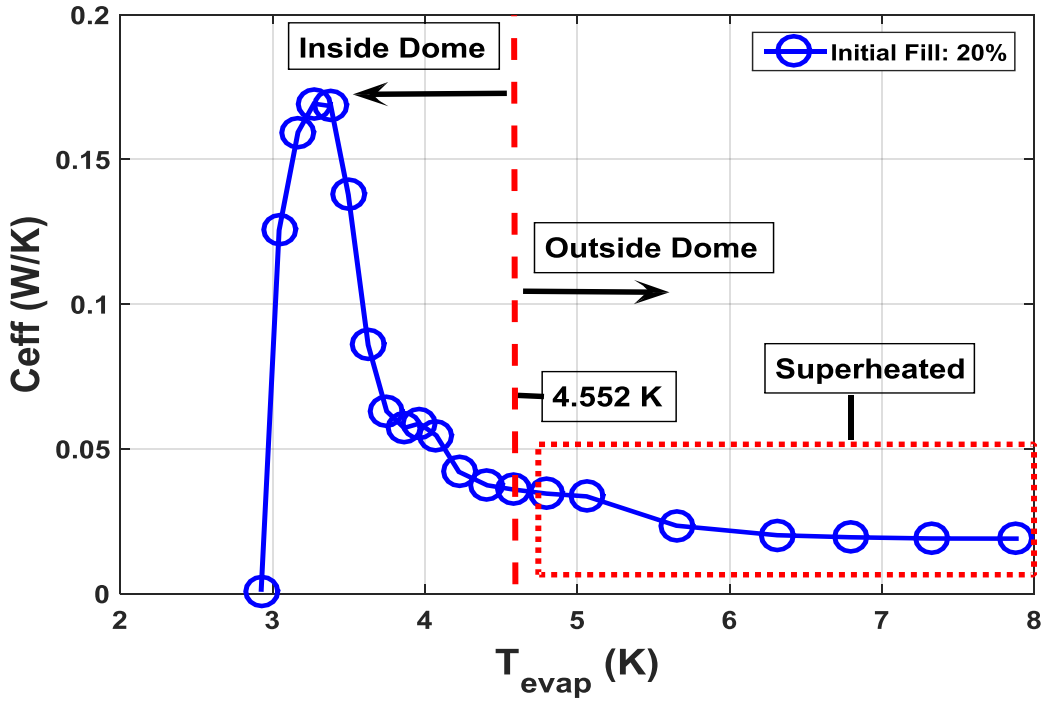

Figure 5-27: Thermal performance for PHP1 with an initial fill of 20 %.

Figure 5-28 shows another extreme case but with a high fill ratio of 80 %. As observed, the evaporator section is located on the far left side of the critical volume and intercepts the liquid saturation line at 4.743 K. Recall the critical temperature and pressure of helium 4 are 5.1953 K and 227 kPa, respectively. Hence, all the evaporator section states above the critical temperature and pressure will fall into the supercritical region, while a couple of states are localized at the subcooled region. Also notice the isobars. The condenser section reaches a subcooled state since does not surpass the critical temperature. Interestingly, this graph shows that the PHP can operate in supercritical and subcooled conditions, in which the extreme changes in density are the driving forces of motion of the fluid. Hence, for this case, latent heat can no longer be accounted for to provide the necessary oscillatory motion. For this reason, as shown in Figure 5-16, we are able to observe extreme temperature oscillations for high fill ratios. In addition, Figure 5-29 shows the thermal performance (C_{eff}) vs the evaporator temperature and points out the effective conductance values where the evaporator section is in a subcooled or supercritical region. It can also be

concluded that the adiabatic section will be partly subcooled and supercritical but there will never be a two-phase flow since no intersection through the dome is possible.

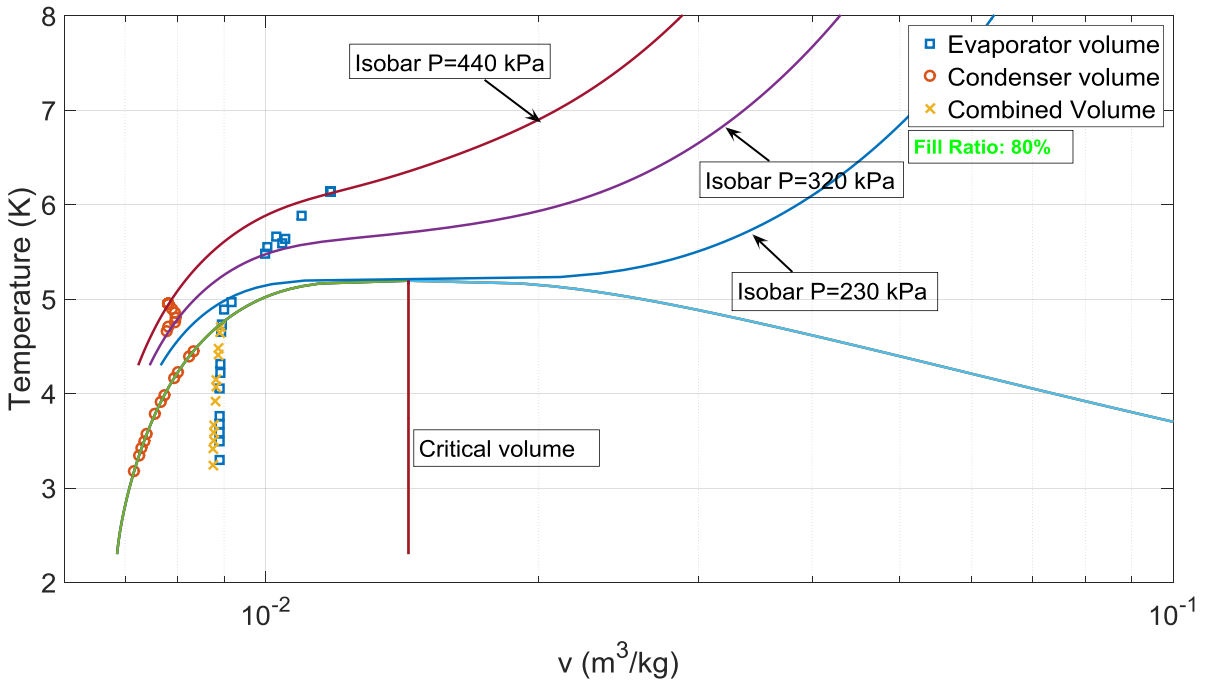

Figure 5-28: T-*v* diagram of PHP1 with an initial fill ratio of 80 %, one meter PHP configuration and equal heat loads

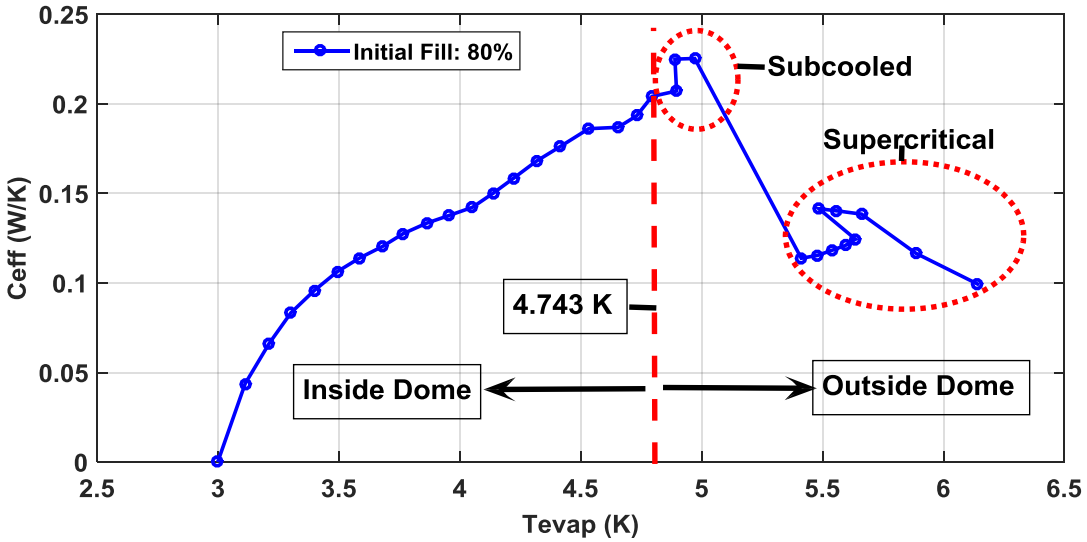

Figure 5-29: Thermal performance for PHP1 with an initial fill of 80 %.

Figure 5-30 shows the behavior of the PHP in a *T-v* diagram at an initial fill ratio of 55 %. It can be observed that the condenser section finally reaches a subcooled state; however the evaporator section is

found to be in either the supercritical and superheated region since it is very close to the critical pressure. Since these last evaporator states have similar temperatures and pressures. The effective conductance as a function of the assumed evaporator temperature is shown in Figure 5-31, notice that the thermal performances when the evaporator is outside the dome are similar to each other.

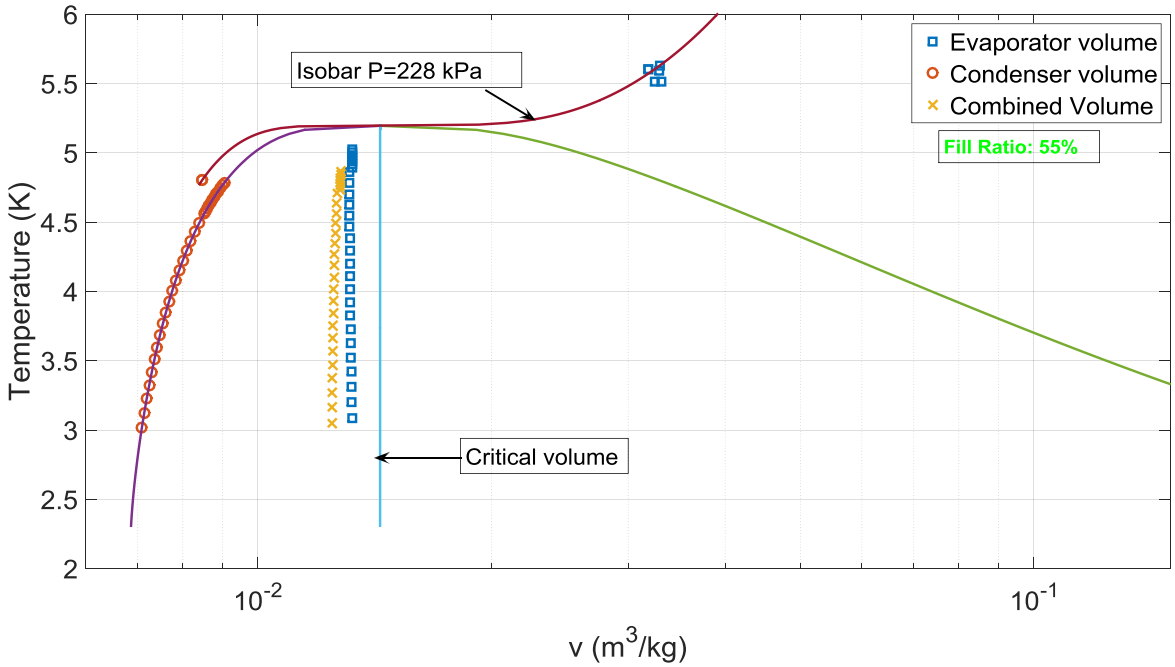

Figure 5-30: T-*v* diagram of PHP1 with an initial fill ratio of 55 %, one meter PHP configuration and equal heat loads

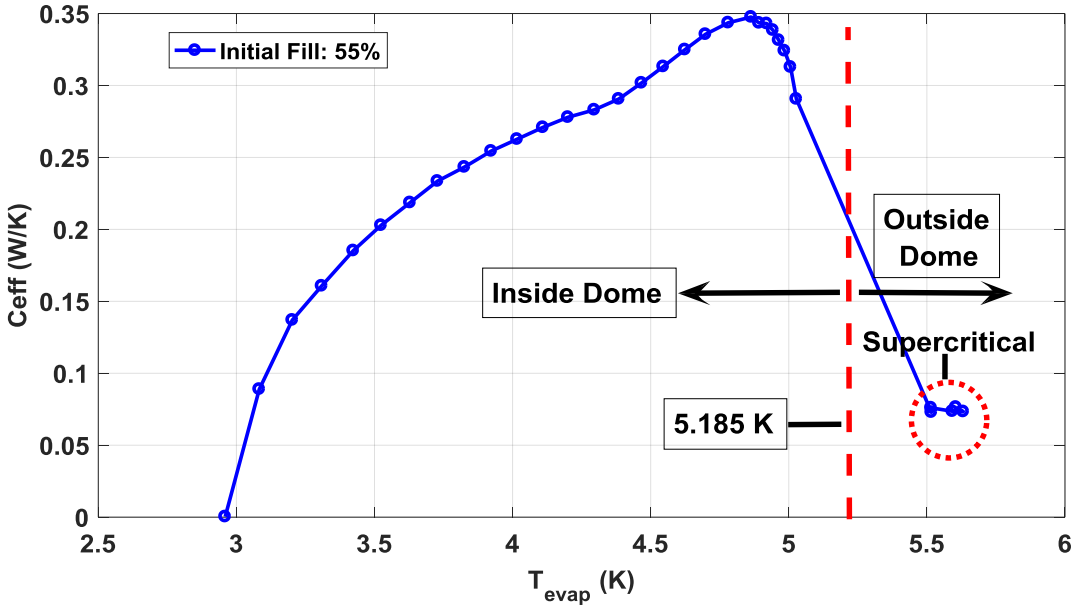

Figure 5-31: Thermal performance for PHP1 with an initial fill of 55 %.

Figure 5-32 shows the T-*v* diagram for the optimal thermal performance achieved at a fill ratio of 58 %. The evaporator section reached a supercritical state at a temperatures of 5.748 K and above the critical pressure (227 kPa). However the last condenser section state is located in the subcooled region and located in through the same isobar (228 kPa) as the evaporator section. Therefore, the adiabatic section will also be in the supercritical region since both the condenser and evaporator sections share the same isobar. It is important to note that the T-*v* diagram is a function of fluid temperature and that the fluid's temperature does not resemble the evaporator section temperature where the heat load was applied (bottom heaters), but was in fact closest to the temperature of the top evaporator section where no heat load is applied. This is due to thermal resistance effects. However, effective thermal conductivities were calculated with the heat load and temperature sensors located at the same evaporator section.

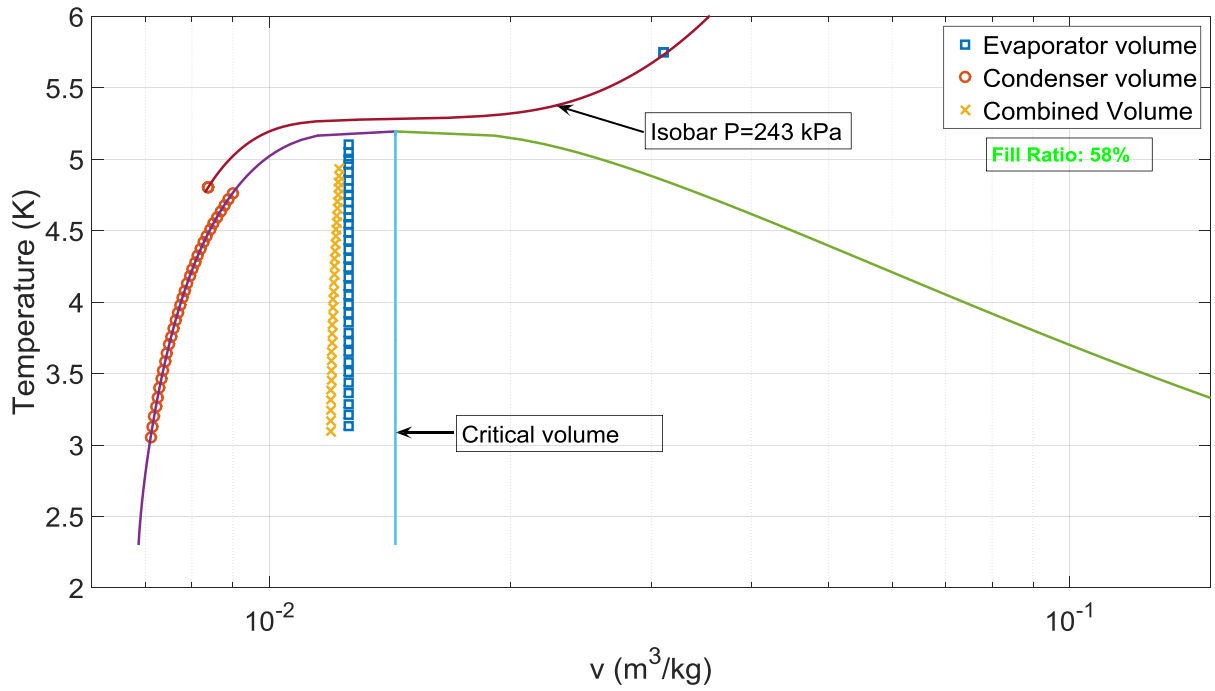

Figure 5-32: T-*v* diagram of PHP1 with an initial fill ratio of 58 %, one meter PHP configuration and equal heat loads

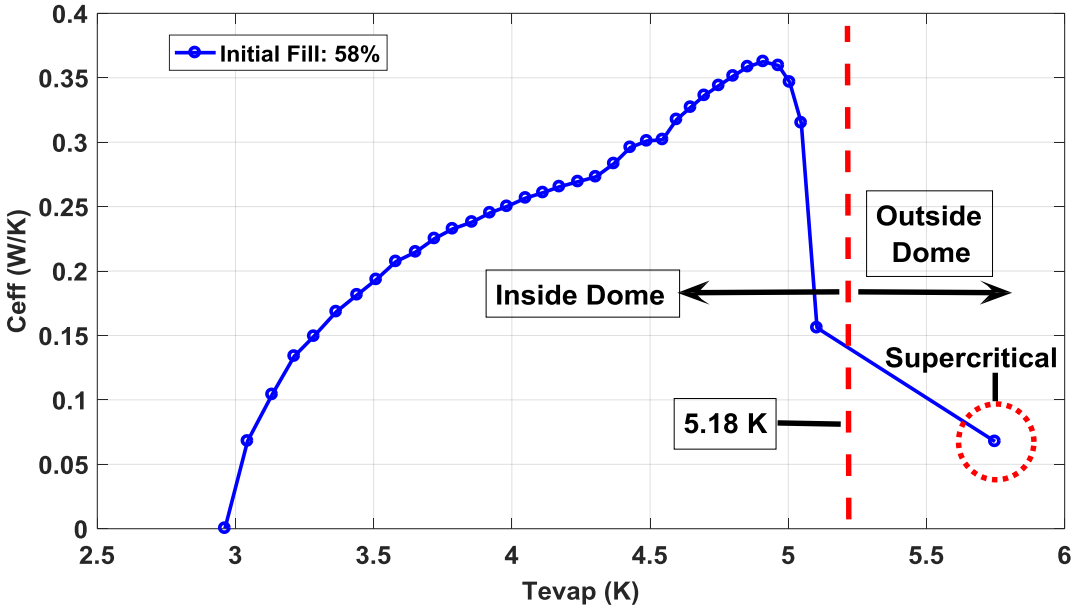

Figure 5-33: Thermal performance for PHP1 with an initial fill of 55 %.

Figure 5-34 shows the evaporator's fill ratio as a function of the fluid temperature at a specific overall initial fill ratio. Recall that the fluid temperature is assumed to be the evaporator sections with no heat load. This figure shows the same behavior as the example shown in Figure 5-24; therefore it is extremely important to use this type of analysis to design and predict the behavior of a helium PHP or PHPs using other working fluids with higher critical points. In addition, Figure 5-35 shows a similar plot but with the combined fill ratio. It is important to note that these fill ratio graphs only show the data inside the T-v dome, and fill ratios outside the dome are nonexistent since no two-phase flow is present.

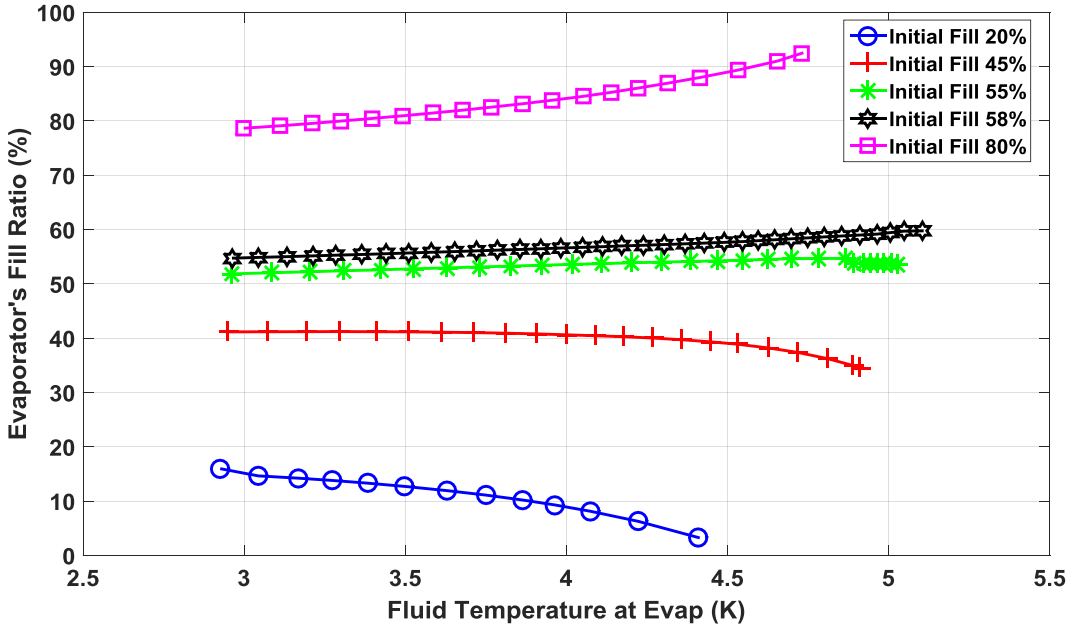

Figure 5-34: Evaporator's Fill ratio vs evaporator's fluid temperature

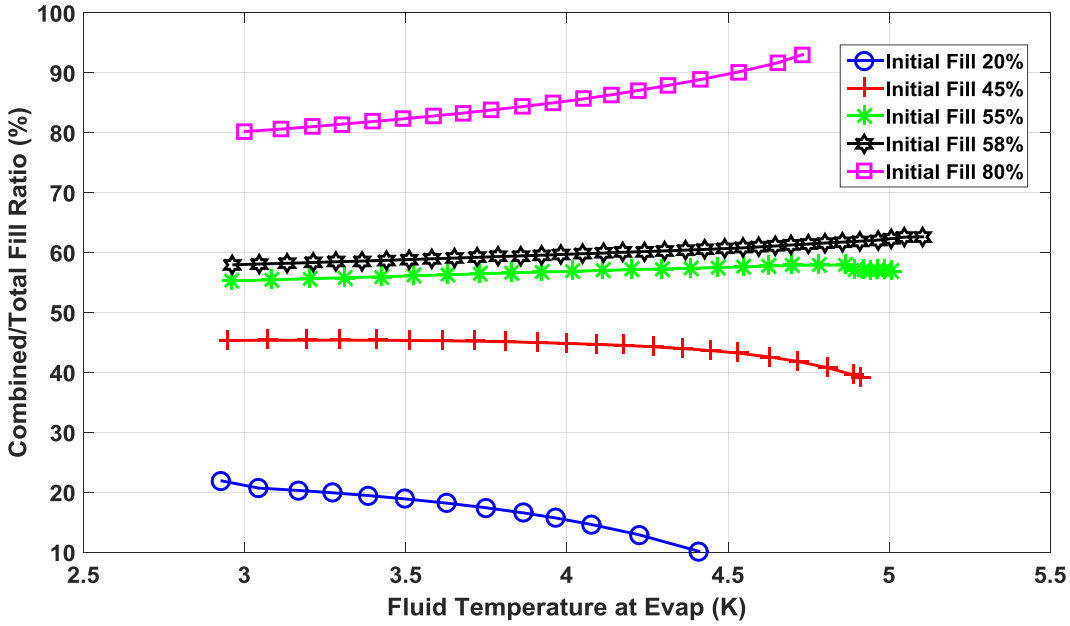

Figure 5-35: Total/combined fill ratio vs evaporator's fluid temperature

5.3.4 Observed Pressure and Temperature Oscillations for the one meter PHP inside the dome

Figure 5-36 shows the raw data of pressure oscillations for both the condenser and PHP1 evaporator section at the maximum thermal performance ant at a fill ratio equal to 80 %, see Figure 5-37. This pressure data was collected using a sampling rate of 50 Hz. It is observable and evident that there are more oscillations

generated in the evaporator section than the condenser section ostensibly due to the high bubble generation. Furthermore, a power spectrum for these pressures are shown in Figure 5-38. Note that for both pressure spectrums there is a small frequency at 0.015 Hz and can be slightly observed in the raw data for the condenser section, Figure 5-36. As shown in Figure 5-38-a, the power spectrum for the condenser section has two dominant peaks at frequencies of 0.166 Hz and 0.668 Hz, but the peaks at frequencies above 2 Hz are minimal. In addition, a peak at 1.2 Hz is observed, which is consistent with the exact frequency of the cryocooler's displacement piston. Furthermore, the evaporator's power spectrum, Figure 5-38-b, shows multiple peaks even above 2 Hz. The most dominant peaks is located at 0.668 Hz. The physical meaning of these frequencies is hard to predict and understand, but the goal is to report these frequencies to help researchers compare and improve their CFD models.

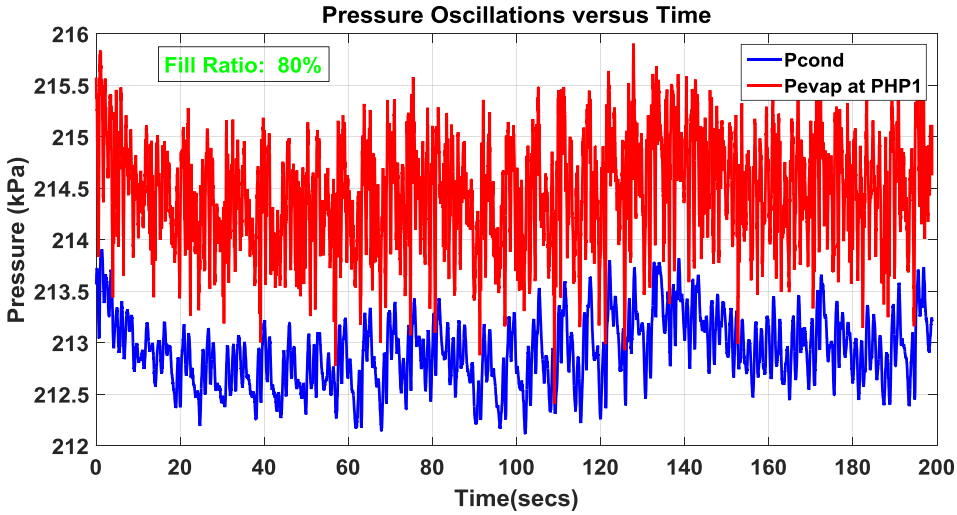

Figure 5-36: Pressure data at maximum thermal performance for a fill at 80 %.

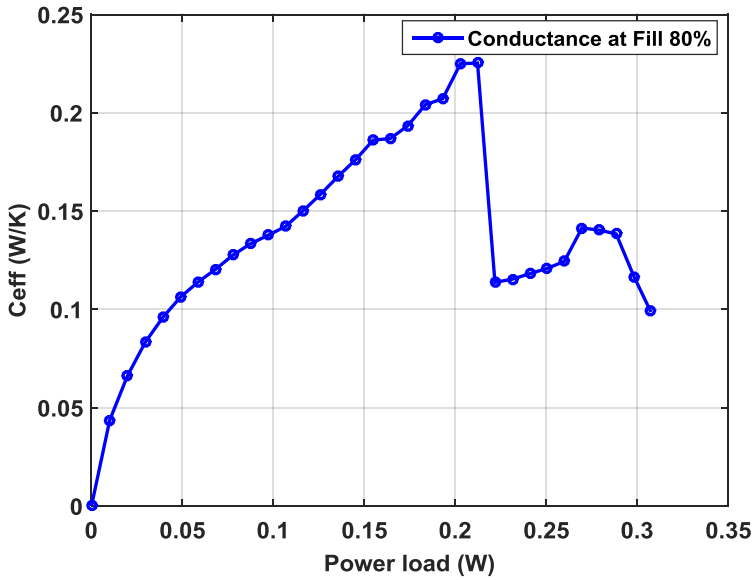

Figure 5-37: Effective conductance vs heat load for 80 % fill.

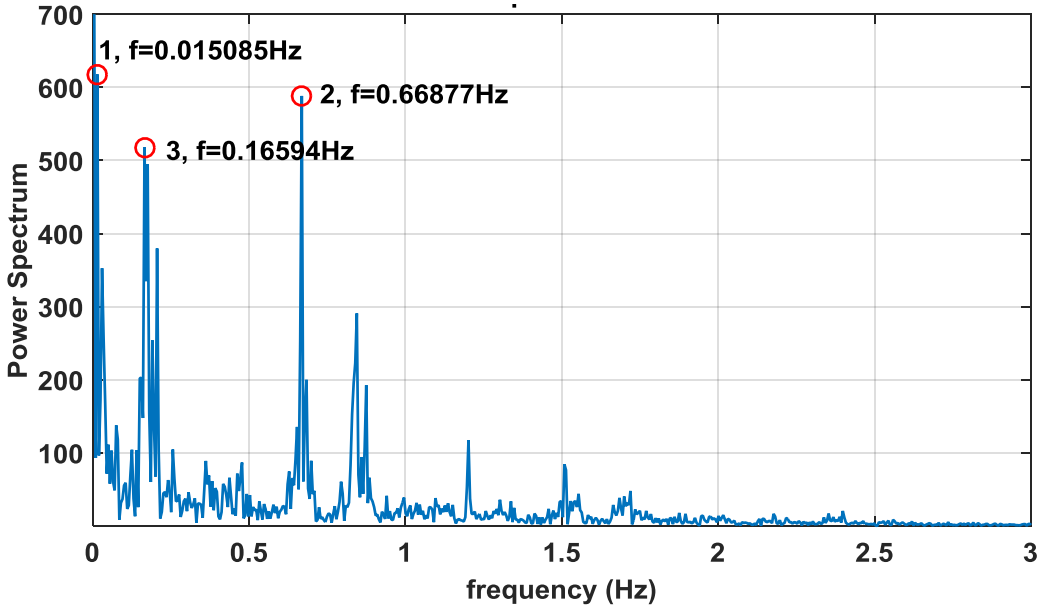

a)

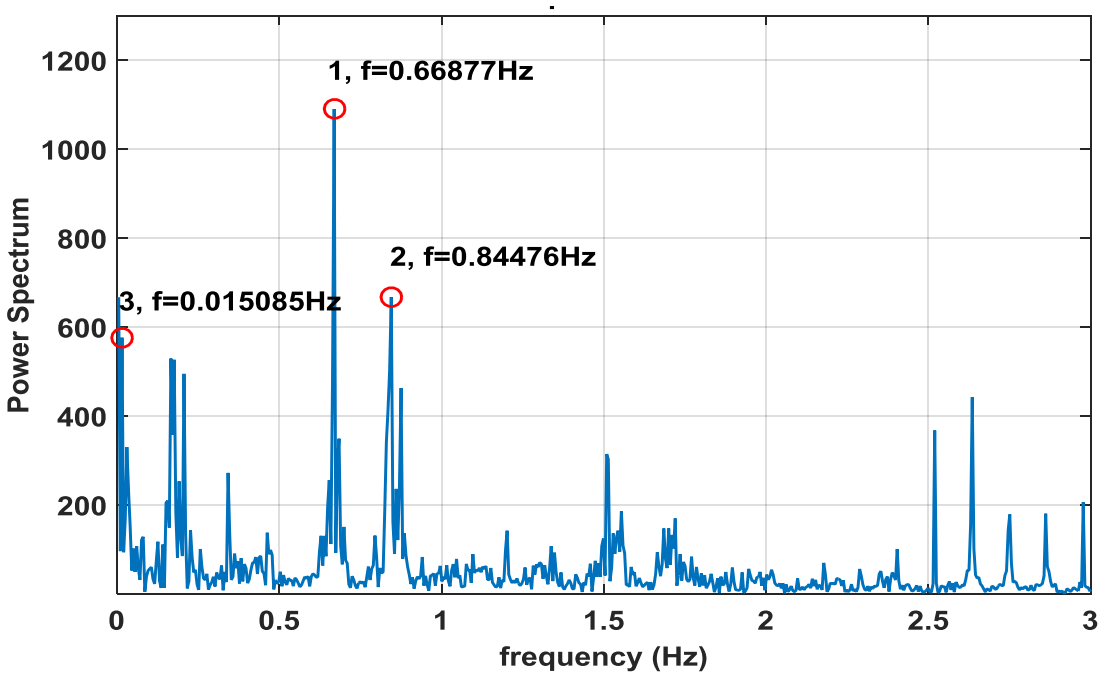

b)

Figure 5-38: Pressure Power Spectrum at maximum thermal performance for a fill at 80 % a) condenser temperature, b) evaporator pressure for PHP1.

Figure 5-39 shows the raw temperature data vs time for the condenser temperature (T1), top evaporator temperature (T5) and bottom evaporator temperature T10 of PHP1. Recall that these cases only have applied heat loads at the bottom evaporators. It is apparent that the condenser temperature oscillates at a much higher frequency (1.2 Hz) than the evaporator sections. Figure 5-40 shows the power spectrum with a dominant frequency is 1.2 Hz, which again is the cryocooler's displacement frequency and therefore will always be observed. In addition, there is a harmonic at 2.4 Hz.

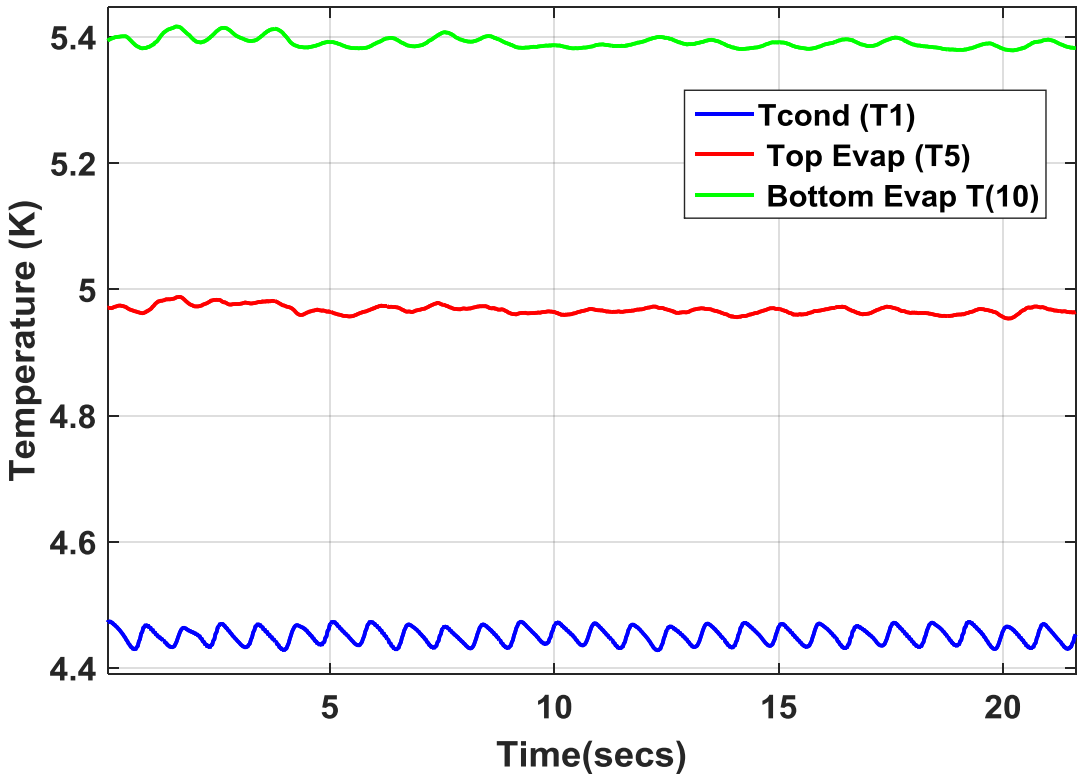

Figure 5-39: Temperature data at maximum thermal performance for 80 % fill

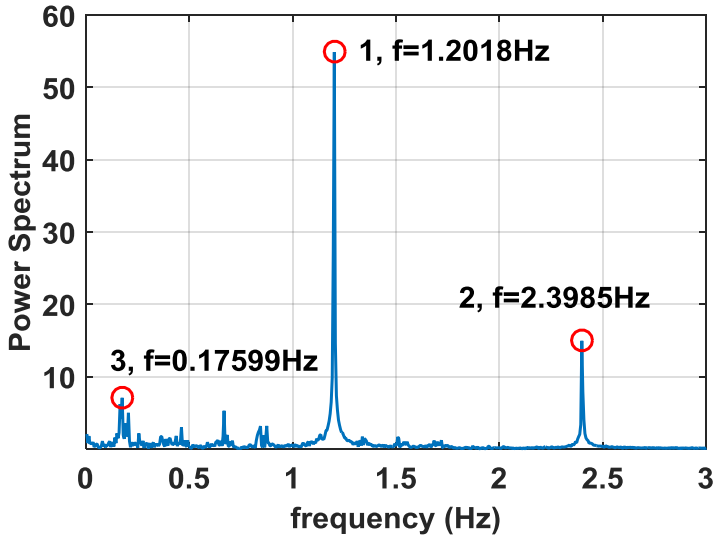

Figure 5-40: Condenser power spectrum at maximum thermal performance for 80 % fill.

In addition, Figure 5-41-a and Figure 5-41-b, shows the temperature power spectrums for the evaporator sections. Notice this spectrum contains similar values to the pressure spectrum and most

importantly at a frequencies at 0.668 Hz and between 0.16 Hz to 0.21 Hz. Observe that peaks at 1.2 Hz are hardly observed and therefore are not dominant in this section.

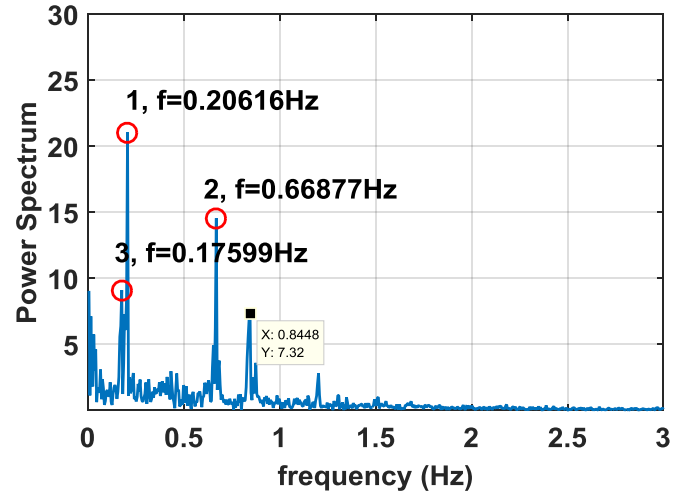

a)

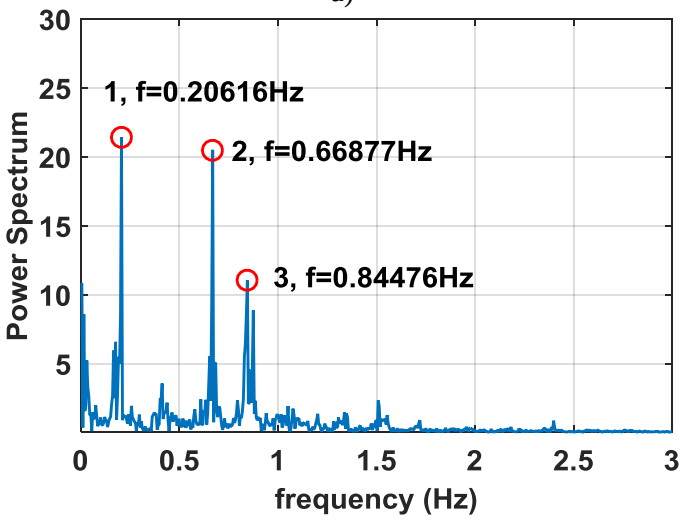

b)

Figure 5-41: PHP1 Evaporator temperature power spectrum at maximum thermal performance for 80 % fill.

It is important to point out that the PHP can operate outside of the dome as discussed previously, Figure 5-42 shows the temperature oscillations of PHP1 at a fill ratio of 80 % and at a maximum heat load of 0.3 W. Unlike the oscillations seen inside the dome, the evaporator section produces higher amplitudes. For example, the bottom section temperature (T10) achieved a sine wave with a peak to peak amplitude of 2 K with an average temperature close to 8 K and at a frequency of 0.147 Hz. The top evaporator (T5)

oscillated between 5.725 K and 6.425 K at a frequency of 0.147 Hz. While the condenser section is oscillating from 4.910 K to 4.997 K but at multiple frequencies below 1 Hz. These frequencies are better observed in power spectrum shown in Figure 5-43. The condenser still shows a peak at a frequency of 1.2 Hz. It is important to mention that the evaporator section and condenser section were able to operate continuously in the supercritical and subcooled regions, respectively.

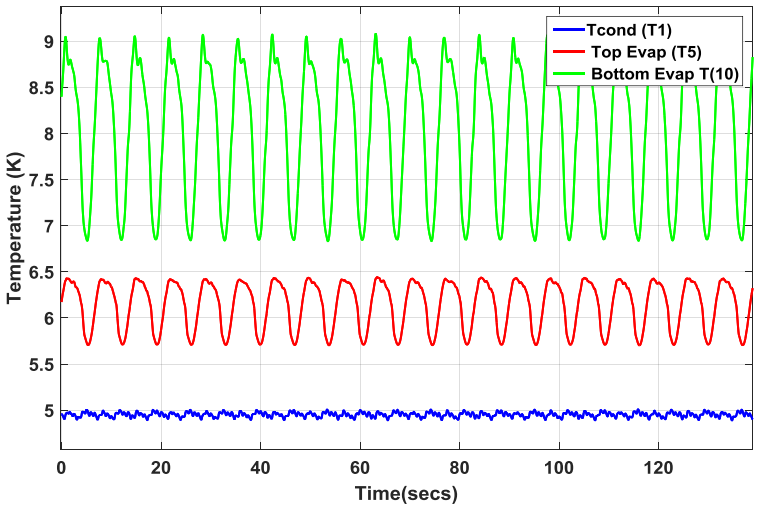

Figure 5-42: PHP1 temperature oscillations outside the dome at initial fill of 80 %

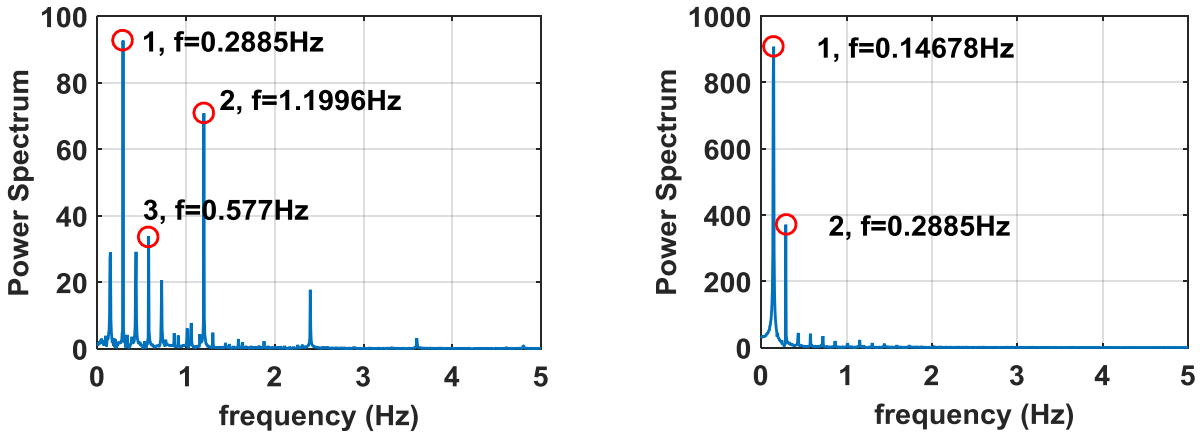

a) b)

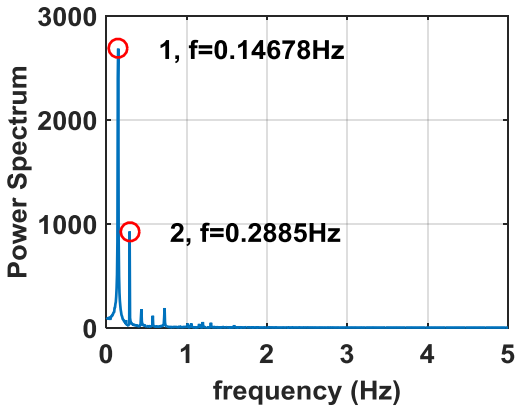

c)

Figure 5-43: Temperature Power Spectrums for a) condenser section T1, b) top evaporator section T5, c) bottom evaporator section T10. Case is at 80 % initial fill ratio and maximum heat load of 0.3 W.

In addition, Figure 5-44 shows the temperature oscillations for all three bottom sections. As observed each bottom section was oscillating at the same frequency of 0.147 Hz but at different phases. For example, as temperature T10 (bottom section of PHP1) increases to its highest peak starting from its average temperature, temperature T6 (bottom section of PHP2) starts to decrease to its lowest peak from its average temperature; however T2 (bottom section PHP3) increases starting from its lowest peak. The phase shift between T10 and T2 was calculated to be 141^{o} degrees and between T10 and T6 was 248^{o} degrees.

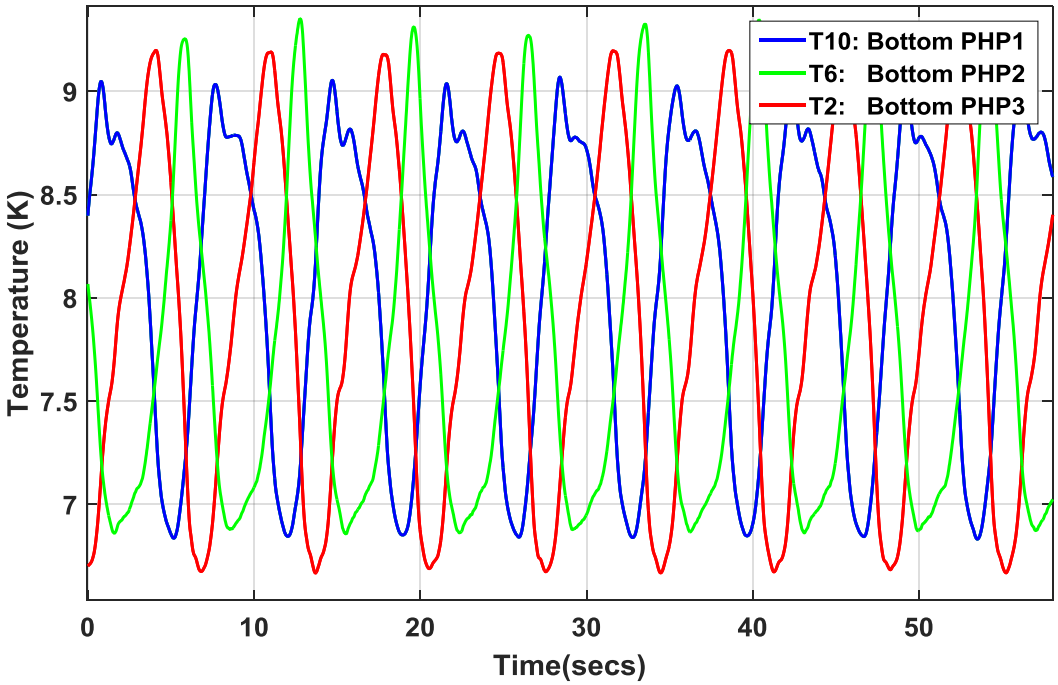

Figure 5-44: Bottom evaporator temperatures oscillating outside the dome at initial fill of 80 %.

Table 5-2 shows a summary of frequencies tested at other initial fill ratios for PHP1. The red highlighted and underline values are the frequencies with maximum peaks values in the power spectrum. Inside the dome, the most common frequency is 1.2 Hz, but the dominant frequencies outside the dome decrease one order of magnitude. In addition, it can be assumed that the frequencies for PHP2 and PHP3 are similar to PHP1.

Table 5-2: Frequency summary inside and outside the dome for PHP1

Fill Ratio (%)	Descripción	P_{cond} frequency (Hz)	P_{evap} frequency (Hz)	T_{cond} (T1) frequency (Hz)	Top Evap (T5) Frequency (Hz)	Bottom Evap Frequency (Hz)
20	Inside Dome, max efficiency (0.1692 W/K)	**0.0704**, 0.1257, 1.2, 6.567	0.01, 1.2, **2.60**, 2.72	**1.2**	**0.1156**, 1.2	0.0603, **0.1559**, 0.3268
20	Outside dome, max heat load (0.2329 W)	0.02, 0.035, 0.05, 0.09, 1.2, 2.62, **3.17**	0.02, 0.035, 0.09, 1.2, 2.62, **3.17**	0.035, 1.2, **3.17**	0.045, 0.09, 0.116, **3.17**	0.035, 0.05, 0.065, 0.09, 1.2, **3.17**

30	Inside Dome, max efficiency (0.2448 W/K)	0.02, 0.04, **1.2**, 6.5	1.2, 2.5, **2.62**, 2.97	**1.2**	0.02, 0.246, 0.297, **1.2**	erratic power spectrum, most common frequecies between 0.2 Hz to 4 Hz
30	Outside dome, max heat load (0.2332 W)	0.075, 0.815, **0.9**, 1.2	0.809, **0.9**, 1.2, 2.6	**1.2**, 0.8, 0.9	0.8, **0.9**	0.03, 0.809, **0.9**
40	Inside Dome, max efficiency (0.2889 W/K)	0.01, 0.03, **1.2**, 6.57	0.01,1.2, **2.62**	**1.2**	0.035, 0.216, 0.287, **1.2**	0.025, 0.14, 0.236, **1.2**
40	Outside dome, max heat load (0.069 W)	**0.01**, 0.025, 0.035	0.025, **0.04, 0.055**, 0.11	0.01, 0.02, **0.055**, 0.065, **1.2**	**0.055**, 0.01, 0.02, 0.04	**0.055**, 0.01, 0.02, 0.04
50	Inside Dome, max efficiency (0.3217 W/K)	0.045, 0.196, 0.447, **1.2**	**1.2**, 2.59, 2.826, 2.710	**1.2**	0.121, 0.172, 0.385, **1.2**	0.415, **1.2**, 1.5, 1.9
50	Outside dome, max heat load (0.2334 W)	**0.045**, 0.085, 0.095, 0.13	**0.045, 0.085**, 0.13	**0.045**,0.1307, 0.216, 1.2	0.045, **0.085**, 0.1307, 0.0176	0.045, **0.085**, 0.1307
58	Inside Dome, max efficiency (0.3625 W/K)	0.015, 0.03, **1.2**	**1.2**, 2.5, 2.62, 2.73	**1.2**	0.01, 0.24 , **1.2**	**1.2**, 1.574, 2.475
58	Outside dome, max heat load (0.2792 W)	**0.1257**, 0.2564, 0.3821, 0.1056	**0.1257**, 0.2564, 0.3821, 0.1056	**0.1257**, 0.2564, 0.6386, 1.2	**0.1257**, 0.2564, 0.3821, 0.5078	**0.1257**, 0.3821, 0.6386, 0.1056
70	Inside Dome, max efficiency (0.3040 W/K)	0.2414, 0.6336, 0.5028, **1.2**	0.2263, **0.3419**, 0.6587, 1.2	**1.2**	0.241, **0.5028**, 0.6334, 1.2	0.015, 0.5028, 0.6335, **1.2**
70	Outside dome, did not reach above critical point	n/a	n/a	n/a	n/a	n/a
75	Inside Dome, max efficiency (0.2606 W/K)	**0.01508**, **0.2313**, 0.352, 0.5028, 0.7140	**0.01508**, 0.025, 0.035, 0.7140	0.2313, 0.7140, **1.2**	0.2111, **0.2313**, 0.5028, 0.71402	0.2111, **0.2313**, 0.4777

75	Outside dome, max heat load (0.0982 W)	0.045, 0.0603, **0.1659**, 0.3318	0.04522, **0.1659**, 0.3318, 0.4978	**0.1659**, 0.4978, 0.6637, 1.2	0.0804, **0.1659**, 0.3318, 0.6637	0.0804, **0.1659**, 0.3318, 0.6637
80	Inside Dome, max efficiency (0.2253 W/K)	**0.01508**, 0.1659, 0.2062, **0.6687**,	0.01508, 0.1659, 0.2062, **0.6687**, 0.8447	**1.2**	0.17560, **0.2061**, 0.6687, 0.8447	**0.2061**, 0.6687, 0.8447, 0.8749
80	Outside dome, max heat load (0.3070 W)	0.0455, **0.1467**, 0.2885, 0.43528	0.0455, **0.1467**, 0.2885, 0.43528	**0.2285**, 0.4352, 0.577, 1.2	**0.1467**, 0.2885	**0.1467**, 0.2885

5.3.5 PHP thermal performance at a constant condenser temperature

The data presented in this section were achieved with the following conditions:

- Initial fill ratio of 55 % was used.
- Temperature of condenser section was controlled at different set points, between 3.8 K and 4.9 K. A PID controller was programmed in Labview ® to control the heat load output of the heater located at the cold head of the cryocooler.
- Equal heat loads to bottom evaporators were applied.

Figure 5-45-a shows the condenser and bottom evaporator temperatures vs the heat load applied at an initial fill ratio of 55 %. The condenser temperature was maintained at 4.208 K until each bottom heaters reached 0.1757 W. Figure 5-45-b and Figure 5-45-c show the thermal performance in terms of temperature difference (condenser section and bottom evaporator sections) and the effective thermal conductance C_{eff} ($Q/\Delta T$). It can be observed that PHP3 shows a slightly lower temperature difference, which resulted in a slightly higher thermal performance. As mentioned previously, these small thermal performance difference between the PHP sections could be due to uneven fill ratio values in each PHP.

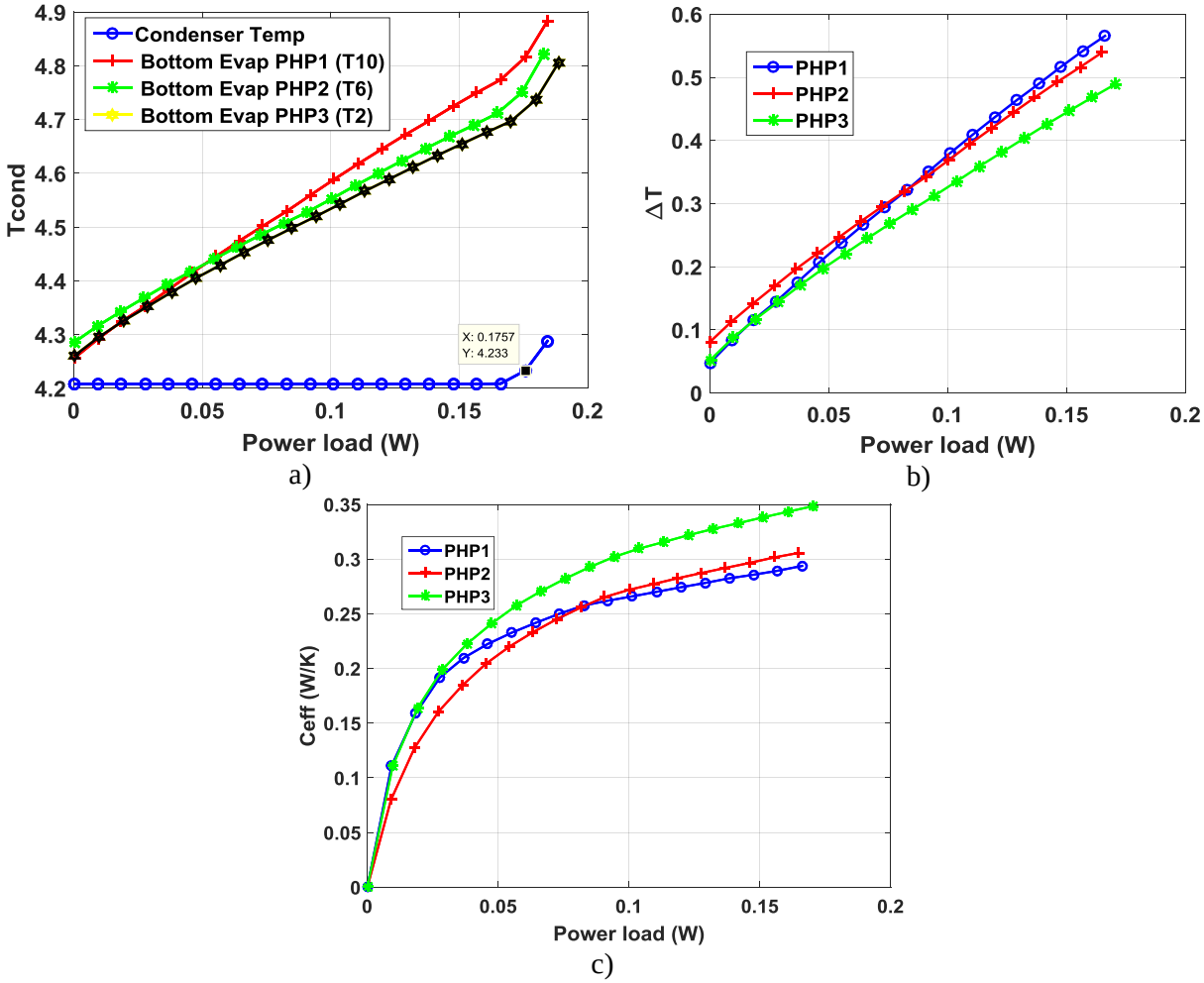

Figure 5-45: Constant condenser temperature at 4.2 K, a) bottom evaporator temperatures, b) temperature difference between bottom evaporator and condenser sections, c) effective conductance per each PHP, d) total fill ratio.

Figure 5-46 shows the temperature difference between the bottom evaporators and the condenser for each PHP section at different constant condenser temperatures T_c (3.8 K, 4.0 K, 4.2 K, 4.5 K 4.7 K and 4.9 K). All these results are operating in the below the critical point (inside the *T*-*v* dome) and at an initial fill ratio of 55 %. It is very important to note that the evaporator temperature at a zero heat load starts at a similar temperature as the condenser section, see Figure 5-45-a. In addition, since the cryocooler has a unique cooling curve; a constant condenser temperature equal to T_c = 3.8 K cannot be maintained at higher heat loads as it can with higher temperature set points. However, when initially operating at a set point of T_c = 4.9 K, the evaporator temperature will be close to the critical temperature of helium and will not be

able to perform at higher heat loads as well. For these reason the PHP is able to operate at higher heat loads at set points of T_c = 4.5 K and 4.7 K as shown in Figure 5-46. Furthermore the effective thermal conductance C_{eff} (Q/ΔT) for each PHP are shown in Figure 5-47. Again, notice that PHP3 achieves the highest thermal performance of 0.4 W/K which is possibly due to the small differences in fill ratio per PHP.

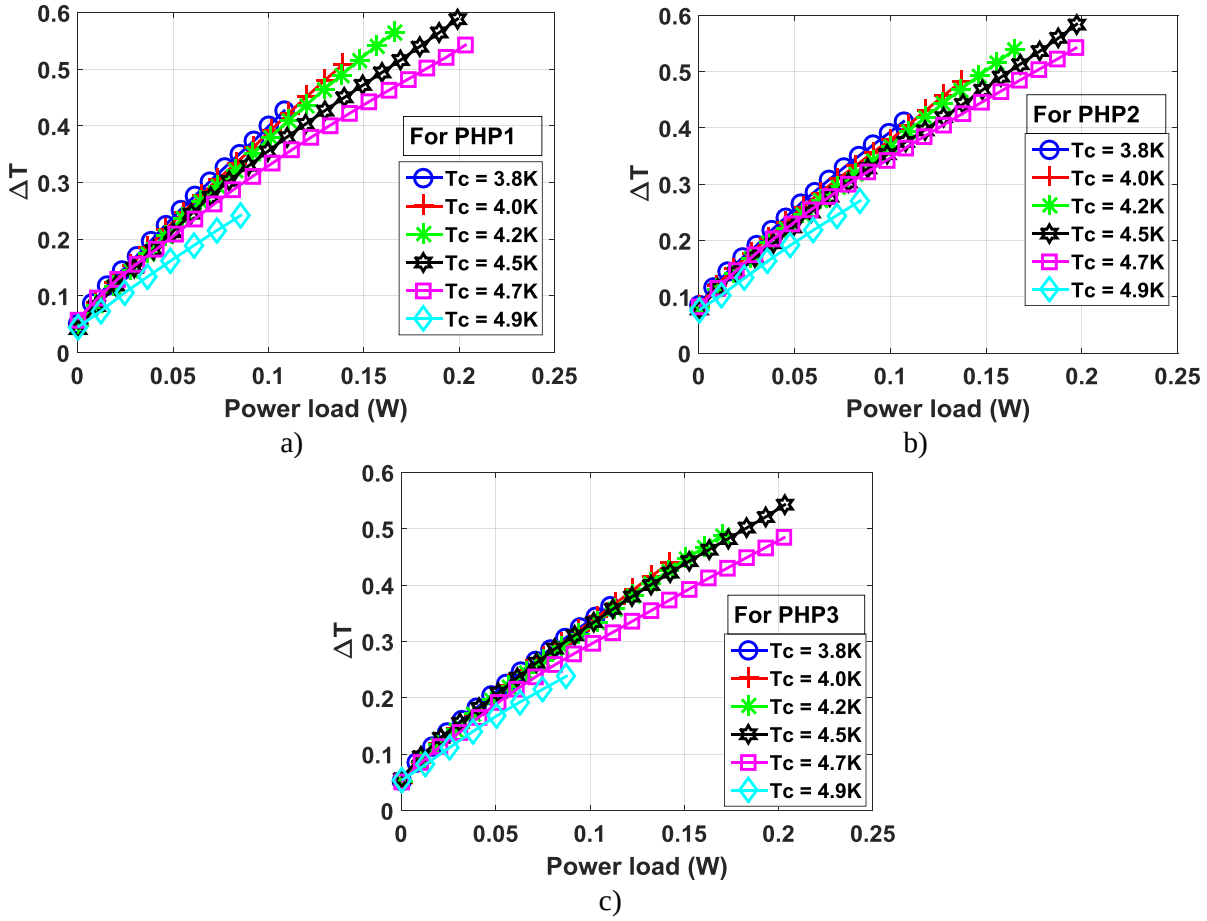

Figure 5-46: Temperature difference between bottom evaporators and condenser sections. Fill at 55 % and equal heat loads, a) temperature difference for PHP1, b) temperature difference for PHP2, c) temperature difference for PHP3.

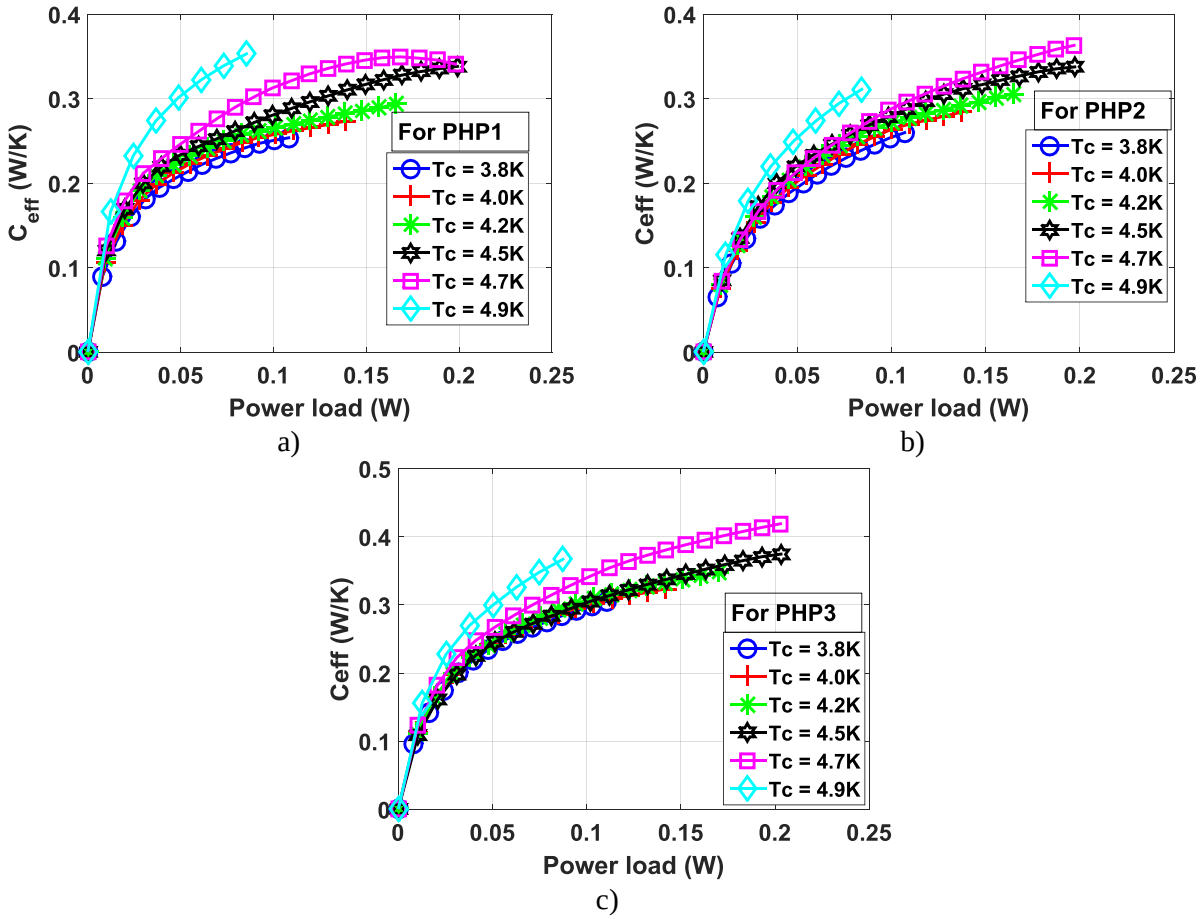

Figure 5-47: Fill at 55 % and equal heat loads, a) Thermal conductance for PHP1, b) Thermal conductance for PHP2, c) thermal conductance for PHP3.

5.4 Random Heat for the one meter PHP

Uneven heat loads were applied to the bottom evaporator sections (H1, H3 and H5). These heat loads were randomized but the sum of all three heaters is constant (H1 + H2 + H3 = Constant). For example, Figure 5-48 shows bottom heat loads applied vs time with a total sum H_{sum} of 0.65 W, that is

$$\mathrm{H1} + \mathrm{H3} + \mathrm{H5} = \mathrm{Constant} = 0.65\ \mathrm{W} \qquad 5\text{-}26$$

This figure shows a total of 21 distinct runs where each heater had a distinct heat load for every run for a given total heat load H_{sum}. Furthermore, Table 5-3 shows a summary of the uneven heat load cases performed for the bottom heaters.

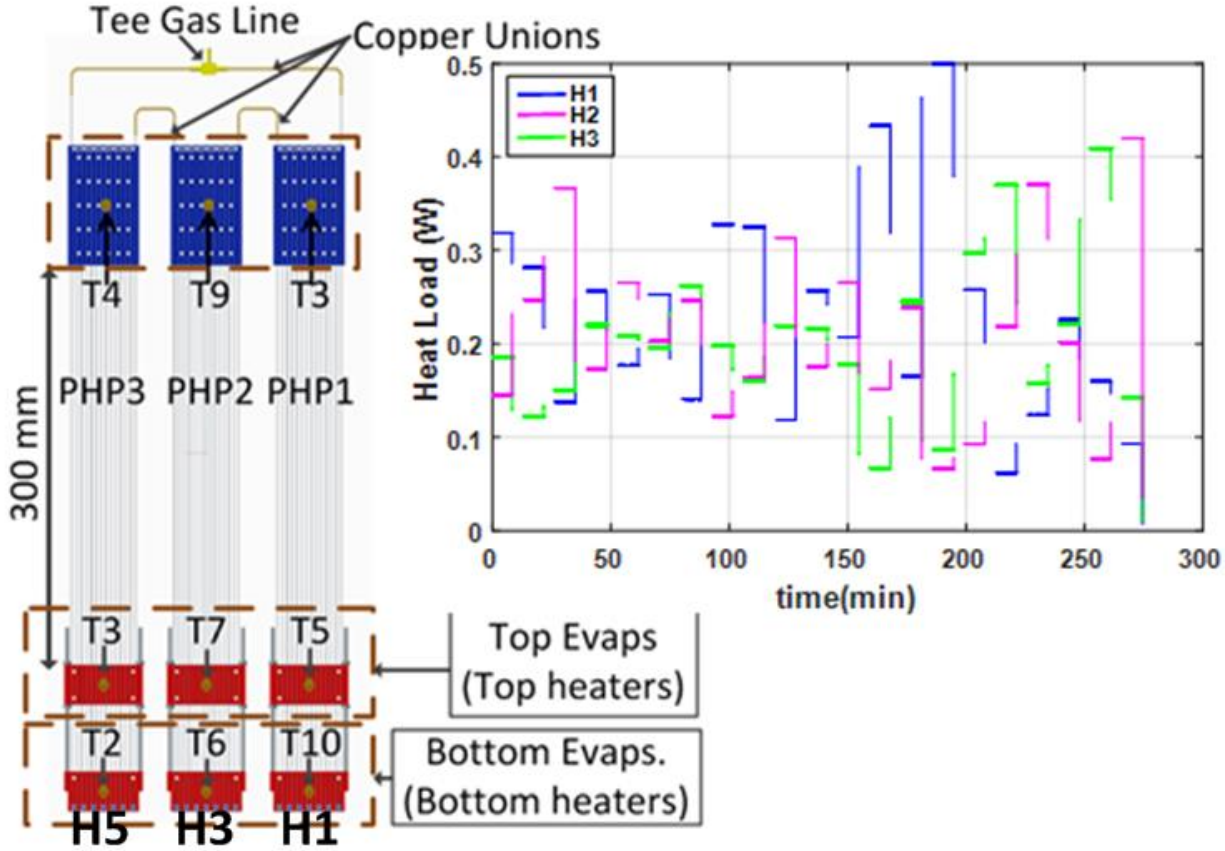

Figure 5-48: Distinct heat load for a total heat load sum of 0.65 W.

Table 5-3: Uneven heat load cases.

Total Heat Load (H_{sum})	Number of runs	Fill Ratio	Date
Case 1, H1+H3+H5= 0.65 W	21	55 %	Sept. 6, 2017
Case 2, H1+H3+H5= 0.55 W	21	55 %	Sept. 7, 2017
Case 3, H1+H3+H5= 0.50 W	21	55 %	Sept. 7, 2017
Case 4, H1+H3+H5= 0.40 W	21	55 %	Sept. 8, 2017
Case 5, H1+H3+H5= 0.30 W	21	55 %	Sept. 8, 2017
Case 6, H1+H3+H5= 0.24 W	21	55 %	Sept. 8, 2017

Figure 5-49 and Figure 5-50 shows the effective conductance and temperature difference vs heat load applied for the uneven case of H_{sum} = 0.65 W. Notice for each PHP section, that the thermal conductance decreases and the temperature difference increases when the heat loads are higher than 0.266 W. In addition, if the desired operating temperature difference for each PHP is below 1 K, then the power applied to each PHP section should be below 41 % of 0.65 W. It is important to note that this 41 % power load (0.266 W)

is close to the heat load where the maximum thermal performance is achieved for even heat loads as shown previously in Figure 5-17.

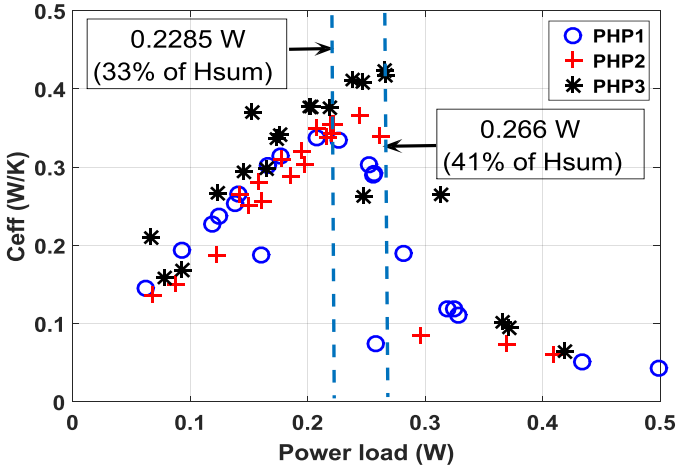

Figure 5-49: Random Heat Load Case. Thermal conductance vs heat load.

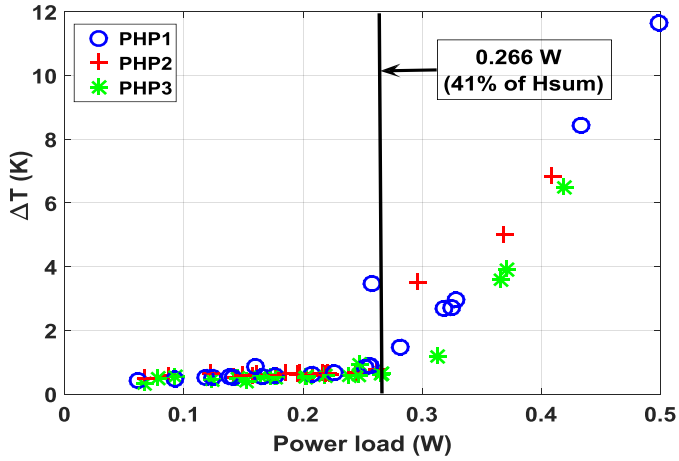

Figure 5-50: Random Heat Load Case. Temperature difference vs heat load.

Figure 5-51 shows the temperature difference as a function of heat load for each PHP and for cases 1, 3, 4 and 6. Data for cases 2 and 5 were not recorded properly due to Labview freezing and will not be analyzed. As shown in Figure 5-51, All the PHP sections show a similar trend: for each total heat load (H_{sum}) case, the temperature difference increases at a different rate. For example, for case 6 (H_{sum} = 0.65 W) the PHP1's temperature difference increases rapidly at 2 K and 0.3 W; however for case 1 (H_{sum} = 0.226 W), the temperature difference increase rapidly at 1 K and 0.15 W. Depending on the total heat load, there will be a different maximum heat load limit per PHP. One possible explanation is that the vapor plugs and liquid

slugs, at the PHP with the highest heat load, migrate to its adjacent PHP sections, this could cause one of the PHPs to lose mass and decreases the number of bubbles necessary to drive the motion of the PHP, causing a dry-out condition.

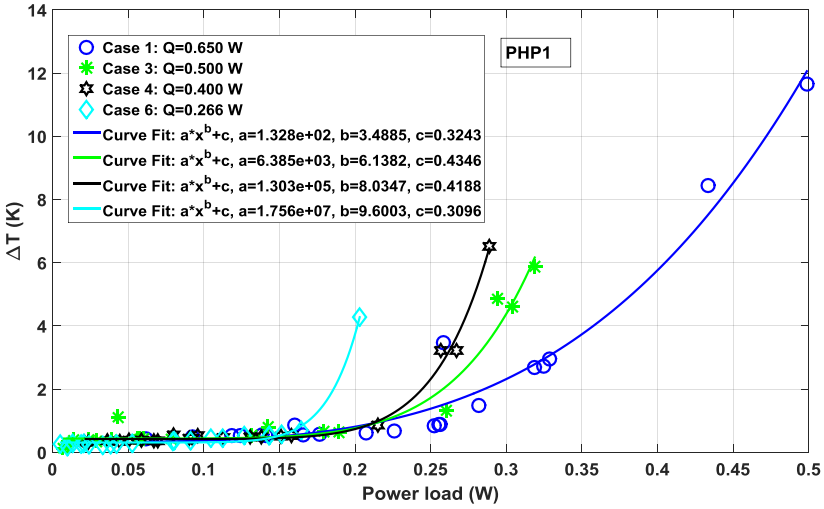

a)

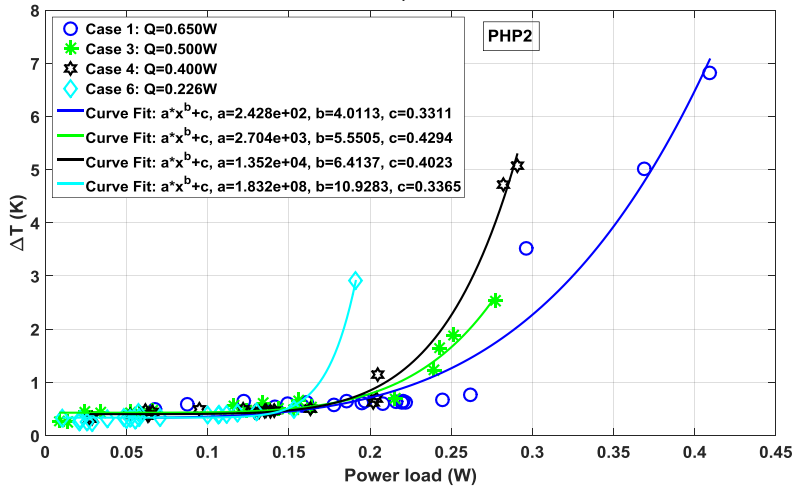

b)

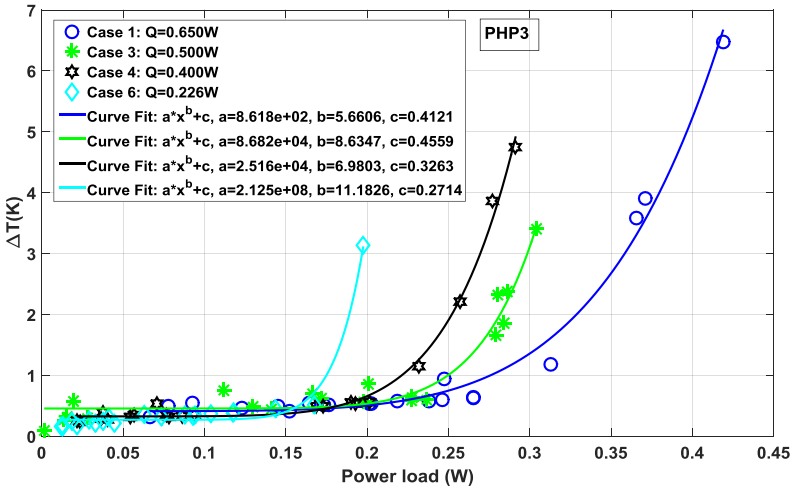

c)

Figure 5-51: Uneven heat load cases per PHP a) PHP1, b) PHP2 and c) PHP3

Table 5-4, shows the maximum heat load limit per PHP for case 1, 3, 4 and 6 for temperature differences lower than 1 K. Where $H_{max,avg}$ is the average heat load limit of all three PHP sections per case. The last column of the table shows the percent ratio of the average heat load limit $H_{max,avg}$ to the total heat load H_{sum}. It can be concluded that the PHP's behavior under uneven heat load conditions is dependent upon the distribution of the loads and limited in total heat load since vapor plugs and liquid slugs can migrate and fill the adjacent PHPs, producing different fill ratios for each PHP section.

Table 5-4: Maximum heat load limit to obtain a temperature difference below 1 K

Case #	H_{sum} (W)	PHP1 (H1) (W)	PHP2 (H3) (W)	PHP3 (H5) (W)	H_{avg} (W)	Havg/Hsum (%)
Case 1	0.6500	0.2817	0.2617	0.2655	0.2696	41.48
Case 3	0.5000	0.2601	0.2151	0.2363	0.2372	47.43
Case 4	0.4000	0.2149	0.2039	0.2013	0.2067	51.68
Case 6	0.2260	0.1645	0.1530	0.1676	0.1617	71.55

5.5 Uncertainty Analysis on results

5.5.1 Uncertainty of temperature sensors

The uncertainty due to resolution of the 16 bit NI-6218 daq, at a voltage reading range of -200 mV to 200 mV, can be calculated as:

$$\mu_{r,daq,V} = \frac{200mV + 200mV}{2^{16} - 1} = \pm 6.1036\,\mu V \qquad 5\text{-}27$$

Both current sources used were stated to have a current uncertainty $\mu_{I,sup,I} = \pm 0.05$ % of the output, which was set to I_{gr} = 20 μA for the germanium sensors and I_c = 3 μA for the Cernox® sensor. In order to calculate the uncertainty. The uncertainty for temperature due to the current supply can be determined as

$$\mu_{I,sup,V} = \frac{R\mu_{I,sup,I}}{dR/dT} = \frac{0.0005R}{dR/dT} \qquad 5\text{-}28$$

Where R is the resistance of of the temperature sensor and dR/dT is the resistor's thermal response.

The uncertainty due to precision was calculated by aquiring 10,000 points per second from the temperature sensors and then averaging them, the higheest value achieved was $\mu_{p,temp,V}$ = 28 μV and will be used as the main reference for all sensors.

The calibration curve fit used to convert resistance to temperature had a standard deviation of $\mu_{eq,K}$ = 0.63 mK for the Cernox® sensor and a $\mu_{eq,K}$ = 1.5 mK for the GR-200A sensors. Using sensitivity values dR/dT for each type of sensor, voltage uncertainties can be converted to units of temperature (K).

$$\mu_{i,T} = \frac{\mu_{i,V}}{I\ dR/dT} \qquad 5\text{-}29$$

Where i represents a specific voltage uncertainty and I is the current supplied to the sensor.

Table 5-5 shows the results of all uncertainties for each type of sensor where μ_{total} is the total uncertainty in units of mK assuming a constant temperature of 4.2 K.

Table 5-5: Uncertainty table for Cernox and GR-200A sensors at 4.2 K

Model	Temp (K)	R (Ohms)	dR/dT	Current Supplied (μA)	$\mu_{r,daq,K}$ (mK)	$\mu_{I,sup,K}$ (mK)	$\mu_{eq,K}$ (mK)	$\mu_{p,temp,K}$ (mK)	μ_{total} (mK)
Cernox 1050	4.2	3340.75	-2594.69	3.0	0.784	0.644	0.63	3.60	3.79
GR-200A	4.2	1689	-861.9	20.0	0.354	0.98	1.5	1.62	4.51

The uncertainty $\mu_{total,C}$ for the Cernox® sensor was calculated using the following equation.

$$\mu_{total,C} = \sqrt{\left(\mu_{r,daq,K}\right)^2 + \left(\mu_{I,sup,K}\right)^2 + \left(\mu_{I,sup,K}\right)^2 + \left(\mu_{p,temp}\right)^2} \qquad 5\text{-}30$$

It is important to note that the germanium sensors were calibrated using the Cernox® sensor; therefore $\mu_{total,C}$ should be added to the the germanium uncertainty $\mu_{total,G}$ and is defined similarly as

$$\mu_{total,C} = \sqrt{\left(\mu_{r,daq,K}\right)^2 + \left(\mu_{I,sup,K}\right)^2 + \left(\mu_{I,sup,K}\right)^2 + \left(\mu_{p,temp}\right)^2 + \left(\mu_{total,G}\right)^2} \qquad 5\text{-}31$$

5.5.2 Effective thermal conductivity uncertainty

As mentioned in Section 4.1, the effective thermal conductivity k_{eff} can be calculated using the following equation

$$k_{eff} = \frac{QL}{NA_c(\bar{T}_e - \bar{T}_c)} \qquad 5\text{-}32$$

Where Q is the heat load applied, L is the adiabatic length, Ac is the cross-sectional area, and N is the number of parallel tubes. $\bar{T}_e$ and $\bar{T}_c$ are the average evaporator and condenser temperatures, respectively. Knowing that N is a constant variable and assuming that L and A_c are also constants, the following equation ca be used to calculate the effective thermal conductivity uncertainty μ_{keff}

$$\mu_{keff} = \sqrt{\left(\frac{\partial k_{eff}}{\partial Q}\mu_Q\right)^2 + \left(\frac{\partial k_{eff}}{\partial \bar{T}_e}\mu_{Te}\right)^2 + \left(\frac{\partial k_{eff}}{\partial \bar{T}_c}\mu_{Tc}\right)^2} \qquad 5\text{-}33$$

Where μ_Q is the uncertainty due to the heat load applied. The evaporator temperature uncertainty μ_{Te} and condenser uncertainty μ_{Tc} were calculated in Table 5-5. The derivative terms can be expressed as

$$\frac{\partial k_{eff}}{\partial Q} = \frac{L}{(\bar{T}_e - \bar{T}_c)NA_c}$$

$$\frac{\partial k_{eff}}{\partial \bar{T}_e} = \frac{-QL}{(\bar{T}_e - \bar{T}_c)^2 NA_c} \qquad 5\text{-}34$$

$$\frac{\partial k_{eff}}{\partial \bar{T}_c} = \frac{QL}{(\bar{T}_e - \bar{T}_c)^2 NA_c}$$

The uncertainty μ_Q can be defined using the following equation

$$\mu_Q = \sqrt{\left(\frac{\partial Q}{\partial R}\mu_R\right)^2 + \left(\frac{\partial Q}{\partial V}\mu_V\right)^2} \qquad 5\text{-}35$$

The heaters used had a resistance of R = 50 Ω and an uncertainty μ_R of ±0.5Ω. The uncertainty of the NI-Daq, μ_V, was calculated in the previous section as $\pm 6.1036 \mu V$. The derivative terms can be calculated using Ohms law and can be rewritten in terms of heat load Q and resistance R

$$Q = VI = I^2 R$$

$$\frac{\partial Q}{\partial R} = I^2 = \frac{I^2 R}{R} = \frac{Q}{R} \qquad \text{5-36}$$

$$\frac{\partial Q}{\partial V} = I = \sqrt{\frac{Q}{R}}$$

Finally the uncertainty of the effective thermal conductivity μ_{keff} for all three PHP sections can be graphed as a function of heat load as shown in Figure 5-52 for cases regarding a fill ratio of 69.68 % and bottom heaters "on". It can be observed that the maximum uncertainty was found at the heat load which gives the maximum k_{eff}. It is important to remember the derivative functions shown in equation 5-34 depend on the temperature difference $\bar{T}_e - \bar{T}_c$ and that the two last derivatives depend on the heat load applied Q, therefore when the temperature difference is greater than 1 $\bar{T}_e - \bar{T}_c > 1$ the uncertainty decreases at the maximum heat load applied.

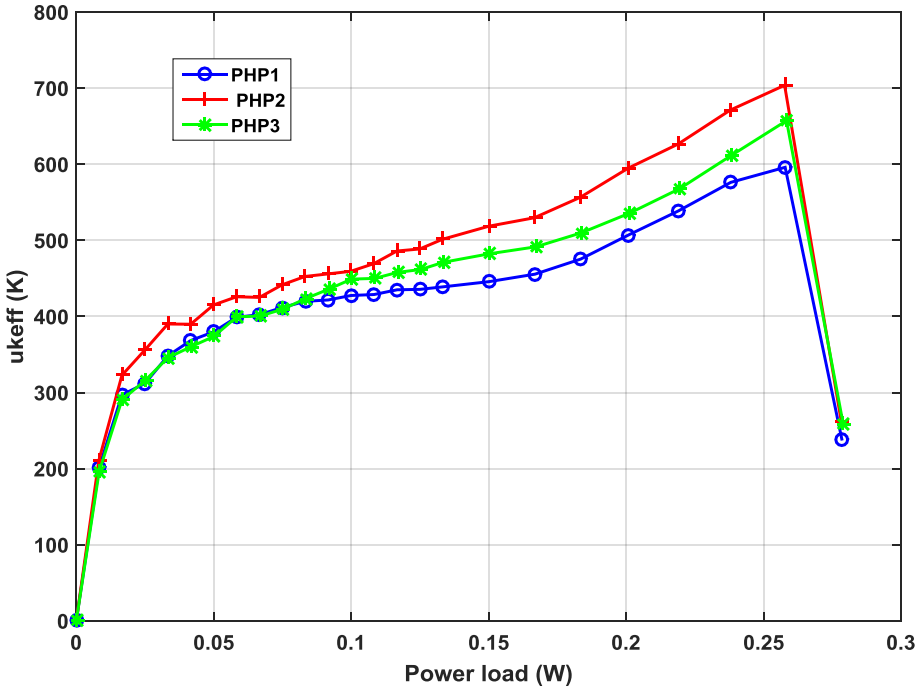

Figure 5-52: Uncertainty in Effective thermal conductivity vs heat load applied

6 Correlations and Theoretical modeling of PHPs

Although significant experimental and theoretical work has been done regarding Pulsating Heat Pipes since Atachi et al [1] introduced the technology in the 1990s, physics based models and empirical correlations are still relatively undeveloped. Here we will be describing 5 approaches that are currently being developed. The first model that was introduced by Ma et al [2] in 2006 is based on the assumption that the PHP behaves as a single spring mass damper system. A second approach consists of dividing the system into multiple spring mass damper systems. In paper published in in 2014 by Gursel et al. [3] results similar to empirical data from Kandekar at al. [4] and Mameli et al. [7] were reported. in yet another approach CFD software such as Ansys is used to model the PHP behavior using equations of continuity, momentum, and energy. Currently a group at therUniversity of Wisconsin - Madison is developing 2-D and 3-D models using Ansys. Umvberto [13] and Pouryoussefi et al. [14] have used CFD software to model PHPs. The fourth approach that was published in 2014 by Senya et al. [16], consists of a numerical model that considers bubble generation, film thickness and dry-out phenomena. The final method involves developing empirical

correlations from actual experimental data and using theses correlations to predict the thermal performance of PHPs for various configurations and operating conditions. These correlations are described in [17]-[20].

6.1 Literature review of CFD software Models

Costa et al. [13] presented a simple 2D model of a water based closed loop PHP using Ansys Fluent 17.1, as shown in Figure 6-1, and assumed a single loop, at a filling ratio of 50 %. Details about the inner diameter, adiabatic, condenser and evaporator lengths were not specified. Costa et al. assumed that the outer wall of the PHP was at a uniform constant temperature of 20 ^{o}C at the condenser section and applied a total heat flux of 10,000 W/m^2. In addition, three phases were considered, water liquid, water vapor and air. Costa et al. [13] states that air was included because if only water liquid and vapor are defined, the simulation starts as if there is already vapor inside the pipe, this assumption is vaguely explained by the author. Finally, he assumes laminar flow, viscous dissipation, and incorporates a constat surface tension properties. The computational time was around 20 hours for a 6 seconds simulation for a 5x10^{-4} s time step. Even though this model is over simplified, Costa et al. concluded that liquid columns are formed and that the fluid indeed oscillates as shown in Figure 6-2.

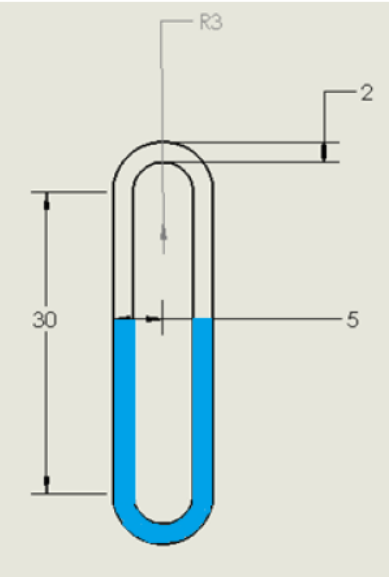

Figure 6-1: PHP Geometry Costa et al.

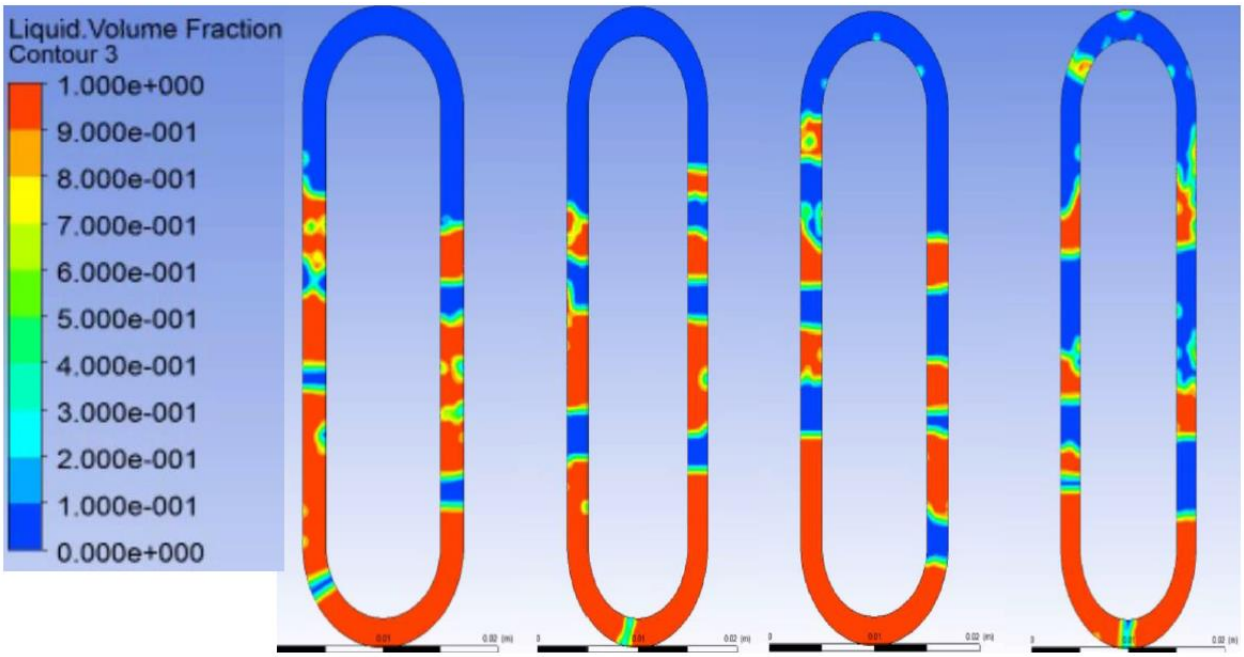

Figure 6-2: Liquid volume fraction, Costa et al.

Pouryoussefi et al. [14] also simulated a water based pulsating heat pipe at filling ratios between 30 to 80 % using a tube with a 3 mm width. A structured meshing configuration and a Volume of Fluid (VOF) method was used in order to simulate a two-phase chaotic flow. The investigated temperature ranges for the evaporator and condenser were 100-180 ^{o}C and 20 – 50 ^{o}C, respectively. Lyapunov exponent and autocorrelation function were used to investigate chaos in the pulsating heat pipe and chaotic behavior was observed. As mentioned by Pouryoussefi et al. [14], applications of the VOF model include stratified flows, free-surface flows, filling, sloshing, the motion of large bubbles in a liquid, the motion of liquid after a dam break, the prediction of jet breakup (surface tension), and the steady or transient tracking of any liquid-gas interface. Figure 6-3 shows the two loop PHP structure used and Figure 6-4 shows the quadrilaterals mesh created. Pouryoussefi et al. mentions that the calculation of surface tension effects on triangular and tetrahedral meshes is not as accurate as on quadrilaterals or hexahedra. All momentum, continuity equation, volume fraction, surface tension and energy equations employed in the simulation are thoroughly described in [14].

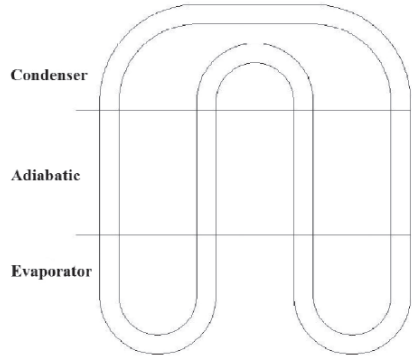

Fig. 1. Pulsating heat pipe structure.

Figure 6-3: Pulsating heat pipe structure, Pouryoussefi et al. [14]

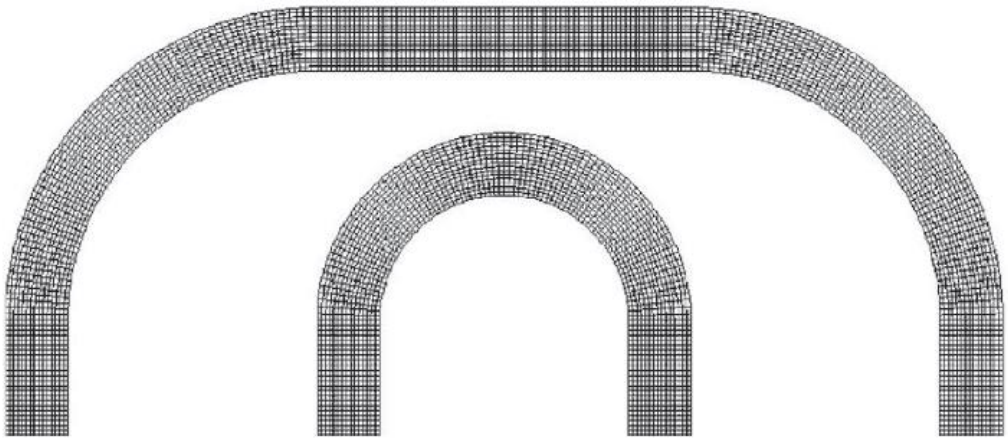

Figure 6-4: Meshing configuration (not in scale), Pouryoussefi et al. [14]

Figure 6-5 and Figure 6-6 represent the volume fraction contours at filling ratios of 30 % and 60 %, respectively. The red contour colors represent the vapor volume fraction while the blue contours represent the liquid volume. The initial conditions at time 0 s where set so that the liquid length was at the same level for all four tubes of the PHP. Pouryoussefi et al. observed in Figure 6-5 that fluid flow finally circulates in one direction (clockwise or counterclockwise). This direction is based on a random process and could be different even under the same operating and boundary conditions [15]. In addition, it was observed that by increasing the fill ratio to 60 %, resulted in an increase in pressure in the PHP, which leads to a longer time duration for boiling to start (because of the increase of the saturation temperature), and slower flow motion in the PHP. It was also observed, that in Figure 6-6, that flow circulation is clockwise in contrast with the fill ratio of 30 %. Pouryoussefi et al. also observed that the liquid film thickness in the condenser section is

thicker than evaporator and adiabatic section which are at higher temperatures, see Figure 6-7. It is important to note that Pouryoussefi et al. [14] did not mention the values of the evaporator, adiabatic and condenser length nor the time it took to run the entire simulation. Comparison to experiment data has not been performed. It is mentioned by Pouryoussefi et al. that future work on the model includes the implementation of heat fluxes in the evaporator section rather the using constant wall temperature and more number of turns will be applied.

Senjaya et al. [16] observed an important result in his CFD simulation where he states that heat is transferred be sensible heat (75 %) and latent heat (26 %). The latent heat transfer rate increase due to the large evaporation rate from liquid film during a bubble growth, while the sensible heat transfer rate increases due to the large amplitude motion of the liquid slugs and vapor plugs.

It can be concluded that CFD simulations are a great help to visualize the motion of the fluid and the thermal performance of a PHP, but will always need verification of experimental data in order to verify it accuracy and improvement.

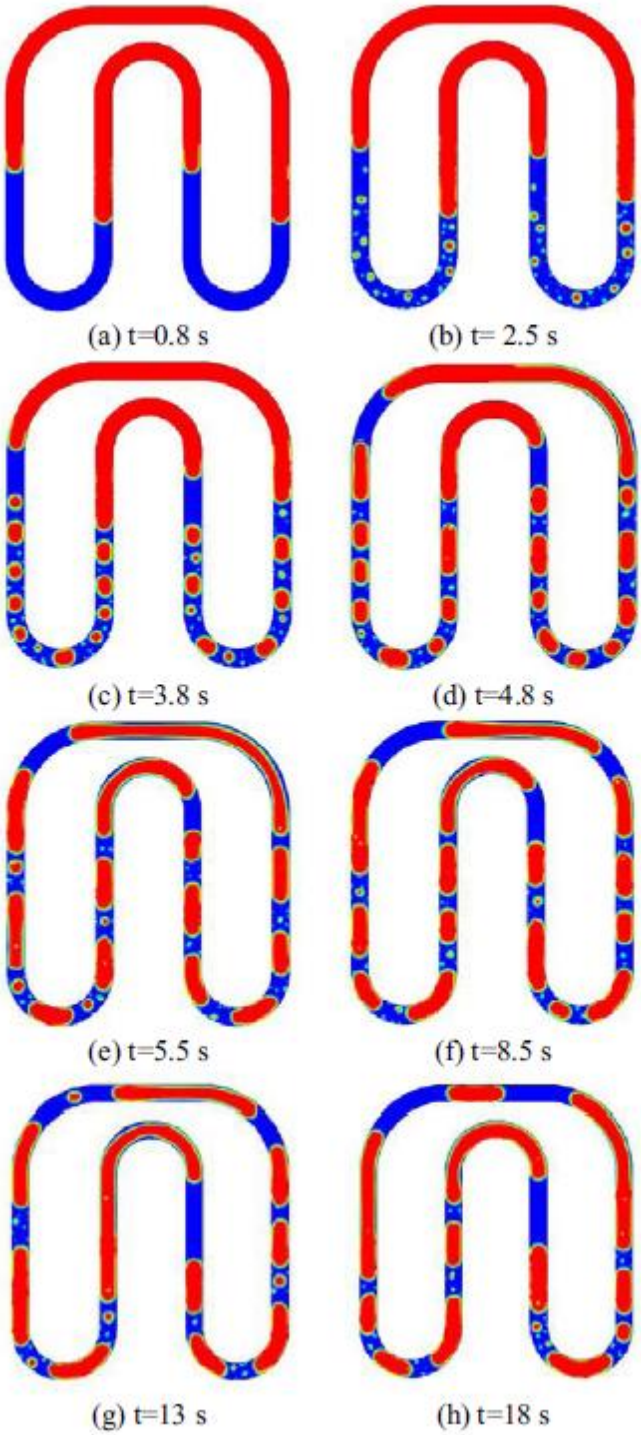

Figure 6-5: Volume fraction for Tevap = 145 ºC, Tcond=35 ºC and filling ratio of 30 %, red vapor volume, blue liquid volume. Pouryoussefi et al. [14]

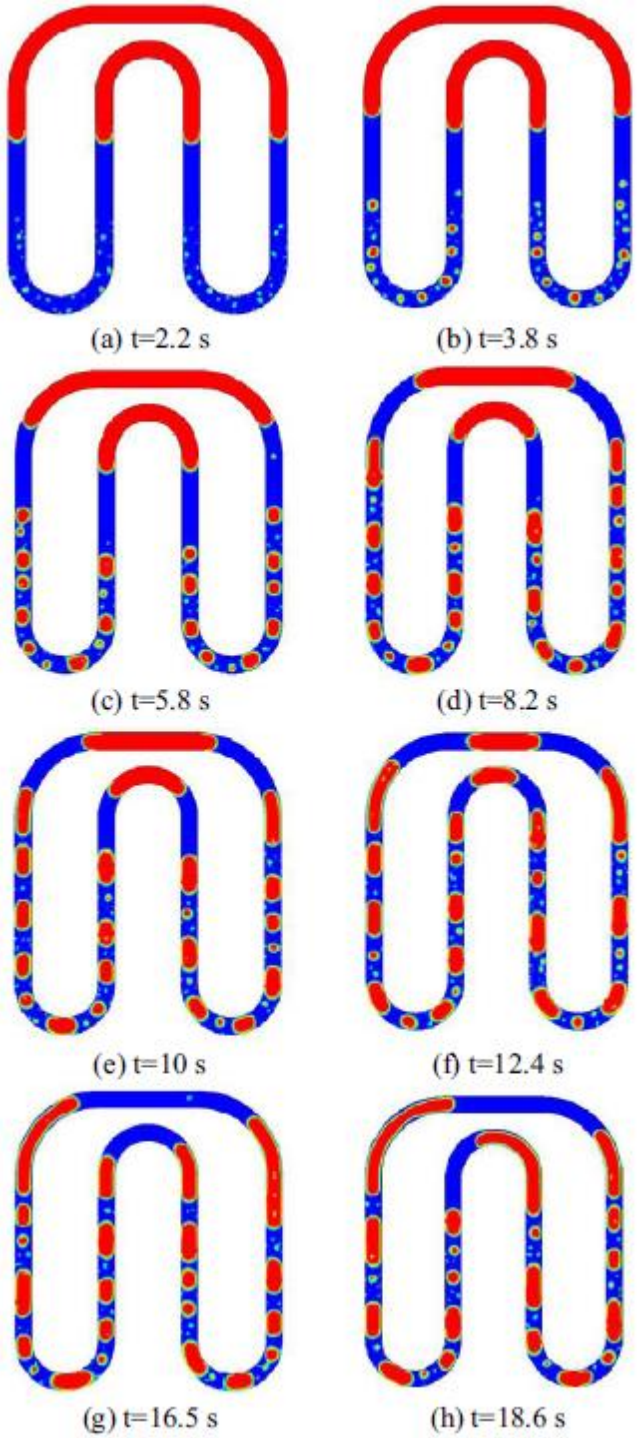

Figure 6-6: Volume fraction for Tevap = 150 ºC, Tcond=35 ºC and filling ratio of 60 %, red vapor volume, blue liquid volume. Pouryoussefi et al. [14]

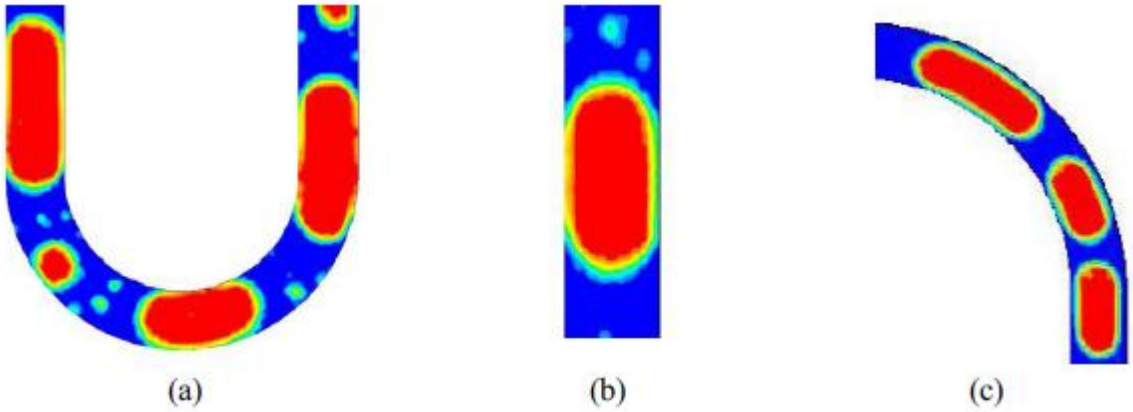

Figure 6-7: Liquid film around the vapor plugs at (a) evaporator, (b) adiabatic, and (c) condenser. Pouryoussefi et al. [14]

6.2 Empirical Correlations

The advantages of using empirical correlations for PHPs is that the thermal performance can be scaled using dimensionless numbers and the computations can be completed more quickly than using a numerical simulation as discussed before. However, since correlations are based on experimental data for certain fluids, predicting the behavior of a PHP using a fluid that was not included in the correlation could result in high inaccuracy. Khandekar et al. formulated an empirical model based on 248 experimental data using R-123 as the working fluid [17], [18], [19]. The following equation calculates the maximum heat fluxes for a closed looped PHP at a 50 % percent filling ratio with an accuracy of ±30 %

$$q^{"} = \frac{q}{2\pi DNL_e} = 0.54[\exp(\beta)]^{0.48} Ka^{0.47} Pr_l^{0.27} Ja^{-1.43} N^{-0.27} \quad 6\text{-}1$$

Where β, Ka, P_{rl}, Ja and N are the inclination angle, Karman number, liquid Prandtl number, Jakob number and number of turns, respectively. The Karman and Jakob numbers can be calculated using the following equations:

$$Ka = \frac{\rho_l (P_{sat,e} - P_{sat,c}) D^3}{\mu_l^2 L_{eff}} \quad 6\text{-}2$$

$$L_{eff} = \frac{L_e + L_c}{2} + L_a$$

$$Ja = \frac{c_{p,l}(T_{sat,e} - T_{sat,c})}{hfg} \quad 6\text{-}3$$

Where ρ_l, $c_{p,l}$ μ_l are the density, specific heat and dynamic viscosity of the liquid respectively. $P_{sat,e}$ and $P_{sat,c}$ are the saturation pressures at the evaporator and condenser sections, respectively. D is inner diameter of the PHP tubing. The effective length L_{eff} depends on the evaporator length (L_e), condenser length L_c and adiabatic length L_a. $T_{sat,e}$ and $T_{sat,c}$ are the saturation temperature at the evaporator and condenser sections, respectively.

Rittedech et al. [20] proposed a correlation based on water, ethanol and R123 fluids at filling ratios of 50 %. The lengths of evaporator, adiabatic and condenser sections were equal and change to 15 cm, 10 cm and 5 cm and the number of turns varied from 19 to 42 [19] The following equation Rittedech et al. [20] presented calculates the heat flux in a horizontal orientation (Ku_0) with a ±30 % accuracy

$$Ku_0 = \frac{q^{"}}{\rho_v h_{fg}[\sigma(\rho_l - \rho_v)/{\rho_v}^2]^{1/4}} = 0.0052\left[\left(\frac{D^{4.3}L_t^{0.1}}{L_e^{4.4}}\right)N^{0.5}\left(\frac{\rho_v}{\rho_l}\right)^{-0.2}Pr_v^{-2.5}\right]^{0.116} \quad 6\text{-}4$$

And for a vertical orientation (Ku_{90})

$$Ku_{90} = \frac{q^{"}}{\rho_v h_{fg}[\sigma(\rho_l - \rho_v)/{\rho_v}^2]^{1/4}} = 0.0067\left[\left(\frac{D^{3.1}L_t^{0.1}}{L_e^{3.2}}\right)N^{0.9}\left(\frac{\rho_v}{\rho_l}\right)^{-0.1}\left(\frac{\omega\mu_v^3}{\sigma^2\rho_v}\right)\right]^{0.116} \quad 6\text{-}5$$

Where Ku is the Kutateladze number, q'' is the heat flux, σ is the surface tension, N is the number of turns, L_t is the total length of the PHP, and μ_v is the dynamic viscosity of vapor. The frequency of oscillation motion of a vapor plug ω can be computed as

$$\omega = \sqrt{\frac{\rho_l g}{\rho_v L_v}} \quad 6\text{-}6$$

Where L_v is the length of the vapor plug. Katpradit et al. [21] developed a correlation for the maximum heat flux when dryout occurs. The correlation is based on R123, ethanol, water and MP39, varied inner diameters, evaporator and condenser lengths and number of parallel channels [19]. Correlations are also related to the Kutateladze number and the following equation predicts the critical heat flux for horizontal and vertical orientations

$$Ku_0 = \frac{q^{"}}{\rho_v h_{fg}[\sigma(\rho_l - \rho_v)/{\rho_v}^2]^{1/4}} = 53680\left(\frac{D}{L_e}\right)^{1.127} Ja^{-1.417} Bo^{0.66} \quad 6\text{-}7$$

$$Ku_{90} = \frac{q^{"}}{\rho_v h_{fg}[\sigma(\rho_l - \rho_v)/{\rho_v}^2]^{1/4}} = 0.0002\left(\frac{D}{L_e}\right)^{0.92} Ja^{-0.212} Bo^{0.295}\left[1 + \left(\frac{\rho_v}{\rho_l}\right)^{0.25}\right]^{13.06} \quad 6\text{-}8$$

Where h_{fg} is the latent heat and *Bo* is the bond number.

Charoensawan et al. [22] developed a correlation a model with a standard deviation of ±30 %. The following correlation was based on 98 experimental data sets of water and ethanol

$$Ku = 2.13 \times 10^{-9} Pr_l^{0.75} (Ja^*)^{-0.38} Bo^{-0.84} Ka^{0.58} k_c/k_a \quad 6\text{-}9$$

Where Ja^* is the modified Jacob number and is defined as

$$Ja^* = \frac{\varphi c_{p,l}(T_{sat,e} - T_{sat,c})}{(1-\varphi)h_{fg}} \quad 6\text{-}10$$

Where φ is the filling ratio, k_c/k_a is the ratio of thermal conductivity of the coolant at the required temperature and at ambient air of 25 °C.

Arslan et al. [23] developed a correlation using the Buckhingam Π theorem that predicts the overall heat transfer coefficient for a water PHP. The temperature difference between the evaporator and condenser surfaces is introduced by a correlation function of dimensionless numbers such as kinetic Reynolds number, Jakob number ($c_p\Delta T/h_{fg}$) and the geometric parameters [23]. A maximum 25 experimental data sets were used to create a correlation with an accuracy of 15 %.

$$\pi_1 = \frac{Ul}{k} = 4.728 \times 10^{-7} Re_w^{1.985596} \pi_3$$

$$\pi_1 = \frac{c_{p,l}\Delta T}{h_{fg}} \quad 6\text{-}11$$

$$\pi_2 = Re_w = \frac{w d_l^2}{v}$$

Where *U* is the overall heat transfer coefficient, *l* is a characteristic length described in [23], π_1 is the Jakob number and ΔT is the temperature difference between the evaporator and condenser section. Re_w is the

kinetic Reynolds number, w is the oscillation frequency of the liquid slugs, d_l is the tube diameter and v is the kinematic viscosity of the liquid.

6.2.1 Nonlinear regression fit using Khandekar's form

The above correlations were used to predict the PHPs heat load curve. Figure 6-8 shows the predictive heat loads for the optimal thermal performance of the 300 mm PHP configuration. It can be shown that, Khandekar's correlation was the closest approximation since its prediction was just one order of magnitude higher. In addition, Mito's correlation uses a similar form as Khandekar, but over predicts the helium PHP as high as 2 orders of magnitude.

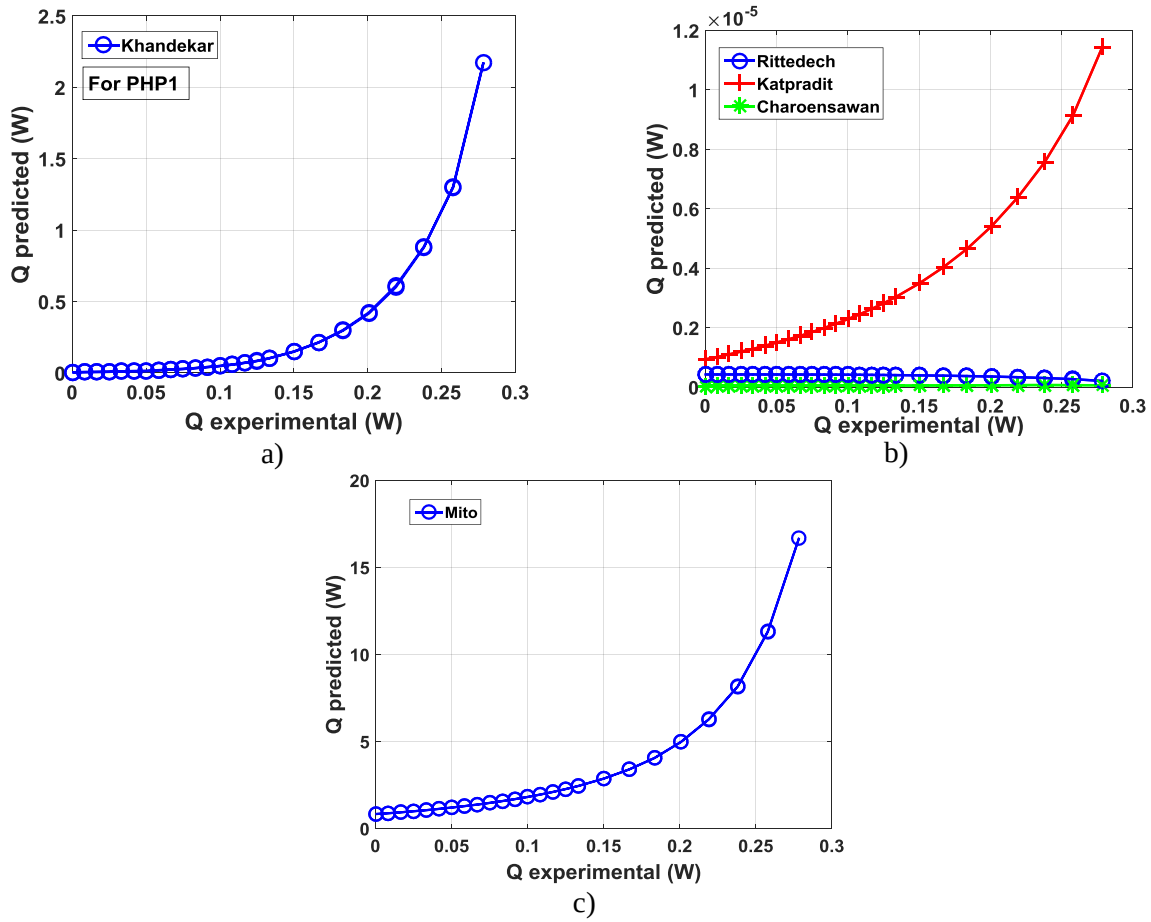

Figure 6-8: PHP correlations, a) Khandekar's b) Rittedech, Katpradit, Charoensawan, c) Mito.

Since the best approximation was Khandekar's correlation, it was used as a basis or starting point to create a correlation for the current helium PHP. Therefore, all the data for both PHP configurations, 300 mm and

1000 mm adiabatic lengths, were non-dimensionalized to the following numbers: Karman (K_a), Jakob (J_a), liquid Prandtl (P_{rl}), fill ratio (f_{liq}) and the adiabatic ratio (Lr). The adiabatic ratio (Lr), is the ratio between the adiabatic length and the total length of the PHP. It is important to note that the inclination angle *Beta* and the number of turns N were not used in the correlation since they were kept constant. For this reason, the correlation can be written as the following:

$$q^{"} = \frac{q}{A_s} = \frac{q}{\pi D N L_e} = C_1 Ka^{C_2} Ja^{C_3} Pr_l^{C_4} f_{liq}^{C_5} L_r^{C_6} \qquad 6\text{-}12$$

Where A_s is the surface area of the evaporator section with respect to the hydraulic diameter D (0.5 mm), and $C_1 \ldots C_i \ldots C_6$ are the corresponding coefficients. These coefficients were then solved using a nonlinear regression fit Matlab function:

```
nlinfit(X,Y,modelfun,beta0)
```

Where each column in matrix X contains the dependent variables X = [*Ka Ja Prl fliq Lr*]. Y is the dependent variable, in this case the heat flux ($q^{"}$). Equation 6-12 **was written as a Matlab function called "modelfun", and finally "beta0" represents initial guesses for the coefficients C_i. Figure 6-9 shows the correlation for all three PHPs. A total of 450 experimental points, for even heat load cases on the bottom evaporator sections, were used to generate the correlations; hence similar plots are observed. All regression fits resulted in an R squared fit close to 97 % and a root mean squared error around 16 W/m^2. Figure 6-10 is similar to Figure 6-9 except it shows the heat load *Q* in watts.**

Table 6-1 summarizes the list of coefficients used for PHP1, PHP2, and PHP3.

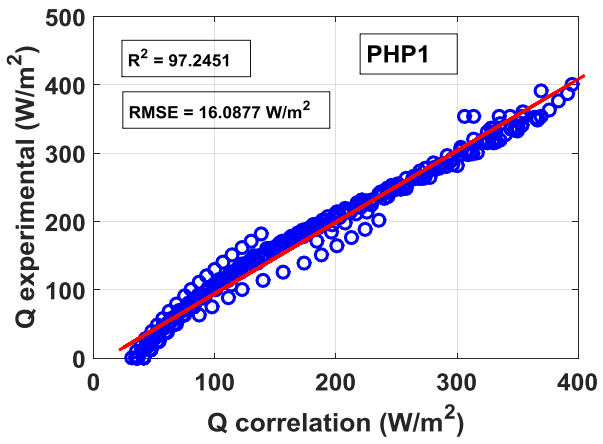

a)

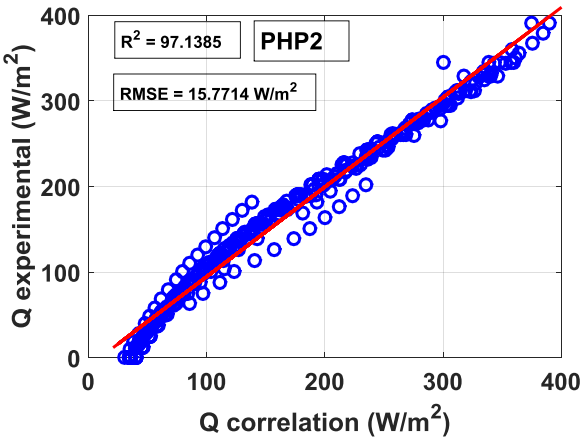

b)

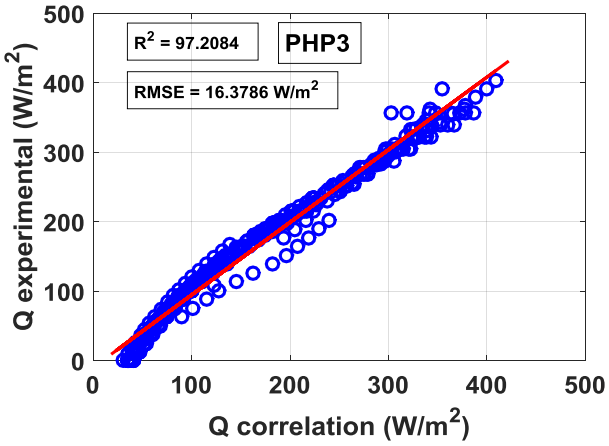

c)

Figure 6-9: Nonlinear regression in Matlab in units of W/m^2.

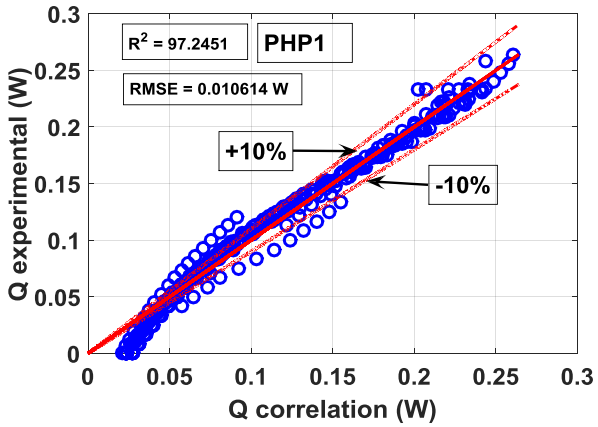

a)

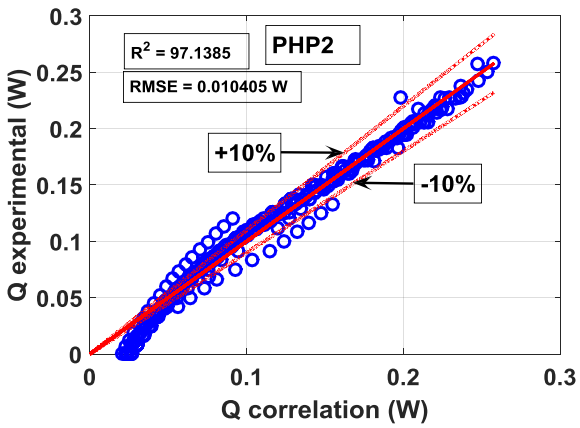

b)

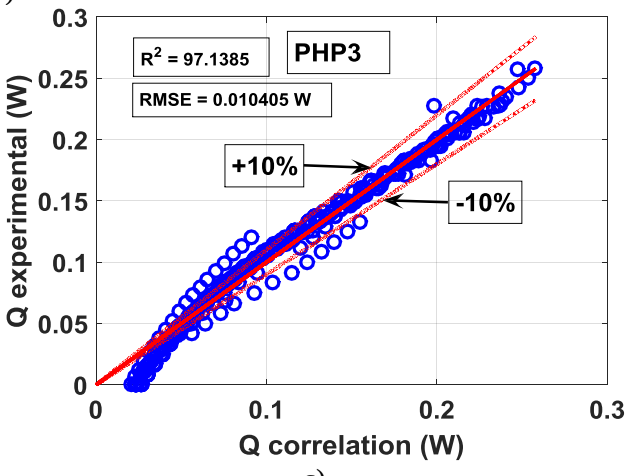

c)

Figure 6-10: Nonlinear regression in Matlab in units of Watts, a) PHP1, b) PHP3, c) PHP3.

Table 6-1: Calculated coefficients for nonlinear regression fit.

PHP#	C_1	C_2	C_3	C_4	C_5	C_6	R^2 (%)	RMSE (W/m^2)
PHP1	4.9127e-7	1.9929	-2.0524	3.2215	-0.025091	7.0134	97.24	16.09
PHP2	1.2522e-6	1.9211	-1.9562	3.1357	-0.031339	6.8144	97.14	15.77
PHP3	1.2722e-6	1.9448	-1.9618	3.0444	-0.04162	6.9746	97.20	16.38

6.2.2 Modified Nonlinear regression fit

The following two observation have been determined from the previous nonlinear regression fit:

- Low heat loads were over-predicted as shown in Figure 6-10.
- Counter-intuitively, omitting the fill ratio did not affect the overall correlation, this is described in Section 6.2.5.

Hence Equation 6-12 can be modified and improved using the following equation:

$$q^{"} = \frac{q}{A_s} = \frac{q}{\pi D N L_e} = C_1 Ka^{C_2} Ja^{C_3} Pr_l^{C_4} L_r^{C_5} + C_6 \qquad 6\text{-}13$$

Where the fill ratio has been omitted and C_6 represents an offset variable in units of W/m^2. Using the *nlinfit* function in Matlab, the following new coefficients were determined:

Table 6-2: Modified nonlinear regression fit

PHP#	C_1	C_2	C_3	C_4	C_5	C_6	R^2 (%)	RMSE (W/m^2)
PHP1	2744.7395	4.1333E-2	-4.4482E-2	1.1908E-1	1.5061E-1	-3829.4332	99.77	4.87
PHP2	2530.3233	4.3234E-2	-4.6530E-2	1.2849E-1	1.5937E-1	-3554.4466	99.84	4.01
PHP3	1986.4286	5.2109E-2	-5.4352E-2	1.4618E-1	1.9374E-1	-2972.4081	99.73	5.31

Figure 6-11 shows the experimental heat flux versus the correlated predictions in units of W/m^2. Note that the low heat fluxes are predicted more accurately, the RMS error decreased by 12 W/m^2, and the R^2 increased as high as 99.84 %.

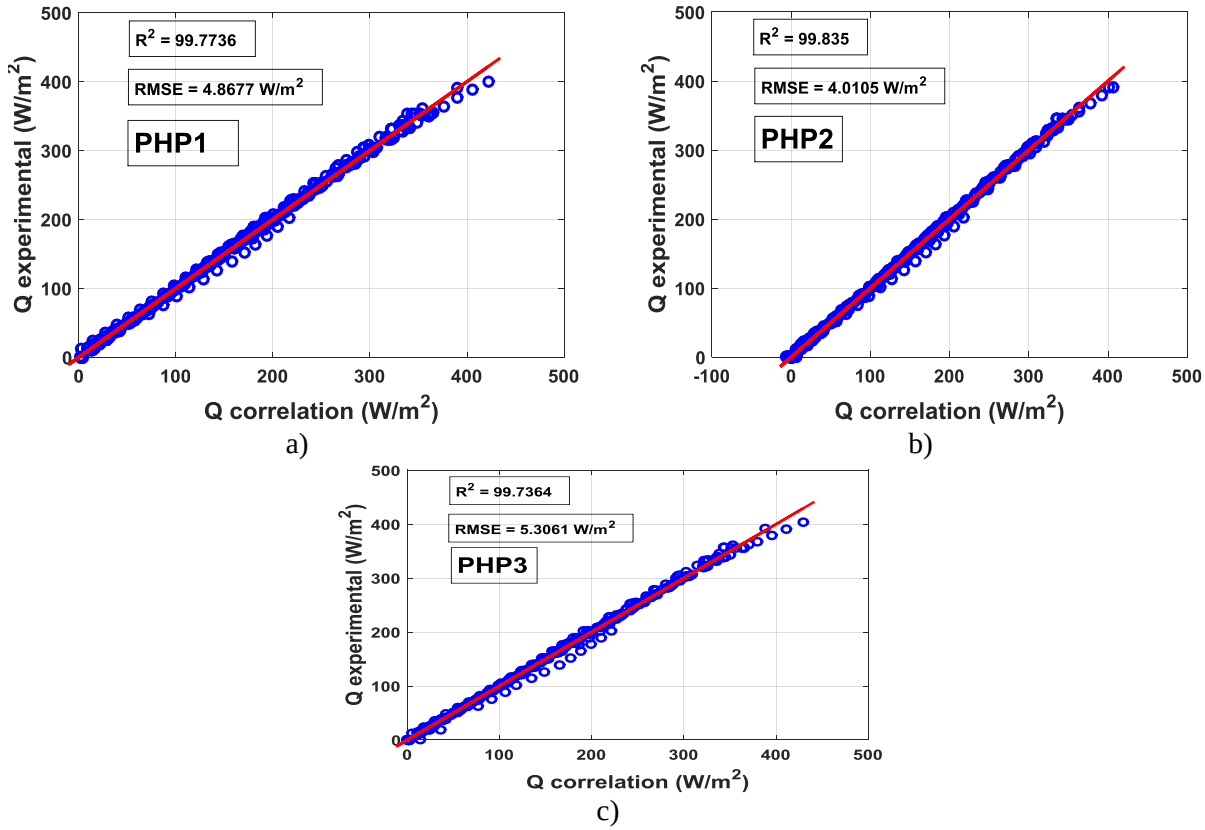

Figure 6-11: Modified nonlinear regression in Matlab in units of W/m^2, a) PHP1, b) PHP2 and c) PHP3.

6.2.3 Adding the bond number to the Modified Nonlinear regression fit

The bond number should be present and added to equation 6-13 due to the fact that it is a major design parameter for PHP devices. Hence the correlation can be written as

$$q^{"} = \frac{q}{A_s} = \frac{q}{\pi D N L_e} = C_1 Ka^{C_2} Ja^{C_3} Pr_l^{C_4} L_r^{C_5} B_o^{C_6} + C_7 \qquad 6\text{-}14$$

Where the coefficients were determined to be:

Table 6-3: Coefficients of the nonlinear regression fit using *Ka*, *Ja*, *Prl*, *Lr* and *Bo* numbers

PHP#	C_1	C_2	C_3	C_4	C_5	C_6	C_7
PHP1	1528.6432	6.0332E-2	-6.4466E-2	1.6453E-1	2.2017E-1	2.3726E-2	-2506.8640
PHP2	1363.7536	6.1087E-2	-6.4705E-2	1.6635E-1	2.2685E-1	5.6270E-2	-2233.2434
PHP3	2409.3245	4.1589E-2	-4.3025E-2	1.1161E-1	1.5565E-1	3.3534E-2	-3343.6300

PHP#	R^2 (%)	RMSE (W/m^2)
PHP1	99.77	4.84
PHP2	99.84	3.96
PHP3	99.74	5.22

Note that for PHP2, the R^2 reached as high as 99.84 % and a RMS error as low 3.96 W/m^2. Overall the R^2 values and RMS error remained the same.

6.2.4 Linear regression correlation

A linear regression fit was created in order to compare it to the nonlinear fit and hence determine which correlation should be used. Therefore, a build in linear regression function in Engineering Equation Solver software (EES) was used to create a second order polynomial fit. The same dimensionless numbers were used as the nonlinear fit. As shown in Figure 6-12, the following options were used:

- Q was chosen at the dependent variable, units of W/m^2.
- The *Ka*, *Ja*, Pr_l, f_{liq} and L_r numbers were chosen as the independent variables.
- The equation form is a polynomial of second order.
- Cross-terms check box was chosen.

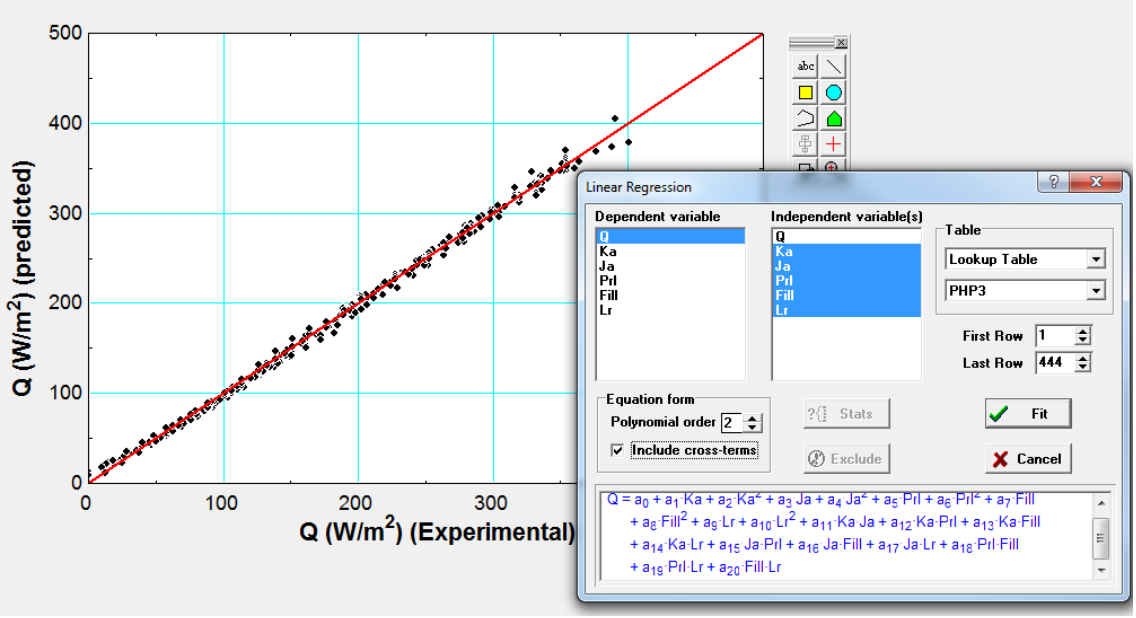

Figure 6-12: Linear regression options in EES

Also shown in the Figure 6-12, the linear regression function created a second order polynomial with 21 coefficients. Table 6-4 summarizes the coefficients obtained for each PHP section. Figure 6-13 shows the general form of the linear regression fit.

$$q^{"} = a_0 + a_1 Ka + a_2 Ka^2 + a_3 Ja + a_4 Ja^2 + a_5 Pr_l + a_6 Pr_l^2 + a_7 f_{liq} + a_8 f_{liq}^2 + a_9 L_r + a_{10} L_r^2 + a_{11} KaJa + a_{12} KaPr_l + a_{13} Kaf_{liq} + a_{14} KaL_r + a_{15} JaPr_l + a_{16} Jaf_{liq} + a_{17} JaL_r + a_{18} Pr_l f_{liq} + a_{19} Pr_l L_r + a_{20} f_{liq} L_r \quad (6\text{-}15)$$

Table 6-4: Linear Coefficients for PHP sections

PHP#	a_0	a_1	a_2	a_3	a_4	a_5	a_6
PHP1	-716.8656	-2.5937E-06	8.5858E-15	1.0014E+04	-4686.6239	3447.5501	-986.4557
PHP2	-1468.9528	1.4738E-06	9.3632E-15	1.4130E+04	-7246.1921	4131.0400	-881.0037
PHP3	-940.0078	-1.6381E-06	5.6672E-15	7.5395E+03	-4302.5843	3742.5574	-716.1904
	a_7	a_8	a_9	a_{10}	a_{11}	a_{12}	a_{13}
PHP1	-42.9183	15.2018	-16745.0457	294920.1830	-5.4584E-06	-7.4541E-06	-3.4985E-07
PHP2	-2.0380	9.8938	4811.5194	158582.2430	-4.2523E-07	-9.6730E-06	1.3632E-08
PHP3	-19.5800	26.3233	-11552.1863	296783.8480	2.4876E-06	-8.2834E-06	-1.5047E-07
	a_{14}	a_{15}	a_{16}	a_{17}	a_{18}	a_{19}	a_{20}
PHP1	9.4873E-05	4290.2054	-5.5930	-182046.3350	87.4943	-2.6164E+04	-365.3471
PHP2	-1.6549E-05	2526.9064	-35.8871	-180314.7690	75.6090	-4.0223E+04	-1178.5073
PHP3	8.3784E-05	2813.6946	-224.4391	-125836.7280	117.2466	-36209.9029	-1298.1066

Notice in Table 6-5, that the fit's R squared values were higher than 99.5 % with a RMS error lower than 6 W/m^2. As observed in Figure 6-13, the predicted results are close to the experimental data showing that a linear fit is more accurate than the nonlinear fit.

Table 6-5: Linear regression properties

PHP#	R^2 (Coefficient of determination)	RMS Error (W/m^2)	RMS Error (W)
PHP1	99.73 %	5.3569	3.5339E-3
PHP2	99.80 %	4.4183	2.9147E-3
PHP3	99.66 %	6.0077	3.9633E-3

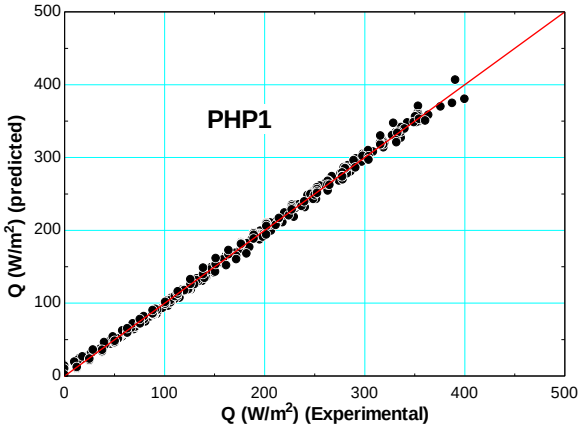

a)

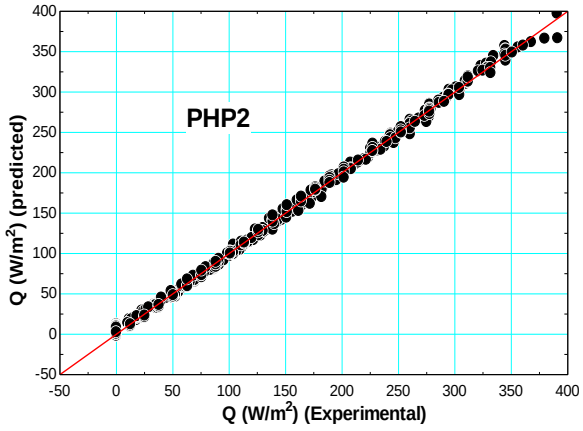

b)

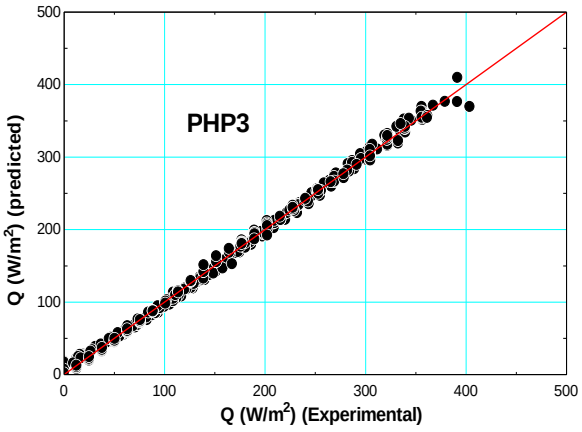

c)

Figure 6-13: Linear regression plot for each PHP in units of W/m^2 for, a) PHP1, b) PHP2, c) PHP3

It can be concluded that a helium PHP is easy to predict using the Karman number (Ka), Jakob number (J_a), liquid Prandtl number (Pr_l), and adiabatic ratio (L_r). Counter-intuitively as described in the next section, omitting the fill ratio did not affect the correlation. The advantage of the nonlinear regression fit is that it has a much simpler form (fewer coefficients) than the linear regression and gives similar results.

6.2.5 Sensitivity Analysis of the regression fits

For this analysis we will using the linear regression fit from PHP1 to determine the sensitivity of the chosen dimensionless numbers, that is Ka, J_a, Pr_l, f_{liq} and L_r. This analysis was performed by comparing the linear regression fit using all 5 dimensionless numbers to a linear fit using 4 numbers. For example, the correlation shown in Figure 6-14-a contains all the dimensionless numbers, while Figure 6-14-b to Figure 6-14-f are regression fits by omitting one of the variables. As observed, by omitting the Prandtl number results in the worst fit with an R-squared of 93.90 %; however the rest of the cases show mild changes. Table 6-6 summarizes the R squared results and the RMS error of each case. Omitting the fill ratio did not change substantially the R^2 or RMS error values as the other cases. For this reason, the fill ratio was omitted in the modified nonlinear regression.

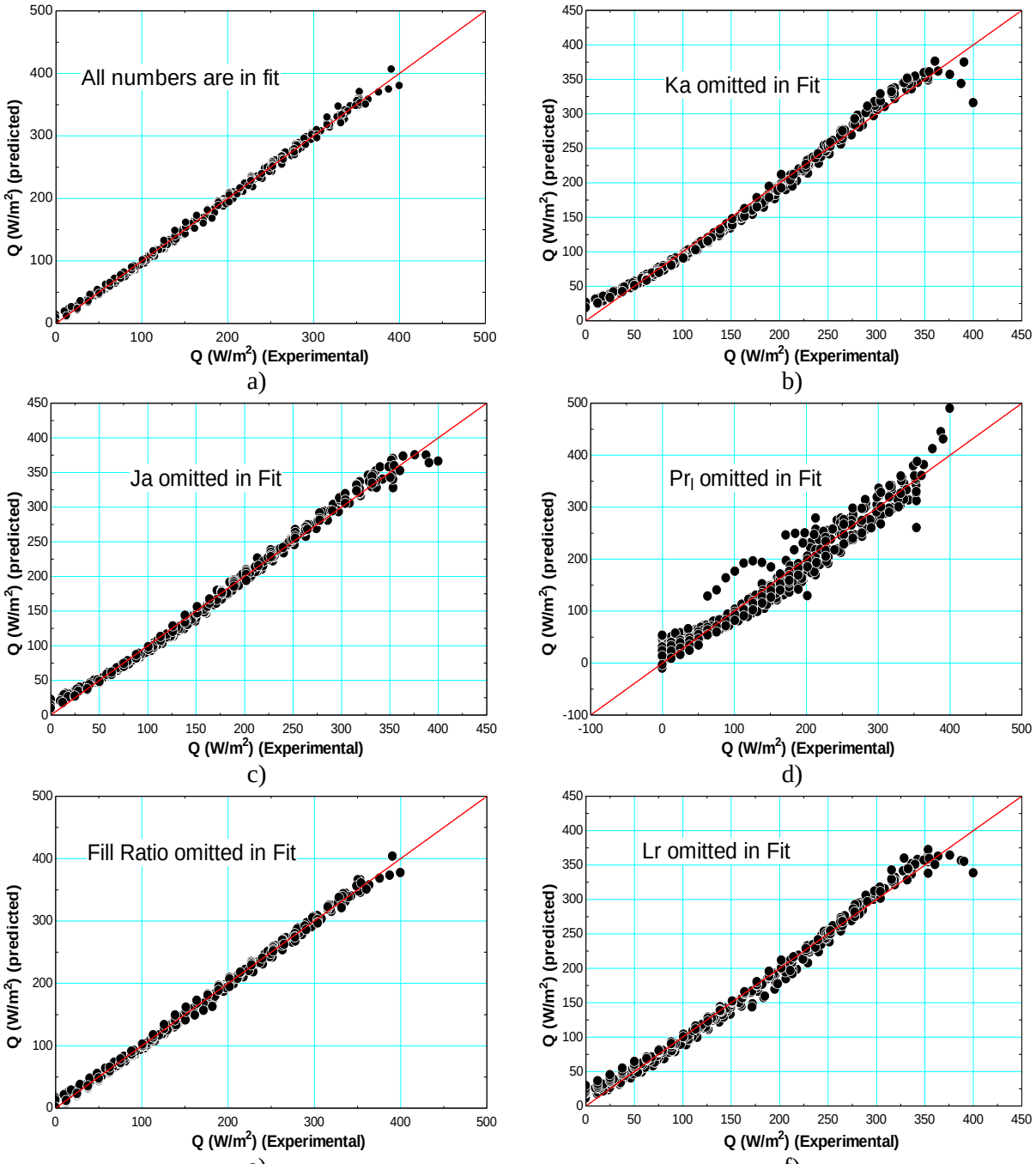

Figure 6-14: PHP1 regression fit, a) all variable in fit, b) omitting *Ka*, c) omittitng *Ja*, d) omitting Pr_l, e) omitting fill ratio, and f) omitting adiabatic ratio.

Table 6-6: Sensitivity analysis of PHP1 by omitting one of the 5 variables.

Case	R^2 (Coefficient of determination)	RMS Error (W/m^2)
All Numbers in fit	99.73 %	5.3569
K_a was omitted	98.88 %	10.825
J_a was omitted	99.29 %	8.611
Pr_l was omitted	93.90 %	25.300
f_{liq} was omitted	99.69 %	5.747
L_r was omitted	99.06 %	9.938

The second method for determining the sensitivity was to solve each variable using the nonlinear or linear regression. For example, if we want a correlation for the Karman number (K_a), we must use Q, J_a, f_{liq}, P_{rl} and L_r as the independent variables and use either equation 6-12 (nonlinear regression fit) or equation 6-15 (linear regression fit). The variables used for this analysis come from the case with the following configuration:

- PHP with 300 mm of adiabatic length.
- Optimal initial fill ratio of 70 %.

Figure 6-15-a shows the predicted K_a number using equation 6-12, where the x-axis shows the predicted value and the y-axis shows the real value. Note, that there is a slope of 1 for the K_a, P_{rl} and J_a. The adiabatic ratio L_r has a constant value of 0.0468 since the adiabatic length for this case is constant, the predicted values are on the same order of magnitude and close to the real value. However the fill ratio is over-predicted as high as 30 orders of magnitude. Similar results were obtained with the linear fit and it can be concluded that the fill ratio is not necessary. It seems that the fill ratio is a redundant variable and perhaps liquid effects are weighted more in the Karman, Jakob and Prandtl number.

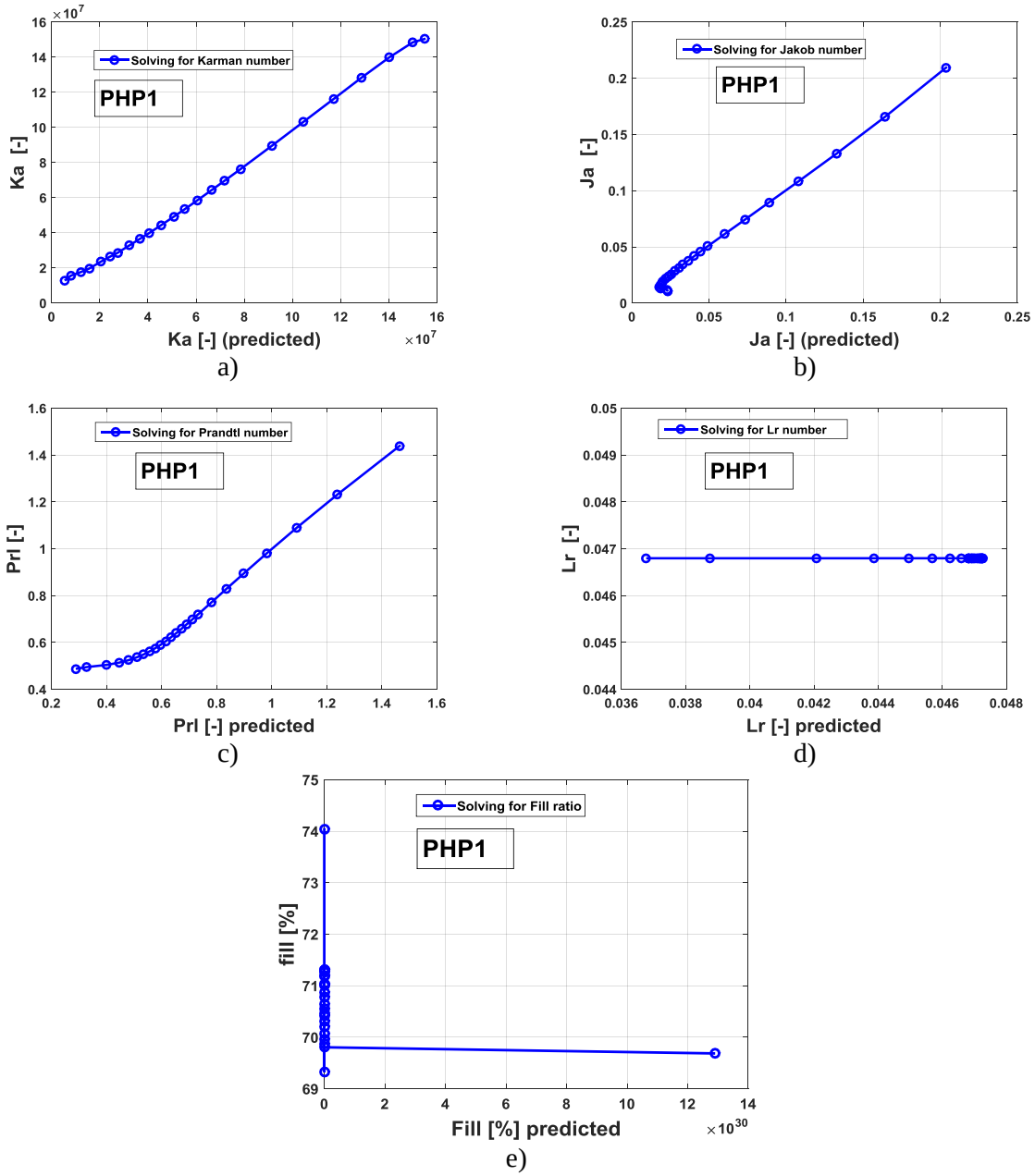

Figure 6-15: Solving one dimensionless number at a time a) Karman, b) Jacok, c) Prandtl, d) Lr and e) Fill ratio.

The third method to determine the sensitivity was to calculate a correlation for each variable in EES. For example, Figure 6-16, shows the linear regression correlation where the Karman number K_a was set as the dependent variable and Q, J_a, P_{rl}, f_{liq}, L_r and B_o where assumed to be the independent variables. Even though L_r just has two values since there are two adiabatic lengths (300 mm and 1000 mm), the predictions is close

to the real value. Notice throughout the figures that each correlation was accurately predicted except for the fill ratio. The fill ratio does not show a distinctive pattern. Recall that the fill ratio values used as the dependent variables are not the initial fill ratios, but are the fill ratios as the heat load is increased, this was described in section 5.3.3. Furthermore, this demonstrates the difficulty of predicting the fill ratio and the reason why it was neglected. Future work should include trying to combine the fill ratio with other dimensionless numbers or find a different correlation form.

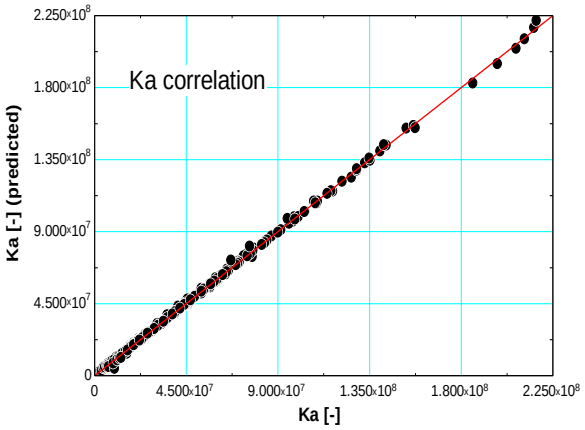

a)

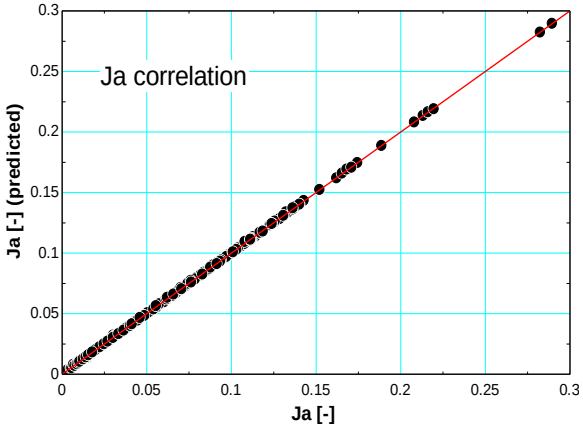

b)

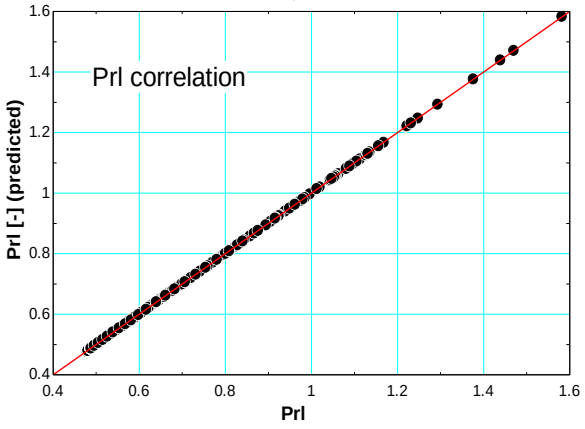

c)

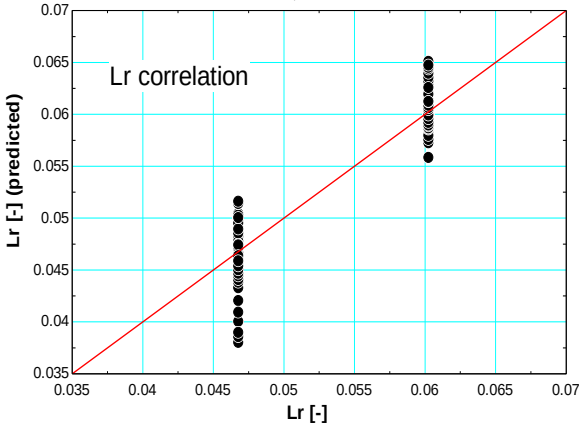

d)

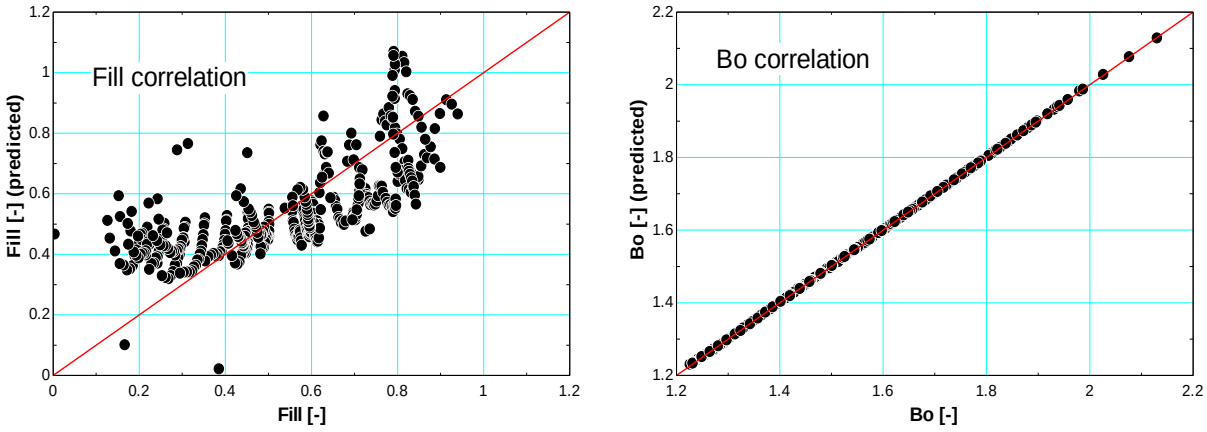

e) f)

Figure 6-16: Correlation example for each variable, a) Karman number, b) Jakob number, c) Prandtl number, d) adiabatic length ratio number, e) Fill ratio number, f) Bond number.

6.2.6 Applying regression fit to temperature controlled condenser section

In some cases the condenser section was maintained at constant temperature by installing a heater on the cryocooler, as mentioned in sections 5.3.5. However, the correlations were generated using the data when gradual and even heat loads were applied to the evaporator sections, resulting in different condenser temperature. For this reason, Figure 6-17-a shows a drastic difference between the predictive heat load and the experimental heat load. In addition, the cryocooler was maintained at 4.2 K at a total heat load of 0.55 W. Notice the last two points, these points show when the heat load on the cryocooler is zero and the total heat load of the evaporator sections are above 0.55 W. Therefore, these last two points are well predicted by the correlation since now it behaves under the same conditions: gradual even heat loads with different condenser temperatures. Another example is shown in Figure 6-17-b, here the condenser temperature is maintained at 3.8 K. A total of 0.35 watts is needed to maintain the condenser section at 3.8 K. Therefore, when the total heat load on the evaporator section exceeds 0.35 watts, the correlation will be accurate. The solution is to subtract the heat load of the cryocooler to the correlation. However, since there are three PHP sections the total heat dissipated by the heater on the cryocooler should be divided by three (as shown in Equation 6-16), since there are three PHP sections.

$$Q_{corr,new} = Q_{corr} - \frac{Q_{heater,cryo}}{N_{PHP}} \qquad 6\text{-}16$$

Where $Q_{corr,new}$ is the updated correction, Q_{corr} is the current correlation, $Q_{heater,cryo}$ is the total heat load applied to the cryocooler to maintain a constant condenser temperature, and finally N_{PHP} is the total number of PHP sections, which is 3. The updated correlation for constant condenser temperature is shown in Figure 6-18.

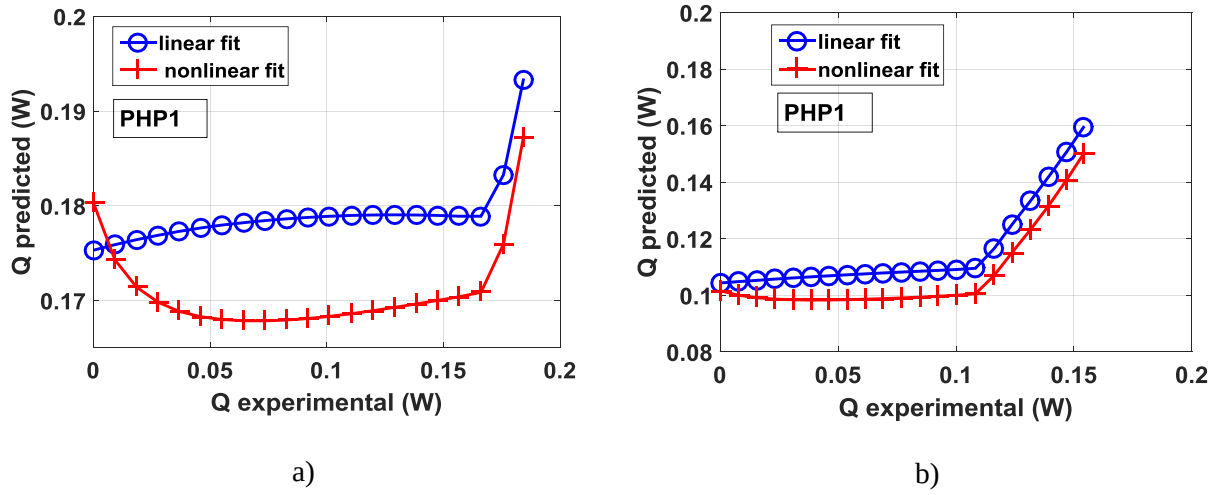

a) b)

Figure 6-17: Correlation at constant condenser temperature of a) 4.2 K and b) 3.8 K

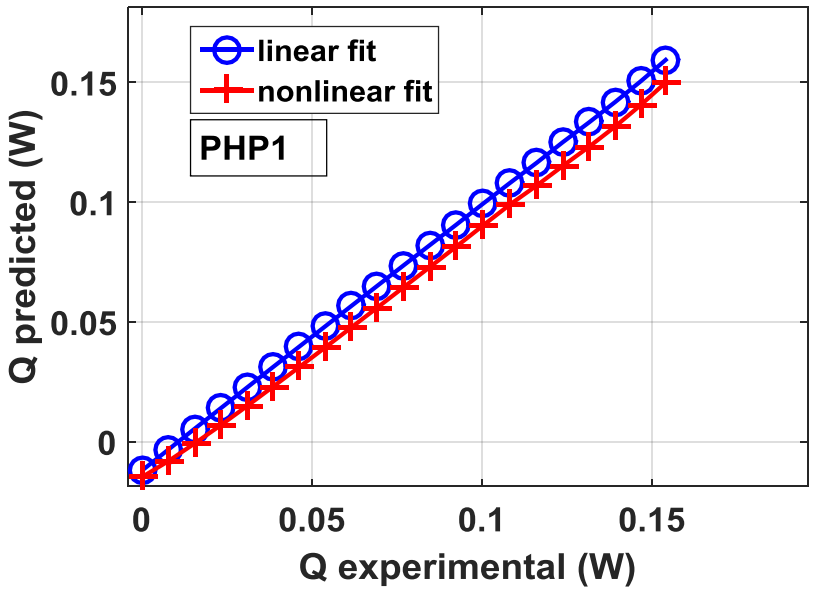

Figure 6-18: Updated correlation for constant condenser temperature

6.3 Modeling using spring mass damper system

6.3.1 Single Mass Damper system by Ma et al. and Borgmeyer

As shown in Figure 6-19, Ma et al. [2] and Borgmeyer [8] represented a pulsating heat pipe with no turns which consists of an evaporating section L_e, an adiabatic section L_a and a condenser section L_c. As heat is added to the evaporator section it will transfer through the walls of the pipe until the working fluid and evaporation will start occurring. Assuming the temperature of the evaporator section T_e is known then the evaporator pressure derived using the Clapeyron equation as shown below

$$p_e = p_o \exp\left(\frac{h_{fg}}{R}\frac{T_e - T_o}{T_e}\right) \quad 6\text{-}17$$

Where To and Po are the reference temperature and pressure, respectively.

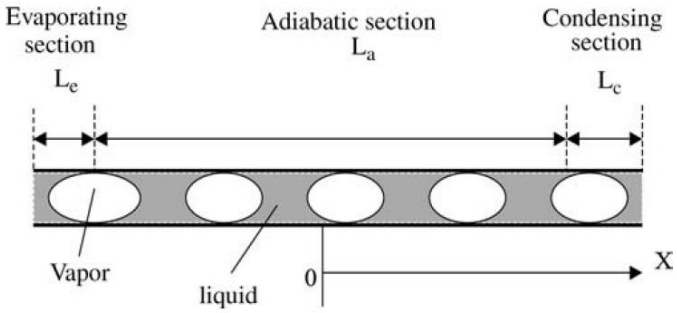

Figure 6-19: Schematic of a pulsating heat pipe Ma et al.

Similarly, the vapor temperature at the condenser temperature T_c can be calculated by equation 6-17, therefore the change of pressure between the evaporator and condenser section Δp can be calculated as the following

$$\Delta p = p_e - pc = p_c\left[\exp\left(\frac{h_{fg}}{R}\frac{T_e - T_c}{T_e}\right) - 1\right] \quad 6\text{-}18$$

Where T_o and P_o are assume to be T_c and P_c as the reference variables mentioned before, R is the gas constant, and h_{fg} is the latent heat of evaporation Equation 6-18 can be expanded using a Taylor series and simplifies to

$$\Delta p = \Delta T \frac{h_{fg}\rho_{v,c}}{T_e} \quad \text{6-19}$$

Where $\rho_{v,c}$ is the density of vapor in the condenser section, ΔT is the temperature difference from the evaporator to the condenser $\Delta T = Te - Tc$. Since the PHP exhibits an oscillatory motion due to the volumetric contraction and expansion, the condenser and evaporator temperature T_e and T_c will also vary in this manner. Figure 6-20 is a representation of these temperatures in a sine waveform while Figure 6-21 represents the temperature difference ΔT resulting in new sine wave at frequency ω with a maximum and minimum temperature difference ΔT_{max} and ΔT_{max} respectively. Hence ΔT can be written as

$$\Delta T = B + A\sin(\omega t)$$

$$B = \frac{(\Delta T_{max} + \Delta T_{min})}{2}$$

$$A = \frac{(\Delta T_{max} - \Delta T_{min})}{2} \quad \text{6-20}$$

Finally

$$\Delta T = \frac{\Delta T_{max} + T_{min}}{2} + \frac{\Delta T_{max} - \Delta T_{min}}{2}\sin(\omega t)$$

Where B represents the offset of the waveform and A represents its amplitude.

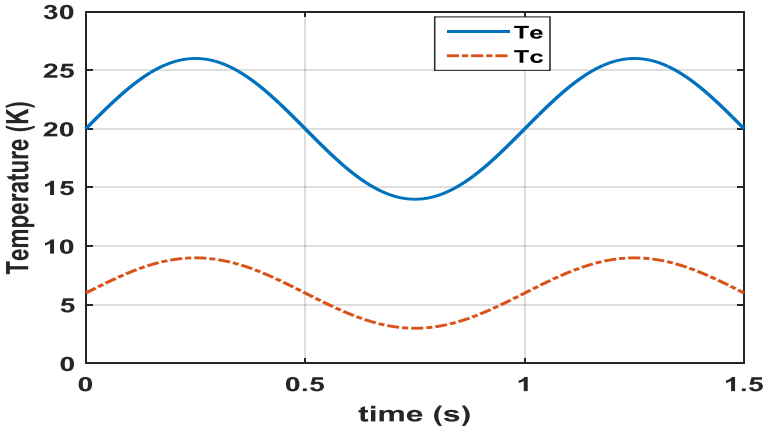

Figure 6-20: Vapor of condenser and evaporator versus time

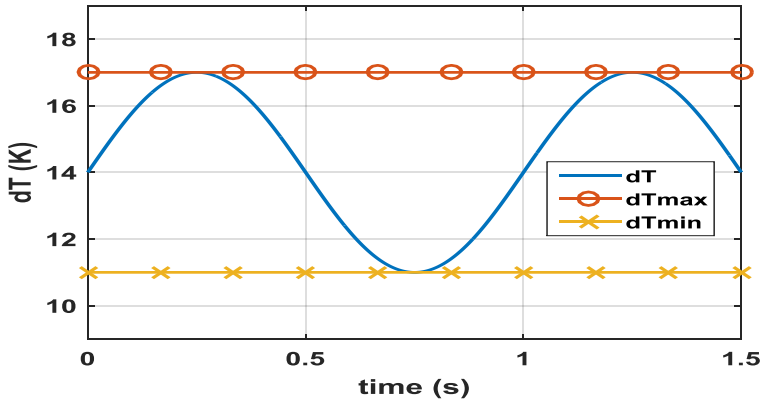

Figure 6-21: Temperature difference

By combining equations 6-19 and 6-20 the driving force F_d can be calculated as

$$F_d \Delta p = \Delta p A_c = \left(\frac{h_{fg}\rho_{v,c}}{T_e}\right)\left[\frac{T_{max}+T_{min}}{2}+\frac{(T_{max}-T_{min}}{2}\right]\sin(\omega t) \qquad 6\text{-}21$$

In addition to the driving force F_d, two more kinds of forces have to be considered:

- And the frictional shear stress F_f caused by the liquid slugs and vapor plugs.
- The elastic restoring force F_e which is represented as the spring effect produced by the vapor slugs as they contract and expand.

Borgmeyer [8] derives the restoring force F_f as

$$F_f = \Delta p_f A_c = \left[\left(f_l \cdot R_{e,l}\right)\left(\frac{\mu_l L_l}{2D_H^2}\right)+\left(f_l \cdot R_{e,v}\right)\left(\frac{\mu_v L_v}{2D_H^2}\right)\right]A_c \frac{dx}{dt} \qquad 6\text{-}22$$

Where f_l and f_v are the fanning friction coefficient, $R_{e,l}$ and $R_{e,v}$ are the Reynold number for liquid and vapor respectively. L_l and L_v are the total lengths for the liquid slugs and vapor plugs respectively. Also u_l and u_v are the liquid and vapor dynamic viscosity terms respectively. D_h is the hydraulic diameter. The cross-sectional area is A_c and can be written as

$$A_c = \frac{PD_H}{4} \qquad 6\text{-}23$$

Where P is the perimeter

$$P = \pi D_H$$

Combining equations 6-22 and 6-23 and assuming that a laminar flow, *f= 64/Re*, the frictional force can be rewritten as

$$F_f = \frac{8P}{D_H}(\mu_l L_l + \mu_v L_v)\frac{dx}{dt} \quad \text{6-24}$$

It is important to note that the fill ratio ϕ can be calculated as

$$\phi = \frac{V_l}{V} \quad \text{6-25}$$

Where V_l is the total volume that is liquid and V is the total volume of the PHP. Therefore L_l and L_v can be solved using the following equations

$$V_l = L_l A_c = \phi V$$
$$L_l = \phi \frac{V}{A_c} \quad \text{6-26}$$

$$V_v = L_v A_c = (1-\phi)V$$
$$L_l = (1-\phi)\frac{V}{A_c} \quad \text{6-27}$$

Where V is calculated as

$$L_t = L_a + L_e + L_c$$
$$\text{V} = L_t A_c \quad \text{6-28}$$

The elastic restoring force F_e of the vapor volume can be calculated using the following

$$\Delta p_v = \frac{\rho_v RT}{L_v} x \quad \text{6-29}$$

Where Δp_v is the pressure variation at the time interval Δt. Hence

$$F_e = \Delta p_v A_c = \frac{A_c \rho_v RT}{L_v} x \quad \text{6-30}$$

Summing all the forces [8] results in

$$\sum F = m\frac{d^2x}{dt^2} = -F_f - F_e + F_d \quad \text{6-31}$$

$$(\rho_l L_l + \rho_v L_v) A_c \frac{d^2x}{dt^2} + \left[(f_l \cdot R_{e,l}) \left(\frac{\mu_l L_l}{2D_H^2} \right) + (f_l \cdot R_{e,v}) \left(\frac{\mu_v L_v}{2D_H^2} \right) \right] A_c \frac{dx}{dt} + \frac{A_c \rho_v RT}{L_v} x = \left(\frac{h_{fg} \rho_{v,c}}{T_e} \right) \left[\frac{T_{max} + T_{min}}{2} + \frac{(T_{max} - T_{min}}{2} \right] \sin(\omega t)$$

Equation **6-31** is has the similar form to a spring mass damper system such as

$$\frac{d^2x}{dt^2} + \frac{c}{m}\frac{dx}{dt} + \frac{k}{m}x = \frac{B}{m}\sin(wt) \quad \text{6-32}$$

Where

$$m = (\rho_l L_l + \rho_v L_v) A_c \quad \text{6-33}$$

$$c = \left[(f_l \cdot R_{e,l}) \left(\frac{\mu_l L_l}{2D_H^2} \right) + (f_l \cdot R_{e,v}) \left(\frac{\mu_v L_v}{2D_H^2} \right) \right] A_c \quad \text{6-34}$$

$$k = \frac{A_c \rho_v RT}{L_v} \quad \text{6-35}$$

$$B = \left(\frac{h_{fg} \rho_{v,c}}{T_e} \right) \left[\frac{T_{max} + T_{min}}{2} + \frac{(T_{max} - T_{min}}{2} \right] \quad \text{6-36}$$

It is important to note that this model just uses the momentum equation and lacks the usage of the energy equation. Therefore the vapor's spring coefficient *k* will increase and exert a higher pressure/force on the adjacent liquid slugs as the vapor length L_v decreases. The damping natural frequency and the damping ratio ξ can be written as

$$\omega_o = \sqrt{\frac{k}{m}} = \sqrt{\frac{A_c \rho_v RT}{m L_v}} \quad \text{6-37}$$

$$\xi = \frac{c}{2m\omega_o} \quad \text{6-38}$$

Ma et al. [2] assumes that there is initially no oscillatory movement in the PHP, and therefore defines the following initial conditions

$$x = 0 \; and \; \frac{dx}{dt} = 0, at \; time \; t = 0 \tag{6-39}$$

Therefore the ODE shown in 6-32 was solved as

$$x(t) = \frac{B}{m}\left[\frac{\left(\sqrt{\xi^2-1}\right)\sin(\omega t) - e^{-\xi\omega t}\sinh\left(\omega t\sqrt{\xi^2-1}\right)}{2\xi\omega^2\sqrt{\xi^2-1}} + \frac{1 - e^{-\xi\omega t}\left[\cosh\left(\omega t\sqrt{\xi^2-1}\right) + \frac{\xi\sinh(\omega t\sqrt{\xi^2-1})}{\sqrt{\xi^2-1}}\right]}{\omega^2}\right] \tag{6-40}$$

6.3.2 Multiple spring damper model

Gürsel et al. [3] developed a spring damper model but using multiple spring mass damper systems as shown in Figure 6-22. Where in Figure 6-22-a, the black and white portions represent the liquid slugs and vapor plugs respectively. And the blue, yellow and red colors represents the condenser, adiabatic and evaporator sections. Figure 6-22-b shows a representation of the forces presents, where vapor plugs are represented by non-liner springs, the liquids slugs are represented by masses and the friction and capillary forces are represented by non-linear dampers.

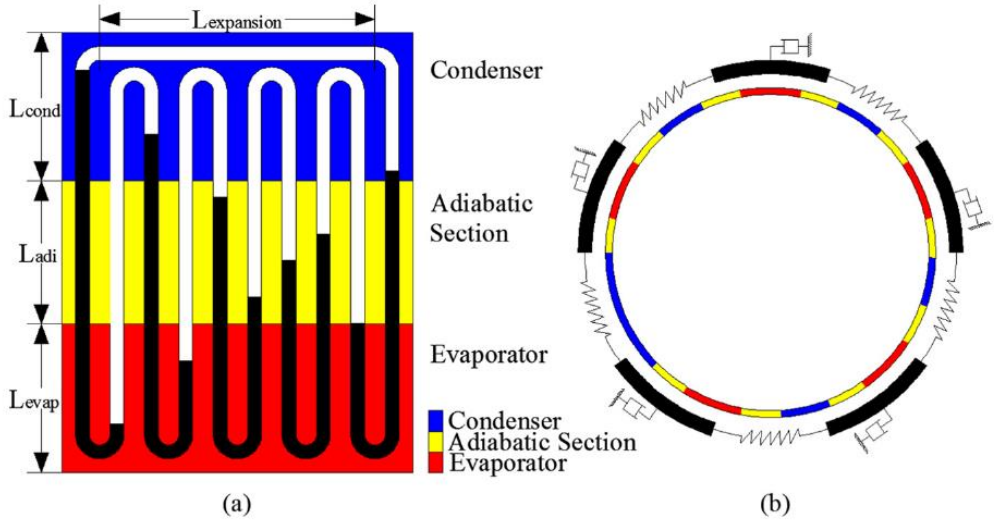

Figure 6-22: a) Five turns schematic of a PHP, b) Spring mass damper representation of the PHP [3]

The force balance of the multiple spring mass damper system can therefore be written as

$$m_{l,i}\ddot{x}_i = F_{pres,i} + F_{fric,i} + F_{cap,i} + F_{grav,i} \quad 6\text{-}41$$

Where $m_{l,i}\ddot{x}_i$, $F_{press,i}$, $F_{fric,i}$, $F_{cap,i}$ and $F_{grav,i}$ are the mass and acceleration, the effective pressure force over the liquid slug, the friction force, the effective capillary force and the gravitational force acting on the i^{th} liquid slug respectively. The effective pressure force over the liquid slug is calculated as

$$F_{pres,i} = A_c(P_{v,left} - P_{v,right}) \quad 6\text{-}42$$

Where A_c is the cross-sectional of the inner diameter of the capillary tubing. $P_{v,left}$ and $P_{v,right}$ are the left and right adjacent vapor plugs acting on the i^{th} plug. Gürsel et al. [3] assume that the vapor behaves as an ideal gas.

The friction force produced by the liquid slug in a laminar flow is calculated using

$$F_{fric,i} = 2\mu_l \pi L_i \dot{x}_i \quad 6\text{-}43$$

Where μ_l is the dynamic viscosity of liquid, $L_{l,i}$ and x_i are the length and velocity of the i^{th} slug respectively [3]. Note: equation 6-43 is mistakenly written in [3], should be written as

$$F_{fric,i} = 8\mu_l \pi L_i \dot{x}_i \quad 6\text{-}44$$

The capillary force on the liquid slug can be calculated using

$$F_{cap,i} = \left(\sigma_i \frac{2}{D}\cos\theta_{d,right} - \sigma_i \frac{2}{D}\cos\theta_{d,left}\right) \quad 6\text{-}45$$

Where σ_i, D, $\theta_{d,right}$ and $\theta_{d,right}$ are the surface tension, tube diameter, and the left and right dynamic contact angle acting on the i^{th} slug. Equations regarding the dynamic contact angle can be found in [5].

The gravitational force can be calculated using

$$F_{grav,i} = m_{l,i} g \sin\alpha_{inc} \quad 6\text{-}46$$

Where m_{li}, g and α_{inc} are the mass of the i^{th} liquid slug, gravitational acceleration and the inclination angle of the PHP.

Gürsel et al. [3] also included heat transfer to the model. Here he assumes a constant temperature within a liquid slug. Hence, the changes in temperature of a vapor plug or a liquid slug are calculated using

$$\frac{dT_i}{dt} = \frac{\dot{Q}_i}{m_i C_p} \quad 6\text{-}47$$

Where the m_i, cp, Ti are the mass, specific heat and temperature of the liquid slug or vapor plug. The heat input $\dot{Q}_i$ added to the mass m_i located at the evaporator section. Therefore the sum of $\dot{Q}_i$ is equal to the total heat input $\dot{Q}$ and the heat transfer to the liquid slugs and vapor slug can be calculated using

$$\dot{Q} = \sum \dot{Q}_i$$

$$\dot{Q}_l = \frac{h_l A_l}{h_l A_l + h_v A_v} \dot{Q} \quad 6\text{-}48$$

$$\dot{Q}_l = \frac{h_l A_l}{h_l A_l + h_v A_v} \dot{Q}$$

Where h, A are the heat transfer coefficients of the liquid (l) or vapor (v), the surface area of the liquid and vapor slug inside the evaporator section. Gürsel et al. noted that these equations are valid if the temperature of the liquid and vapor in the evaporator section are equal. In addition, in order to calculate the heat transfer coefficients it was assumed tht a Nusselt number for constant heat load at the evaporator section was Nu = 4.36 and was Nu = 3.66 for constant temperature at the condenser section. Therefore the heat transfer $\dot{Q}_{out}$ of the condenser section can be calculated using the following equation

$$\dot{Q}_{out,i} = h_i A_{s,i} (T_i - T_{cond}) \quad 6\text{-}49$$

Where $A_{s,i}$ is the surface area of the liquid slug or vapor plug inside the condenser section and T_{cond} is the temperature of the condenser section. If the temperature T_i of a liquid slug is above the saturation temperature T_{sat}, then the liquid will evaporate, if the temperature T_i of a vapor plug is below T_{sat} then the vapor will condense. Hence the saturation temperature can be calculated using the Antoine equation [6] the following equation

$$T_{sat} = \frac{\beta_1}{\beta_2 - \log(P_v)} - \beta_3 \quad 6\text{-}50$$

Where $\beta 1$, $\beta 2$ and $\beta 3$ are constant for a specific fluid. It is important to note that the Antoine equation is derived by the Clausius–Clapeyron relation and the vapor pressure P_v is in units of mmHg. The evaporation and condensation mass flow rates are calculated using

$$\dot{m} = \frac{Q_{l,v}}{h_{fg}} \qquad 6\text{-}51$$

Where h_{fg} is the latent heat of evaporation and $Q_{l,v}$ is calculated using equation 6-48. This model was solved using Matlab Simulink in order to solve all systems of equations.

Figure Figure 6-23 and Figure 6-24 show the experimental results obtained by Mameli et al. [7] and Khandekar et al. [4] respectively, and are compared to the Gürsel et al. model [3]. Figure Figure 6-23, is based on an ethanol PHP with 65 % filling ratio while Figure 6-24 is based on a water PHP at a filling ratio of 60 %.

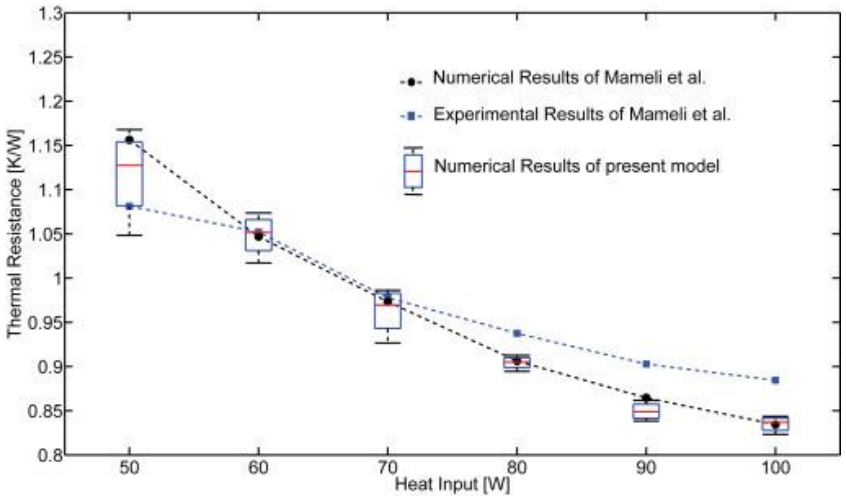

Figure 6-23: Numerical and experimental results for an ethanol based PHP at a filling ration of 65 %

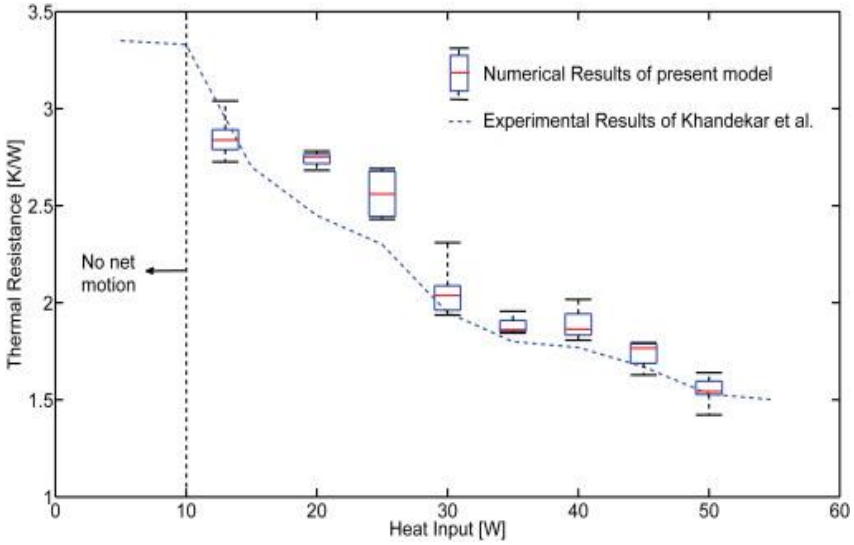

Figure 6-24: Numerical model of Gürsel et al. [3] and Experimental results of Khandekar et al. [4] for a water based PHP with a filling ratio of 60 %.

6.3.3 Helium based PHP model

The momentum equations used by Gursel et al. were used as a starting point to develop a multiple spring mass damper system in Matlab®. Some major differences with Gursel's developed model are

- The code was modeled and programmed in Matlab scripts and functions. Unlike Gursel et al., that developed their model using Matlab's toolbox Simulink.
- Energy balances on the liquid slug, vapor plug and capillary tubing were added to the model.
- The equation of state of helium was incorporated to the code.

The Matlab code is complex but the following diagram illustrates the functions and steps required to develop this code:

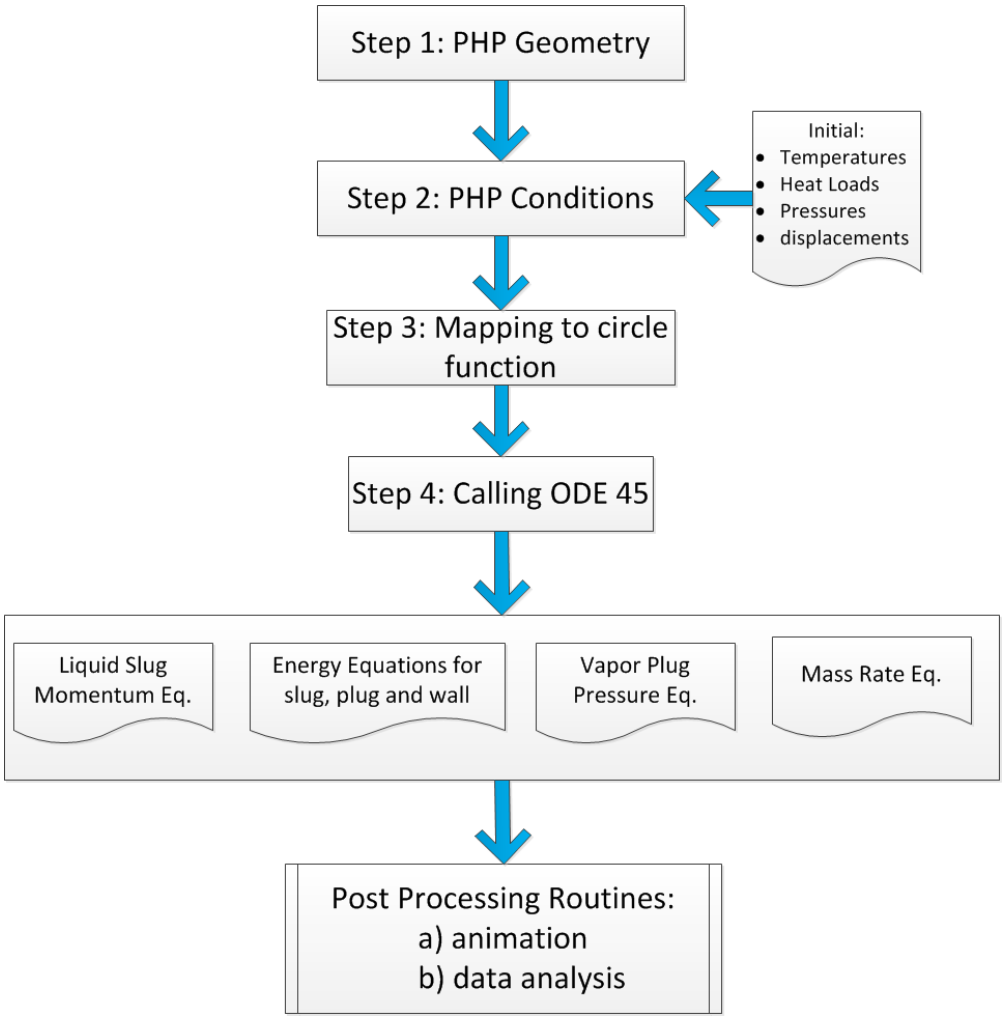

Figure 6-25: Flow chart for model

6.3.4 Step 1: Developing a function for the geometry of the PHP

Figure 6-26 shows the centerline of the PHP, it can be observed that that the geometry is composed of horizontal, vertical and semicircular lines. The inputs required for such a geometry are:

- L_c: condenser length
- L_a: adiabatic length
- L_e: evaporator length
- r_{bend}: bend radius of semicircles.
- N: number of parallel capillary tubes.

- *dh*: step size increment between points/nodes.

It is extremely important to create these lines subsequently, that is the last point of the first line has to be the initial point of the second and so on. For example, a vertical line can be constructed using the following code:

```
L1Y = 0:dh:La;          % create a vector from 0 to La with an increment of dh
L1X = zeros(size(L1)); % vertical line will pass through x = 0.
```

All the lines should be merged in one single matrix **M** where the first column represents the X-coordinates and the second column represents the Y-coordinates. It is important to mention that the matrix will have repeated values at the initial and final points. Therefore before merging, these repeated points should be deleted.

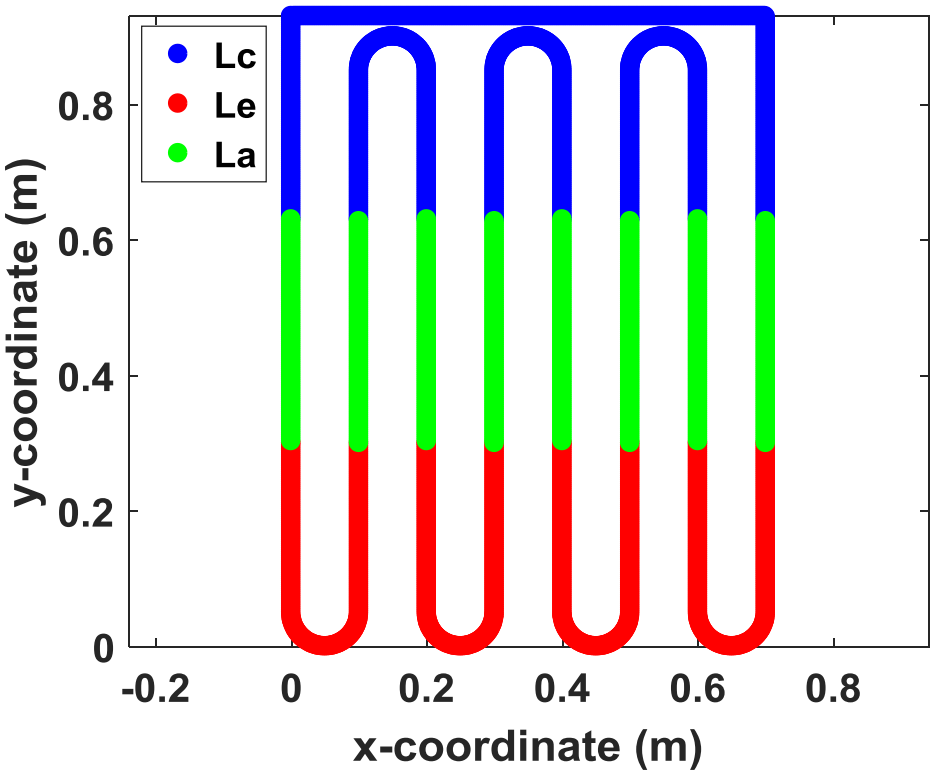

Figure 6-26: PHP geometry, created in Matlab

6.3.5 Step 2: Mapping PHP geometry to a Circular path

In Matlab, function ODE45 is one of many solvers for ordinary differential equations and was chosen to solve the momentum and energy equations that models the PHP system. It is important to note that the spring mass damper system is a method to simulate the behavior of a PHP; therefore the main goal of performing such an analysis is to develop a simple model that captures the important physical behavior rather than using CFD software. However, the PHP geometry has a 2-D geometry (cartesian coordinate system), but can be easily be manipulated if mapped to a polar coordinate system. The trick to using ODE45 to solve the equations is to map the 2-D geometry to a circular form, in order to convert it to a 1-D geometry, as shown in Figure 6-27-a and b. Where the arc length L_{arc} of each point will be used as the dimensional parameter for ODE45. In addition, each point/node of the PHP line must be referenced to point 1 (*P1*). The importance of referencing all the meshing points/nodes to *P1* is that each point will have a unique arc length L_{arc}, which is easy to calculate using matrix **M**. In addition the radius of the circular PHP (*rcir*) can be calculated by dividing the total length of the PHP (L_{PHP}) to 2π.

$$rcir = \frac{L_{PHP}}{2\pi} \tag{6-52}$$

Furthermore, the radius *rcir* can now be used to calculated the rest of the points in the circular map by calculating their respective angle θ_i (in radians)

$$\theta_i = \frac{L_{arc,i}}{rcir} \tag{6-53}$$

Where the index *i* represents a specific point/node. Now matrix **M** can be updated to include a third and fourth column which represent the angle θ_i and arc length $L_{arc,i}$ for each point, respectively. The matrix **M** enables one to map the PHP from a x-y coordinate system to a polar coordinate system and vice versa. Recall that the polar coordinate system will have one spatial coordinate unit (L_{arc}) in meters, while the second coordinate (θ_i) is in radians. For example, Figure 6-27-a represents a PHP with a total length of

L_{PHP} = 8.3596 m and a spatial step size of d_h = 0.1 mm, which results in a total of number of nodes of N_{nodes} = 83596. Note that the figure is not up to scale and is just a general representation.

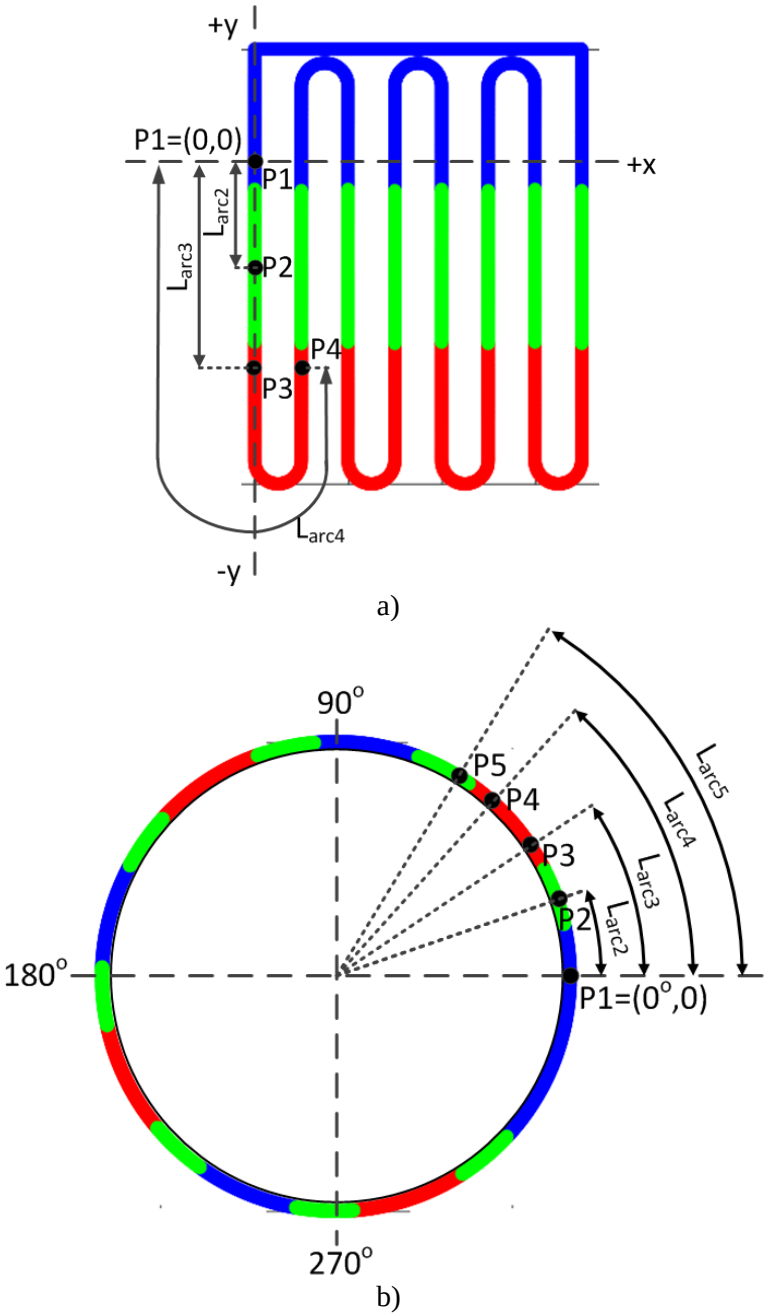

Figure 6-27: 2-D pathline to circular pathline

The next step requires to place the liquid slugs along the 2-D geometry pathline. For example, Figure 6-28 represents 32 liquid slugs equally spaced with an initial length per slug of L_{slug} = 10 cm.

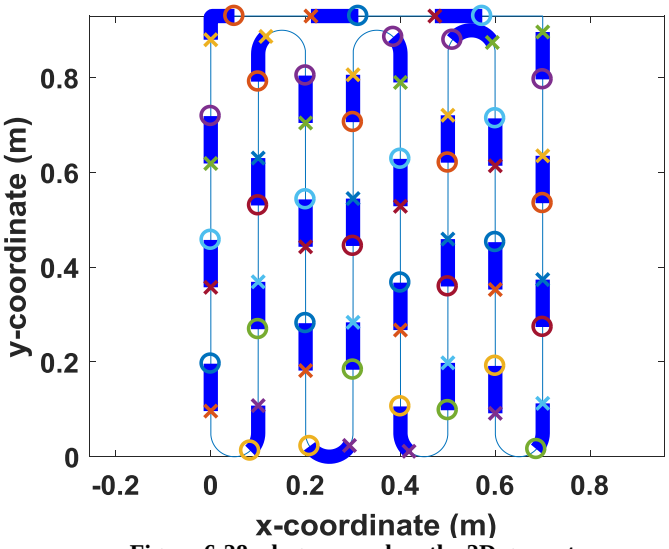

Figure 6-28: slug mapped on the 2D geometry

The "X" and "O" markers in Figure 6-28, represent the sides/edges of the slugs, which are important to observe when debugging, applying a force balance, and assuring that the slugs do not intersect each other. It is important to note that ODE45 is used to calculate the center nodes C_i of each slug as displacement, and these center nodes are also referenced with respect to point P1. In other words, the center node C_i is an arc length or displacement unit. For this reason, an algorithm using matrix **M** was used to position the liquid slugs throughout any geometry. For example, as illustrated in Figure 6-29, if one of the slugs is positioned at arc length C_j = 1 m, then the mapping algorithm will find the two adjacent arc lengths ($L_{arc,i}$,$L_{arc,i+1}$) in matrix **M** and their respective x-y points (x_i, y_i) (x_{i+1}, y_{i+1}). The index *j* represents the respective slug number being analyzed, then indexes *i* and *i+1* represent the left and right adjacent points, respectively.

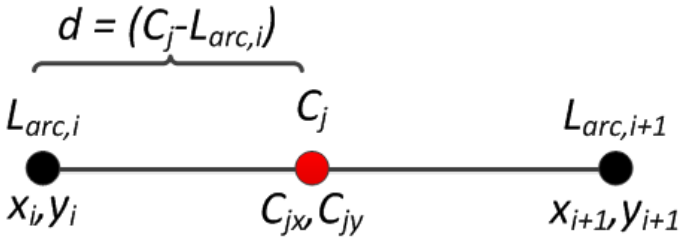

Figure 6-29: Example for mapping the position of center node C_j in a 2D geometry

Where the variable d is the distance between point C_j and $L_{arc,i}$. Hence, the center arc length C_j can be mapped in a x-y coordinate (C_{jx},C_{jy}) using the following equations.

$$d = \left(C_j - L_{arc,i}\right) \tag{6-54}$$

$$m = \frac{y_{i+1} - y_i}{x_{i+1} - x_i} \tag{6-55}$$

Where m is the slope between the adjacent points

$$m = \frac{y_{i+1} - y_i}{x_{i+1} - x_i} \tag{6-56}$$

$$\theta_c = \tan^{-1}(m) \tag{6-57}$$

Finally, using simple trigonometry, the center node, in x-y coordinate, can be calculated as

$$C_{jx} = d\cos(\theta_c) + x_i \quad \text{and} \quad C_{jy} = d\sin(\theta_c) + y_i \tag{6-58}$$

6.3.6 Step 3: PHP's initial conditions

In order to set initial conditions, we must first know what we want ODE45 to output from to the ordinary differential equations implemented. As shown in Figure 6-30, the momentum equation will solve the slug node's center displacement (C_j) and velocity (V_j). The energy equation will solve for the liquid slug temperature (T_{slug}), vapor plug temperature (T_{vapor}) and capillary tubing's wall temperature T_{wall}. The liquid and vapor masses will be solved using the latent heat and the heat transfer to the slug and plug masses.

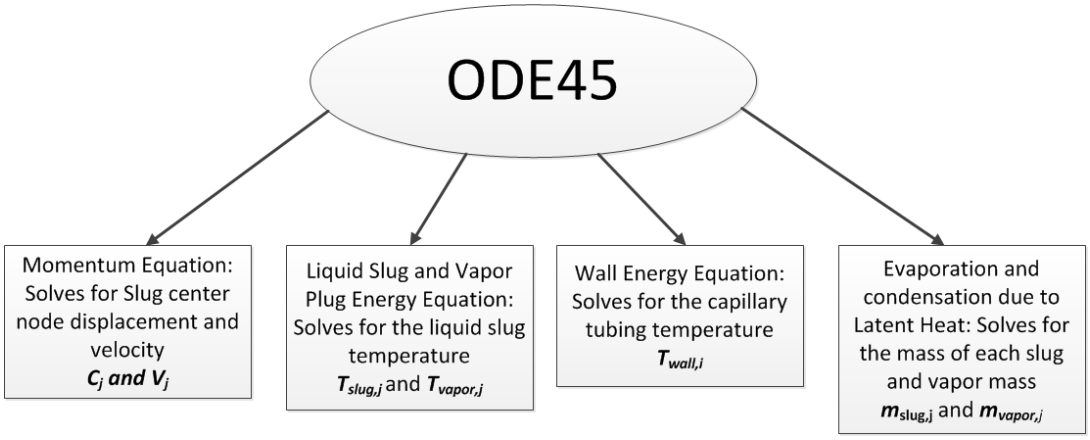

Figure 6-30: ODE45 outputs

ODE45 requires an input of initial conditions for the variables mentioned in Figure 6-30 and are described in the following

- C_j variables were initial set to the center location of the slugs before running ODE45. While the velocity variables V_j were set to zero.
- T_{slug}, and T_{vapor} were set to 3 K. this is the temperature that the cryocooler reaches at a zero heat load.
- The initial wall temperature T_{wall} of the capillary tubing was set to 3 K. However, the condenser wall temperature was held constant at the specific temperature consistent with the cryocooler's heat load curve.
- The initial masses, were calculated using the saturation densities at 3 K and the given initial slug length L_{slug} mentioned in Figure 6-28.

Other input variables can be added to ODE45 and not be output variables. Such a variable is the evaporator heat load ($\dot{Q}_{evap}$), condenser heat load ($\dot{Q}_{cond}$) if applicable, and the adiabatic heat load ($\dot{Q}_{ad}$) if applicable. It is important to note that the heat load on the adiabatic section is not required to be exactly zero, but if needed a heat load could be added; however, the adiabatic heat load was set to zero for this model. The evaporator heat load $\dot{Q}_{evap}$ serves as the heat source. The temperature of the wall (T_{wall}) in the condenser section was held constant, as mentioned before. However, the model can be modified to use constant heat

load instead of constant temperature. As mentioned before the PHP's position points/nodes are represented as $L_{arc,i}$; however these nodes contain additional information such as wall temperature T_{wall} and heat load values $\dot{Q}_{php}$. Since, certain sections contain different temperature and heat loads, indexing is very important to specify these values. For example, the following Matlab code is used to find the row indexes of matrix **M** that are located in the condenser, evaporator and adiabatic section and creates a heat load distribution array.

```
%% Finding the condenser sections
yy = M(:,4);                    % get locations in y-coordinates of each node
ycond = Le+La;                  % condenser location lower limit
icond = find(yy>=ycond);        % get condenser indexes and save them in icond


%% Finding the evaporator section indexes
yevap = Le;                     % evaporator location lower limit
ievap = find(yy<=yevap);        % get condenser indexes and save them in ivap

%% Finding the adiabatic section indexes
iad   = find(yy>yevap & yy<ycond); % get adiabatitc indexes: iad

%% Heat load distribution on PHP
Qphp   = zeros(size(yy));       % create a heat load vector.
Qphp(icond) = Qcond;            % set condenser heat load (W), Qcond = 0
Qphp(ievap) = Qevap;            % set evaporator heat load (W)
Qphp(iad)   = Qad;              % set adiabatic heat load (W), Qad = 0
```

As mentioned at the beginning of section 6.3.2, the momentum equation acting on each liquid slug can be expressed as:

$$m_{l,j}\ddot{x}_j = F_{pres,j} + F_{fric,j} + F_{cap,j} + F_{grav,j} \qquad 6\text{-}59$$

Where now j is the index of the slug used.

It is important to mention that ODE45 calls a main function that contains the momentum and energy equations. Figure 6-31 represents two cases where the liquid slug could be located. For case "a", the liquid slug will be located in vertical position. However for case "b", the liquid slug could be partially or completely positioned inside the bend of the capillary tubing. For this reason, the height difference of the slug (Δy) is calculated in the x-y coordinate system in order to solve for the gravitational force

$$\Delta y = y_2 - y_1 \tag{6-60}$$

and

$$F_{grav,j} = -\rho_{l,j} g A_c \Delta y = \rho_{l,j} g A_c (y_1 - y_2) \tag{6-61}$$

Where g is 9.81 m/s^2 and $\rho_{l,j}$ is the density of the j^{th} liquid slug. It is important to note that the mapping algorithm will be required to solve for Δy, as mentioned previously.

The slugs are assumed to be incompressible, therefore the velocities at point 1 and point 2 are equal ($V_1 = V_2$). The force due to the vapor plugs $F_{pres,j}$, similar to equation 6-42, can be written as:

$$F_{pres,j} = A_c (P_{v,1} - P_{v,2}) \tag{6-62}$$

Where the pressures at point 1 and point 2 of Figure 5-76 are respectively $P_{v,1}$and $P_{v,2}$. Finally, the friction force can also be rewritten as

$$F_{fric,j} = -2\mu_{l,j} \pi L_{slug,j} \dot{x}_j = -2\mu_{l,j} \pi L_{slug,j} V_j \tag{6-63}$$

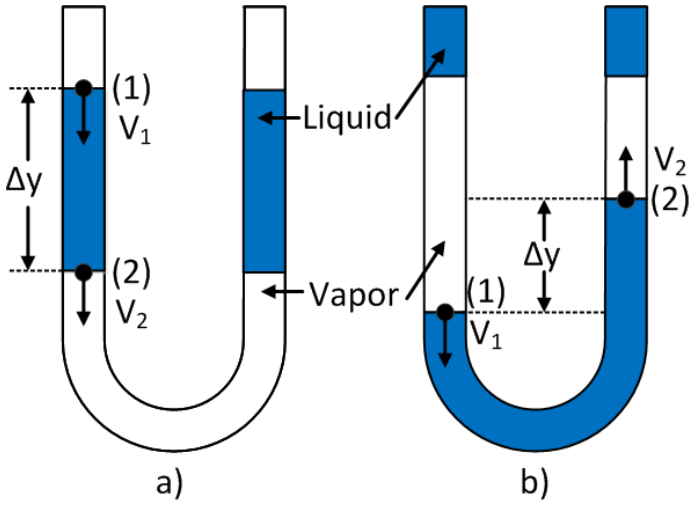

Figure 6-31: Slug position cases in U-turn, a) vertical location, b) bend location

In addition, the following assumptions regarding the slug's flow direction were made:

- If direction of slug moves counterclockwise, then slug's velocity is positive, $V_j > 0$.
- If direction of slug moves clockwise, then slug's velocity is negative, $V_j < 0$.

Continuing with Figure 6-31, the liquid slug will have a contact angle (θ_1) at point 1 and another contact angle (θ_2) at point 2; therefore equation 6-64 can be rewritten as

$$F_{cap,j} = A_c\left(\sigma_j \frac{2}{D}\cos\theta_1 - \sigma_j \frac{2}{D}\cos\theta_2\right) \quad 6\text{-}64$$

As described by Zhang et al. [9], the contact angles at two ends depend of the direction of the slug movement. Hence, depending on the flow direction, the force balance can be rewritten as

$$m_{l,j}\ddot{x}_j = \begin{cases} F_{pres,j} + F_{fric,j} + F_{cap,j} + F_{grav,j} & if\ V_j \geq 0 \\ F_{pres,j} + F_{fric,j} - F_{cap,j} + F_{grav,j} & if\ V_j < 0 \end{cases} \quad 6\text{-}65$$

6.3.7 Step 4: Calculating the pressure of the vapor plug

In contrast to Gursel et al. the equation of state of helium was coded in Matlab in order to obtain thermodynamic properties functions for enthalpy, internal energy, saturation temperature and pressure, density, compressibility factor and more. These properties were obtain using the equation of state developed by Diego Orlando [10]. Furthermore, the ideal gas law for helium cannot be used as these temperature ranges due to its inaccurate predictions; therefore the compressibility factor is crucial for predicting the behavior of a real gas. The vapor pressure P_j of slug j was calculated using

$$P_j = Z_j \rho_{v,j} R_{gas} \bar{T}_{v,j} \quad 6\text{-}66$$

Where j represents the index of the vapor plug being analyzed, Z is the compressibility factor, ρ_v is the density of the vapor plug and R_{gas} in the gas constant of helium. It is important to note that the vapor plugs and liquid slugs are subdivided in smaller control volumes when calculating their temperature distribution using the equations of energy (which will be explained further); therefore $\bar{T}_{v,j}$ is the average temperature of the j^{th} slug. This assumption of using average temperature was made in order to simplify the problem and to lower the computational time.

Figure 6-32 shows an example of two slugs moving in opposite direction or in the same direction, they will be compressing or expanding the vapor plug. In addition, the vapor plug will be contracting or expanding due to its change in temperature. These two factors are linked in equation 6-66 (P_j)

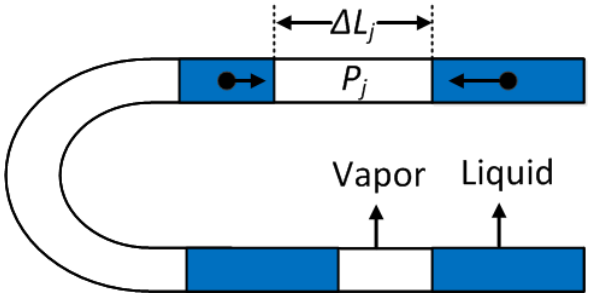

Figure 6-32: Illustration of length change of vapor slug

For example, the vapor plug's density can be calculated as

$$\rho_{v,j} = \frac{m_{v,j}}{Vol_{v,j}} \tag{6-67}$$

Where $m_{v,j}$ and $Vol_{v,j}$ are the vapor plug's mass and volume respectively. Since ODE45 iterates for solutions until a certain tolerance is met, the vapor mass is continuously being calculated inside another function as illustrated previously in Figure 6-30. In other words, we use the output of the vapor mass function as an input to calculate the vapor's pressure. This is the beauty of ODE45, we can exchange outputs of each function and input them in others. This is similar for the average vapor temperature $\bar{T}_{v,j}$, where this variable is calculated in one of the energy equation functions and then set as an input for this pressure function shown in equation 6-66.

Furthermore, the $Vol_{v,j}$ was calculated by getting the distance from the adjacent edges of the liquid slugs ΔL_j and can be expressed as:

$$Vol_{v,j} = \Delta L_j A_c \tag{6-68}$$

Where A_c is the cross-sectional area of the inside diameter of the capillary tubing. As observed we have completed calculating one of the variables of equation 6-66, and next we must calculate the compressibility factor *Z.* As shown below, the compressibility factor is a function of density and temperature as described by Diego Orlando [10].

$$Z = f(\rho, T) \tag{6-69}$$

Therefore equation 6-70 can be rewritten using the following vapor plug properties:

$$Z_j = f(\rho_{v,j}, \bar{T}_{v,j}) \quad 6\text{-}70$$

Furthermore, we have shown the calculation of the pressure of each vapor plug P_j which will serve as inputs for the liquid slug's momentum equation, as previously discussed.

6.3.8 Step 5: Calculating the energy equations for the liquid and vapor volumes

As shown in Figure 6-33, the liquid and vapor volumes are subdivided into sections in order to perform an accurate energy balance. The liquid and vapor nodes will not necessarily align to the wall nodes of the tube due to their unique displacement at every time step; therefore an algorithm was created in order to interpolate the temperature of the wall nodes (T_{wall}) to the chosen liquid or vapor nodes positions (T_{slug} or T_{vapor}). The slug position shown in Figure 6-33, can be the angle locations of nodes or arc lengths. It has been determined, that it is easier or more simple to use the angles since interpolation functions usually require a monatomic increasing vector, and angles can be reconfigured to fall in a range from 0 to 2π. For example, the position angles of the wall nodes will always be between 0 to 2π; however, if a slug cycles the entire PHP more than once, for example 3π, we can easily reset this angle to just π. Matrix **M** again comes in handy to create such an interpolation algorithm.

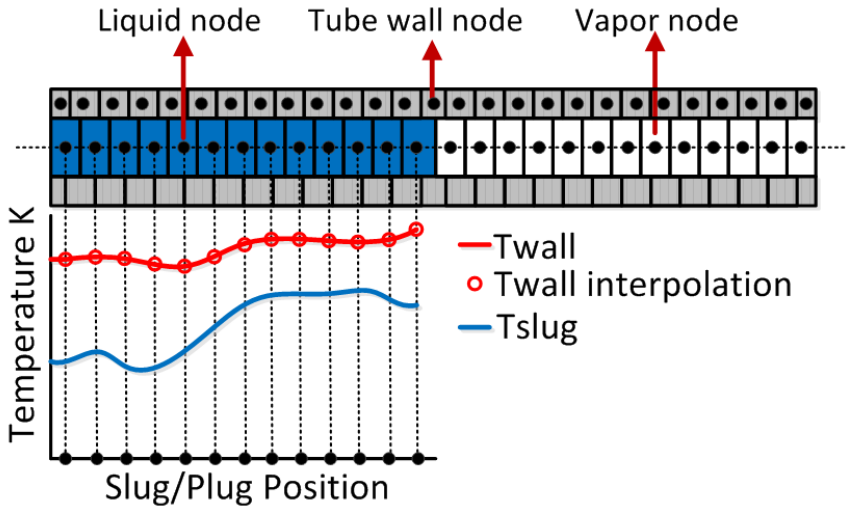

Figure 6-33: Interpolation scheme for liquid/vapor nodes

Figure 6-34 shows three of the main heat rates into i^{th} liquid control volume.

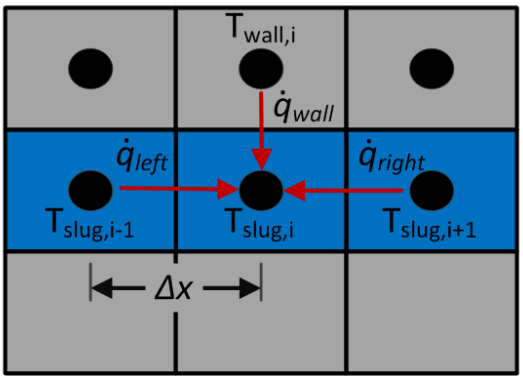

Figure 6-34: heat transfer of adjacent nodes

It was assumed that the liquid slug is compressible; therefore the general and simplified form of the energy balance, as described by Zhang et al. [9], for the liquid node *i* can be written as

$$m_{l,i}C_p\frac{dT_{slug,i}}{dt} = \dot{q}_{left} + \dot{q}_{right} + \dot{q}_{wall} \quad 6\text{-}71$$

Where C_p is the heat capacity. Variables $\dot{q}_{left}$, $\dot{q}_{right}$ and $\dot{q}_{top}$ are the heat transfer between the adjacent nodes. The conduction heat transfer due to the left and right node can be expressed as:

$$\dot{q}_{left} = \frac{\bar{k}A_c(T_{slug,i-1} - T_{slug,i})}{\Delta x} \quad 6\text{-}72$$

$$\dot{q}_{right} = \frac{\bar{k}A_c(T_{slug,i+1} - T_{slug,i})}{\Delta x} \quad 6\text{-}73$$

Where $\bar{k}$ is the average thermal conductivity using the average temperature of the entire slug:

$$\bar{k} = fun(\bar{T}_{slug}) \quad 6\text{-}74$$

Average thermal properties are useful to improve computational performance, if not adopted, computing *k* for each control volume would be overwhelming. In addition, the same assumption was made for heat capacities and densities (incompressible fluid).

The heat transfer from the wall node was assumed to be a resistance network, such as

$$\dot{q}_{wall} = \frac{(T_{Wall,i} - T_{slug,i})}{R_{total}} \quad 6\text{-}75$$

Where R_{total} is the total thermal resistance due to the thermal conductivity of the stainless steel and the heat transfer coefficient between the inner surface of the wall and fluid, and can be expressed as

$$R_{total} = R_{cyl} + R_{other} \quad (6\text{-}76)$$

The thermal resistance due to the stainless steel control volume can be computed as

$$R_{cyl} = \frac{\ln(D_{out}/ID)}{2\pi\Delta x k_{ssl}} \quad (6\text{-}77)$$

Where D_{out} was assumed to be the average of the inner and outer diameters, $D_{out} = (ID+OD)/2$. Since the wall is thin, the radial temperature distribution can be assumed constant. The thermal conductivity of stainless steel 304 does not vary at low cryogenic temperature ranges; therefore, it was assigned a constant value of k_{ssl} = 0.4149 W/m-K.

If the liquid slug is located inside the evaporator section, the thermal resistance is dependent on the convection and nucleate boiling heat transfer coefficients can be written as:

$$R_{other} = \frac{1}{(h_{conv} + h_{boiling}A_s)} \quad (6\text{-}78)$$

If the liquid slug is located inside the condenser section or adiabatic section, the heat transfer coefficient due to nucleate boiling can be neglected:

$$R_{other} = \frac{1}{h_{conv}A_s} \quad (6\text{-}79)$$

Where A_s is the inner surface area which is equal to the product of the inner perimeter (*per*) and the control volume's length Δx :

$$A_s = per\Delta x = \pi ID\Delta x \quad (6\text{-}80)$$

The heat transfer coefficient due to nucleate boiling was defined using the following Chen's correlation:

$$h_{boiling} = 0.00122\left(\frac{k_l^{0.79}C_{p,l}^{0.45}\rho_l^{0.49}}{\sigma^{0.5}\mu_l^{0.29}h_{fg}^{0.24}\rho_g^{0.24}}\right)\Delta T_{sat}^{0.24}\Delta P_{sat}^{0.75} \quad (6\text{-}81)$$

Where the subscript *l* stands for liquid. The fluid properties k, Cp, ρ, σ, μ and hfg are the thermal conductivity, specific heat capacity, density, surface tension, viscosity and heat of evaporization, respectively. ΔT_{sat} is the temperature difference between the evaporator wall and the temperature of the fluid. While ΔT_{sat} is the saturation pressure difference between the evaporator pressure and the saturation pressure of the liquid. The heat transfer coefficient h_{conv}, at the evaporator section was calculated using the Nusselt number for uniform surface heat flux in circular tubes:

$$Nu = \frac{h_{conv} ID}{\bar{k}} = 4.36 \tag{6-82}$$

However, since the condenser temperature was maintained at a uniform temperature, a Nusselt number of 3.66 was used.

It is important to mention that the vapor plugs located inside the condenser section will start to condense; therefore the following approximate equation (which is further justified) can be used to calculate the vapor mass for each vapor subvolume:

$$\dot{m}_{v,out,i} = \frac{\dot{q}_{wall,i}}{h_{fg}} \tag{6-83}$$

The total mass rate for vapor plug *j* is equal to

$$\dot{m}_{v,out,j} = \sum_{1}^{N} \dot{m}_{v,out,i} \tag{6-84}$$

The following conditions for the mass leaving a vapor slug were assumed:

$$\dot{m}_{v,out,j} = \begin{cases} \dot{m}_{v,out,j} < 0, \quad vapor\ leaving: inside\ condenser\ section \\ 0\ or\ \text{negligible}, evaporator\ \ section \\ 0\ or\ \text{negligible}\ , adiabatic\ section, assumption \end{cases} \tag{6-85}$$

Note, calculation of the liquid mass flow rate in the condenser section will be explained further.

As described by Shao et al. [9], the energy equation for an entire vapor plug *j* (no subdivisions) and behaving as an ideal gas can be written as:

$$m_{v,j}C_v\frac{dT_{v,j}}{dt} = \left(\dot{m}_{v,c,j} - \dot{m}_{v,e,j}\right)RT_{v,j} - \dot{W}_{v,j} \quad 6\text{-}86$$

Where C_v is the heat capacity at constant volume. Variable are $\dot{m}_{v,e,j}$ and $\dot{m}_{v,c,j}$ are the vapor mass flow rates due to evaporation and condensation, respectively. $T_{v,j}$ and $\dot{W}_{v,j}$ are the entire j^{th} vapor plug temperature and work rate. However, the following assumptions for this model were made:

- Vapor plugs do not behave as an ideal gas, therefore equation 6-86 cannot be used.
- Similarly to the liquid slugs, the vapor plugs were also subdivided into subvolumes to account for heat conduction from the adjacent nodes.

Hence, the following derivations for a real gas must be followed for each node i, similar to Figure 6-34

$$\frac{d(m_{v,i}u_{v,i})}{dt} = \dot{m}_{v,i}h_{v,i} - \dot{W}_{v,i} + \dot{q}_{left} + \dot{q}_{right} + \dot{q}_{wall} \quad 6\text{-}87$$

Where, the left hand side can be written as

$$\frac{d(m_{v,i}u_{v,i})}{dt} = \dot{m}_{v,i}u_{v,i} + m_{v,i}\dot{u}_{v,i} = \dot{m}_{v,i}u_{v,i} + m_{v,i}C_v\frac{dT_{v,i}}{dt} \quad 6\text{-}88$$

The following conditions were assumed when liquid mass is transferred out of a slug:

$$\dot{m}_{v,i} = \dot{m}_{l,out,j} = \begin{cases} 0, & inside\ condenser\ section \\ \dot{m}_{l,out,j} < 0, & inside\ evaporator\ section \\ 0, & inside\ adiabatic\ section \end{cases} \quad 6\text{-}89$$

A close approximation, is justified further, can be made to calculate the liquid mass rate evaporated $\dot{m}_{l,out,i}$ in each subvolume:

$$\dot{m}_{l,out,i} = \frac{\dot{q}_{wall,i}}{h_{fg}} \quad 6\text{-}90$$

Hence, the total liquid mass rate out slug j is equal to

$$\dot{m}_{l,out,j} = \sum_{1}^{N}\dot{m}_{v,out,i} \quad 6\text{-}91$$

Since $\dot{q}_{wall,i}$ was the highest energy rate, the equations for vapor and liquid mass rates (equations 6-83 and 6-90) omitted the following three energy rates:

a) Axial conduction was omitted.

b) Work rate was omitted.

c) The internal energy was omitted.

The axial conduction was omitted by calculating the ratio between axial conduction and radial conduction (or enthalpy carried out by the flow) Nellis [12]:

$$\frac{axial\ conduction}{radial\ conduction\ \&\ convection} \approx \frac{1}{Pe_{Dh}^2} \tag{6-92}$$

The Peclet number (Pe_{Dh}^2) is equal to:

$$Pe_{Dh} = \frac{\bar{V} D_h}{\alpha} \tag{6-93}$$

Where $\bar{V}$, D_h and α are the average velocity, hydraulic diameter and thermal diffusivity, respectively. Recall that the hydraulic diameter of the tubing is D_h = 0.5 mm. In addition, assuming the velocity is equal to $\bar{V}$ = 0.5 m/s (common velocity during simulation trials) and thermal diffusivity α = 5.457E^{-8} m^2/s at 4.2 K, hand calculation lead to the following thermal ratio:

$$\frac{axial\ conduction}{radial\ conduction\ \&\ convection} = 1.067E^{-7} \tag{6-94}$$

During multiple simulations, the rms work rate for vapor plug 1 ($\dot{W}_{rms,1}$) was calculated using the momentum equation and resulted in orders of magnitude of $\dot{W}_{rms,1}$ = 1.0E^{-4} W. These simulations were conducted at an evaporator heat load of $\dot{Q}_{\text{wall,total}}$ = 0.1 W. In addition, the initial lengths of the vapor and liquid slugs were set to L_o = 5 cm. Where the total length of the evaporator is equal to L_{et} = 0.42 m. The total heat load on a vapor/liquid volume *j* can be estimated as

$$\dot{Q}_{wall,j} = \frac{\dot{Q}_{\text{wall,total}} Lo}{L_{et}} = 1.19E^{-2} W \tag{6-95}$$

Furthermore, the energy ratio of the between the work and radial heat load $\dot{Q}_j$ can be calculated as

$$\frac{\dot{W}_j}{\dot{Q}_{wall,j}} = \frac{1.000E^{-4}}{1.190E^{-2}} = 8.4E^{-3} \tag{6-96}$$

The internal energy of the liquid slug shown in equation 6-71 can be rewritten as

$$m_{l,j}C_v\frac{dT_{slug,j}}{dt} = m_{l,j}C_v\frac{dT_{slug,j}}{dP}\frac{dP}{dt} \quad 6\text{-}97$$

During the simulation, the change of pressure with respect to the change in time resulted in dP/dt = 1.574E^4, that is for a time step of dt = 1E-5 s resulted in a change of pressure of ΔP = 0.1574 Pa. While the change of saturation temperature with respect to the change of saturation pressure at 4.2 K resulted in dT/dP = 1.064E^{-5} K/Pa. The initial mass of the slug was estimated to be 1.23E-6 kg; therefore a rough estimated of internal energy was calculated to be:

$$\dot{U} = m_{l,j}C_v\frac{dT_{slug,j}}{dt} = 1.23E^{-6}C_v 1.064\text{E}^{-5}1.574\text{E}^{4} = 5.1\text{E}^{-4}\ W \quad 6\text{-}98$$

Therefore the energy ratio between the internal and the radial heat load $\dot{Q}_j$ was calculated to be

$$\frac{\dot{U}_j}{\dot{Q}_{wall,j}} = \frac{5.1\text{E}^{-4}}{1.190E^{-2}} = 4.285E^{-2} \quad 6\text{-}99$$

Finally we have shown that the mass rate of evaporation and condensation can be approximated using equations 6-83 and 6-90.

As shown in Figure 6-35, it was assumed that liquid evaporation will take place when the slug is located inside the evaporator section. In addition, it was assume that 50 % of liquid mass rate ($\dot{m}_{l,out,j}$) of slug j will be transported to the adjacent vapor nodes. For example, vapor node 6 will receive mass from the liquid node 6 and 7, therefore the continuity equation for vapor plug 6 can be written as:

$$\frac{dm_{v,in,6}}{dt} = \frac{1}{2}(\dot{m}_{l,out,6} + \dot{m}_{l,out,7}) \quad 6\text{-}100$$

Or the general form

$$\frac{dm_{v,in,j}}{dt} = \frac{1}{2}(\dot{m}_{l,out,j} + \dot{m}_{l,out,j+1}) \quad 6\text{-}101$$

In the case of the condenser section, the liquid node j will receive mass from its adjacent vapor nodes and can be written as:

$$\frac{dm_{l,in,j}}{dt} = \frac{1}{2}(\dot{m}_{v,out,j} + \dot{m}_{v,out,j+1}) \quad 6\text{-}102$$

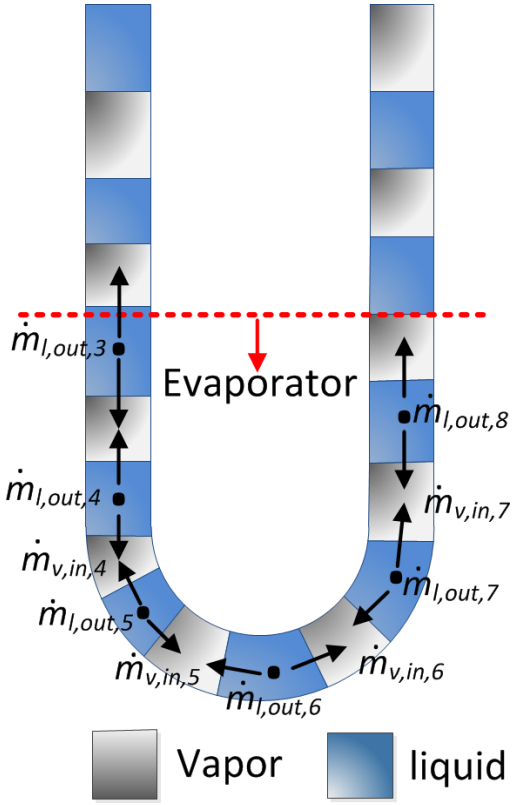

Figure 6-35: mass transfer in evaporator section

Recall that $\dot{q}_{wall,i}$ can be calculated using equation 6-75, but $T_{v,i}$ should be used instead of $T_{slug,i}$. In addition, the Nusselt number, equation 6-82, should be used using the thermal conductivity of vapor.

Finally, The internal energy ($u_{v,i}$) and enthalpy ($h_{v,i}$) can be calculated using the equation of state of helium, where the inputs would be the vapor temperature of the of node i ($\bar{T}_{v,i}$) and the vapor pressure (P_j) calculated in section 6.3.7. For example:

$$u_{v,i} = f(T_{v,i}, P_j) \quad 6\text{-}103$$

$$h_{v,i} = f(T_{v,i}, P_j) \quad 6\text{-}104$$

The work rate $\dot{W}_{v,j}$ performed on or done by vapor plug *j* is illustrated in Figure 6-36. As shown, V_R and V_L represent the resulting slug velocities on the right and left edges, respectively. Compression and expansion cases of the vapor bubble are described as the following:

- Case A, compression results when the left velocity is $V_L > 0$ and right velocity $V_R < 0$.
- Case B, expansion results when $V_L < 0$ and $V_R > 0$.
- Case C, expansion results when right and left velocities are positive; however $V_R > V_L$.
- Case D, compression results when right and left velocities are positive; however $V_L > V_R$.
- Case E, compression results when right and left velocities are negative; however the magnitude of the velocities obey $|V_R| > |V_L|$.
- Case F, expansion results when right and left velocities are negative; however the magnitude of the velocities obey $|V_L| > |V_R|$.

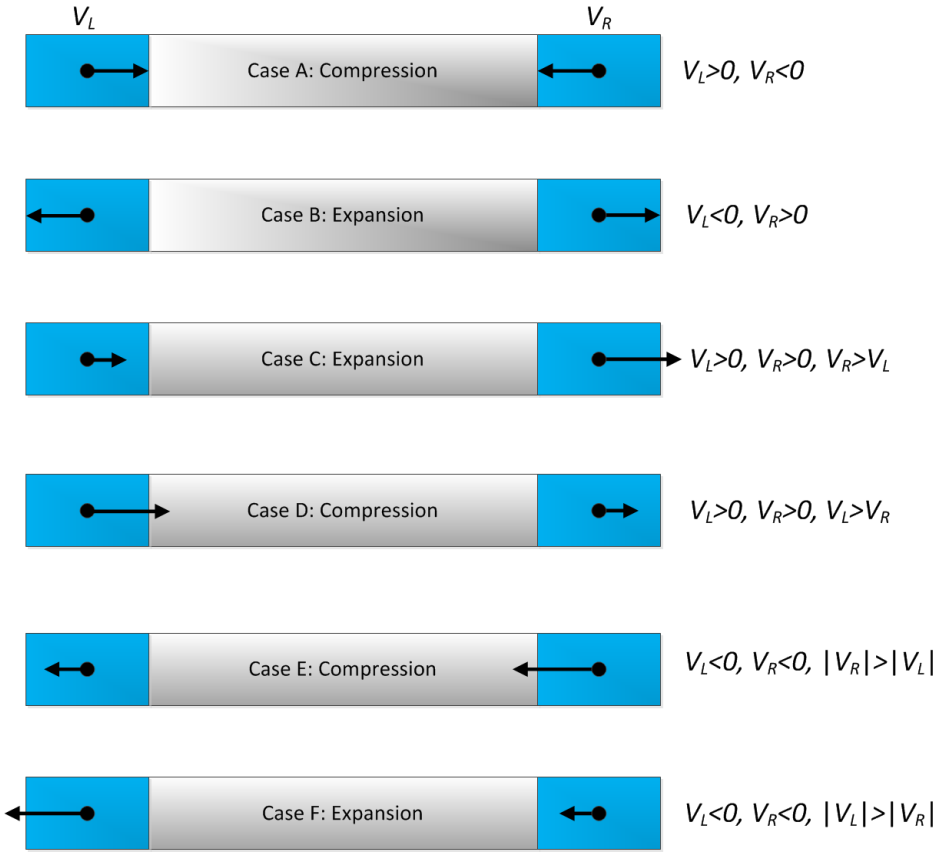

Figure 6-36: Vapor bubble work rate cases.

The work of a system can be expressed as:

$$W = \int PdVol \tag{6-105}$$

Where variable *Vol* is the volume of the system. Therefore, the work rate can be expressed as

$$\dot{W} = \int Pd\dot{V}ol \tag{6-106}$$

The time step used by ODE45 is around 1e-5 s; therefore, the pressure P was assumed to be constant between consecutive times. Hence, the work rate can be rewritten as

$$\dot{W} = P\int d\dot{V}ol = P\int A_c dV = PA_c\Delta V \tag{6-107}$$

Where A_c and V are the cross-sectional area and velocity, respectively. The change in velocity can be expressed in terms of the left and right slug velocities of vapor bubble *j*:

$$\dot{W}_j = P_j A_c |V_R - V_L| \quad 6\text{-}108$$

Observe that $\dot{W}_j$ will give a positive value. The temperature of the vapor bubble will increase if compressed and decrease if expanded. Therefore when compressed (Cases A, D and E), the first law of thermodynamics can be expressed as:

$$\dot{Q}_j + \dot{W}_j = \dot{E}_j \quad 6\text{-}109$$

And when expanded (Cases B, C and F)

$$\dot{Q}_j - \dot{W}_j = \dot{E}_j \quad 6\text{-}110$$

Since it was assumed that the vapor bubble *j* has a constant pressure throughout its entire volume, then the work rate per subvolume was assumed to be:

$$\dot{W}_i = \frac{\dot{W}_j}{N_v} \quad 6\text{-}111$$

Where N_v is the is the number of subvolumes in vapor plug *j*.

6.3.9 Step 6: Calculating the energy equation for the tube wall

Similarly to the previous section, the temperature liquid and vapor nodes were interpolated to match the exact locations of the wall temperature nodes $T_{wall,i}$, as shown in Figure 6-37. Hence, the energy equation can be written as written as

$$\rho_{ssl} C_{p,ssl} A_{c,wall} \Delta x \frac{dT_{wall,i}}{dt} = \dot{q}_{left,wall} + \dot{q}_{right,wall} + \dot{q}_{wall} \quad 6\text{-}112$$

The density (ρ_{ssl} = 8072 kg/m^3) and specific heat capacity ($C_{p,ssl}$ = 2.58 J/kg-K) of stainless steel 304 were held constant at these cryogenic temperatures. $A_{c,wall}$ is the cross-sectional area of the tubing.

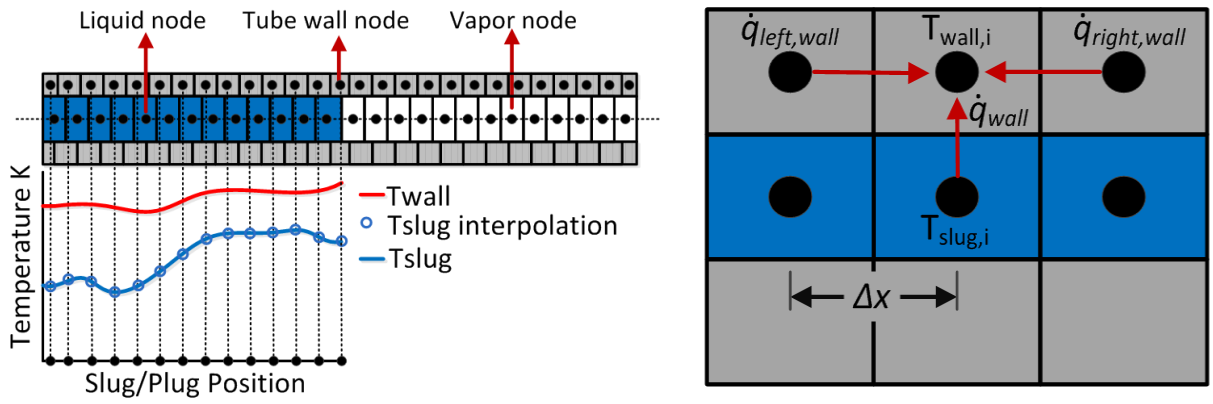

Figure 6-37: Interpolation scheme for the wall temperature nodes

Heat transfer due to the adjacent nodes ($\dot{q}_{left,wall}$, $\dot{q}_{right,wall}$ and $\dot{q}_{wall}$) can be expressed using the following equations

$$\dot{q}_{left,wall} = \frac{k_{ssl} A_{c,wall} (T_{wall,i-1} - T_{wall,i})}{\Delta x} \quad 6\text{-}113$$

$$\dot{q}_{right,wall} = \frac{k_{ssl} A_{c,wall} (T_{wall,i+1} - T_{wall,i})}{\Delta x} \quad 6\text{-}114$$

$$\dot{q}_{wall} = \frac{(T_{wall,i} - T_{slug,i})}{R_{total}} \quad 6\text{-}115$$

Where the thermal conductivity was held at a constant value of k_{ssl} = 0.4149 W/m-K. The thermal resistance network R_{total} is equal to equation 6-76.

6.3.10 Results of model

Table 6-7 shows 5 important preliminary results for a PHP similar to the experimental geometry, with the exception that the model's adiabatic section was parameterized and that the condenser section was set to 7 cm instead of 9 cm. The main goal of these preliminary simulations were to observe the behavior of the PHP and later in the section, the final cases will show a comparison with the actual experimental data. Recall that the experimental test bed is composed of three PHP sections; however the model just simulates one PHP section. As shown, all these cases have a constant evaporator heat load ($\dot{Q}_{evap}$) of 0.1 W and a constant condenser temperature (T_{cond}) of 3 K. Furthermore, the table provides a video link of the liquid

slugs and vapor plugs displacement in time. Figure 6-38 shows a snapshot of time t = 0.4375 s, where the slugs were given a red color, except for the first slug which is shown as blue, the vapor slugs are given a black color. The average velocity of the blue slug ($\bar{V}_{slug,1}$) is also shown in the table. Finally, the cases from 1 to 5 were set with a fill ratio of 50 % but the length of the slug was set to 5 cm. Case 6 represent a model with a total number of 8 turns.

Table 6-7: Preliminary models for PHP

Case #	$\dot{Q}_{evap}$ (W)	T_{cond} (K)	L_c,L_a,L_e (cm)	L_{slug} (cm)	N_{slug} [-]	$\bar{V}_{slug,1}$ (m/s)	Video Link
1	0.1	3	7,15,3	5	40	0.4025	https://youtu.be/d-FNc7L4qOA
2	0.1	3	7,20,3	5	49	0.5443	https://youtu.be/wgE__Wk5Lno
3	0.1	3	7,30,3	5	60	0.5820	https://youtu.be/zly3eOK5RNM
4	0.1	3	7,40,3	5	77	0.5962	https://youtu.be/IVUlPSgcojM
5	0.1	3	7,50,3	5	90	0.6095	https://youtu.be/i0DrFkF62Wo
6	0.1	3	10,20,3	5	20	-0.6968	https://youtu.be/xg_betSA7pw

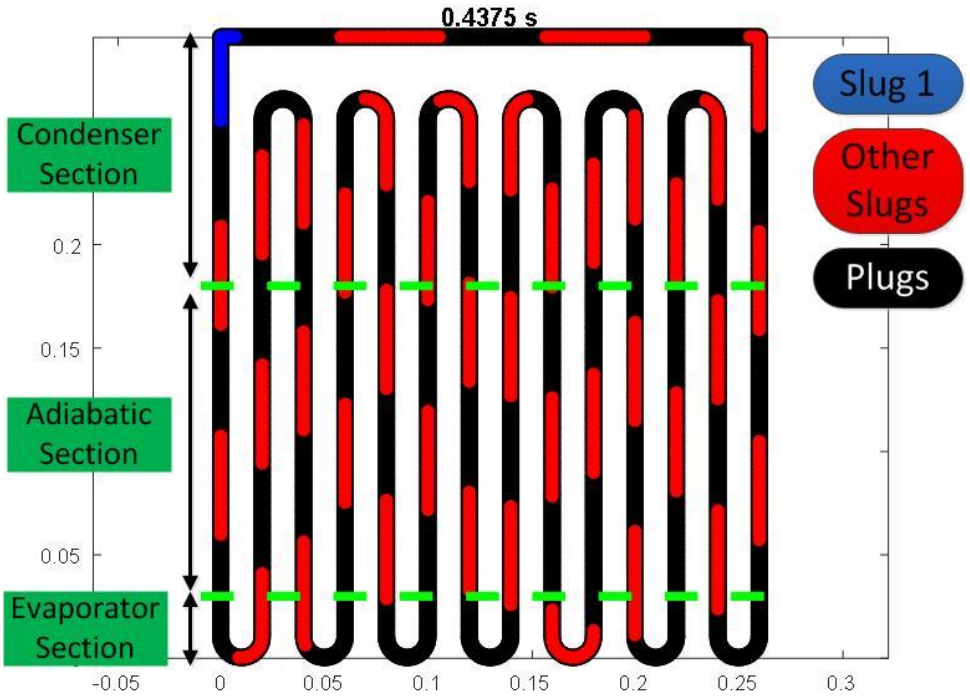

Figure 6-38: Model snapshot description

Figure 6-39 shows the average temperature of slug 1 as it displaces in time, which is also shown in the videos. It is evident that the slug's high temperatures were reached when the slug was located inside the evaporator section while the lowest temperature occur inside the condenser section.

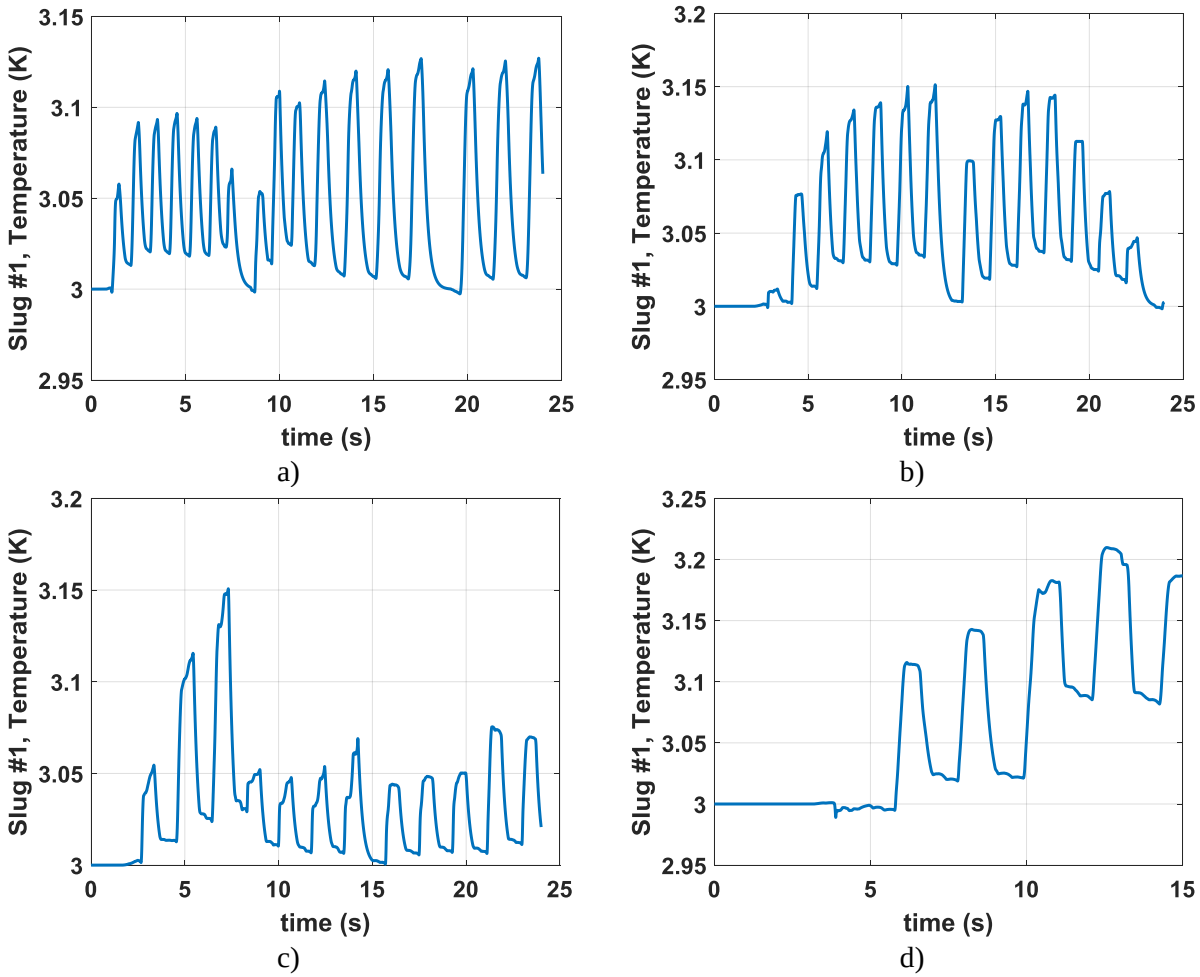

Figure 6-39: Slug # 1 temperature oscillation for a) Case 1 b) Case 3 c) Case 4 d) Case 5.

Figure 6-40 shows the temperature of one of the evaporator wall nodes inside the evaporator section, note how initially the wall temperatures increase due to the fact that the flow has not started to circulate and drastically decreases once circulations starts. In addition, the figure shows the frequency spectrum for one of the wall temperature nodes, observe that the highest peaks occurs at frequencies between 0.8 and 4 Hz, which are very close to the experimental condenser frequency of 1.2 Hz, shown in Table 5-2. However it is important to note that in the experiment the evaporator section is soldered to a copper plate and therefore

the temperature recorded is dependent on the heat transfer between the adjacent tubing. The model does not account for this heat conduction and we are just reporting one of the evaporator nodes.

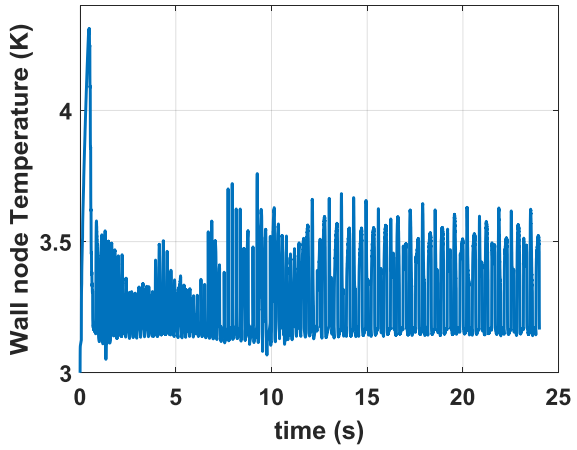

a)

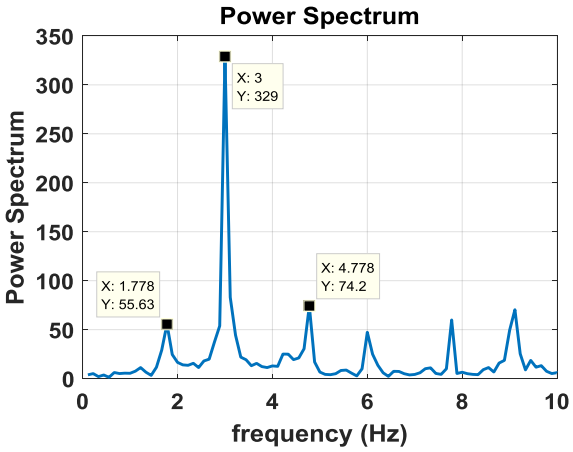

b)

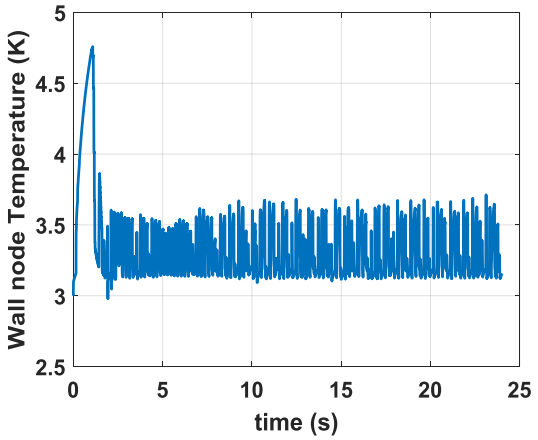

c)

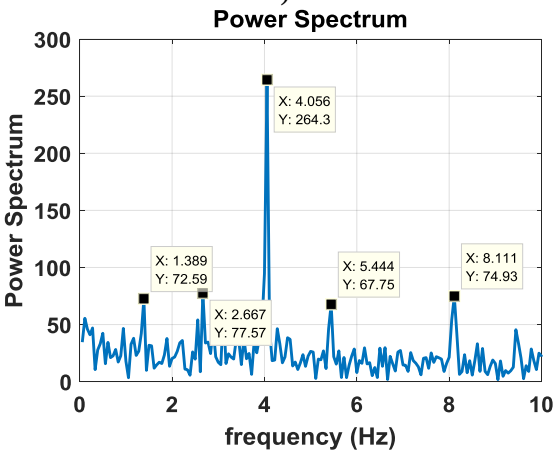

d)

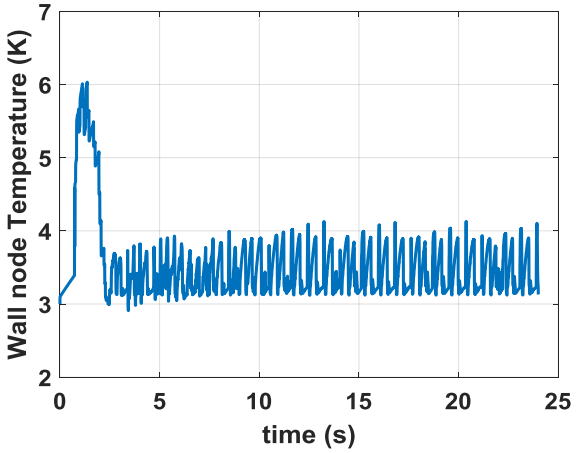

e)

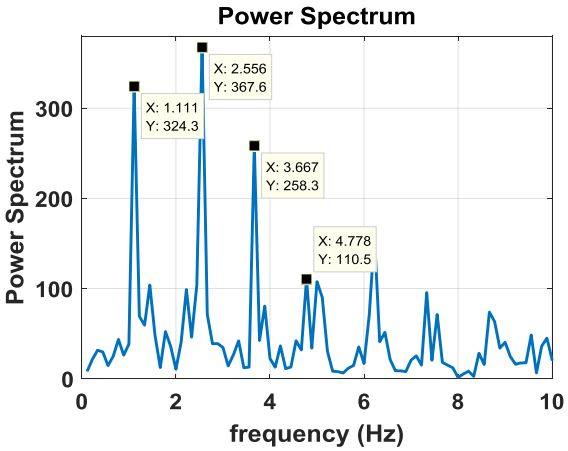

f)

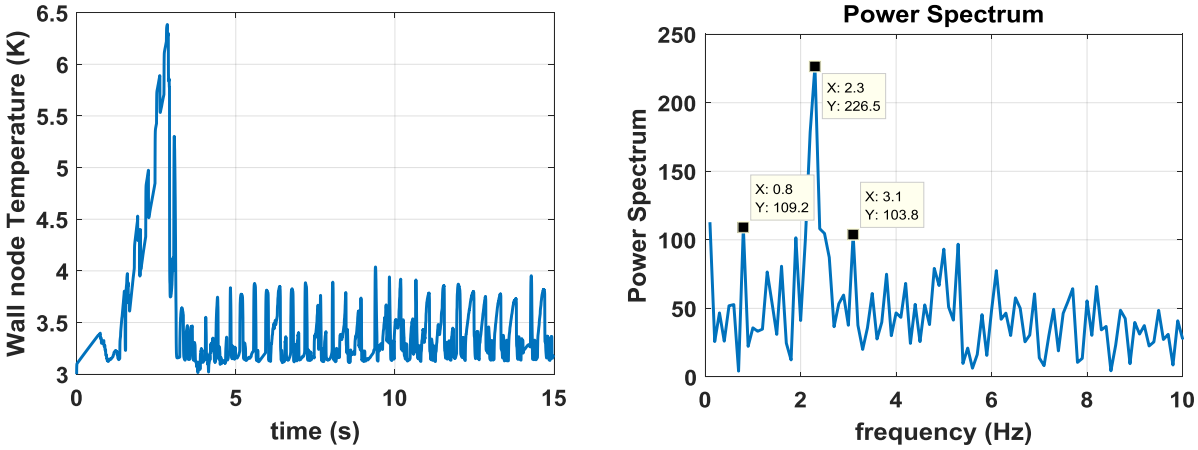

g) h)

Figure 6-40: a) Temperature oscillations Case 1, b) Spectrum Case 1. c) Temperature oscillations Case 3. d) Spectrum for Case 3. e) Temperature oscillations Case 4. f) Spectrum Case 4. g) Temperature oscillations Case 5. h) Spectrum Case 5.

Various conclusions can be observed from this preliminary analysis:

- The model shows circulation movement in this type of slug/vapor pattern. CFD models, which are discussed in the next section, report the same behavior.
- For case 6, it was observed that the velocity was negative. As observed in the video, the slug is circulating clockwise; while a counterclockwise movement was shown for the other cases. This behavior has been reported in Khandekar's room temperature PHP experimental results [11]. It is believe for this model that, the flow can choose either movement depending mostly on the initial positions of the liquid slugs and vapor plugs.
- The PHP does not circulate immediately, vapor slugs require some time to contract and expand before kicking in.
- The slug velocity increases as the adiabatic length increases. This observation makes sense since the slug requires to move faster for a longer length to ensure a constant heat rate.

Figure 6-41 shows a comparison of the experimental data and model, where the model temperature T_{node} is the temperature of one of the nodes inside evaporator section. The experimental configuration data comes from the 300 mm length PHP. For case 7 in Table 6-8, the condenser temperature of the model was set up

to 3.794 K, which is the temperature that the cryocooler achieved when 0.1 W were applied to each PHP section. Table 6-8 summarizes other cases performed at different heat loads.

Table 6-8: Model information for comparison to experimental

Case #	$\dot{Q}_{evap}$(W)	T_{cond} (K)	L_c,L_a,L_e (cm)	L_{slug} (cm)	$\bar{V}_{slug,1}$ (m/s)	Video Link
7	0.1	3.794	9,38,3	5	0.3768	https://youtu.be/azSgrKJrxeo
8	0.025	3.189	9,38,3	5	0.2061	https://youtu.be/YFIKY4CW71o
9	0.050	3.382	9,38,3	5	0.2451	https://youtu.be/7f9AqHHHPAU
10	0.0749	3.564	9,38,3	5	0.3172	https://youtu.be/1V6Bv3v787A
11	0.1332	3.949	9,38,3	5	0.5194	https://youtu.be/ni9ZpdLGkxw
12	0.2000	4.342	9,38,3	5	0.4989	https://youtu.be/2MZEyV5Hhm8
13	0.2378	4.537	9,38,3	5	0.4770	https://youtu.be/WHGoxyS_6ts

Note that the experimental data is already in steady state; however the evaporator node reached a stable oscillatory behavior after 3 seconds. In addition, the top evaporator temperature was used to compare to the model since thermal resistances between the heater and sensor are avoided. Interestingly, the model shows higher oscillations than the experimental data, this is caused since the copper block composing the evaporator section damps out the adjacent tubing temperatures due to heat transfer by. Therefore, Figure 6-42 shows a comparison between the experimental data and model's average evaporator section $T_{model,avg}$. Note that averaging the evaporator temperature is a rough approximation and future work should include heat transfer between the tubing.

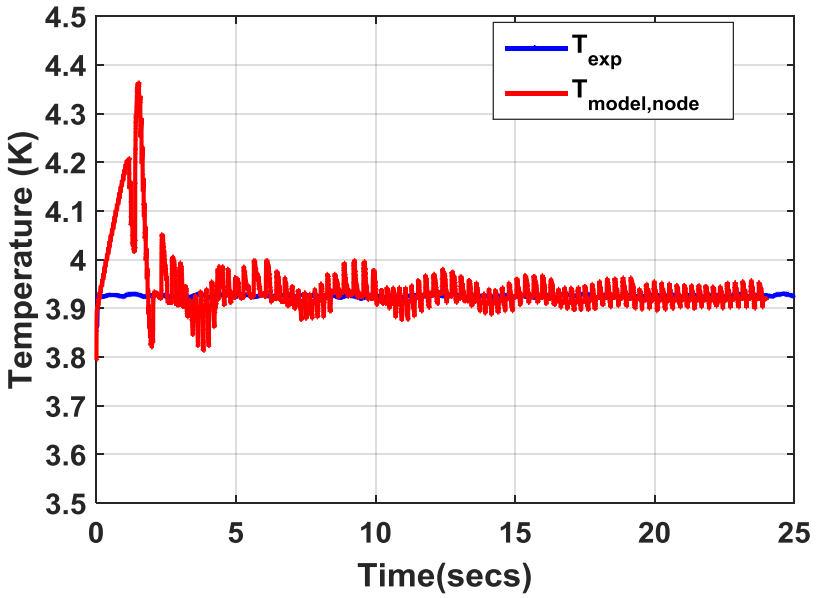

Figure 6-41: Case 7, Experimental data vs model temperature at one evaporator node

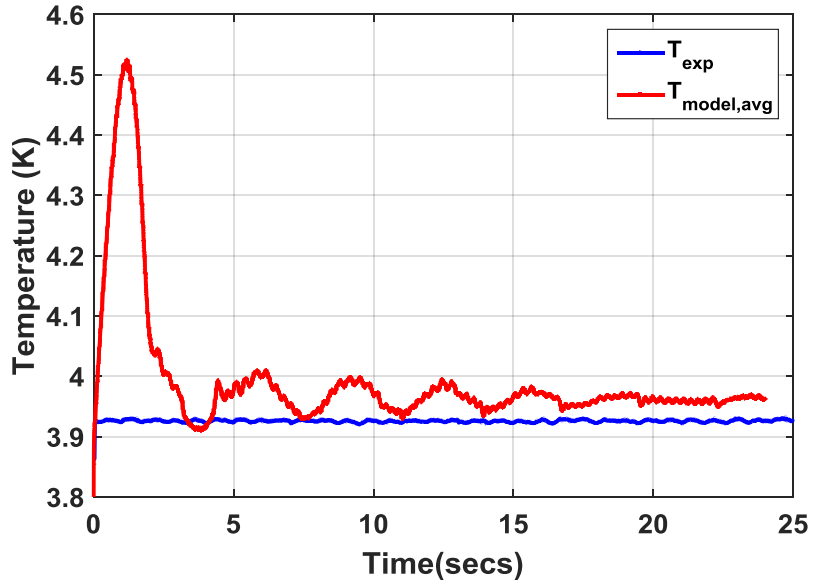

Figure 6-42: Cases 7, experimental temperature vs average model temperature

Figure 6-43-a, -b and -c shows the power spectrum of the experimental evaporator temperature, model's wall node temperature and slug # 1 temperature, respectively. For Figure 6-43-a, note that the maximum peak oscillates at a frequency close to the cryocooler oscillation frequency (1.2 Hz); however there are lower frequencies close to 0.3 Hz and are observed in the model's wall node and slug spectrums. In addition the slug temperature shows an additional peak at 1.056 Hz which are most likely due to the sudden and fast

movements of the slug, as can be observed in the videos. The physical temperature oscillation of the cryocooler should be implemented in the model in order to observe any behavior similarities. It can be concluded that the experimental temperature oscillations are not orders of magnitude different from the model and that spring mass damper system with equations of energy are sufficient to predict the behavior of a PHP; however models should be used as a starting point to build experimental prototypes in order verify its real performance.

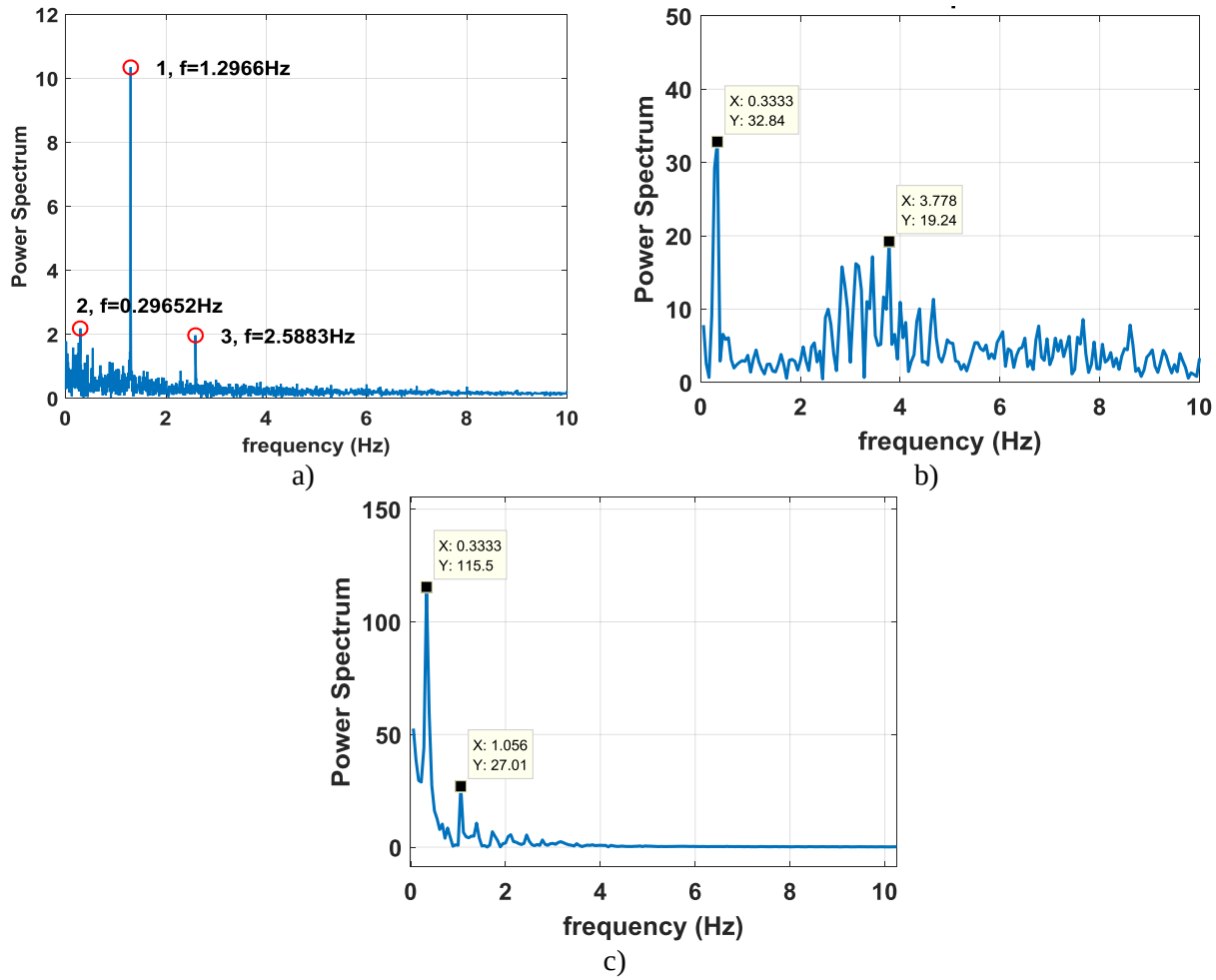

Figure 6-43: Cases 7, temperature spectrum for a) experimental data, b) model's wall node c) model's slug # 1 .

Figure 6-44 shows a comparison of the experimental evaporator temperature vs the model's averaged evaporator temperature. It was observed that the simulation under predicted when the experimental data operated above the critical temperature of helium T_{crit} = 5.19 K. However, the rms error for the data below

the critical temperature resulted in E_{rms} = 0.045 K. It can be concluded that this type of model predicts with high accuracy the thermal behavior of the PHP as long as it operates inside the two-phase region. In addition, it was observed that Bond numbers above Bo = 2 will be achieved at saturation temperatures above T_{sat} = 4.529 K; therefore a slug flow would no longer be dominant. This observation could be related to the under predicted results.

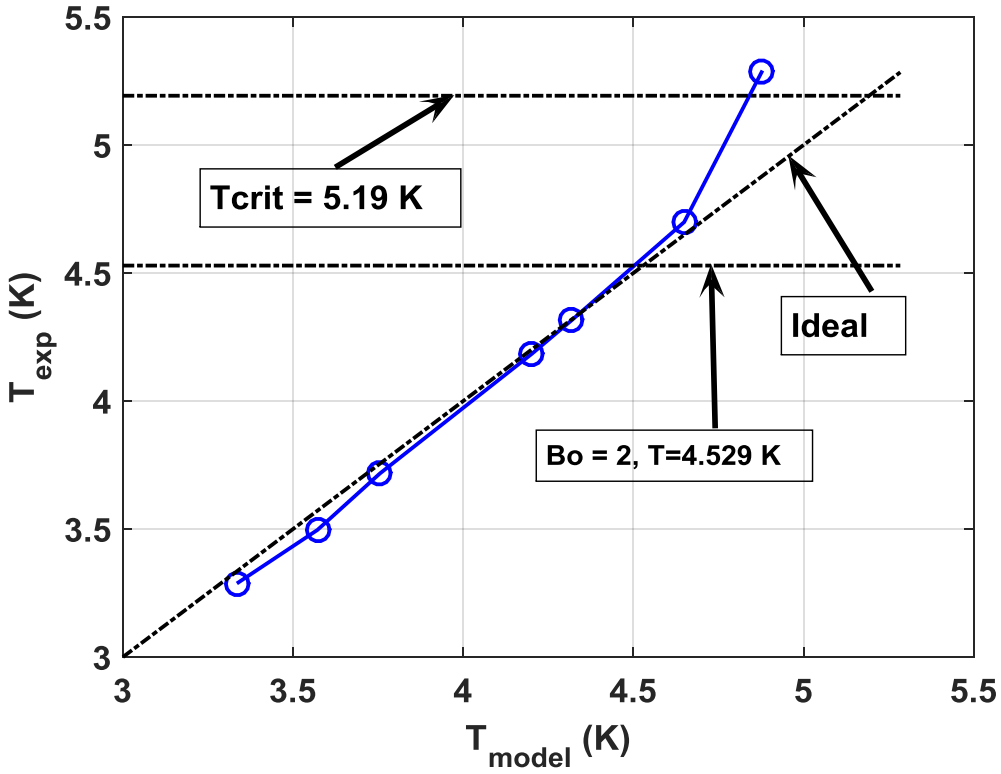

Figure 6-44: Experimental evaporator data versus model for cases 7-13

6.4 References

[1] H. Akachi, Structure of a heat pipe, U. S. Patent No. 4921041 (05 1990). URL http://www.lens.org/lens/patent/US_4921041_A.

[2] Ma, H. B., Hanlon, M. A., & Chen, C. L. (2006). An investigation of oscillating motions in a miniature pulsating heat pipe. *Microfluidics and Nanofluidics*, *2*(2), 171-179.Gürsel, G., Frijns, A. J. H., Homburg, F. G. A., & van Steenhoven, A. A. (2015). A mass-spring damper model of a pulsating heat pipe with a non-uniform and asymmetric filling. *Applied Thermal Engineering*, *91*, 80-90.

[3] Gürsel, G., Frijns, A. J. H., Homburg, F. G. A., & van Steenhoven, A. A. (2015). A mass-spring damper model of a pulsating heat pipe with a non-uniform and asymmetric filling. *Applied Thermal Engineering*, *91*, 80-90.

[4] Khandekar, Sameer, Nicolas Dollinger, and Manfred Groll. "Understanding operational regimes of

closed loop pulsating heat pipes: an experimental study." *Applied Thermal Engineering* 23.6 (2003): 707-719.

[5] J. Berthier, Micro-drops and Digital Microfluids, *William Andrew Publishingring*, Norwich, NY*, 2008*, 390-401.

[6] G. Thomson. The Antoine equation for vapor pressure data. Chem. Revs 38 (1), 1946, pp 1-39.

[7] Mameli, Mauro, Marco Marengo, and Sameer Khandekar. "Towards quantitative validation of a closed loop pulsating heat pipe numerical model." *Proc. 16th International Heat Pipe Conference.* 2012.

[8] Borgmeyer, Brian V. "Theoretical Analysis and Experimental Investigation of a Pulsating Heat Pipe for Electronics Cooling". ProQuest, 2005.

[9] Zhang, Y., & Shao, W. (2011). Effects of Capillary and Gravitational Forces on Performance of An Oscillating Heat Pipe. Frontiers in Heat Pipes (FHP), 2(2).

[10] Ortiz Vega, D. O. (2013). A New Wide Range Equation of State for Helium-4 (Doctoral dissertation).

[11] Khandekar, S. (2004). Thermo-hydrodynamics of closed loop pulsating heat pipes.

[12] Nellis, G., Klein, S., (2009). Heat Transfer. Cambridge University Press.

[13] Costa, Umvberto. "CFD simulation of a Pulsating Heat Pipe using ANSYS FLUENT", Submitted Paper, 2016.

[14] Pouryoussefi, S. M., and Yuwen Zhang. "Numerical investigation of chaotic flow in a 2D closed-loop pulsating heat pipe." Applied Thermal Engineering 98 (2016): 617-627.

[15] Khandekar, S., M. Schneider, and M. Groll. "Mathematical modeling of pulsating heat pipes: state of the art and future challenges." Heat and Mass Transfer, SK Saha, SP Venkateshen, BVSSS Prasad, and SS Sadhal, eds., Tata McGraw-Hill Publishing Company, New Delhi, India (2002): 856-862.

[16] Senjaya, Raffles, and Takayoshi Inoue. "Oscillating heat pipe simulation considering bubble generation Part I: Presentation of the model and effects of a bubble generation." International Journal of Heat and Mass Transfer 60 (2013): 816-824.

[17] Khandekar, S., Charoensawan, P., Groll, M., & Terdtoon, P. (2003). Closed loop pulsating heat pipes: Part A: parametric experimental investigations. Applied thermal engineering, 23(16), 2009-2020.

[18] Khandekar, S., Charoensawan, P., Groll, M., & Terdtoon, P. (2003). Closed loop pulsating heat pipes Part B: visualization and semi-empirical modeling. Applied thermal engineering, 23(16), 2021-2033.

[19] Zhang, Y., & Faghri, A. (2008). Advances and unsolved issues in pulsating heat pipes. *Heat Transfer Engineering*, 29(1), 20-44.

[20] Rittidech, S., Terdtoon, P., Murakami, M., Kamonpet, P., & Jompakdee, W. (2003). Correlation to predict heat transfer characteristics of a closed-end oscillating heat pipe at normal operating condition. Applied Thermal Engineering, 23(4), 497-510.

[21] Katpradit, T., Wongratanaphisan, T., Terdtoon, P., Kamonpet, P., Polchai, A., & Akbarzadeh, A. (2005). Correlation to predict heat transfer characteristics of a closed end oscillating heat pipe at critical state. Applied thermal engineering, 25(14), 2138-2151.

[22] Charoensawan, P., & Terdtoon, P. (2007, April). Nondimensional correlation to predict the thermal performance of horizontal closed-loop pulsating heat pipe. In 14th Int. Heat Pipe Conference, Florianopolis, Brazil.

[23] Arslan, G., & Özdemir, M. (2008). Correlation to predict heat transfer of an oscillating loop heat pipe consisting of three interconnected columns. Energy Conversion and Management, 49(8), 2337-2344.

7 Conclusion and Future Work

A helium based PHP with 3 sections and an adiabatic length of 300 mm and 1000 mm has been operated successfully. The following conclusions can be made from the experimental data:

- Most significantly, increasing the adiabatic length from 300 mm to 1000 mm did not alter the thermal conductance of the PHP. The temperature difference between the evaporator and condenser section remained the same.
- The PHP reached an optimal performance when equal heat loads were applied to each PHP section. Uneven heat loads were able to operate in a certain range but some cases showed high temperature differences.
- Applying sinusoidal heat loads to the PHP sections did not affect the performance of the PHP.
- Sweeping fill ratio values should always be conducted in order to determine the PHPs optimal performance for a given adiabatic length.
- The helium PHP was able to operate continuously and never showed a sudden stop.
- The PHP was able to operate in the supercritical and superheated region achieving higher amplitude oscillations than in the two-phase region.
- It was determined that the fill ratio changes as the heat load is increased. The fill ratio increases or decreases depending on PHPs specific volume.
- A thorough non-dimensional correlation was performed and showed high accuracy.
- An improved spring mass damper model was developed and showed reasonable results. Such type of models should be used as a starting point to design PHP prototypes.

Experimental future work includes

- Most frequent thermal and pressure oscillations were found to be at 1.2 Hz due to the cryocooler's physical oscillations. It is possible to change the crycooler's frequency using a special power

adapter recommended by Sumitomo, therefore future tests could verify how the thermal performance changes as a function of the cryocooler's frequency.

- It was proven the helium PHP's thermal performance for cases with uneven heat loads were different than the results for even heat loads. Therefore, it is highly recommended to reconfigure each PHP section with separate gas lines or just test one of the PHP sections. This could provide important data for cooling systems that have multiple and high heat flux differences.
- As mentioned previously, increasing the adiabatic length did not degrade the performance; therefore, longer adiabatic section should be tested until a critical length is determined.
- The test facility has reached an expertise level in which the helium PHP device can be integrated to a superconducting magnet. Such testing could provide relevant data for MRI manufactures and space agencies.
- Creating and updating the presented correlation by testing other cryogenic fluids. Currently, the PHP is being adapted to a cryocooler with a cooling capacity of 200 W at 77 K and nitrogen will be tested as the working fluid.
- PHPs with different inner diameters and number of turns should be constructed to update empirical correlations. Currently a new PHP has been constructed in which the number of turns can be easily changed.
- Due to the constraints of the test facility, the PHP has only been operated in a vertical position; however, different inclination angles should be tested since to verify its thermal performance.

The modified spring mass damper model should be improved but without forgetting the main scope "A useful tool that can give fast and approximate results to design PHP prototypes". Future work for this model should include the following:

- Run model at different fill ratios, slug lengths, inner diameter, number of turns and heat loads. Parameterizing these variables could provide important information to predict an optimal thermal performance.
- Instead of using a single computer to solve one model at a time, multiple models should be processed in parallel at UW-Madison's Center for High Throughput Computing.
- Different methods other than Matlab's built-in ODE solvers should be studied and implemented to increase computational performance if possible.
- Heat transfer coefficients regarding Nusselt numbers for Reynolds numbers above 2300 should be added to the model.
- Many correlations of heat transfer coefficient due to nucleate boiling exist; however, flow boiling correlations regarding cryogenic fluids should be investigated in order to improve predictions.
- Different cryogens should be added to the model: nitrogen, hydrogen, neon, etc. A fluid property library should be built.
- When interpolating temperatures for the energy equations, Matlab built-in interpolation functions consumed most computational power. Therefore, if possible, faster interpolation methods should be applied to the model.
- The physical temperature oscillation of the cryocooler should be implemented in the model in order to observe any behavior similarities. This includes adding the cryocooler's heat curve.
- It was determined that the Peclet number was small; therefore removing the fluid's heat conduction from the energy equation should be verified. This would improve significantly the processing time of the model.

8 Appendix

8.1 Results on thermal conductivity

8.1.1 Fill ratio at 22.45 % and bottom heaters on

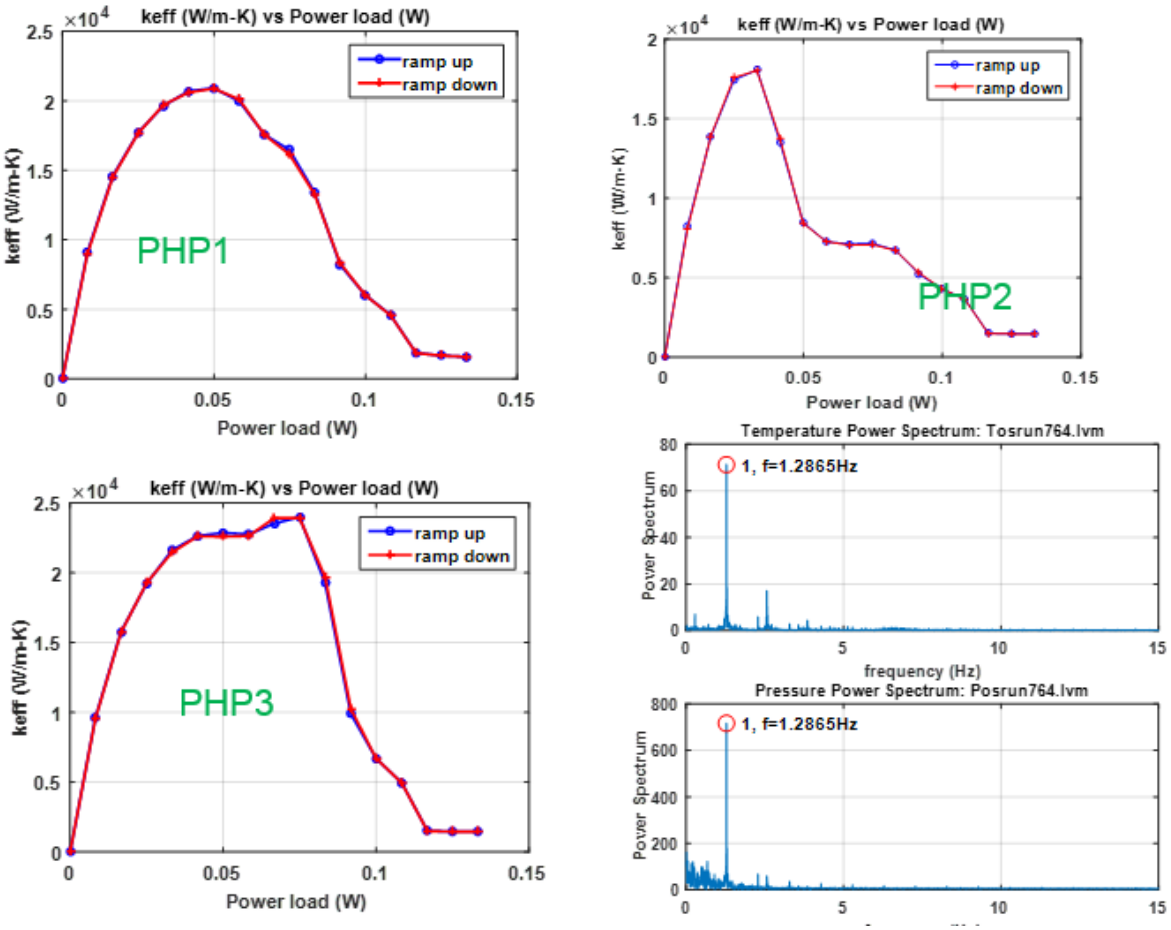

Figure 8-1

8.1.2 Fill ratio at 22.45 % and top heaters on

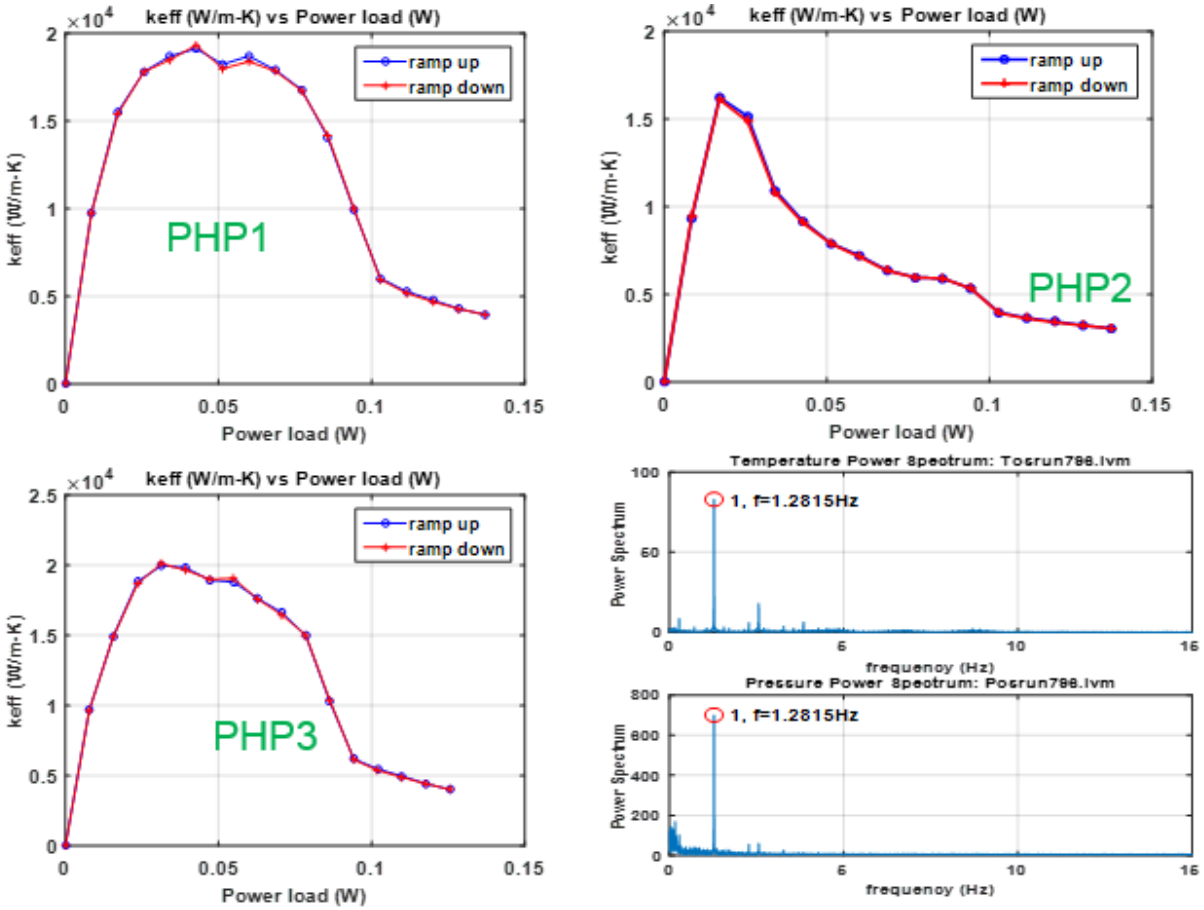

Figure 8-2

8.1.3 Fill ratio at 22.45 % and all heaters on

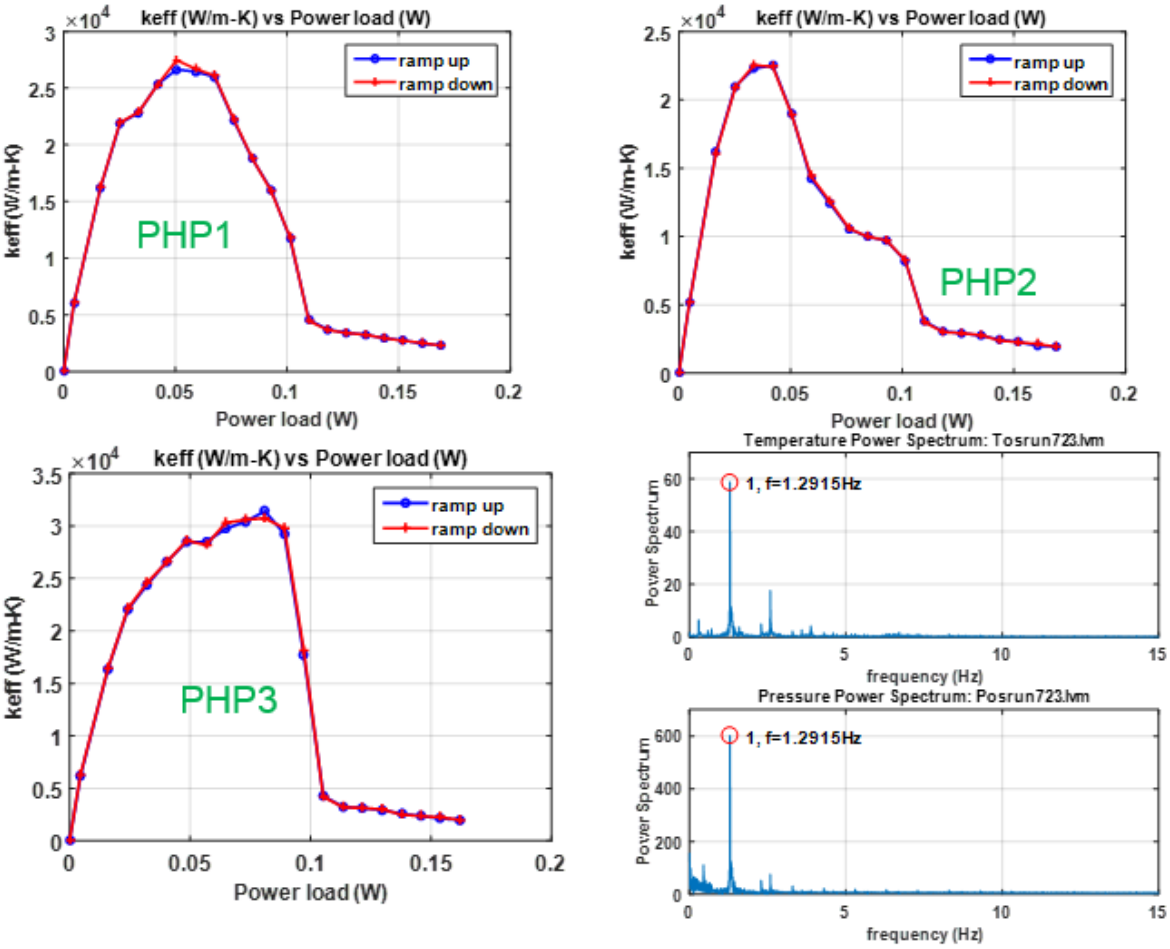

Figure 8-3

8.1.4 Fill ratio at 30.61 % and bottom heaters on

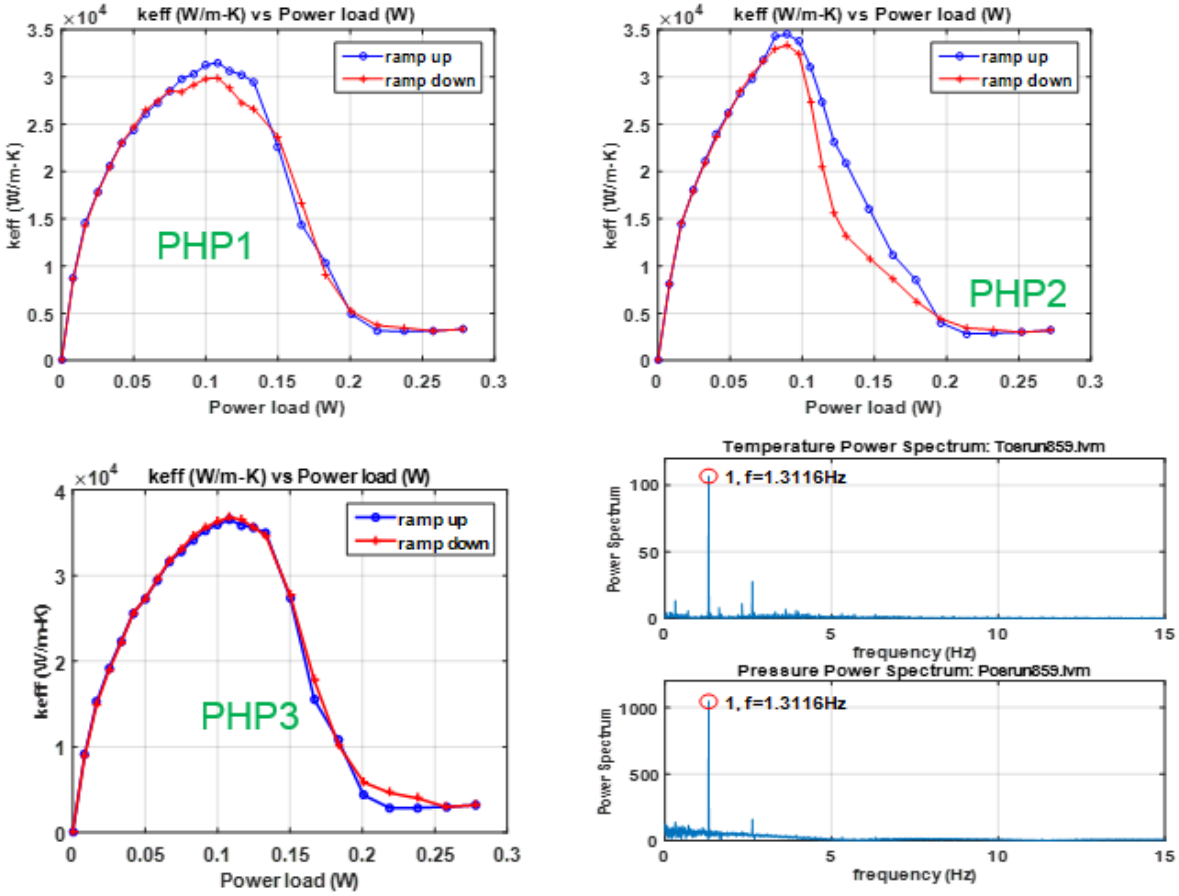

Figure 8-4

8.1.5 Fill ratio at 30.61 % and top heaters on

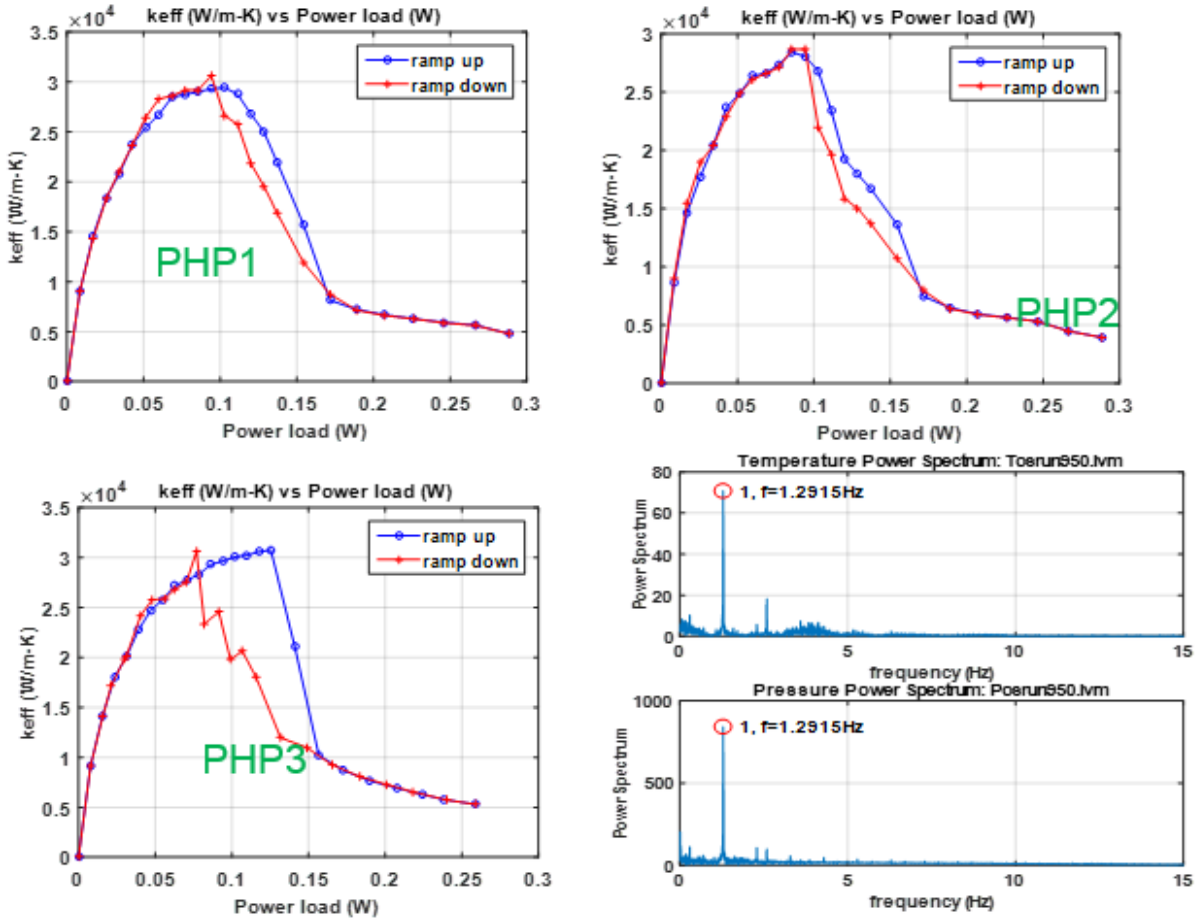

Figure 8-5

8.1.6 Fill ratio at 30.61 % and all heaters on

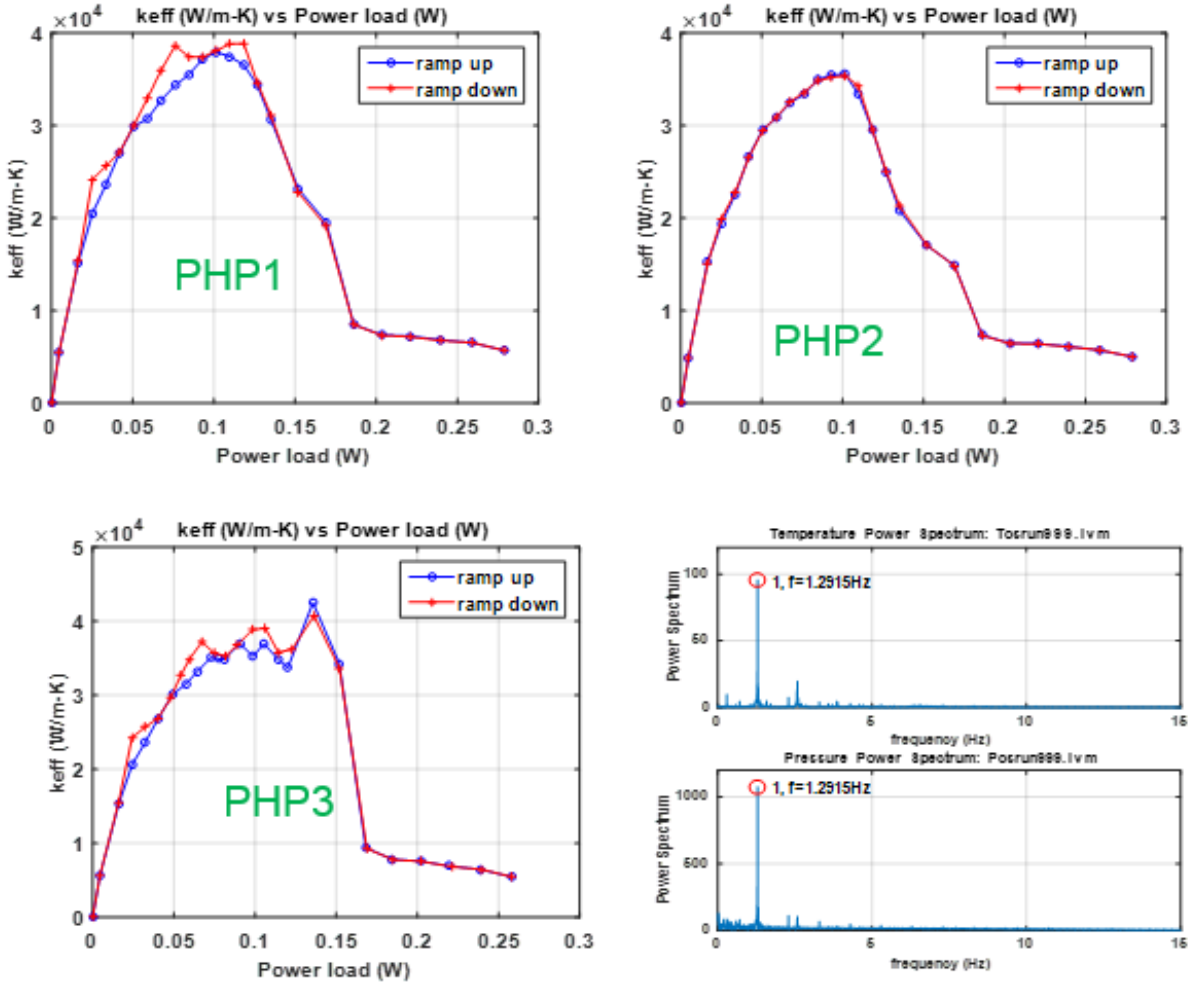

Figure 8-6

8.1.7 Fill ratio at 43.65 % and bottom heaters on

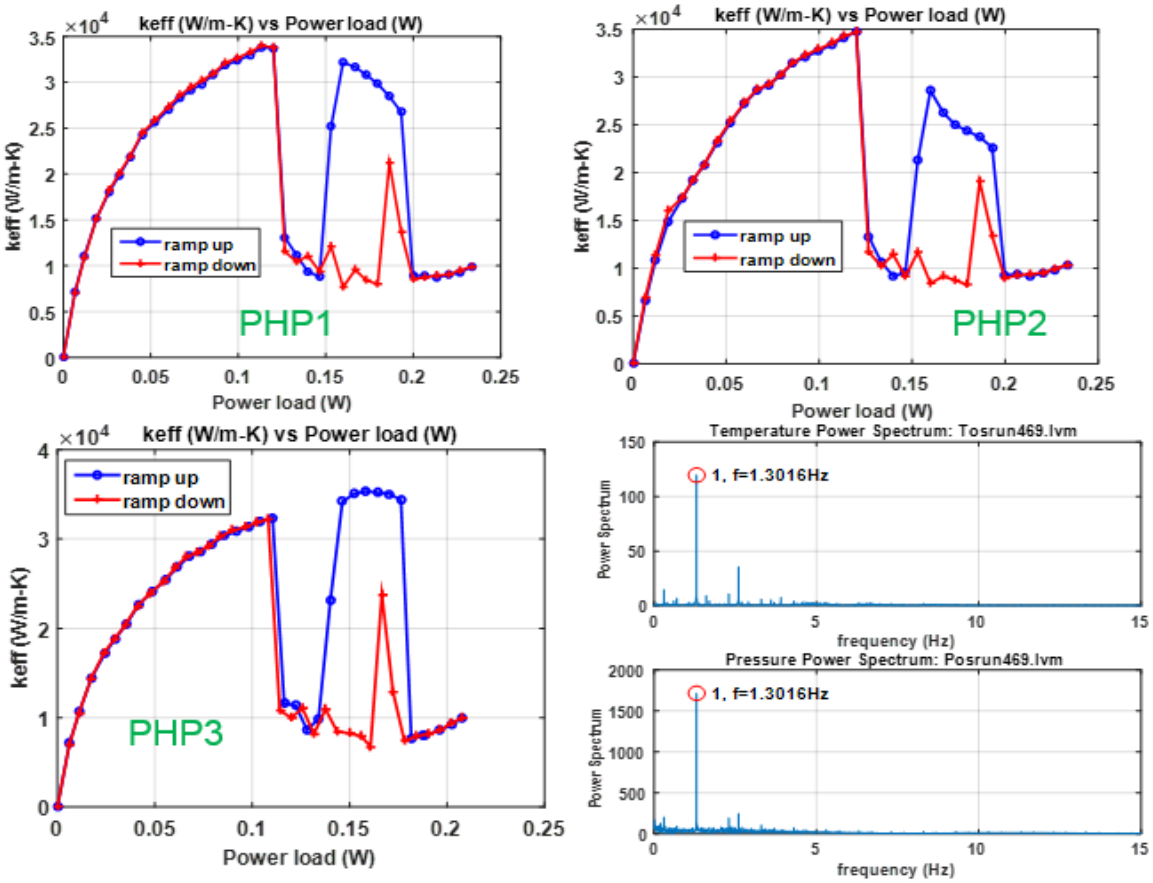

Figure 8-7

8.1.8 Fill ratio at 43.65 % and top heaters on

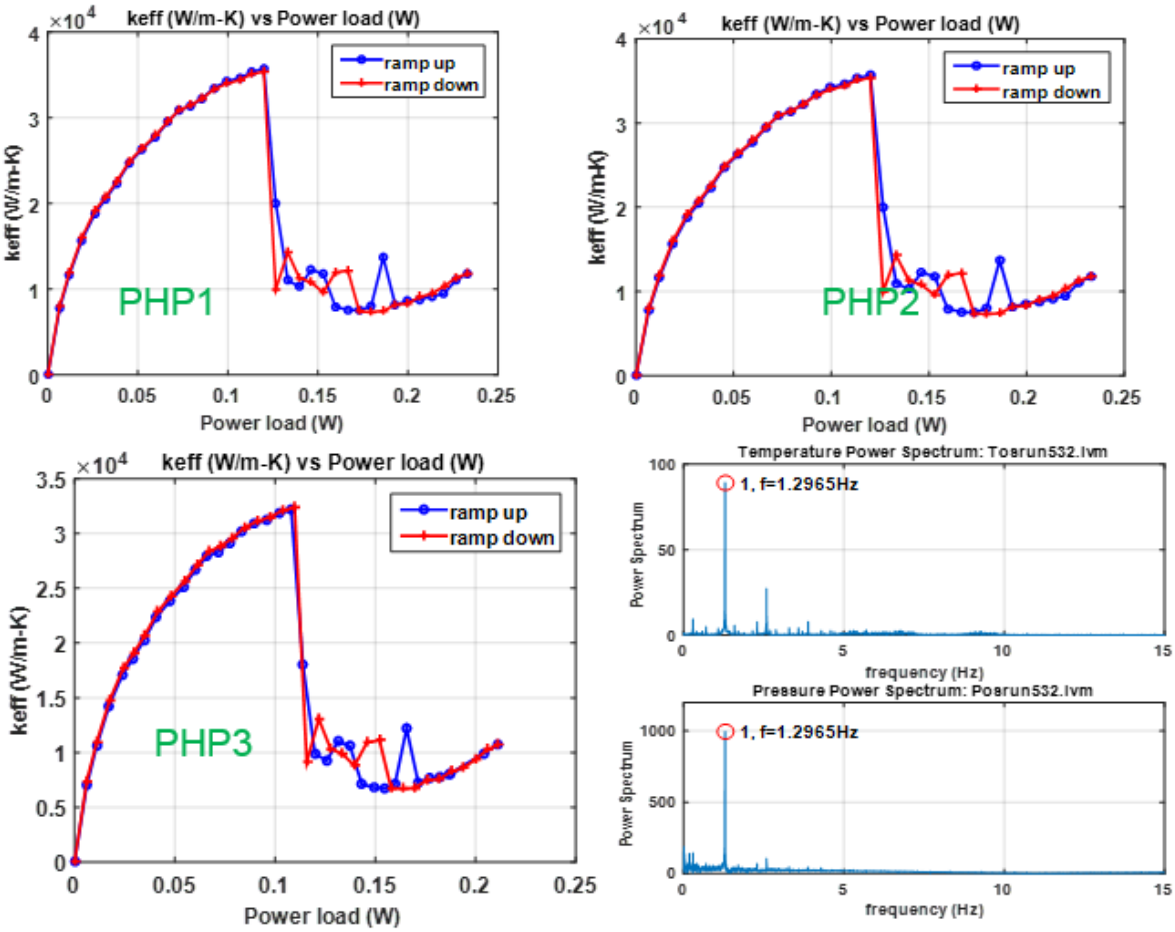

Figure 8-8

8.1.9 Fill ratio at 43.65 % and all heaters on

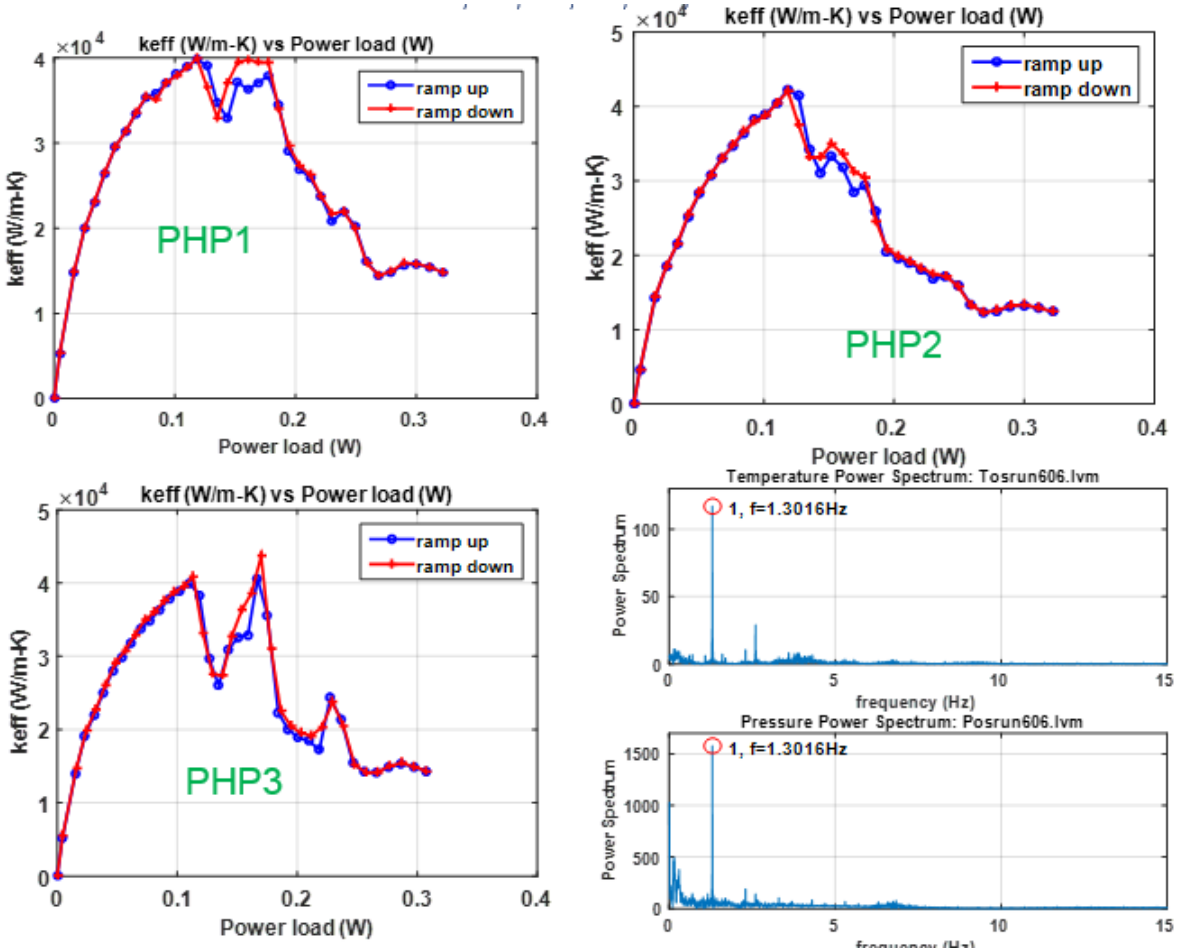

Figure 8-9

8.1.10 Fill ratio at 50.62 % and bottom heaters on

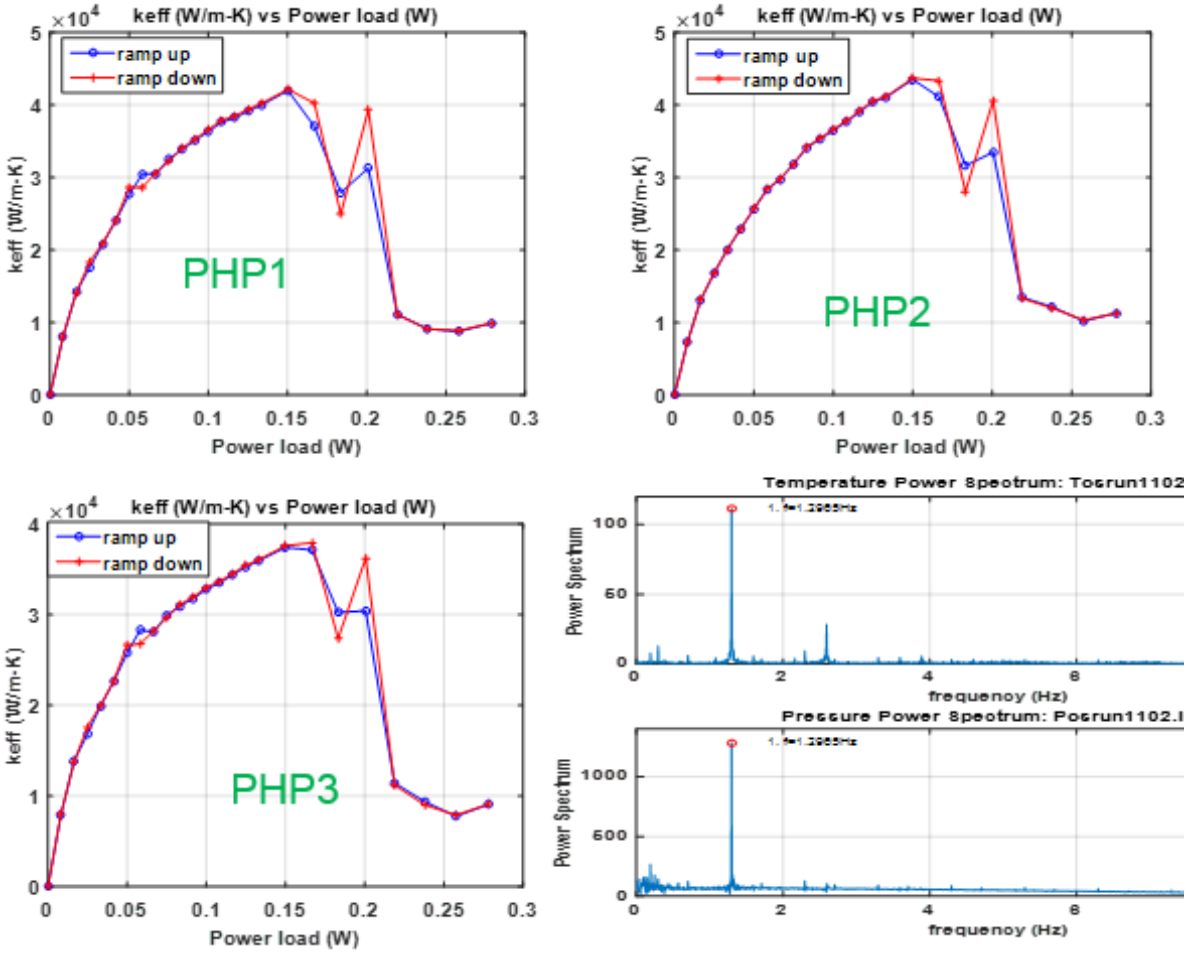

Figure 8-10

8.1.11 Fill ratio at 50.62 % and top heaters on

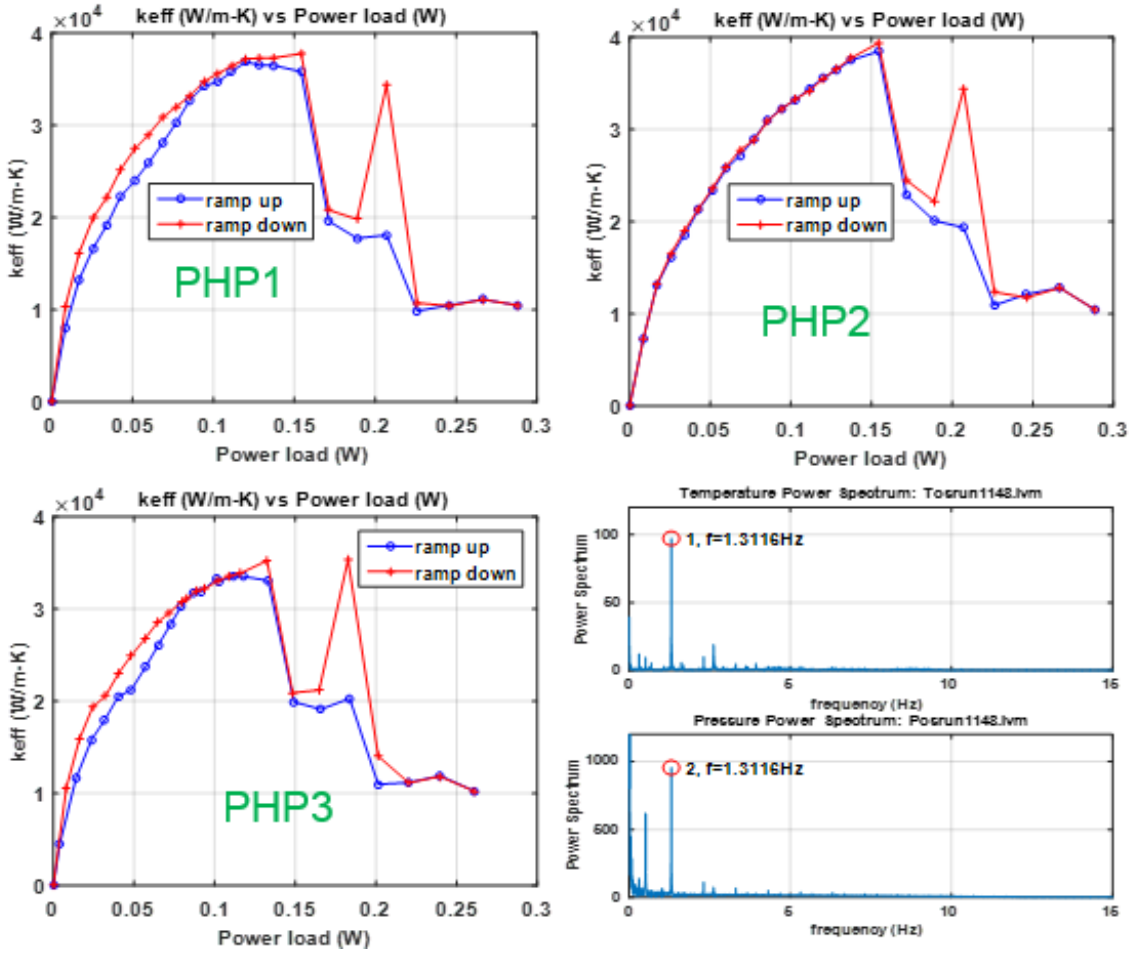

Figure 8-11

8.1.12 Fill ratio at 50.62 % and all heaters on

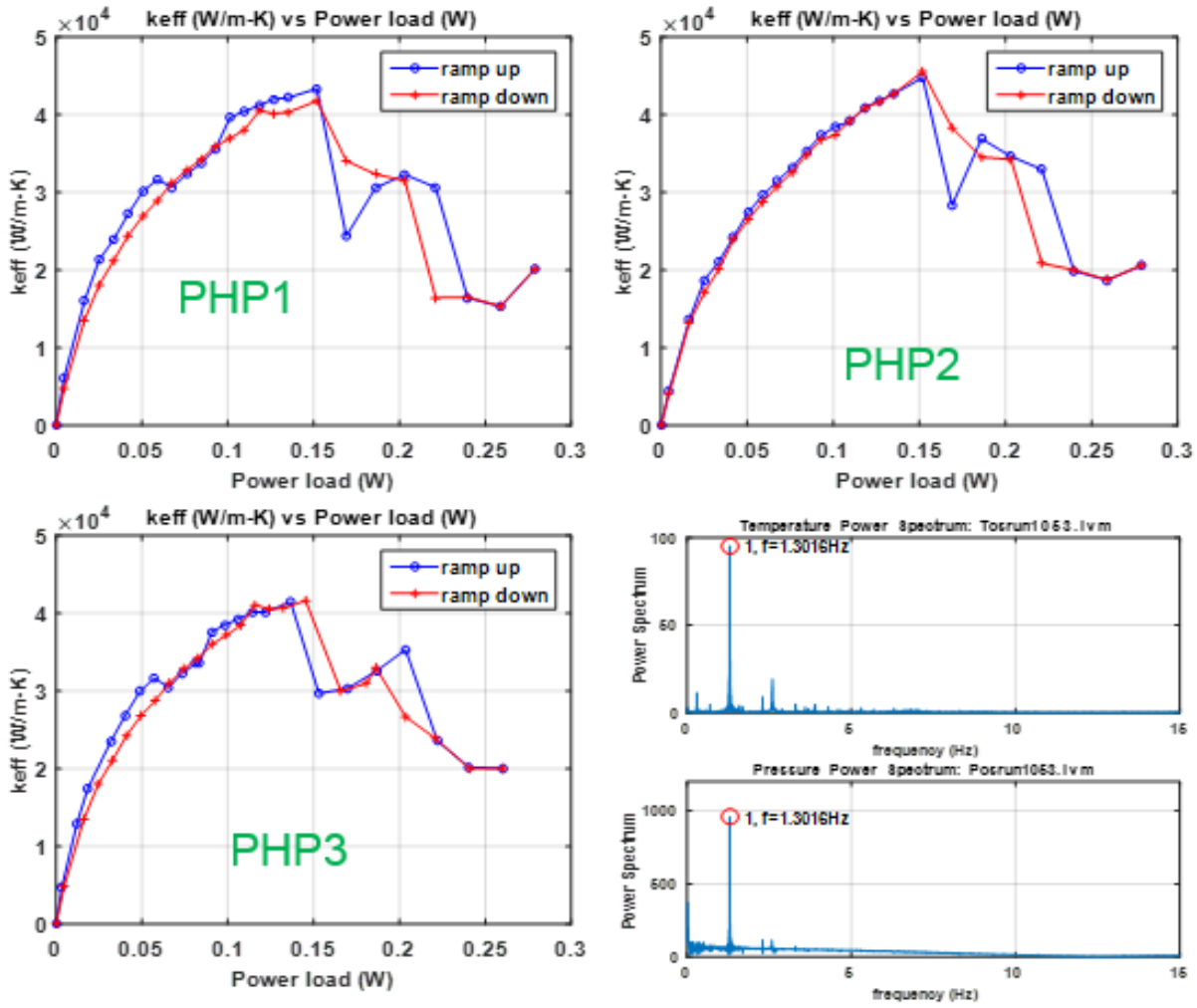

Figure 8-12

8.1.13 Fill ratio at 59.77 % and bottom heaters on

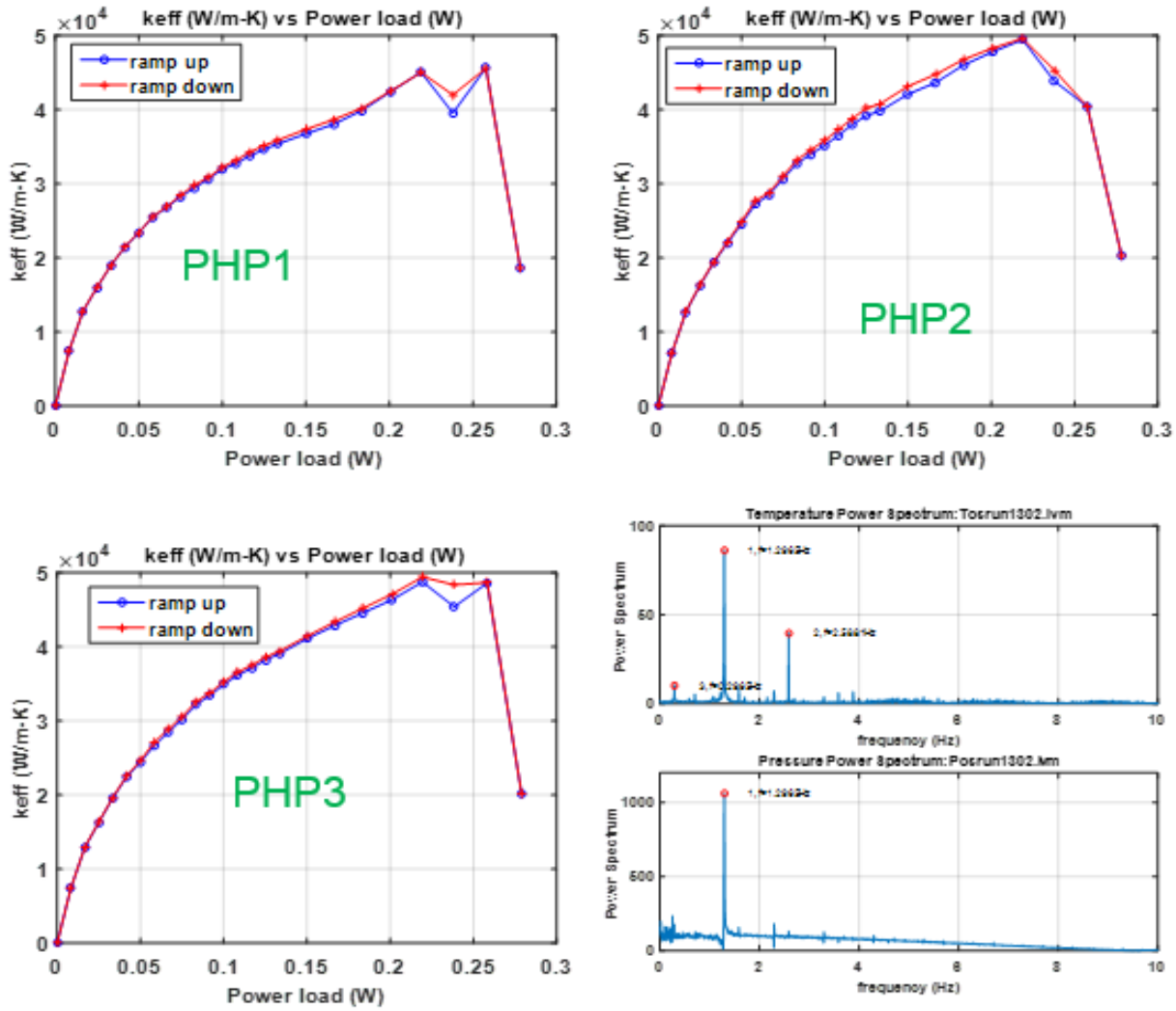

Figure 8-13

8.1.14 Fill ratio at 59.77 % and top heaters on

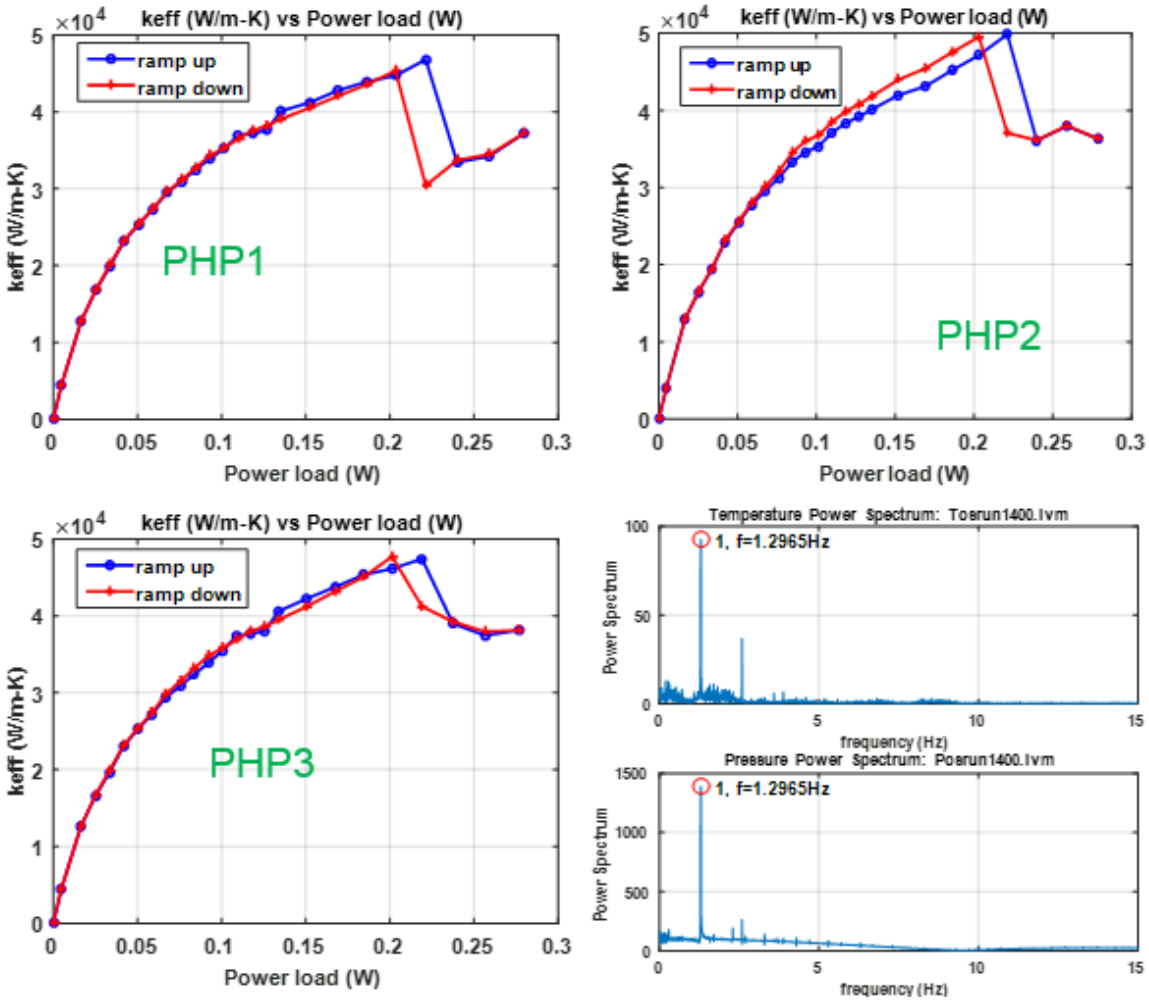

Figure 8-14

8.1.15 Fill ratio at 59.77 % and all heaters on

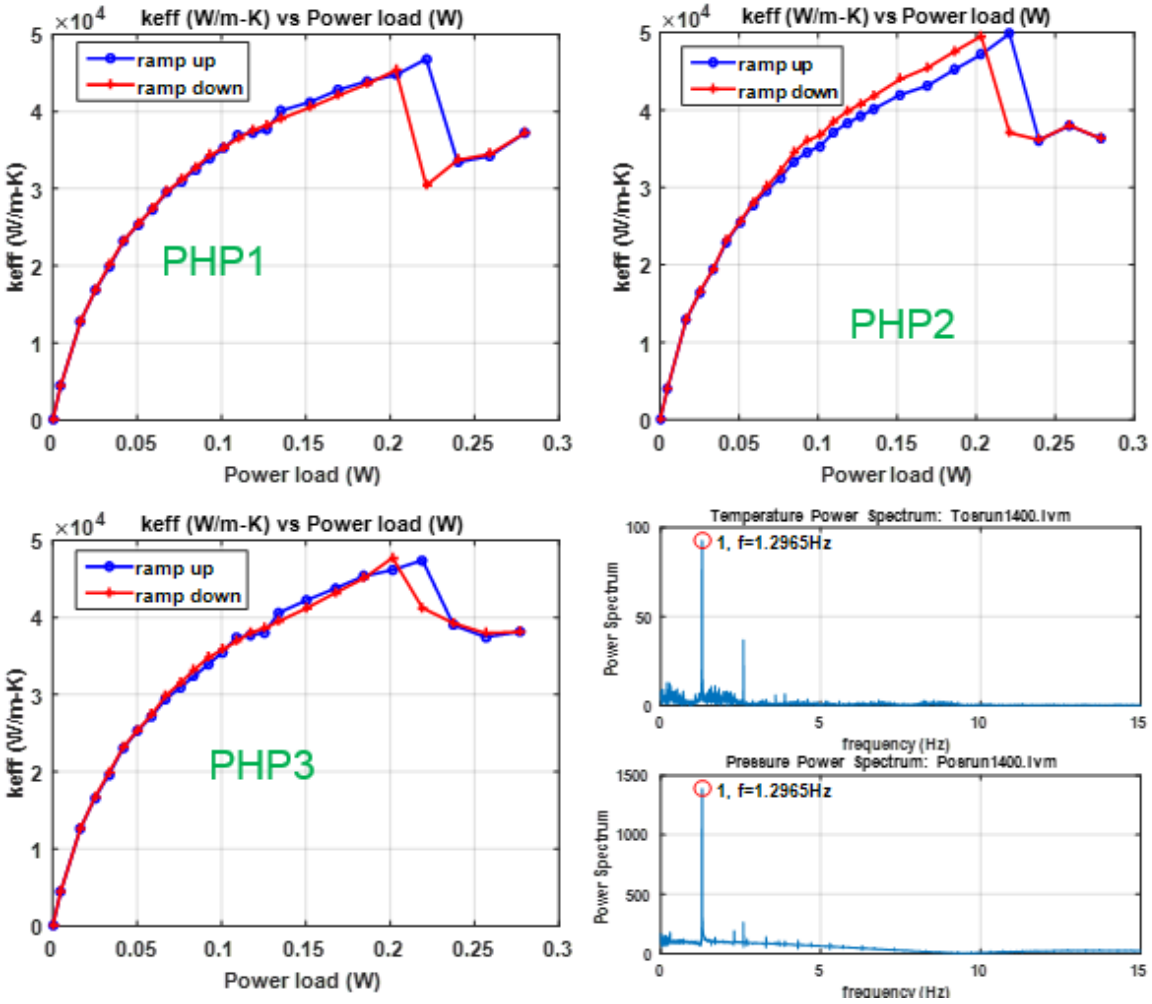

Figure 8-15

8.1.16 Fill ratio at 69.68 % and bottom heaters on

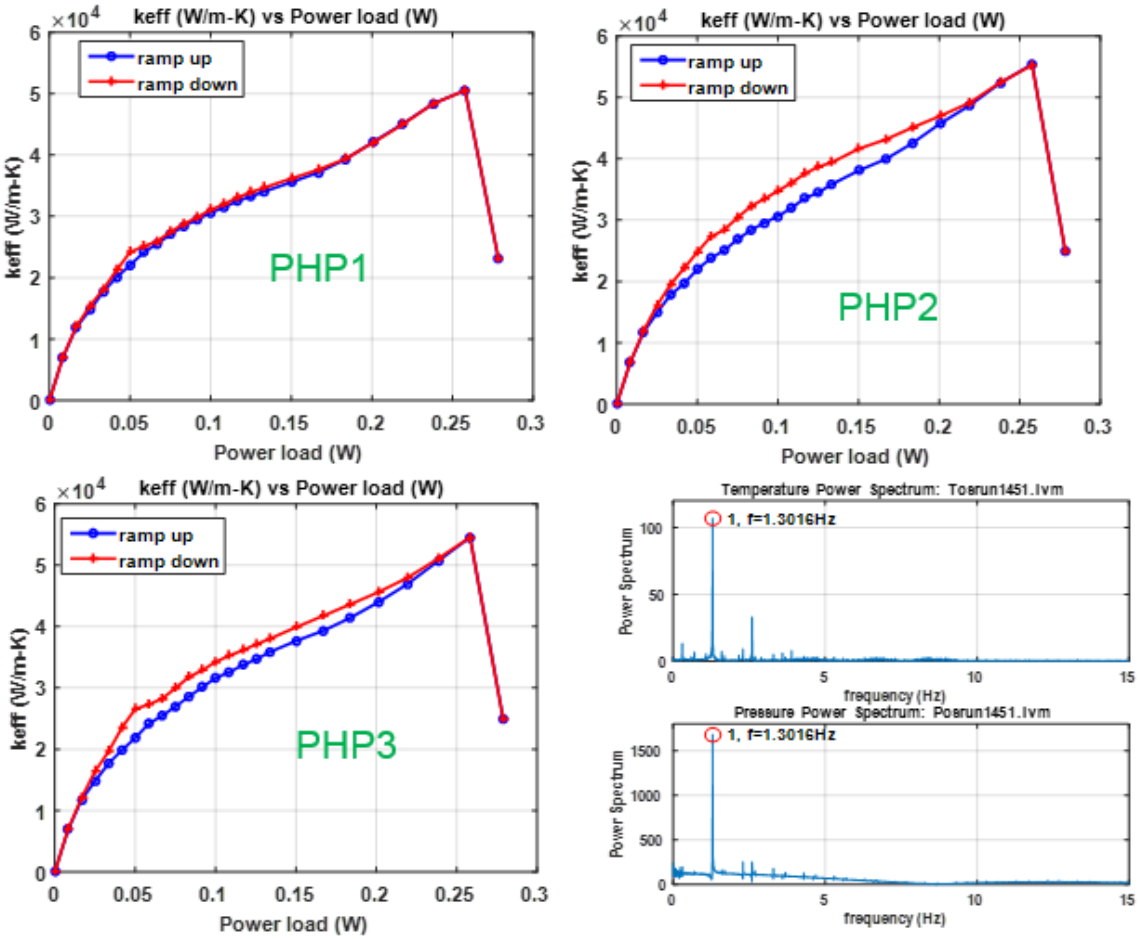

Figure 8-16

8.1.17 Fill ratio at 69.68 % and top heaters on

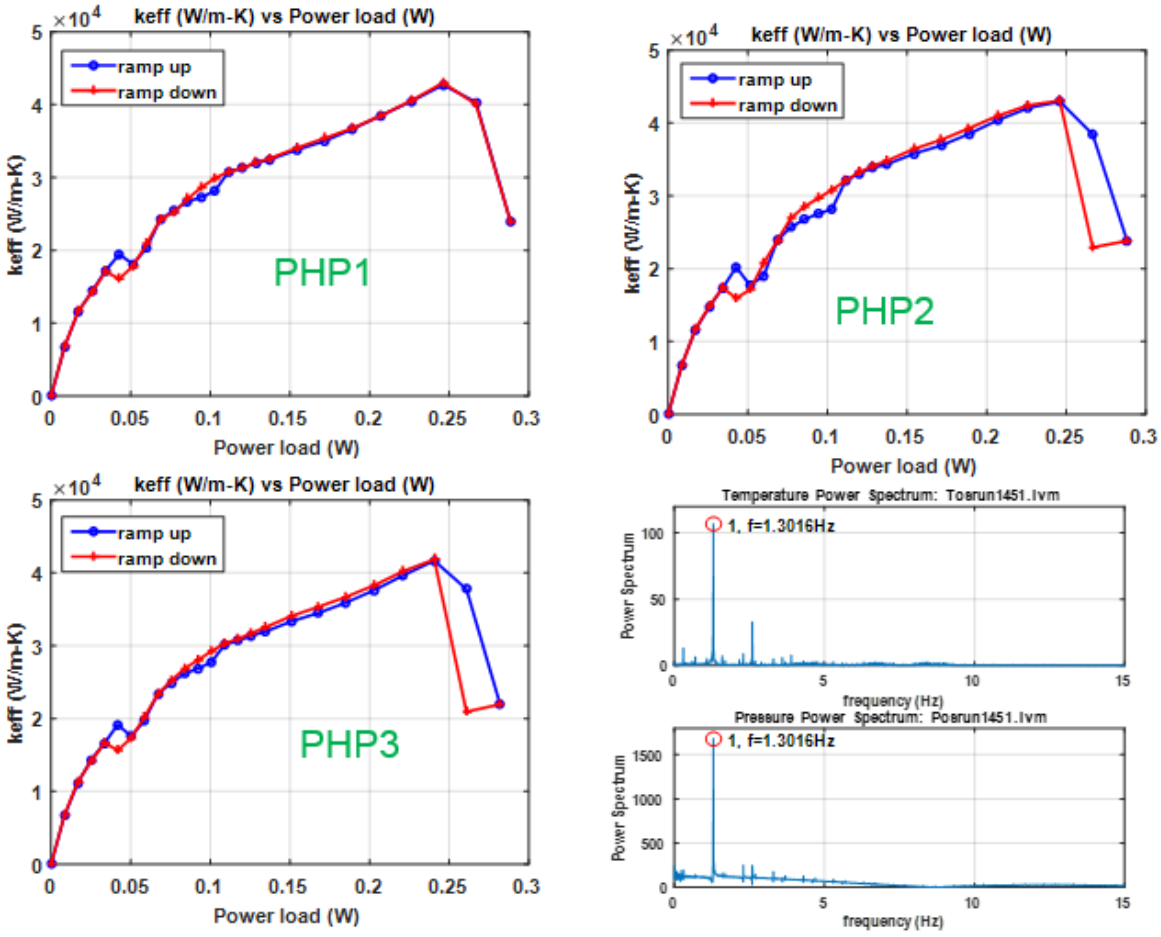

Figure 8-17

8.1.18 Fill ratio at 69.68 % and all heaters on

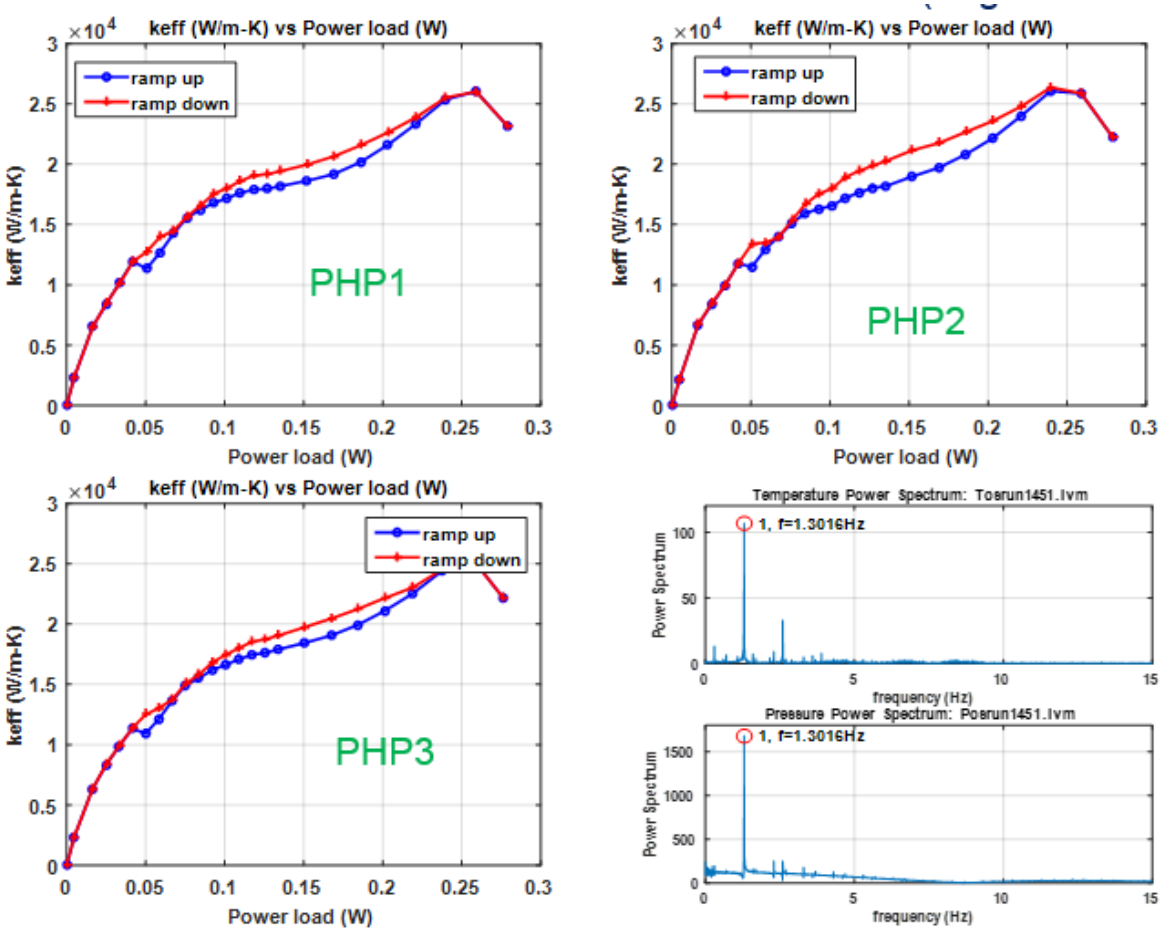

Figure 8-18

8.1.19 Fill ratio at 79.5 % and bottom heaters on

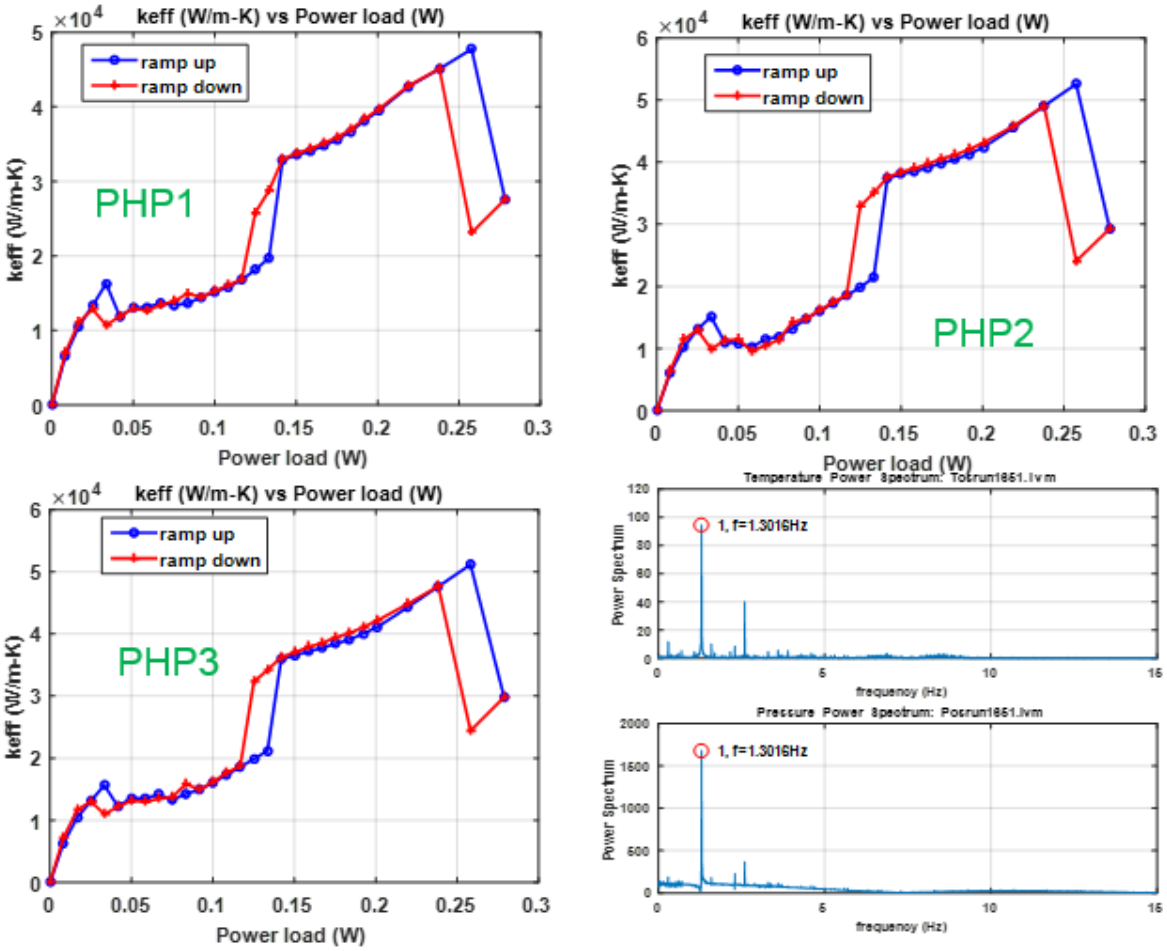

Figure 8-19

8.1.20 Fill ratio at 79.5 % and top heaters on

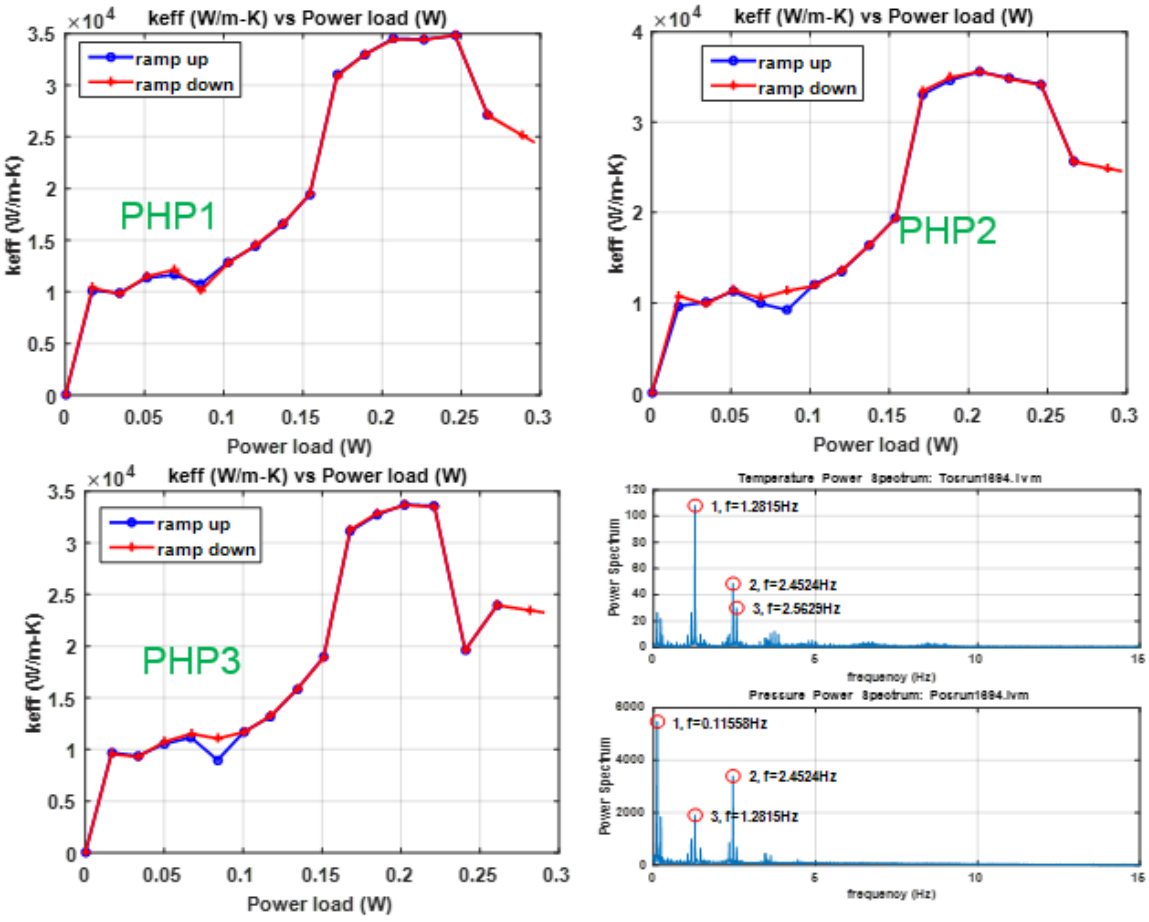

Figure 8-20

8.1.21 Fill ratio at 79.5 % and all heaters on

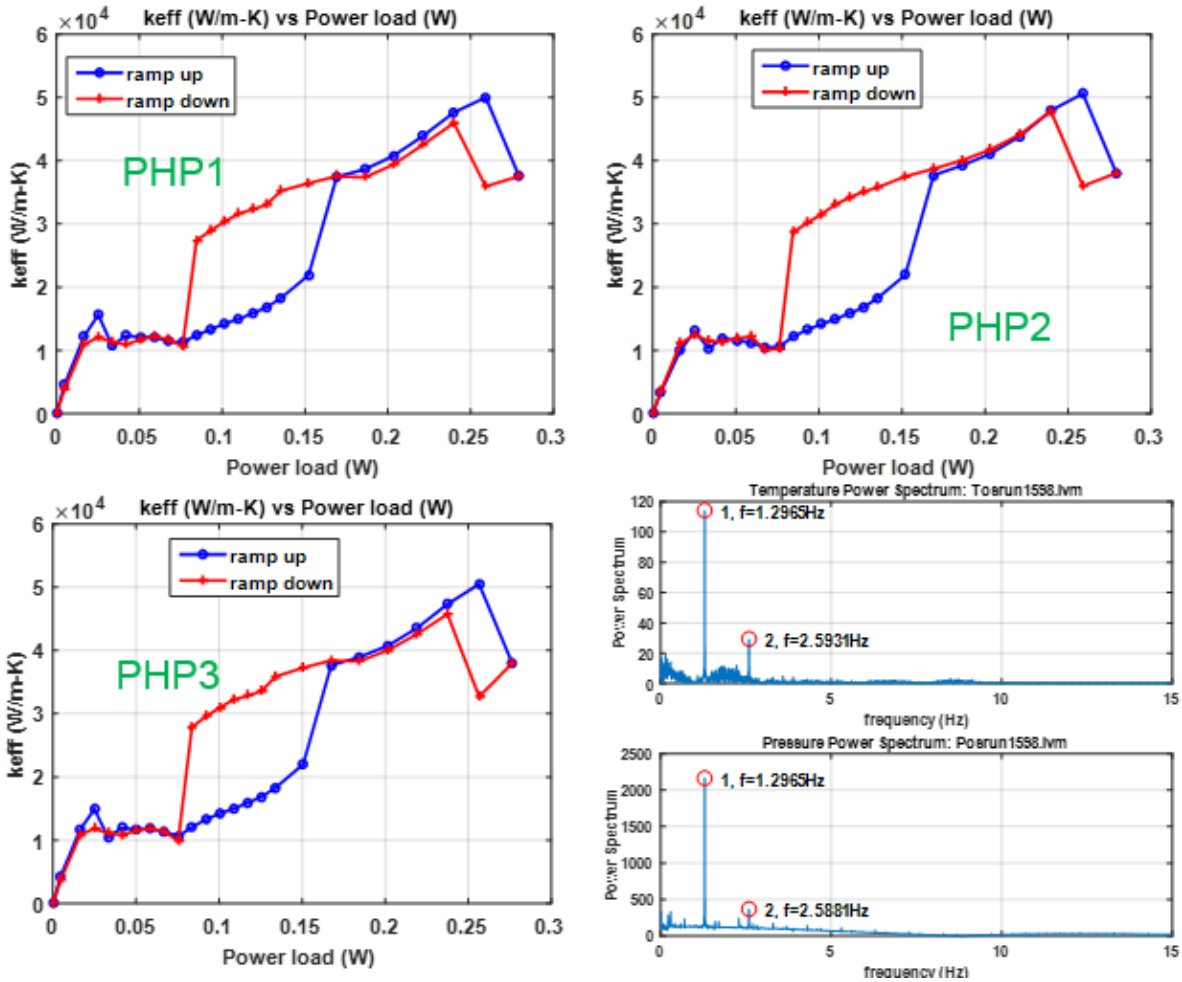

Figure 8-21

8.1.22 Fill ratio at 90.9 % and bottom heaters on

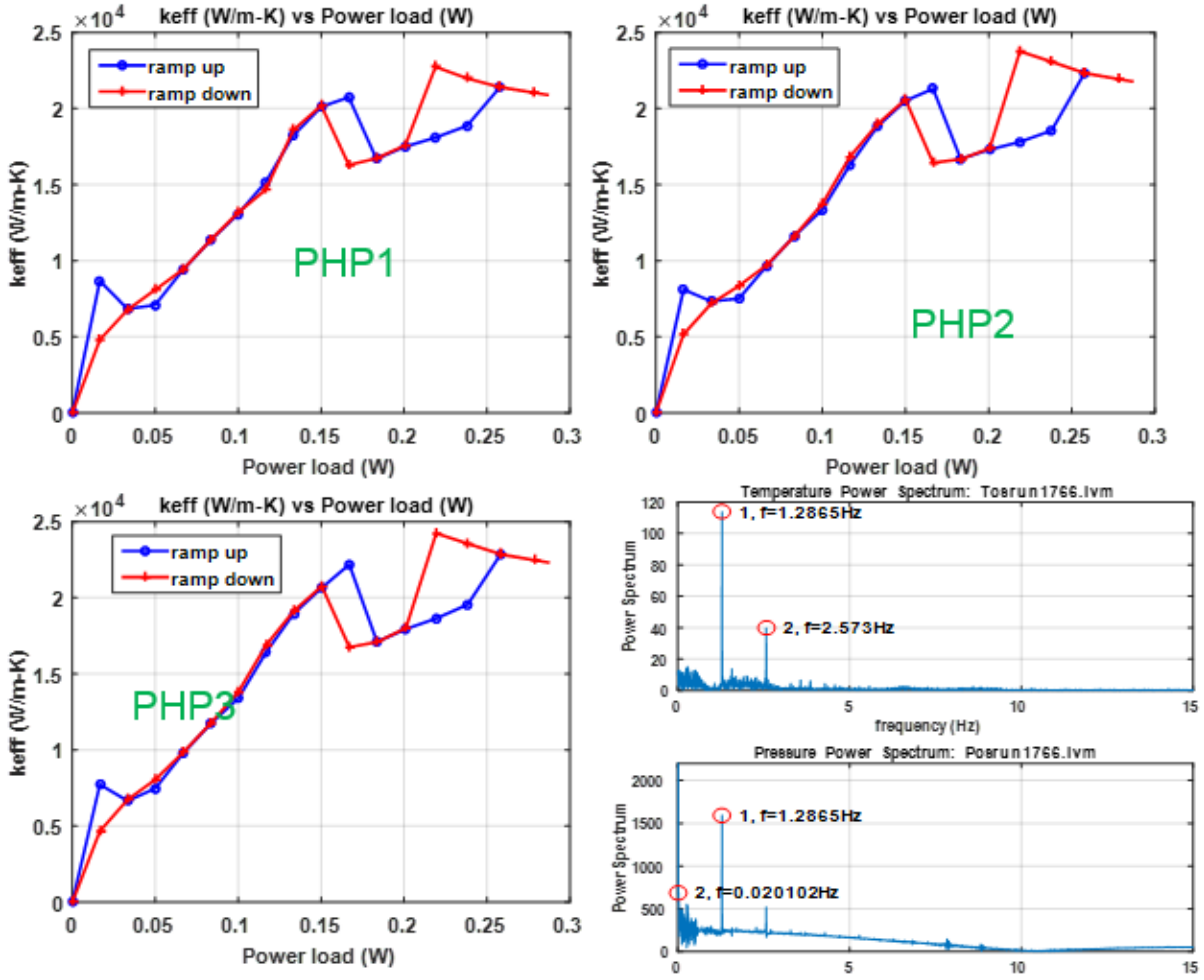

Figure 8-22

8.1.23 Fill ratio at 90.9 % and top heaters on

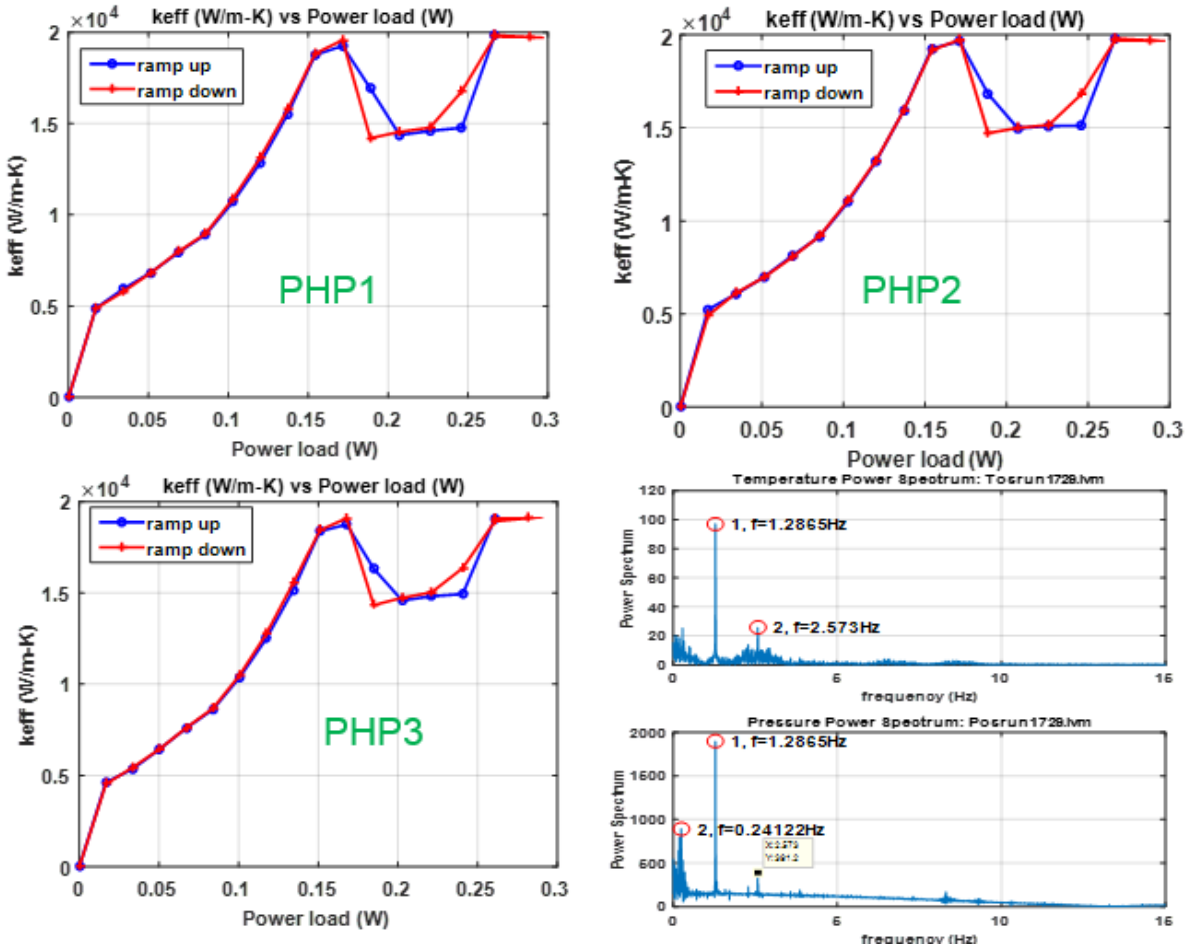

Figure 8-23

8.1.24 Fill ratio at 90.9 % and all heaters on

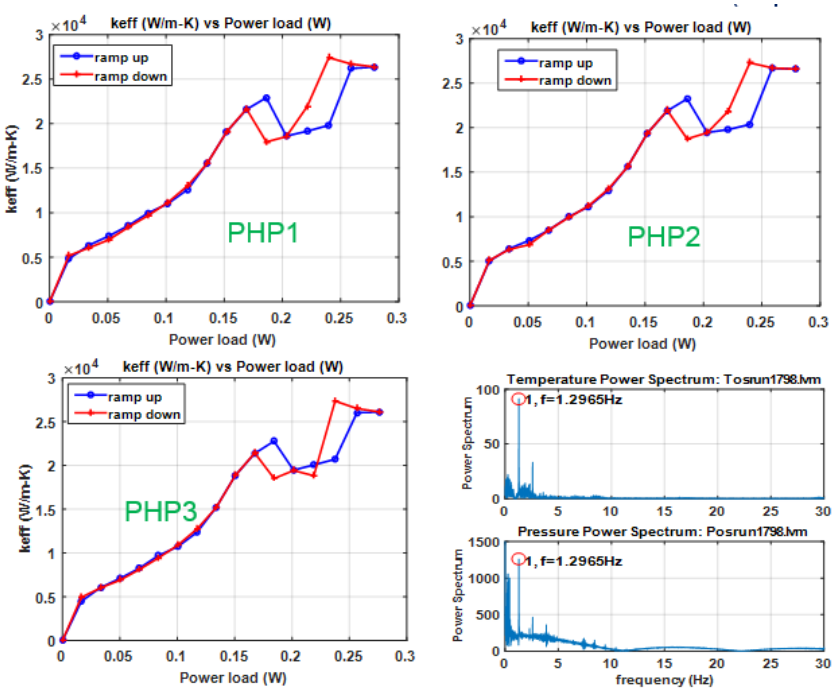

Figure 8-24

8.2 Data with one meter adiabatic length

8.2.1 Raw temperature data at different fill ratios and uniform heat loads with bottom heaters on

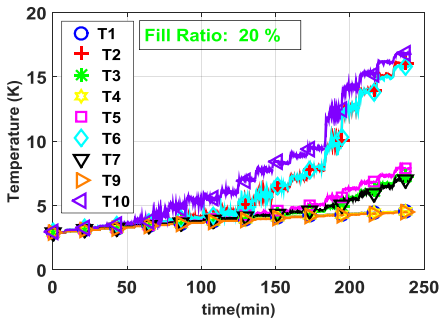

a)

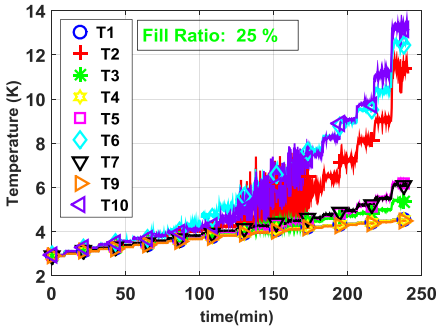

b)

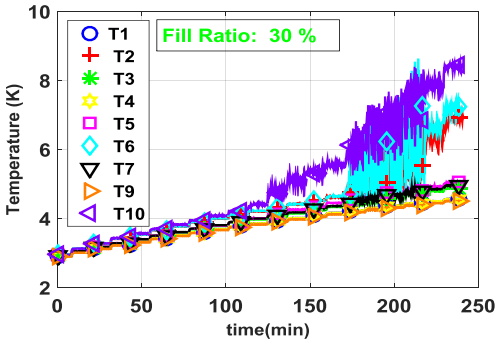
Fill Ratio: 30 %
T1
T2
T3
T4
T5
T6
T7
T9
T10
Temperature (K)
time(min)

c)

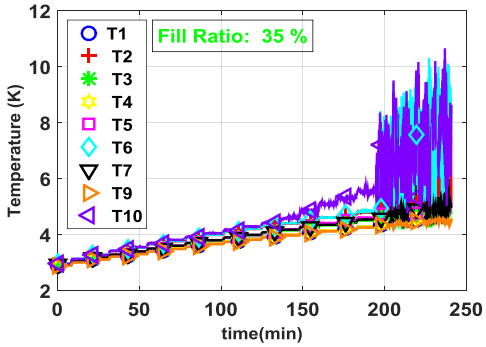
Fill Ratio: 35 %
T1
T2
T3
T4
T5
T6
T7
T9
T10
Temperature (K)
time(min)

d)

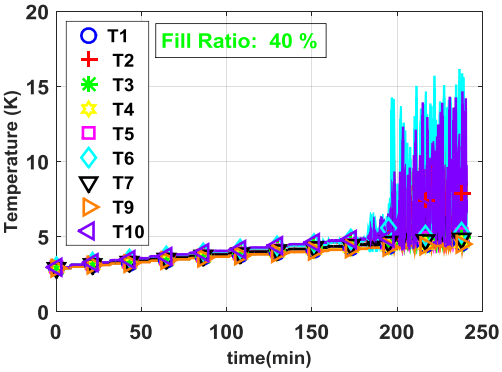
Fill Ratio: 40 %
T1
T2
T3
T4
T5
T6
T7
T9
T10
Temperature (K)
time(min)

e)

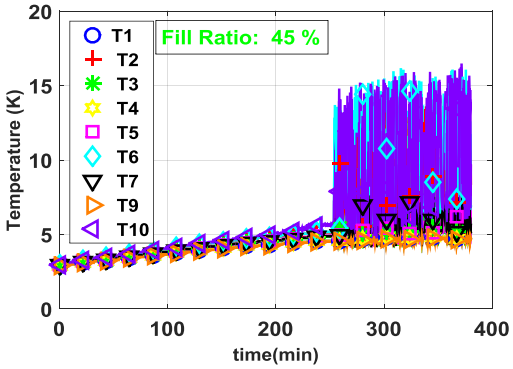
Fill Ratio: 45 %
T1
T2
T3
T4
T5
T6
T7
T9
T10
Temperature (K)
time(min)

f)

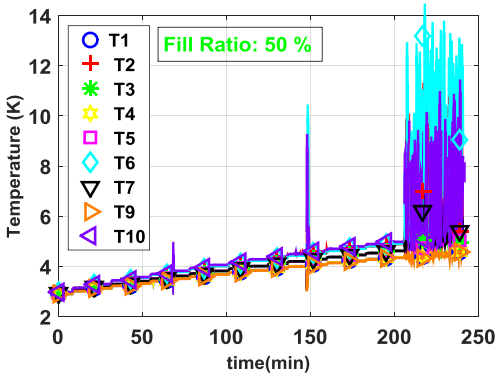
Fill Ratio: 50 %
T1
T2
T3
T4
T5
T6
T7
T9
T10
Temperature (K)
time(min)

g)

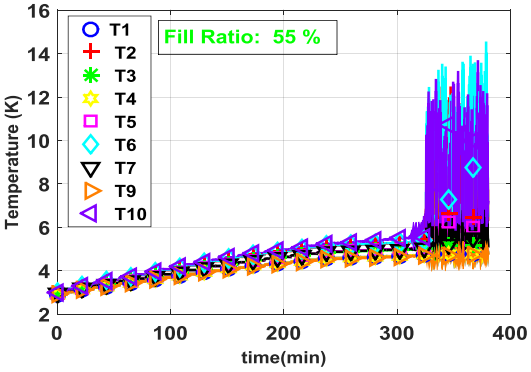
Fill Ratio: 55 %
T1
T2
T3
T4
T5
T6
T7
T9
T10
Temperature (K)
time(min)

h)

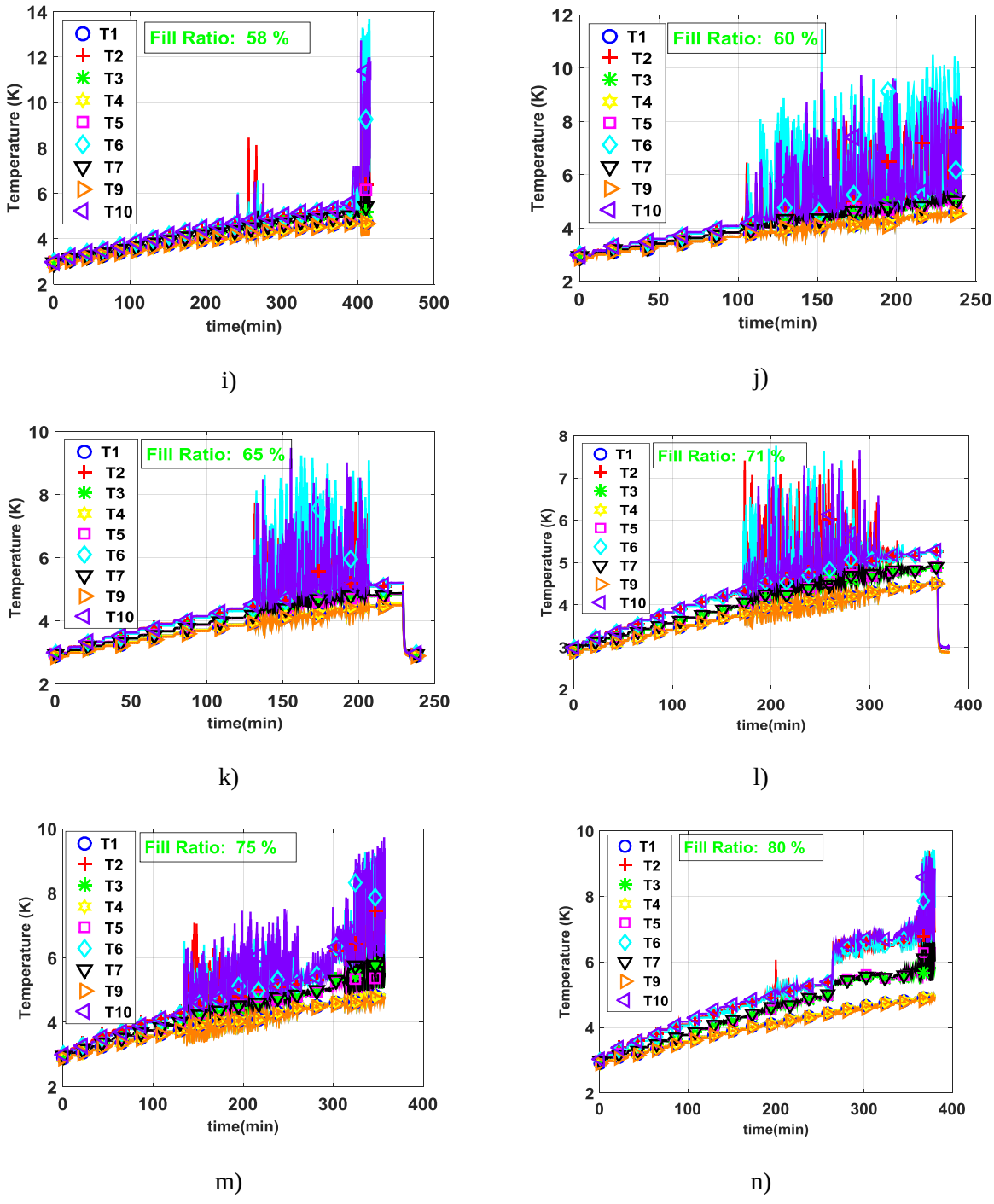

Figure 8-25: Raw temperature data with uniform heat loads applied at bottom heater at initial fill ratios of a) 20 %. b) 25 %. c) 30 %. d) 35 %. e) 40 %. f) 45 %. g) 50 %. h) 55 %. i) 58 %. j) 60 %. k) 65%. l) 71 %. m) 75 %. n) 80 %.